

Alma Mater Studiorum - Università di Bologna

DOTTORATO DI RICERCA IN

Meccanica e Scienze Avanzate dell'Ingegneria

Ciclo XXXII

Settore Concorsuale: 09/C2

Settore Scientifico Disciplinare: ING-IND/10

**DYNAMIC MODELS FOR THE ANALYSIS
OF VAPOUR-COMPRESSION
REFRIGERATING MACHINES**

Presentata da: Michael Lucchi

Coordinatore Dottorato

Prof. Marco Carricato

Supervisore

Prof. Marco Lorenzini

Esame finale anno 2020

Acknowledgments

In the end of these three years, I would like to acknowledge many people without whom this work would not have been possible.

First of all, I want to express my gratitude to my supervisor, Prof. Marco Lorenzini: with your precious suggestions and patience, you always helped me to overcome the obstacles that research and University often put on the way. I want also to take the occasion to thank you for the good times and all the pints we had in UK.

Special thanks go to Prof. Luca Molinaroli, who kindly allowed me to take measurements at the laboratories of the Polytechnic of Milan, thus making it possible to complete this work.

Thanks and infinite gratitude to Lucia, Leonardo, Alessandro, Claudia, Annalisa, Niccolò, Eleonora, Filippo, Marco, Andrea, Giulia, Enrico: you have always been next to me, ready to support and to share good and bad moments. Thanks to all members of my family, for the trust they have always had on me.

I want also to thank all the good friends I met or found in London, during the period I spent at Brunel University, and with whom I shared unforgettable experiences: Johannes, Lauren, Susanna, Matteo, Agnese, Andrea, Vincenzo, Paolo and Valentina.

Abstract

Refrigeration systems represent one of the most relevant fields in terms of energy consumption: about 15% of the worldwide electric energy demand is related to refrigeration processes and a further increase is foreseen for the next decades. Because of the high environmental impact of such plants, many research works have been devoted to finding strategies to reduce their energy consumption. Among them, those related to control systems are appealing, since they usually involve lower costs than interventions at system level.

Control of industrial vapour-compression refrigeration systems directly affects energy consumption and conduction costs of a plant and is decisive for the success of many industrial processes. Simulating the dynamic behaviour of such processes allows to determine the most suitable control systems in terms of energy consumption and of process variables for a given plant configuration. In this work, a library of models able to reproduce the dynamics of the main components of a vapour-compression refrigeration machine (evaporator, condenser, electronic expansion valve, compressor) has been developed to supply the building blocks to investigate the effects of different control strategies on the energy performance and on the control quality of the system. In order to keep the computational cost as low as possible, the switched moving-boundary approach was adopted for the mathematical model of the heat exchangers, considering both finned-tube and brazed-plate heat exchangers.

Because of its large number of solvers available, Matlab/SIMULINK[®] was chosen as implementation platform for the models, which were written under the form of Matlab Level 2 S-Functions.

Firstly, the models were numerically verified, using Thermosys[®], a Matlab toolbox created at the University of Illinois, Urbana-Champaign, as a benchmark. In particular, the dynamic behaviour of an air-to-air refrigerating machine was simulated through both models and the responses were compared, showing a good agreement between the results obtained. The in-house models showed a better repeatability in the prediction of important quantities like refrigerant superheating, subcooling and charge.

The dynamic models were also experimentally validated, comparing their numerical predictions with the experimental data acquired on a water-to-water refrigerating machine equipped with brazed-plate evaporator and condenser and subject to transients typical of actions imposed by the control systems (e.g. variations in valve aperture and in compressor speed). Results showed a very good agreement between numerical and experimental data in terms of refrigerant and secondary fluid conditions at the heat exchangers and in terms

of electric power absorption and COP, thus proving the usefulness of the model in transient energy analysis.

The effects of components like suction accumulator and liquid receiver on the dynamics of the machine were also investigated. In particular, a novel lumped-parameter model combining the dynamics of the condenser and of the receiver was developed, allowing the coexistence of a non-zero subcooling at the condenser outlet and a partial filling condition of the receiver. The results obtained simulating the transient behaviour of the whole water-to-water machine were compared to experimental data. Introducing the dynamics of the receiver and of the suction accumulator allowed to better capture the refrigerant pressure and temperature at the compressor outlet.

Contents

Introduction	1
1 Vapour compression refrigerating machines: an overview	3
1.1 Single-stage vapour compression cycle	3
1.2 Refrigerants	5
1.3 Overview of the main components of a vapour compression re- frigeration machine	6
1.3.1 Compressors	6
1.3.2 Condensers	9
1.3.3 Evaporators	12
1.3.4 Expansion valves	14
1.3.5 Auxiliary components	18
1.4 Multi-stage vapour compression cycles	19
1.5 Strategies to improve cycle thermodynamic efficiency	20
1.6 Research on secondary loop refrigeration systems	22
1.7 Control systems in a refrigeration plant	23
1.7.1 Basic principles on control systems	24
1.7.2 Influence of control systems on energy efficiency of re- frigeration plants	28
2 Dynamic model of the VCC system	33
2.1 General characteristics of dynamic models for VCS	34
2.2 Overview of the applications of the MB approach to VCSs	35
2.3 Modelling approach for the heat exchangers	38
2.4 Mean void fraction correlation	39
2.5 Evaporator	41
2.5.1 Two-regions formulation: two-phase and superheated vapour	42
2.5.2 One-region formulation: two-phase	46
2.5.3 Off-duty formulation	48
2.5.4 Calculation of the refrigerant outlet conditions	50
2.5.5 Calculation of the refrigerant-side heat transfer rate	51
2.5.6 Calculation of the secondary fluid heat transfer rate	52
2.5.7 Correction factors for heat transfer coefficients	55
2.5.8 Switching criteria	55
2.6 Condenser	56

2.6.1	Three-region formulation: superheated vapour, two-phase and subcooled liquid	57
2.6.2	Two-region formulation: superheated vapour and two-phase	60
2.6.3	Two-region formulation: two-phase and subcooled liquid	61
2.6.4	One-region formulation: two-phase	63
2.6.5	Off-duty formulation	64
2.6.6	Calculation of the refrigerant outlet conditions	66
2.6.7	Calculation of the refrigerant-side heat transfer rate	66
2.6.8	Calculation of the secondary fluid heat transfer rate	67
2.6.9	Correction factors for the heat transfer coefficients	69
2.6.10	Switching criteria	69
2.7	Compressor	71
2.8	Electronic expansion valve	72
3	Model implementation	75
3.1	Structure of a Matlab Level 2 S-Function	76
3.2	S-Function for the heat exchanger models	77
3.2.1	Evaporator initialization	79
3.2.2	Condenser initialization	83
3.3	S-Function for the compressor model	86
3.4	S-Function for the EEV model	87
3.5	Fluid properties	87
3.5.1	Refrigerant	88
3.5.2	Secondary fluids	88
4	Numerical Verification	91
4.1	Description of the system	92
4.2	Verification of the EEV model	92
4.3	Verification of the finned-tube evaporator model	93
4.3.1	Results for Test 1	94
4.3.2	Results for Test 2	95
4.4	Verification of the finned-tube condenser model	96
4.4.1	Results for Test 1	97
4.4.2	Results for Test 2	99
4.5	Verification of the air-to-air machine model	100
4.5.1	Results for Test 1	101
4.5.2	Results for Test 2	102
4.6	Conclusions	105
5	Experimental Validation	107
5.1	The machine and the experimental setup	108
5.1.1	Components of the refrigerating machine	109
5.1.2	Measurement instrumentation	110
5.2	Experimental campaign	112
5.2.1	Test 1: steps in the valve opening	112
5.2.2	Test 2: steps in the compressor frequency	116

5.3	Valve tuning and validation	118
5.3.1	Validation under Test 1 conditions	119
5.3.2	Validation under Test 2 conditions	119
5.4	Compressor tuning and validation	120
5.4.1	Validation under Test 2 conditions	122
5.4.2	Validation under Test 1 conditions	123
5.5	Evaporator tuning and validation	125
5.5.1	Validation under Test 1 conditions	125
5.5.2	Validation under Test 2 conditions	128
5.6	Condenser tuning and validation of the machine model	132
5.6.1	Validation under Test 1 conditions	133
5.6.2	Validation under Test 2 conditions	143
5.7	Conclusions	148
6	Effects of the refrigerant accumulators on the dynamics of the VCS	155
6.1	Brazed-plate evaporator and suction accumulator model	155
6.2	Brazed-plate condenser and liquid receiver model	158
6.2.1	Subcooled liquid at the condenser outlet	159
6.2.2	Two-phase conditions at the condenser outlet	160
6.3	Results	161
6.3.1	Test 1	161
6.3.2	Test 2	165
6.4	Conclusions	168
	Conclusions	171

List of Figures

1.1	Basic schematic of a vapour compression refrigerating machine. . .	4
1.2	P-h diagram of a simple vapour compression cycle.	4
1.3	Range of refrigeration capacity of various types of compressor . .	6
1.4	Cutaway view of a multi-cylinder reciprocating compressor . . .	7
1.5	Cutaway view of a screw compressor.	8
1.6	Cutaway view of a scroll compressor	9
1.7	Simplified schematic of a sliding vanes compressor	10
1.8	Air-cooled condenser for domestic applications.	10
1.9	Roof mounted air-cooled condenser	10
1.10	Double-pipe water-cooled condenser.	11
1.11	Shell-and-tube water-cooled condenser.	11
1.12	Brazed-plate heat exchanger.	12
1.13	Evaporative condenser	12
1.14	Finned-tubes evaporator.	14
1.15	Shell-and-tube flooded evaporator.	14
1.16	Coils flooded evaporator	15
1.17	Shell-and-tube direct expansion evaporator for water cooling . .	15
1.18	Coils direct expansion evaporator	15
1.19	Capillary tube.	16
1.20	Circuit of a thermostatic expansion valve	16
1.21	Cutaway view of a thermostatic expansion valve	17
1.22	Cutaway view of an electronic expansion valve and view of the shutter positions	17
1.23	Schematic of a low-pressure float valve	18
1.24	Effects of subcooling on the isenthalpic expansion and the re- frigerating capacity	19
1.25	Schematic of a vapour compression cycle with an expander in- stead of an expansion valve and characteristic points on the $P - h$ diagram.	21
1.26	Schematic of a vapour compression cycle with an ejector and characteristic points on the $P - h$ diagram.	21
1.27	Schematic of a refrigeration system with a secondary loop. . . .	22
1.28	Generic schematic of a controlled system with the main signals involved.	25
1.29	Generic schematic of a feedback control.	25
1.30	Generic schematic of an on-off controller.	26
1.31	Schematic of the proportional action in a PID controller.	26

1.32	Schematic of the integral action in a PID controller.	27
1.33	Schematic of the derivative action in a PID controller.	27
2.1	Scheme of the model of a vapour compression refrigeration system: input-output connection of the models of the single components.	34
2.2	Evaporator discretization using the SMB approach: two-regions formulation.	41
2.3	Possible switches for the evaporator model.	55
2.4	Condenser discretization using the SMB approach: three-region formulation.	57
2.5	Possible switches for the condenser model.	70
3.1	Scheme of the basic operating principle of an S-Function.	76
3.2	Main stages of a dynamic simulation carried out in Simulink environment	77
3.3	S-Function block of the brazed-plate evaporator: inputs and outputs on the left and right end sides respectively.	78
3.4	View of the parameters mask for the brazed-plate evaporator.	79
3.5	S-Function block of the compressor: inputs and outputs on the left and right end sides respectively.	87
3.6	S-Function block of the electronic expansion valve: inputs and outputs on the left and right end sides respectively.	88
3.7	Scheme for the calculation of partial derivatives in the interpolation procedure.	89
4.1	Refrigerant mass flow rate through the valve in the EEV model verification: comparison between Thermosys [®] and Unibo	94
4.2	Evaporation pressure (a) and refrigerant mass (b) in the finned-tube evaporator model verification: comparison between Thermosys [®] and Unibo in Test1.	95
4.3	Non-dimensional extension of the TP region in the finned-tube evaporator model: comparison between Thermosys [®] and Unibo in Test 1.	95
4.4	Refrigerant superheating (a) and air outlet temperature (b) in the finned-tube evaporator model verification: comparison between Thermosys [®] and Unibo in Test 1.	96
4.5	Evaporation pressure (a) and refrigerant mass (b) in the finned-tube evaporator model verification: comparison between Thermosys [®] and Unibo in Test 2.	96
4.6	Non-dimensional extension of the TP region in the finned-tube evaporator model: comparison between Thermosys [®] and Unibo in Test2.	97
4.7	Refrigerant superheating (a) and air outlet temperature (b) in the finned-tube evaporator model verification: comparison between Thermosys [®] and Unibo in Test 2.	97

4.8	Condensation pressure (a) and refrigerant mass (b) in the finned-tube condenser model verification: comparison between Thermosys [®] and Unibo in Test1.	98
4.9	Non-dimensional extension of the V (a) and TP (b) regions in the finned-tube condenser model verification: comparison between Thermosys [®] and Unibo in Test 1.	98
4.10	Refrigerant subcooling (a) and air outlet temperature (b) in the finned-tube condenser model verification: comparison between Thermosys [®] and Unibo in Test 1.	99
4.11	Condensation pressure (a) and refrigerant mass (b) in the finned-tube condenser model verification: comparison between Thermosys [®] and Unibo in Test2.	100
4.12	Non-dimensional extension of the V (a) and TP (b) regions in the finned-tube condenser model: comparison between Thermosys [®] and Unibo in Test 2.	100
4.13	Refrigerant subcooling (a) and air outlet temperature (b) in the finned-tube condenser model verification: comparison between Thermosys [®] and Unibo in Test 2.	101
4.14	Condensation (a) and evaporation (b) pressure in the verification of the air-to-air machine: comparison between Thermosys [®] and Unibo in Test1.	102
4.15	Refrigerant mass flow rate through the EEV (a) and global refrigerant mass (b) in the verification of the air-to-air machine: comparison between Thermosys [®] and Unibo in Test1.	102
4.16	Refrigerant subcooling (a) and superheating (b) in the verification of the air-to-air machine: comparison between Thermosys [®] and Unibo in Test1.	103
4.17	Air outlet temperatures at the condenser (a) and at the evaporator (b) in the verification of the air-to-air machine: comparison between Thermosys [®] and Unibo in Test1.	103
4.18	Refrigerant mass flow rate through the EEV (a) and global refrigerant mass (b) in the verification of the air-to-air machine: comparison between Thermosys [®] and Unibo in Test2.	104
4.19	Condensation (a) and evaporation (b) pressure in the verification of the air-to-air machine: comparison between Thermosys [®] and Unibo in Test2.	104
4.20	Refrigerant subcooling (a) and superheating (b) in the verification of the air-to-air machine: comparison between Thermosys [®] and Unibo in Test2.	105
4.21	Air outlet temperatures at the condenser (a) and at the evaporator (b) in the verification of the air-to-air machine: comparison between Thermosys [®] and Unibo in Test2.	105
5.1	Experimental facility located at the Polytechnic of Milan.	108
5.2	Layout of the experimental facility.	109
5.3	Measured refrigerant mass flow rate during Test 1.	113

5.4	Measured pressures during Test 1. (a) Compressor Inlet. (b) Compressor outlet, condenser inlet and outlet.	114
5.5	Electric power absorbed by the compressor during Test 1.	114
5.6	Inlet and outlet temperatures of the water-glycol mixture at the evaporator (a) and of the water at the condenser (b) during Test 1.	115
5.7	Measured refrigerant temperatures, superheating and subcooling during Test 1. (a) Evaporator. (b) Condenser.	115
5.8	Measured mass flow rate of water-glycol mixture at the evaporator (a) and of the water at the condenser (b) during Test 1.	115
5.9	Measured refrigerant mass flow rate during Test 2.	116
5.10	Measured pressures during Test 2. (a) Compressor Inlet. (b) Compressor outlet, condenser inlet and outlet.	117
5.11	Electric power absorbed by the compressor during Test 2.	117
5.12	Inlet and outlet temperatures of the water-glycol mixture at the evaporator (a) and of the water at the condenser (b) during Test 2.	117
5.13	Measured refrigerant temperatures, superheating and subcooling during Test 2. (a) Evaporator. (b) Condenser.	118
5.14	Measured mass flow rate of water-glycol mixture at the evaporator (a) and of the water at the condenser (b) during Test 2.	118
5.15	Validation of the valve model. Comparison between the experimental mass flow rate and the value predicted by the valve model (a) and percentage deviation (b) with $C_{D0} = 0.25$ under Test 1 conditions.	119
5.16	Validation of the valve model. Comparison between the experimental mass flow rate and the value predicted by the valve model (a) and percentage deviation (b) with $C_{D0} = 0.58$ under Test 1 conditions.	120
5.17	Validation of the valve model. Comparison between the experimental mass flow rate and the value predicted by the valve model (a) and percentage deviation (b) with $C_{D0} = 0.25$ under Test 2 conditions.	120
5.18	Validation of the valve model. Comparison between the experimental mass flow rate and the value predicted by the valve model (a) and percentage deviation (b) with $C_{D0} = 0.58$ under Test 2 conditions.	121
5.19	Refrigerant temperature at the compressor discharge section in Test 2. The steps in frequency occur at τ_i and τ_f ; the time constant τ_k is evaluated when the the temperature reaches the 63% of its value at τ_f	121
5.20	Validation of the compressor model. Comparison between the predicted and experimental refrigerant mass flow rate (a) and percentage deviation (b) with $C_{m_r} = 1$ under Test 2 conditions.	122

5.21	Validation of the compressor model. Comparison between the predicted and experimental refrigerant mass flow rate (a) and percentage deviation (b) with $C_{\dot{m}_r} = 1.02$ under Test 2 conditions.	123
5.22	Validation of the compressor model. Comparison between the predicted and experimental electric power absorbed (a) and percentage deviation (b) with $C_{\dot{W}_{el}} = 1$ under Test 2 conditions.	123
5.23	Validation of the compressor model. Comparison between the predicted and experimental electric power absorbed (a) and percentage deviation (b) with $C_{\dot{W}_{el}} = 1.05$ under Test 2 conditions.	124
5.24	Validation of the compressor model. Comparison between the predicted and experimental refrigerant temperature at the compressor outlet (a) and absolute deviation (b) with $C_T = 1$ under Test 2 conditions.	124
5.25	Validation of the compressor model. Comparison between the predicted and experimental refrigerant temperature at the compressor outlet (a) and absolute deviation (b) with $C_T = 0.95$ under Test 2 conditions.	125
5.26	Validation of the compressor model. Comparison between the predicted and experimental refrigerant mass flow rate (a) and percentage deviation (b) with $C_{\dot{m}_r} = 1$ under Test 1 conditions.	125
5.27	Validation of the compressor model. Comparison between the predicted and experimental refrigerant mass flow rate (a) and percentage deviation (b) with $C_{\dot{m}_r} = 1.02$ under Test 1 conditions.	126
5.28	Validation of the compressor model. Comparison between the predicted and experimental electric power absorbed (a) and percentage deviation (b) with $C_{\dot{W}_{el}} = 1$ under Test 1 conditions.	126
5.29	Validation of the compressor model. Comparison between the predicted and experimental electric power absorbed (a) and percentage deviation (b) with $C_{\dot{W}_{el}} = 1.05$ under Test 1 conditions.	127
5.30	Validation of the compressor model. Comparison between the predicted and experimental refrigerant temperature at the compressor outlet (a) and absolute deviation (b) with $C_T = 1$ under Test 1 conditions.	127
5.31	Validation of the compressor model. Comparison between the predicted and experimental refrigerant temperature at the compressor outlet (a) and absolute deviation (b) with $C_T = 0.95$ under Test 1 conditions.	128
5.32	Validation of the evaporator model. Comparison between the predicted and experimental evaporation pressure (a) and percentage deviation (b) with $C_{TP} = 1$, $C_V = 1$ and $C_f = 1$ under Test 1 conditions.	128
5.33	Validation of the evaporator model. Comparison between the predicted and experimental refrigerant temperature at the evaporator outlet (a) and absolute deviation (b) with $C_{TP} = 1$, $C_V = 1$ and $C_f = 1$ under Test 1 conditions.	129

5.34	Validation of the evaporator model. Comparison between the predicted and experimental refrigerant superheating at the evaporator outlet (a) and absolute deviation (b) with $C_{TP} = 1$, $C_V = 1$ and $C_f = 1$ under Test 1 conditions.	129
5.35	Validation of the evaporator model. Comparison between the predicted and experimental water-glycol temperature at the evaporator outlet (a) and absolute deviation (b) with $C_{TP} = 1$, $C_V = 1$ and $C_f = 1$ under Test 1 conditions.	130
5.36	Validation of the evaporator model. Comparison between the predicted and experimental evaporation pressure (a) and percentage deviation (b) with $C_{TP} = 1$, $C_V = 2$ and $C_f = 1$ under Test 1 conditions.	130
5.37	Validation of the evaporator model. Comparison between the predicted and experimental refrigerant temperature at the evaporator outlet (a) and absolute deviation (b) with $C_{TP} = 1$, $C_V = 2$ and $C_f = 1$ under Test 1 conditions.	131
5.38	Validation of the evaporator model. Comparison between the predicted and experimental refrigerant superheating at the evaporator outlet (a) and absolute deviation (b) with $C_{TP} = 1$, $C_V = 2$ and $C_f = 1$ under Test 1 conditions.	131
5.39	Validation of the evaporator model. Comparison between the predicted and experimental evaporation pressure (a) and percentage deviation (b) with $C_{TP} = 1$, $C_V = 1$ and $C_f = 1$ under Test 2 conditions.	132
5.40	Validation of the evaporator model. Comparison between the experimental and numerical refrigerant mass flow rate predicted by the valve and the compressor models, with $C_{TP} = 1$, $C_V = 1$ and $C_f = 1$ under Test 2 conditions.	132
5.41	Validation of the evaporator model. Comparison between the predicted and experimental refrigerant temperature at the evaporator outlet (a) and absolute deviation (b) with $C_{TP} = 1$, $C_V = 1$ and $C_f = 1$ under Test 2 conditions.	133
5.42	Validation of the evaporator model. Comparison between the predicted and experimental refrigerant superheating at the evaporator outlet (a) and absolute deviation (b) with $C_{TP} = 1$, $C_V = 1$ and $C_f = 1$ under Test 2 conditions.	133
5.43	Validation of the evaporator model. Comparison between the predicted and experimental water-glycol temperature at the evaporator outlet (a) and absolute deviation (b) with $C_{TP} = 1$, $C_V = 1$ and $C_f = 1$ under Test 2 conditions.	134
5.44	Validation of the evaporator model. Comparison between the predicted and experimental evaporation pressure (a) and percentage deviation (b) with $C_{TP} = 1$, $C_V = 2$ and $C_f = 1$ under Test 2 conditions.	134

5.45	Validation of the evaporator model. Comparison between the predicted and experimental refrigerant temperature at the evaporator outlet (a) and absolute deviation (b) with $C_{TP} = 1$, $C_V = 2$ and $C_f = 1$ under Test 2 conditions.	135
5.46	Validation of the evaporator model. Comparison between the predicted and experimental refrigerant superheating at the evaporator outlet (a) and absolute deviation (b) with $C_{TP} = 1$, $C_V = 2$ and $C_f = 1$ under Test 2 conditions.	135
5.47	Validation of the complete model with the main system components. Comparison between the predicted and experimental pressure at the condenser ((a) and (b)) and at the evaporator ((c) and (d)), with $C_V = 1$, $C_{TP} = 1$, $C_L = 1$ and $C_f = 1$ under Test 1 conditions.	136
5.48	Validation of the complete model with the main system components. Model-predicted and experimental refrigerant mass flow rate, with $C_V = 1$, $C_{TP} = 1$, $C_L = 1$ and $C_f = 1$ under Test 1 conditions.	136
5.49	Validation of the complete model with the main system components. Comparison between the predicted and experimental temperature of the refrigerant at the outlet of the condenser ((a) and (b)) and the evaporator ((c) and (d)), with $C_V = 1$, $C_{TP} = 1$, $C_L = 1$ and $C_f = 1$ under Test 1 conditions.	137
5.50	Validation of the complete model with the main system components. Comparison between the predicted and experimental subcooling and superheating of the refrigerant at the outlet of the condenser ((a) and (b)) and the evaporator ((c) and (d)), with $C_V = 1$, $C_{TP} = 1$, $C_L = 1$ and $C_f = 1$ under Test 1 conditions.	138
5.51	Validation of the complete model with the main system components. Comparison between the predicted and experimental temperature of the secondary fluids at the outlet of the condenser ((a) and (b)) and the evaporator ((c) and (d)), with $C_V = 1$, $C_{TP} = 1$, $C_L = 1$ and $C_f = 1$ under Test 1 conditions.	139
5.52	Validation of the complete model with the main system components. Comparison between the predicted and experimental electric power absorbed by the compressor (a) and percentage deviation (b), with $C_V = 1$, $C_{TP} = 1$, $C_L = 1$ and $C_f = 1$ under Test 1 conditions.	140
5.53	Validation of the complete model with the main system components. Comparison between the predicted and experimental COP (a) and percentage deviation (b), with $C_V = 1$, $C_{TP} = 1$, $C_L = 1$ and $C_f = 1$ under Test 1 conditions.	140
5.54	Nusselt number for the calculation of the single-phase heat transfer coefficients in brazed-plate heat exchangers using different correlations. (a) Refrigerant side. (b) Secondary fluid side.	141

5.55	Validation of the complete model with the main system components. Comparison between the predicted and experimental pressure at the condenser ((a) and (b)) and at the evaporator ((c) and (d)), with $C_V = 1.35$, $C_{TP} = 1$, $C_L = 1.35$ and $C_f = 1.35$ under Test 1 conditions.	141
5.56	Validation of the complete model with the main system components. Model-predicted and experimental refrigerant mass flow rate, with $C_V = 1.35$, $C_{TP} = 1$, $C_L = 1.35$ and $C_f = 1.35$ under Test 1 conditions.	142
5.57	Validation of the complete model with the main system components. Comparison between the predicted and experimental temperature of the refrigerant at the outlet of the condenser ((a) and (b)) and the evaporator ((c) and (d)), with $C_V = 1.35$, $C_{TP} = 1$, $C_L = 1.35$ and $C_f = 1.35$ under Test 1 conditions. . . .	142
5.58	Validation of the complete model with the main system components. Comparison between the predicted and experimental subcooling and superheating of the refrigerant at the outlet of the condenser ((a) and (b)) and the evaporator ((c) and (d)), with $C_V = 1.35$, $C_{TP} = 1$, $C_L = 1.35$ and $C_f = 1.35$ under Test 1 conditions.	143
5.59	Validation of the complete model with the main system components. Comparison between the predicted and experimental electric power absorbed by the compressor (a) and percentage deviation (b), with $C_V = 1.35$, $C_{TP} = 1$, $C_L = 1.35$ and $C_f = 1.35$ under Test 1 conditions.	144
5.60	Validation of the complete model with the main system components. Comparison between the predicted and experimental COP (a) and percentage deviation (b), with $C_V = 1.35$, $C_{TP} = 1$, $C_L = 1.35$ and $C_f = 1.35$ under Test 1 conditions. . . .	144
5.61	Validation of the complete model with the main system components. Comparison between the predicted and experimental pressure at the condenser ((a) and (b)) and at the evaporator ((c) and (d)), with $C_V = 1$, $C_{TP} = 1$, $C_L = 1$ and $C_f = 1$ under Test 2 conditions.	145
5.62	Validation of the complete model with the main system components. Model-predicted and experimental refrigerant mass flow rate, with $C_V = 1$, $C_{TP} = 1$, $C_L = 1$ and $C_f = 1$ under Test 2 conditions.	145
5.63	Validation of the complete model with the main system components. Comparison between the predicted and experimental temperature of the refrigerant at the outlet of the condenser ((a) and (b)) and the evaporator ((c) and (d)), with $C_V = 1$, $C_{TP} = 1$, $C_L = 1$ and $C_f = 1$ under Test 2 conditions.	146

5.64	Validation of the complete model with the main system components. Comparison between the predicted and experimental subcooling and superheating of the refrigerant at the outlet of the condenser ((a) and (b)) and the evaporator ((c) and (d)), with $C_V = 1$, $C_{TP} = 1$, $C_L = 1$ and $C_f = 1$ under Test 2 conditions.	147
5.65	Validation of the complete model with the main system components. Comparison between the predicted and experimental temperature of the secondary fluids at the outlet of the condenser ((a) and (b)) and the evaporator ((c) and (d)), with $C_V = 1$, $C_{TP} = 1$, $C_L = 1$ and $C_f = 1$ under Test 2 conditions.	148
5.66	Validation of the complete model with the main system components. Comparison between the predicted and experimental electric power absorbed by the compressor (a) and percentage deviation (b), with $C_V = 1$, $C_{TP} = 1$, $C_L = 1$ and $C_f = 1$ under Test 2 conditions.	149
5.67	Validation of the complete model with the main system components. Comparison between the predicted and experimental COP (a) and percentage deviation (b), with $C_V = 1$, $C_{TP} = 1$, $C_L = 1$ and $C_f = 1$ under Test 2 conditions.	149
5.68	Validation of the complete model with the main system components. Comparison between the predicted and experimental pressure at the condenser ((a) and (b)) and at the evaporator ((c) and (d)), with $C_V = 1.35$, $C_{TP} = 1$, $C_L = 1.35$ and $C_f = 1.35$ under Test 2 conditions.	150
5.69	Validation of the complete model with the main system components. Model-predicted and experimental refrigerant mass flow rate, with $C_V = 1.35$, $C_{TP} = 1$, $C_L = 1.35$ and $C_f = 1.35$ under Test 2 conditions.	150
5.70	Validation of the complete model with the main system components. Comparison between the predicted and experimental temperature of the refrigerant at the outlet of the condenser ((a) and (b)) and the evaporator ((c) and (d)), with $C_V = 1.35$, $C_{TP} = 1$, $C_L = 1.35$ and $C_f = 1.35$ under Test 2 conditions.	151
5.71	Validation of the complete model with the main system components. Comparison between the predicted and experimental subcooling and superheating of the refrigerant at the outlet of the condenser ((a) and (b)) and the evaporator ((c) and (d)), with $C_V = 1.35$, $C_{TP} = 1$, $C_L = 1.35$ and $C_f = 1.35$ under Test 2 conditions.	152
5.72	Validation of the complete model with the main system components. Comparison between the predicted and experimental electric power absorbed by the compressor (a) and percentage deviation (b), with $C_V = 1.35$, $C_{TP} = 1$, $C_L = 1.35$ and $C_f = 1.35$ under Test 2 conditions.	153

5.73	Validation of the complete model with the main system components. Comparison between the predicted and experimental COP (a) and percentage deviation (b), with $C_V = 1.35$, $C_{TP} = 1$, $C_L = 1.35$ and $C_f = 1.35$ under Test 2 conditions.	153
6.1	Inputs and outputs to the suction accumulator model.	156
6.2	Inputs and outputs to the liquid receiver model.	159
6.3	Validation of the complete model. Pressure at the condenser ((a) and (b)) and at the evaporator ((c) and (d)) under Test 1 conditions.	162
6.4	Validation of the complete model. Refrigerant outlet temperature (a) and subcooling (b) at the condenser outlet under Test 1 conditions.	163
6.5	Receiver degree of filling (a) and refrigerant mass in the high pressure side of the circuit (b) under Test 1 conditions.	163
6.6	Validation of the complete model. Refrigerant outlet temperature (a) and superheating (b) at the evaporator outlet under Test 1 conditions.	164
6.7	Void fraction in the accumulator under Test 1 conditions.	164
6.8	Validation of the complete model. Outlet temperature of the secondary fluid at the condenser (a) and at the evaporator (b) under Test 1 conditions.	165
6.9	Validation of the complete model. Electric power absorption (a) and its percentage deviation (b) under Test 1 conditions.	165
6.10	Validation of the complete model. COP under Test 1 conditions.	165
6.11	Validation of the complete model. Pressure at the condenser ((a) and (b)) and at the evaporator ((c) and (d)) under Test 2 conditions.	166
6.12	Validation of the complete model. Refrigerant outlet temperature (a) and subcooling (b) at the condenser outlet under Test 2 conditions.	167
6.13	Receiver degree of filling (a) and refrigerant mass in the high pressure side of the circuit (b) under Test 2 conditions.	167
6.14	Validation of the complete model. Refrigerant outlet temperature (a) and superheating (b) at the evaporator outlet under Test 2 conditions.	168
6.15	Validation of the complete model. Outlet temperature of the secondary fluid at the condenser (a) and at the evaporator (b) under Test 2 conditions.	168
6.16	Validation of the complete model. Electric power absorption (a) and its percentage deviation (b) under Test 2 conditions.	169
6.17	Validation of the complete model. COP under Test 2 conditions.	169

List of Tables

1.1	Compressors classification.	6
2.1	Tracking values for the evaporator inactive variables during machine stops as a function of the whole mean void fraction $\bar{\gamma}_{off}$	49
3.1	Parameters for the brazed-plate heat exchangers.	80
3.2	Parameters for the finned-tube heat exchangers.	81
3.3	Initialization of the SMB framework for the evaporator model	81
3.4	Initialization of the SMB framework for the condenser model	83
3.5	Parameters for the compressor.	87
3.6	List of the look-up tables implemented for the refrigerant side.	88
4.1	Characteristics of the finned-tube heat exchangers.	93
4.2	Characteristics of the test.	93
5.1	Frascold D3-13.1Y VS data.	109
5.2	Evaporator and condenser data.	109
5.3	Data of the Endress-Hauser mass flow meter for the refrigerant.	111
5.4	Data of the Huba sensors for the refrigerant pressure.	111
5.5	Data of the Huba sensors for the refrigerant pressure.	111
5.6	Data of the Huba sensors for the refrigerant pressure.	111
5.7	Data of the Endress-Hauser mass flow meter for the refrigerant.	112
5.8	National Instrument boards for data acquisition.	112
5.9	Characteristics of Test 1.	113
5.10	Characteristics of Test 2.	116

Nomenclature

A_C	Cross-sectional area	(m^2)
A_S	Surface of the heat exchanger	(m^2)
A_v	Fully-open area of the electronic expansion valve	(m^2)
b	Offset between plates in a brazed-plates heat exchanger	(m)
c_p	Specific thermal capacity at constant pressure	$(J \cdot kg^{-1} \cdot K^{-1})$
c_w	Specific thermal capacity of heat exchanger wall	$(J \cdot kg^{-1} \cdot K^{-1})$
C_{D0}	Fully-open discharge coefficient of the electronic expansion valve	$(-)$
C_L	Correction factor for the refrigerant heat transfer coefficient in the subcooled region	$(-)$
C_{TP}	Correction factor for the refrigerant heat transfer coefficient in the two-phase region	$(-)$
C_V	Correction factor for the refrigerant heat transfer coefficient in the superheated vapour region	$(-)$
C_{off}	Correction factor for the refrigerant heat transfer coefficient during machine off periods	$(-)$
C_f	Correction factor for the secondary fluid heat transfer coefficient	$(-)$
$C_{\dot{m}_r}$	Correction factor for the refrigerant mass flow rate across the compressor	$(-)$
C_T	Correction factor for the temperature at the compressor outlet	$(-)$
$C_{\dot{W}_{el}}$	Correction factor for electric power absorbed by the compressor	$(-)$
COP	Coefficient of performance	$(-)$
d_h	Hydraulic diameter	(m)
f	Compressor rotational frequency	(Hz)
h	Specific enthalpy	$(J \cdot kg^{-1})$
H	Enthalpy	(J)
$K_{\bar{\gamma}}$	Relaxation factor for mean void fraction tracking equation	(s^{-1})
K_{ξ}	Relaxation factor for non-dimensional length tracking equation	(s^{-1})
K_h	Relaxation factor for enthalpy tracking equation	(s^{-1})
K_T	Relaxation factor for temperature tracking equation	(s^{-1})
l	Plate length in a brazed-plates heat exchanger	(m)
L_j	Length of the generic zone j in the SMB formulation	(m)

L_{tot}	Total length of a single refrigerant path	(m)
m	Mass	(kg)
\dot{m}	Mass flow rate	($kg \cdot s^{-1}$)
$N_{channel}$	Number of channels in a brazed-plates heat exchanger	($-$)
p	Non-dimensional position of the EEV shutter	($-$)
P	Pressure	(bar)
PL	Part load condition for the reciprocating compressor model	($-$)
\dot{Q}	Heat transfer rate	(W)
s	Specific entropy	($J \cdot kg^{-1} \cdot K^{-1}$)
S	Slip ratio	($-$)
T	Temperature	($^{\circ}C$)
T_{int}	Wall temperature transported by the moving interface	
U	Internal energy	(J)
V	Volume	(m^3)
V_{eff}	Compressor effective displacement	(m^3)
V_k	Compressor total displacement	(m^3)
w	Plate width in brazed-plates heat exchanger	(m)
\dot{W}_{el}	Compressor electric power consumption	(kW)
x	Vapour quality	($-$)
z_m	Polynomials for the calculation of the compressor mass flow rate	
z_W	Polynomials for the calculation of the compressor electric power consumption	
z_T	Polynomials for the calculation of the compressor refrigerant outlet temperature	

Greek letters

α	Heat transfer coefficient	($W \cdot m^{-2} \cdot K^{-1}$)
γ	Local void fraction	($-$)
$\bar{\gamma}$	Mean void fraction	($-$)
$\bar{\gamma}_{off}$	Mean void fraction in the whole heat exchanger during the off-duty periods	($-$)
$\bar{\gamma}_{TOT}$	Mean void fraction in the case of complete evaporation or condensation	($-$)
ΔT	Temperature variation	(K)
ε	Switching threshold value for the maximum vapour/liquid excess in the heat exchangers	($-$)
η_{is}	Compressor isentropic efficiency	($-$)
η_{vol}	Compressor volumetric efficiency	($-$)
θ	Chevron angle in a brazed-plate heat exchanger	($^{\circ}$)
λ	Thermal conductivity	($W \cdot m^{-1} \cdot K^{-1}$)
μ	Dynamic viscosity	($Pa \cdot s$)
ξ_j	Non-dimensional length of the generic zone j in the SMB formulation	($-$)

$\xi_{j\ min}$	Switching threshold value of the non-dimensional length of the generic zone j in the SMB formulation	(-)
ρ	Density	($kg \cdot m^{-3}$)
τ	Time	(s)
τ_k	Compressor time constant	(s)
Φ	Area enlargement factor in a brazed-plates heat exchanger	(-)

Subscripts

0	Initial condition
<i>ac</i>	Accumulator
<i>amb</i>	Ambient
<i>c</i>	Condenser
<i>e</i>	Evaporator
<i>exp</i>	Experimental data
<i>f</i>	Secondary fluid
<i>i</i>	Inlet
<i>int</i>	Intermediate
<i>is</i>	Isentropic
<i>l</i>	Saturated liquid
<i>k</i>	Compressor
<i>m</i>	Mean value
<i>model</i>	Model result
<i>o</i>	Outlet
<i>off</i>	Off period
<i>plate</i>	Plate of a brazed-plate heat exchanger
<i>r</i>	Refrigerant
<i>rec</i>	Liquid receiver
<i>sat</i>	Saturation property
<i>sc</i>	Subcooled liquid
<i>sh</i>	Superheated vapour
<i>track</i>	Tracking value
<i>v</i>	Dry-saturated vapour
<i>w</i>	Heat exchanger wall

Acronyms

<i>BPHE</i>	Brazed-plate heat exchangers
<i>CFCs</i>	ChloroFluoroCarbons
<i>COP</i>	Coefficient of performance
<i>EEV</i>	Electronic expansion valve
<i>FCV</i>	Finite-control volume
<i>GWP</i>	Global warming potential
<i>HCs</i>	HydroCarbons
<i>HCFCs</i>	HydroChloroFluoroCarbons
<i>HEX</i>	Heat exchanger
<i>HFCs</i>	HydroFluoroCarbons

<i>HFOs</i>	HydroFluoroOlefins
<i>HVAC</i>	Heating, Ventilation and Air Conditioning
<i>L</i>	Subcooled liquid region
<i>MB</i>	Moving-boundary
<i>ODE</i>	Ordinary differential equations
<i>ODP</i>	Ozone depletion potential
<i>SEI</i>	System efficiency index
<i>SMB</i>	Switched moving-boundary
<i>TEV</i>	Thermostatic expansion valve
<i>TEWI</i>	Total equivalent warming impact
<i>TP</i>	Two-phase region
<i>V</i>	Superheated vapour region
<i>VCC</i>	Vapour compression cycle
<i>VCS</i>	Vapour compression system
<i>WLSC</i>	Water-Loop Self-Contained

Introduction

Industrial and commercial refrigeration systems represent one of the most relevant fields in terms of energy consumption: about 15% of the worldwide electric energy demand is due to refrigeration processes and is expected to increase in the next decades, thus greatly affecting CO_2 emissions [1]. In addition, refrigeration systems using HydroFluoroCarbons (HFCs) in vapour-compression cycles, still largely employed in supermarket refrigeration or HVAC systems, heavily contribute to the greenhouse effect also due to leakages, which become more and more important, the larger the refrigerant charge [2]. Owing to their strong environmental impact, vapour compression refrigeration systems play a central role among the research works in the field of energy savings.

As reviewed in [3, 4], many works are focused on the energy performance of different configurations of refrigeration systems/heat pumps, with the authors mainly interested in investigating different ways of reducing the energy consumption and subsequently the environmental impact through improvements in the thermodynamic efficiency of the cycle considering different plant layouts. Yet, the cost of modifying an already existent plant to make it more environmentally friendly is usually significant.

Among the main technologies aimed at improving the energy performance of vapour compression refrigeration systems without heavy interventions on the plant layout and with subsequent cost savings, the use of advanced and suitable control strategies is one the most important [1]. Moreover, in several industrial fields, such as the food processing and conservation, a careful control of temperature and relative humidity is also required for smooth operation and successful preservation of product quality [5].

To evaluate the performance of an industrial vapour-compression refrigerating machine under time-dependent thermal loads and different control strategies, dynamic modelling represents a useful analysis tool and a potential source of economic savings, because it allows the choice of the best control logic for a certain application and to pinpoint any critical situations which might lead to system failure [6].

Starting from these considerations, the main aim of this project is to create dynamic models of each component of a vapour-compression refrigerating machine and capable of being coupled together in order to investigate the influence of control systems on energy consumption, efficiency and control quality of the refrigeration system.

The work is organized as follows. In Chapter 1 an overview on vapour-compression refrigerating machines is given, describing their components and

the basic principles behind their operation, and highlighting the main strategies aimed at improving the energy efficiency of such systems. After an overview on the main modelling approach applied to vapour-compression refrigeration systems, Chapter 2 is devoted to the detailed description of the mathematical models realized. In Chapter 3 the software architecture used to implement the mathematical models is presented. The results obtained in the numerical verification and experimental validation of the models are reported in Chapter 4 and Chapter 5 respectively. In particular, in Chapter 4 the numerical predictions of the in-house models is compared to those of Thermosys[®], a Matlab/SIMULINK[®] toolbox developed at the University of Illinois, Urbana-Champaign (UIUC), whilst in Chapter 5 the model prediction capability will be investigated through comparisons with experimental data obtained from a water-to-water refrigerating machine located at the Polytechnic of Milan. Finally, in Chapter 6 the effects of the suction accumulator and of the liquid receiver on the dynamics of a vapour-compression refrigerating machine are investigated. Particular care has been used in the modelling approach used for the receiver in order to allow a subcooled liquid condition of the refrigerant at the condenser outlet and a partial filling condition of the receiver. Also in this case, the numerical predictions are compared to experimental data.

Chapter 1

Vapour compression refrigerating machines: an overview

Refrigeration technology is widely employed in different industrial and commercial fields, like food industry and air-conditioning, and it is responsible for about 15% of the worldwide electric energy demand [1]. The high energy consumption which characterizes this kind of technology and the type of fluids often used involve a high environmental impact, thus attracting the attention of researchers.

This chapter gives at first an overview of the basic principles and the main components of a vapour compression refrigerating machine. Then, the main strategies acting at the thermodynamic cycle level and aimed at increasing the energy efficiency are highlighted. The last part of the chapter is devoted to a description of the main control strategies in a refrigeration plant and their influence on the performance of such systems.

1.1 Single-stage vapour compression cycle

A refrigerating machine is a device which allows to transfer heat from a source at low temperature T_{low} to a source at high temperature T_{high} , reversing the natural energy flow. Among mechanically-driven refrigeration cycles, the *vapour compression cycle* is often preferred to gas cycles, because it allows to obtain more compact equipment by exploiting the high evaporation and condensation enthalpies of the refrigerant, thus reducing the required fluid mass flow rate [7].

In Fig. 1.1 the schematic of a single-stage vapour compression refrigeration cycle is reported, where \dot{Q}_e and \dot{Q}_c are the heat transfer rates at the low and high temperature sources respectively and \dot{W}_{el} is the electric power required to accomplish the thermodynamic cycle, whilst in Fig. 1.2 the four transformations the refrigerant experiences in an ideal cycle are shown. At a constant low pressure level, the refrigerant absorbs heat from the refrigerated ambient and thus completely evaporates; depending on the machine configuration, a

slight superheat may be experienced at the outlet. The refrigerant then enters the compressor where its pressure, temperature and enthalpy are increased by adiabatic compression; subsequently the fluid passes through the condenser where it is cooled to saturated conditions, then condensed at constant pressure and often exits with a certain degree of subcooling. The refrigerant is then brought back to the evaporation pressure through an expansion valve which subjects the fluid to an isenthalpic transformation.

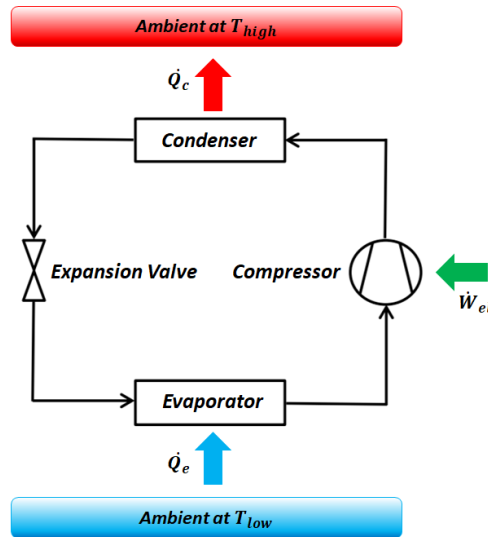


Figure 1.1: Basic schematic of a vapour compression refrigerating machine.

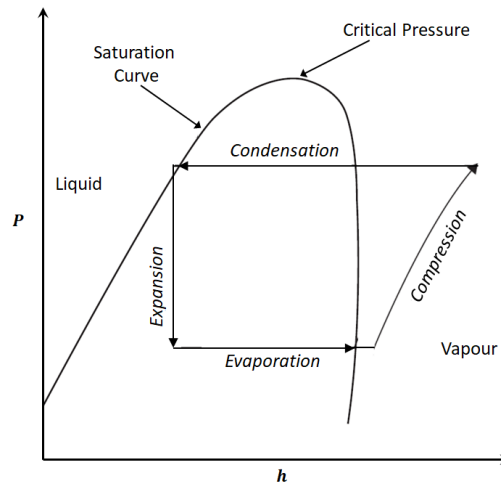


Figure 1.2: P-h diagram of a simple vapour compression cycle.

The energy performance of a refrigerating machine is usually evaluated through the *coefficient of performance (COP)*, also called *EER* (energy efficiency ratio) when the purpose is cooling the ambient at low temperature. Taking into account irreversibilities (e.g. pressure drops, finite temperature differences) that make the cycle deviate from the ideal one shown in Fig. 1.2, the *COP* in working systems is the ratio of the cooling effect to the compressor

input electric power, which can be expressed through Eq. 1.1, where \dot{m}_r is the refrigerant mass flow rate, h_{ero} and h_{eri} are the refrigerant enthalpies at the outlet and inlet of the evaporator respectively:

$$COP = \frac{\dot{m}_r \cdot (h_{ero} - h_{eri})}{\dot{W}_{el}} \quad (1.1)$$

Taking into account also the electric energy consumptions of flow devices like pumps and fans in addition the compressor consumption leads to a *system efficiency index (SEI)*.

1.2 Refrigerants

Among the main characteristics which contribute to define the configuration, the performance and the environmental impact of a refrigeration plant, the type of refrigerant plays a central role. To evaluate the environmental impact of a refrigerant, two parameters can be defined. The first is the *ozone depletion potential* (ODP), which evaluates the effects of the fluid on the atmospheric ozone layer. ODP is set to 1 for R11, a refrigerant belonging to the ChloroFluoroCarbons (CFCs) category. The second parameter is the *global warming potential* (GWP) which evaluates how much a refrigerant impacts on the global warming, estimating the climate impact due to its emission in comparison to that due the emission of the same amount of CO_2 .

As a response to the Montreal Protocol on Substances that Deplete the Ozone Layer, HydroFluoroCarbons (HFCs) were introduced to substitute ChloroFluoroCarbons and HydroChloroFluoroCarbons (HCFCs). HFCs, like R404A, R134a and R507A, are currently among the most common fluids used in commercial refrigeration and are characterized by a high GWP; therefore, leakages in large plants using this kind of fluids can have a strong environmental impact. As a response to the Kyoto Protocol many researchers focused on finding new highly efficient, environmental friendly refrigerants: HydroCarbons (HCs), natural refrigerants, lower GWP HFCs and HydroFluoroOlefins (HFOs) represent the main option as HFCs substitutes, [1].

HydroCarbons are efficient, non-toxic fluids with low GWP, [1], but, because of their high flammability, they can be used only in unmanned facilities or low-charge plants [8].

Among natural refrigerants, the most important are CO_2 (R744), which is non-flammable, non-toxic and it is finding more and more applications, and ammonia (R717), which is very efficient but also flammable and toxic, thus limiting its use.

HFOs, like HFO-1234yf and HFO-1234ze, are non-toxic refrigerants and have usually lower efficiency and flammability than other fluids; they are often mixed with HFCs to increase efficiency while maintaining lower GWP, [1].

1.3 Overview of the main components of a vapour compression refrigeration machine

In this section, an overview on the main components of a vapour compression refrigerating machine is presented. For a detailed analysis of the structural characteristics, the reader is referred to [7].

1.3.1 Compressors

The compressor of a refrigerating machine has the aim of increasing the refrigerant pressure from the evaporation to the condensation level. Basically, compressors can be divided into two main categories: positive displacement, which increase the pressure by reducing the refrigerant volume, and dynamic, which raise the velocity of gas and then reduce it in order to increase pressure. Table 1.1 summarizes the main compressor types, whilst in Fig. 1.3 the approximate range of capacity covered is reported, [7].

Table 1.1: Compressors classification.

<i>Compressors</i>			
<i>Positive displacement</i>		<i>Dynamic</i>	
Reciprocating	Rotary	Turbo	Ejector
	Vane	Centrifugal	
	Scroll	Axial	
	Rolling piston		
	Screw		

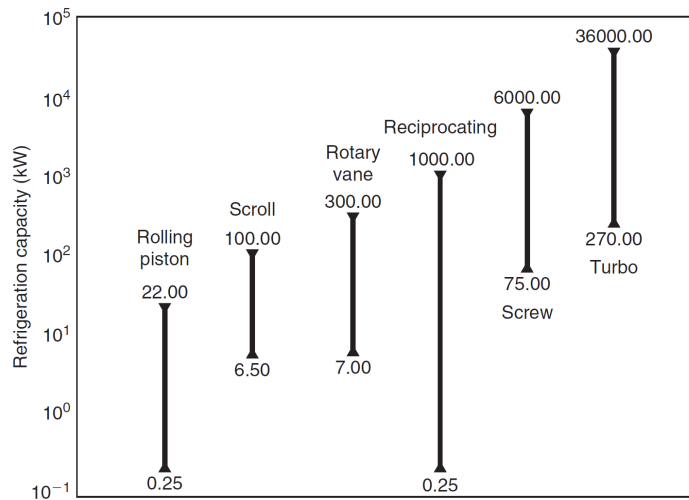


Figure 1.3: Range of refrigeration capacity of various types of compressor [7].

Another classification of compressors for refrigeration plants can be done on the basis of the *accessibility* to the main components, [9]:

- *Hermetic*
- *Semi-hermetic*
- *Open*

In the following the main compressor types will be described in their main characteristics, focusing on positive displacement compressors, since for the range of capacities investigated in this thesis they are more often used than dynamic compressor.

Reciprocating compressors

As emerges from Fig. 1.3, reciprocating compressors can operate through a wide range of cooling load and for this reason they are very common in industrial and commercial applications. The operating principle is based on the two-stroke cycle, and the suction and discharge of gas is managed by pressure-actuated valves, which open/close once pressure in the cylinder becomes sufficiently lower/higher than the pressure in the suction/discharge pipe. At the end of the discharge phase, a certain amount of gas remains trapped in the clearance at the end of the stroke and must be re-expanded in order to let the suction valve open: the more the gas trapped in the clearance, the further the piston must travel to have pressure drop enough for valve to open and, therefore, thus the smaller the cylinder volume available for gas suction, with a subsequent reduction in the mass flow rate. Owing to the operating principle of this type of machine, the mass flow rate is pulsating and it adapts to the operating pressures in the circuit.

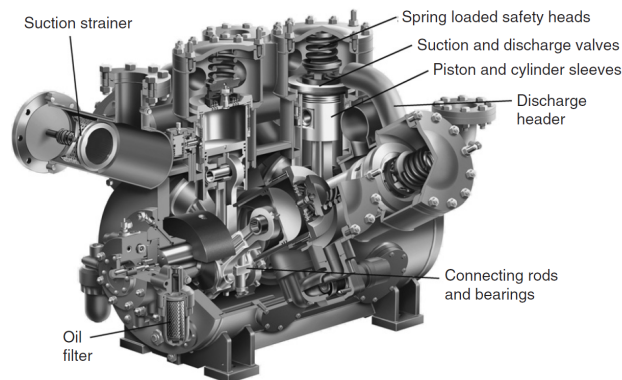


Figure 1.4: Cutaway view of a multi-cylinder reciprocating compressor [7].

In order to increase the cooling capacity, multi-cylinder reciprocating compressors are used in commercial and industrial applications, typically with four, six and eight cylinders; an example is shown in Fig. 1.4. To allow the machine to match the actual cooling load, the main practical solutions for a reciprocating compressor are:

- on-off control logic;
- control of the angular speed through an inverter;
- in multi-cylinders machines, switching some cylinders off;
- by-pass between inlet and outlet.

Screw compressors

As shown in Fig. 1.5, in a screw compressor two reverse pitch screws engage and form with the compressor case a volume. The gas is trapped in it and moves toward the outlet reducing its size and thus increasing its pressure. These machines operate at constant *volumetric compression ratio* since the volume occupied by the gas at the inlet and at the outlet is independent of the operating pressures: therefore, the minimum absorbed power will be obtained when the operating pressure ratio corresponds to the design volume ratio. Unlike in reciprocating compressors, the mass flow rate is continuous with subsequent less noise and vibrations, no inlet and outlet valves are needed and no clearance volume is present. In this type of compressor the losses in refrigerant mass flow rate are mainly due to leakages back to the suction line (dependent on the rotational speed), solution of refrigerant in lubricant oil and heating due to lack of lubrication.

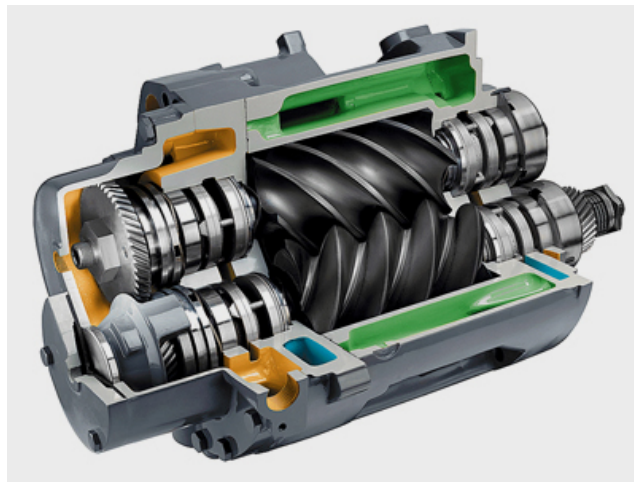


Figure 1.5: Cutaway view of a screw compressor.

Flow rate control in screw compressors is usually obtained through sliding blocks which allow part of the gas to be recirculated to the suction line, thus reducing the operation mass flow rate; in this type of compressors the flow rate can be reduced down to 10%. In part load conditions, the size of the discharge port is also adjusted in order to maintain the volume ratio approximatively constant.

Scroll compressors

In scroll compressors, whose a cutaway view is shown in Fig 1.6, the refrigerant is compressed by means of two inter-fitting spiral-shaped scroll members, one of which is fixed and the other orbits inside the first.

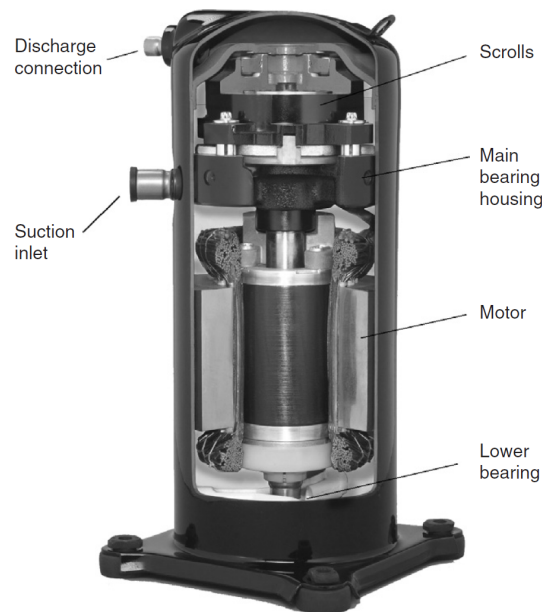


Figure 1.6: Cutaway view of a scroll compressor [7].

Like screw compressors, scrolls have a design volume ratio and no clearance volume, but they do not have a direct path between inlet and outlet, because of the direct contact between the scrolls, thus significantly reducing leakages. Flow rate control is often controlled using variable speed inverters.

Sliding vane compressors

Sliding vane compressors consist of an eccentric rotor with blades which define sliding vanes whose volume varies by centrifugal force, and the injection of oil along the length of the blades ensures the sealing. Also in this case no clearance volume is present, but the stress on the blades limits their application.

1.3.2 Condensers

In a vapour compression machine, the condenser cools the refrigerant exiting the compressor, bringing it from superheated vapour to saturated or slightly subcooled liquid. The cooling media are usually air or water, and three are the main types of condenser used in commercial and industrial applications:

- *air-cooled condensers*;
- *water-cooled condensers*;
- *evaporative condensers*.

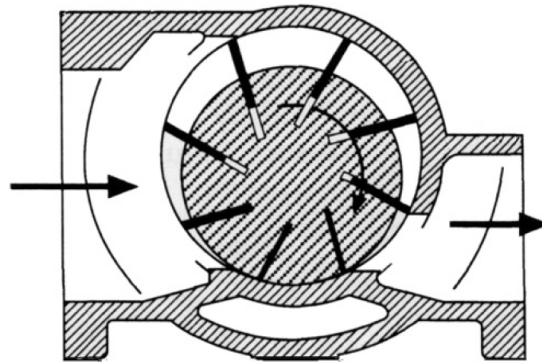


Figure 1.7: Simplified schematic of a sliding vanes compressor [7].

Air-cooled condensers

The simplest air-cooled condenser is composed by a plane tube placed in still air wherein the refrigerant flows: the heat transfer occurs by natural convection. Such heat exchangers are typically used for small systems like domestic refrigerators, where supporting and spacing wires are also used, to increase the heat transfer area, as shown in Fig. 1.8.

For larger systems, forced-convection is required to prevent oversized heat exchangers, and one or more fans are installed. Also, the heat transfer area is enhanced by the use of finned-tubes. Air-cooled condensers are often used in plants with sizes from a few kW to several hundred kW [7], and can be wall-mounted (e.g. air conditioners), roof-mounted (larger plants, see Fig. 1.9) and used in mobile systems.

In order to control the condensation pressure level and to prevent it to sink to too low values, the air mass flow rate is usually controlled by modulating the fan power, i.e. switching off fans in multiple fan units or varying fan speed.

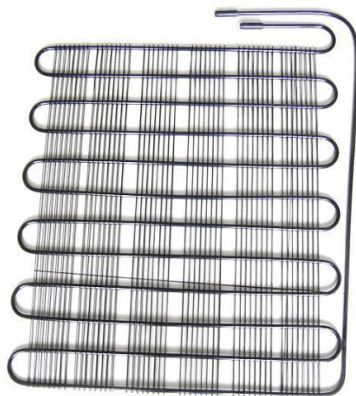


Figure 1.8: Air-cooled condenser for domestic applications.



Figure 1.9: Roof mounted air-cooled condenser [7].

Water-cooled condensers

For small size plant, *double pipe* condenser can be used: they consist of two concentric pipes where the water and the refrigerant are in counterflow, an example is shown in Fig. 1.10.

When plant size increases, larger water-cooled condensers are required, and *shell-and-tube* heat exchangers are used (see Fig. 1.11), again to keep the size of heat transfer devices as small as possible.



Figure 1.10: Double-pipe water-cooled condenser.



Figure 1.11: Shell-and-tube water-cooled condenser.

Another solution is represented by the use of brazed-plate heat exchangers (BPHE) as condensers, obtaining a lower cost alternative to shell-and-tube. The structure of a BPHE and the fluids flow configuration is shown in Fig. 1.12. They consist of a pack of steel-made, herringbone-patterned, corrugated plates which define a certain number of counter-current channels, and which are held together by copper solder. They usually work with a low volume of refrigerant, thus reducing the overall charge, but, in order to operate properly, they need to be kept fully drained into a liquid receiver.

When using water as a medium for the condenser, cooling towers are usually required when the water supply is limited.

Evaporative condensers

In evaporative condensers the water latent heat of evaporation is used to reject heat from the refrigerant and, because of its high value, increases efficiency of the heat exchangers, with operating condensation temperatures lower than those obtained with air-cooled condensers. In Fig. 1.13 a schematic of an evaporative condenser is shown: to operate properly, pipes must be sufficiently wet and thus the water mass flow rate must be significantly higher than the amount evaporated. As for the air flow, it must be sufficiently high to bring away the



Figure 1.12: Brazed-plate heat exchanger.

water vapour.

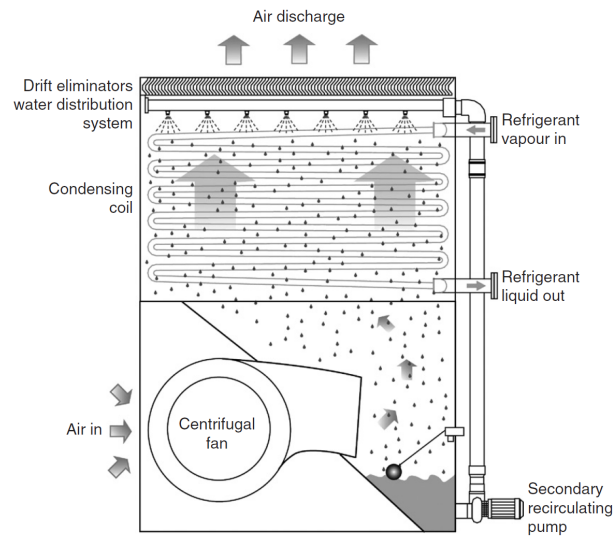


Figure 1.13: Evaporative condenser [7].

1.3.3 Evaporators

In the evaporator, the refrigerant at low pressure and in two-phase conditions absorbs heat from the medium to be cooled, and exits the heat exchanger as superheated vapour. Two main classifications can be made for evaporators. On the basis of the fluid flow pattern, two types of evaporators can be distinguished:

- *Direct expansion evaporators*: they are characterized by a continuous fluid flow and the refrigerant exits as superheated vapour. This is the most common configuration.
- *Flooded evaporators*: the refrigerant is contained in a vessel at low pressure and evaporates whilst absorbing heat from the load. The fluid usually exits as a saturated vapour.

The second classification can be made on the basis of the function performed by the evaporator:

- *Air-cooling*: the medium to be cooled is air. Typical applications are refrigerated display cabinet in supermarkets.
- *Liquid-cooling*: the medium to be cooled is a liquid, often water. Typical applications are industrial and commercial refrigeration plants with intermediate fluid and water chiller systems for air-conditioning.

In the following the main configurations of evaporators on the basis of their function will be presented.

Air-cooling

Similar to air-cooled condensers, air-cooling evaporators are usually finned-tube heat exchangers with fans for air blowing which guarantee forced-convection heat transfer. Air-cooling evaporators are of the direct-expansion type and in Fig. 1.14 an example of such heat exchanger is shown, highlighting how vertical fins are used in order to allow water condensed from the air flow to slip away from the surface.

Liquid-cooling

For liquid-cooling applications both flooded and direct-expansion evaporators can be used. One of the most common configuration among the flooded evaporators is the shell-and-tube, where the liquid flows within tubes immersed in boiling refrigerant, with the shell full to three quarter of liquid refrigerant, as shown in Fig. 1.15. In the top of the shell, some pipes are removed to allow the refrigerant to flow freely upwards.

Another configuration of flooded evaporator is shown in Fig. 1.16, where the refrigerant flows in a coil which passes through a tank full of liquid to be cooled. The coil is connected to a *surge drum* which allows both accumulation of liquid refrigerant and evaporation. The expansion valve allows to maintain a certain level of liquid refrigerant within the surge drum.

Shell-and-tube evaporators and configurations with coils immersed in liquid tanks can be also of the direct expansion type, as shown in Fig. 1.17-1.18. In the case of direct expansion shell-and-tube evaporators, the refrigerant flows in the tubes and the liquid in the shell.

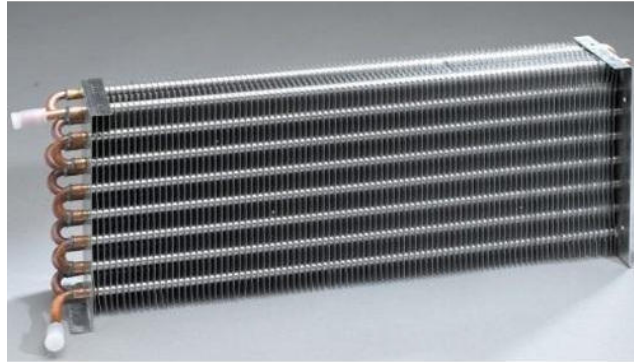


Figure 1.14: Finned-tubes evaporator.

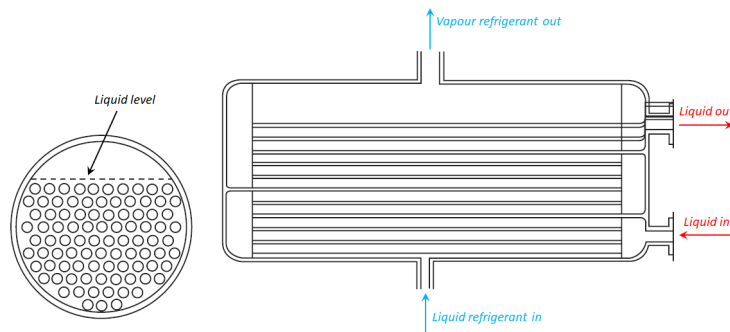


Figure 1.15: Shell-and-tube flooded evaporator.

Among the liquid-cooling evaporators, brazed-plate heat exchangers are widely used, because of their high efficiency and low volume, which allows to reduce the overall refrigerant charge. An example of BPHE is shown in Fig. 1.12.

1.3.4 Expansion valves

Expansion valves control the refrigerant mass flow rate from the high to the low pressure level; this kind of device is usually classified on the basis of its control method.

Capillary tubes

For small capacity application like small air conditioning systems and domestic refrigerators, non-modulating expansion devices like capillary tubes can be used. As shown in Fig. 1.19, they are long, small-diameter tubes in which the refrigerant flow rate is a function of the pressure difference and of the degree of

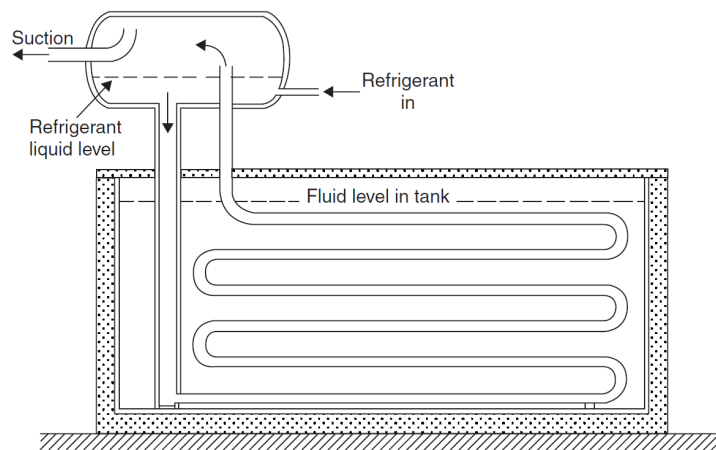


Figure 1.16: Coils flooded evaporator [7].



Figure 1.17: Shell-and-tube direct expansion evaporator for water cooling [7].

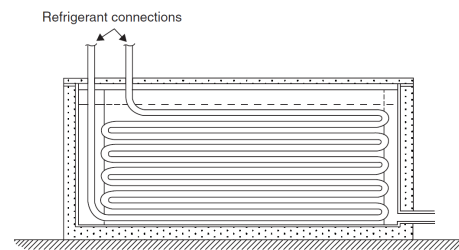


Figure 1.18: Coils direct expansion evaporator [7]

subcooling at its inlet. They are used on factory-built and tested equipment, with exact refrigerant charges and they are not applicable to systems requiring on-site installation.

Thermostatic expansion valves

Used in combination with direct expansion evaporators, thermostatic expansion valve (TEVs) ensure that the refrigerant exits the heat exchanger with a certain amount of superheat, usually of the order of 5 K . TEVs are able to sense the degree of superheat, as sketched in Figs. 1.20-1.21: a phial is filled with the same refrigerant operating in the plant and is connected to the suction line; the phial is then connected to the valve diaphragm through a capillary tube. The refrigerant in the phial is usually in saturated condition at the refrigerant temperature at the evaporator outlet T_{ero} and pressure $P(T_{ero})$, whilst the refrigerant on the other side of diaphragm is at the evaporator pressure P_e . An adjustable spring is also mounted on the device in order to modify the amount of superheat. As an example, should the superheat decrease, the pressure within the phial and the detection device would decrease as well and a resultant force would start to close the valve thus diminishing the refrigerant mass flow rate. In the opposite situation the net force would increase



Figure 1.19: Capillary tube.

valve opening thus increasing the refrigerant mass flow rate. If the capacity of the phial is not sufficient, it fills with vapour and, thus, the relationship between temperature and pressure does not match the boiling curve any more but follows the gas law. This phenomenon is sometimes used to limit the maximum evaporation pressure (e.g. cold-start) by keeping the valve close when the temperature sensed is above a certain threshold. The superheat control actuated by a TEV is basically a proportional control, which is often subjected to hunting, and needs a practically constant condensation pressure.

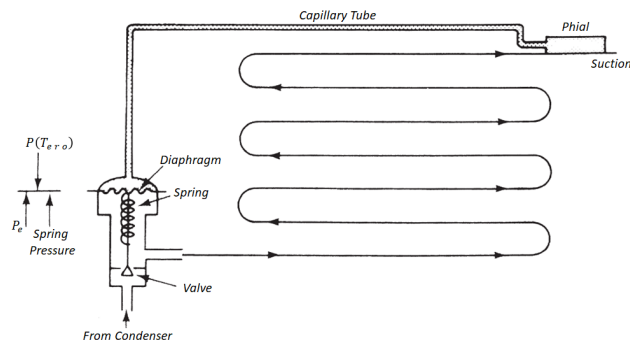


Figure 1.20: Circuit of a thermostatic expansion valve [7].

Electronic expansion valves

When a more refined control is needed, electronic expansion valves (EEVs) are used: in Fig. 1.22 a cutaway section of an EEV is shown together with a schematic of the various pin positions. They allow a more precise control of the refrigerant mass flow rate, respond faster to load changes, allow the user to set lower degrees of superheat thus increasing the operating pressure and the system efficiency and can close during off-duty periods avoiding the

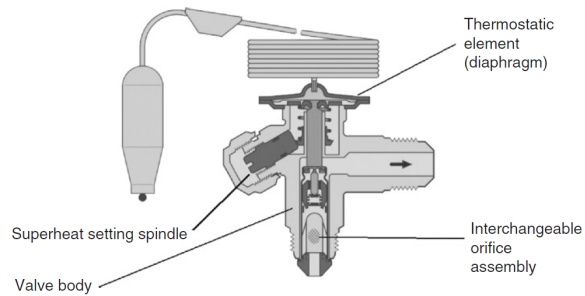


Figure 1.21: Cutaway view of a thermostatic expansion valve [7].

use of an additional solenoid valve. EEVs can be controlled both continuously through a stepper motor which varies the valve orifice size or by means of a PWM (pulse width modulation) logic, which allows to control a mean flow through a sequence of openings and closures of the valve. The controller of an EEV can be used to control different variables like superheat, suction pressure and condensation pressure. When the controlled variable is that superheat, pressure and temperature must be measured at the evaporator outlet.

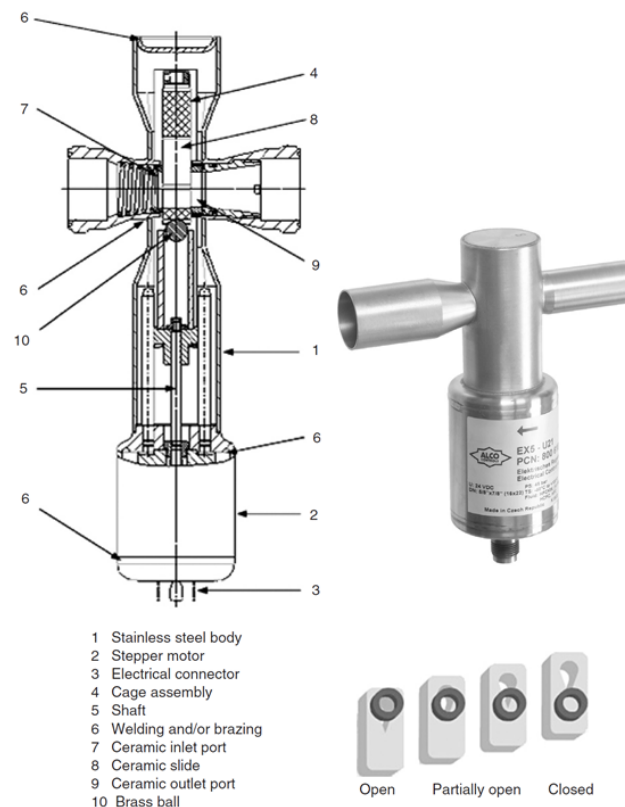


Figure 1.22: Cutaway view of an electronic expansion valve and view of the shutter positions [7].

Float valves

Float valves allow to control the level of refrigerant within components like flooded evaporators and condensers: in the former case they are referred to as low-pressure whilst in the latter as high-pressure. In Fig. 1.23 the schematic of a low-pressure float valve is reported, highlighting how the presence of an additional solenoid valve is required in order to prevent pressure equalization during system shut down.

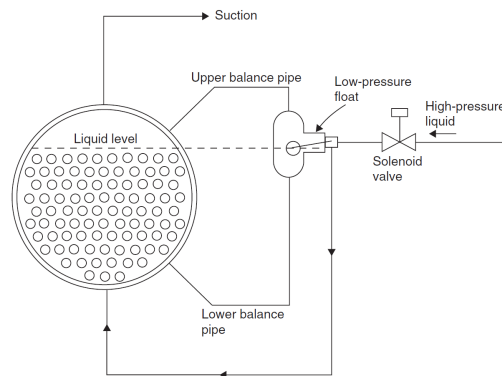


Figure 1.23: Schematic of a low-pressure float valve [7].

1.3.5 Auxiliary components

Basically, to build a vapour compression refrigerating machine, only four components are essential: evaporator, condenser, compressor and expansion valve. However, in practice, several additional devices like receivers, accumulators and internal heat exchangers are required to ensure the plant operates safely.

Receiver

A liquid receiver is placed after the condenser and to store the excess refrigerant charge in order to let the system operate safely under varying conditions, always providing liquid to the valve inlet. A minimum operating charge must be guaranteed within this device, thus increasing the overall cost of the system. To operate correctly, the degree of fill should not exceed 85%.

Suction accumulator

The suction accumulator is used to act as a temporary reservoir to prevent liquid from entering the compressor with subsequent slugging, which implies a loss of lubricant with damage to compressor components.

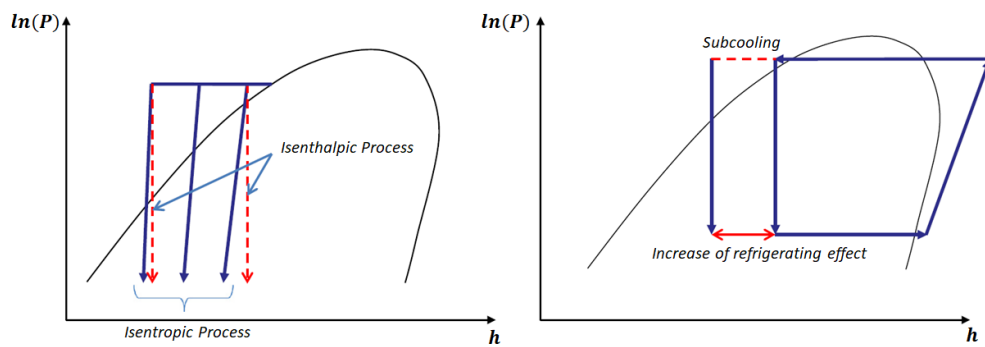


Figure 1.24: Effects of subcooling on the isenthalpic expansion and the refrigerating capacity [3].

Suction-to-liquid heat exchangers

In many systems, a suction-to-liquid heat exchanger is used to cool the warm liquid exiting the condenser through the cold superheated gas exiting the evaporator; the result is a more pronounced subcooling of the liquid refrigerant which enhances the refrigerating effect, as shown in Fig. 1.24, but which is compensated by the increase in gas superheat thus reducing the refrigerant mass flow rate. The increase in thermodynamic efficiency gained by using this device depend on the refrigerant and the operating conditions. Moreover, the suction-to-liquid heat exchanger guarantees safe operation of the compressor, since it increases the superheat. Sometimes, this device is placed within the suction accumulator.

1.4 Multi-stage vapour compression cycles

Multi-stage vapour compression cycles are used when the ratio between compressor discharge to suction pressure is high and a strong decrease in compressor volumetric efficiency together with too high a discharge temperature can occur: in these cases, compression must be carried out in more than one stage. A first solution consists of using more than one compressor. Usually, the hot gas exiting the low-stage compressor passes through an intercooler before entering the high-stage compressor in order to limit the maximum temperature reached; the intercooler can be either a subcooler, an evaporator partly fed by the refrigerant leaving the condenser, or a water-cooled heat exchanger. Alternatively, a flash intercooler can be used, where all the liquid exiting the condenser is expanded to an intermediate pressure and the flash gas and the saturated liquid are separated in a vessel; the vapour then enters the high-stage compressor and the liquid is again expanded to the low pressure.

The multi-stage compression can be accomplished also in single machines like multi-cylinder reciprocating compressors or scroll and screw compressors. In the latter case, an *economizer cycle* is created, where the intermediate pressure is obtained through injection of vapour from subcooled liquid into the compressor case via an additional port during the compression process.

An other way of dealing with high pressure ratios is represented by *cascade cycles*, where one refrigeration system acts as a condenser for another one. Basically, two different refrigerants can be used in the circuits.

1.5 Strategies to improve cycle thermodynamic efficiency

As reviewed in [3], many works are focused on the energy performance of different configurations of refrigeration systems/heat pumps, with the authors mainly interested in investigating different ways of reducing the energy consumption and subsequently the environmental impact by improving the thermodynamic efficiency of the cycle considering different plant layouts.

Due to the importance of refrigerant subcooling at the condenser outlet, which improves the system energy performance and allows liquid to be fed to the expansion valve, several researchers focused on subcooling cycles, aimed at increasing the degree of subcooling. A first solution consists in the use of a suction-to-liquid heat exchanger placed between the condenser outlet and the expansion device and between the evaporator outlet and the compressor, in such a way that the enthalpy of the liquid leaving the condenser is decreased, thus increasing the evaporator capacity; however, the temperature of the low-pressure gas is increased and subsequently the compressor mass flow rate is decreased. As demonstrated in [10], the benefits of a suction-to-liquid heat exchangers depend strongly on the refrigerant properties and the operating conditions; the effects on the COP of this device have been extensively investigated for CO_2 cycles, [11, 12], and for automotive air conditioning systems using R-1234yf and R134a as refrigerants, [13–16]. As an alternative to suction-to-liquid heat exchangers, mechanical subcoolers can be used, mainly consisting of integrated or dedicated cooling systems aimed at improving the performances of the condenser, [17–20]. Most recently, some authors investigated the effect of a mechanical subcooler on the performance of transcritical booster CO_2 cycles, [21, 22]; alternatively, it is also possible to increase the performance of transcritical CO_2 cycles by installing thermoelectric refrigerators exploiting the Peltier effect, which usually have high COP when working with low temperature differences, as demonstrated in [23–25].

Another field of interest for researchers concerns the strategies to recover available energy losses typical of the expansion process in thermostatic or electronic expansion valves, [3]. The main goal is to make the normally isenthalpic expansion approach an isentropic transformation, substituting the valve with devices like expanders and ejectors. The expanders are reverse compressors and thus operate through very similar mechanisms. The higher COPs due to the use of an expander instead of a traditional expansion device mainly rely on the increase in the refrigerating capacity because the expansion is closer to an isentropic transformation and in the possibility of using the recovered thermodynamic losses to partially power the compressor, as sketched in Fig. 1.25. Particular attention must be paid to the high pressure control. In an ejection

tor cycle, the energy stored in the high-pressure flow is firstly converted into kinetic energy, thus reducing the thermodynamic losses, and then converted again into pressure, after mixing with the low-pressure flow. As shown in Fig. 1.26, the constitutive parts of an ejector are a nozzle, where the high-pressure flow is accelerated, a mixing chamber where high and low-pressure flows mix and a diffuser to recover pressure. After the ejector, a separator allows to feed the compressor with pure vapour and an additional expansion device with pure liquid.

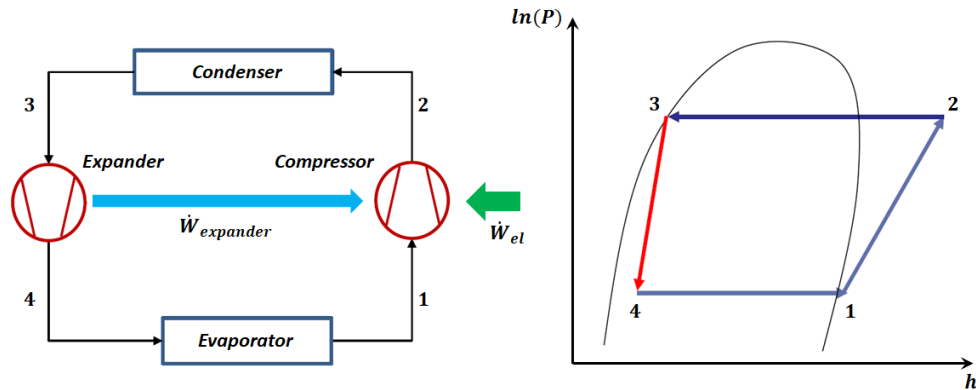


Figure 1.25: Schematic of a vapour compression cycle with an expander instead of an expansion valve and characteristic points on the $P - h$ diagram.

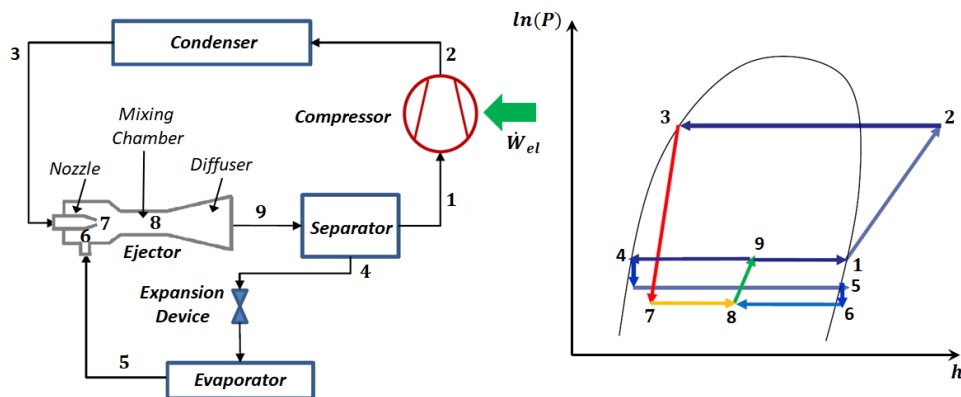


Figure 1.26: Schematic of a vapour compression cycle with an ejector and characteristic points on the $P - h$ diagram.

Another line of research focuses on multi-temperature vapour compression cycles typical of supermarket refrigeration systems, as reviewed in [4], where different plant configurations are investigated; in particular, the authors classified the multi-temperature cycles into different families (multi-stage compressors, expansion valves, ejectors, cascades, cascades with secondary loop, separated gas coolers) and carried out a comparison considering aspects like system capacity control, operating temperatures, energy efficiency calculation and costs.

Cecchinato et. al, [26], compared through simulations different plant solutions

considering the integration between air-conditioning liquid chillers and heat pumps and the refrigeration plant of a medium-size supermarket. Different levels of integration and climate conditions were investigated: energy savings up to 15.6, 22.5 and 14.9% were highlighted considering Treviso, Stockholm and Singapore respectively. Moreover, the benefits due to floating water temperature set-point were also confirmed.

1.6 Research on secondary loop refrigeration systems

The amount of refrigerant charge is one of the major concerns in plants because it directly affects the performance of the system; in fact, if correctly sized, it prevents system failure regardless of changes in thermal load. The higher the refrigerant charge in the system, however, the higher the yearly refrigerant leakage, the stronger the environmental impact. Thus, the study of refrigeration plants with secondary loop, which allows to reduce the amount of refrigerant charge and leakages, represents a central field of investigation. In fact, in the secondary loop more environmental friendly refrigerants can be used and, moreover, they are characterized by a simpler design than multiple direct expansion systems which brings to an easier maintenance, [27]. In Fig. 1.27, a schematic of a refrigeration system with a secondary loop is shown.

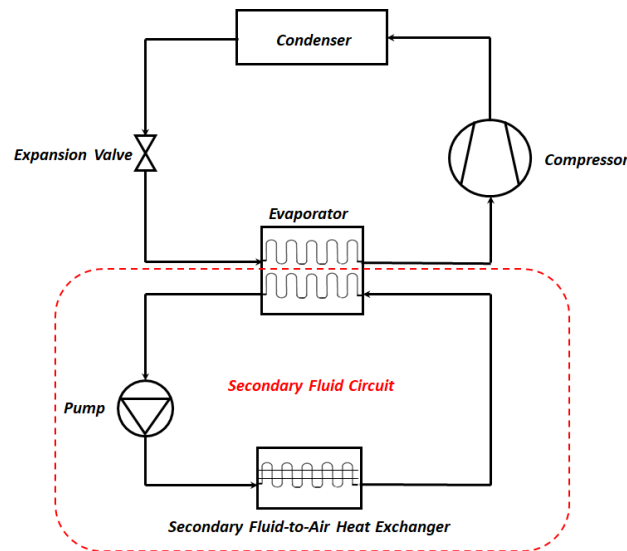


Figure 1.27: Schematic of a refrigeration system with a secondary loop.

As reported in [27], the secondary refrigerants are mainly divided into two categories: single phase and two-phase fluids. For single-phase fluids, a distinction can be made between aqueous and non-aqueous solutions: the former have long been in use as secondary fluids, and their freezing point must be no less than 5–10 K below operating conditions. Among the two-phase solutions, ice slurries in aqueous solutions and CO_2 are the most widespread.

Secondary loop refrigeration systems have gained more attention in commercial refrigeration, especially in supermarkets, since, in their conventional "multiplex" form, they are responsible for high CO_2 emissions, due to high energy consumption and large leakages, [28]. The term multiplex originates from the fact that multiple compressors have the same suction and discharge manifolds; usually, two compressor racks are used: one for the medium temperature (MT) and one for the low temperature (LT). The multiplex refrigeration systems for supermarkets use direct expansion evaporators, whilst compressors and the condensers are usually placed on the roof, far from the refrigerated cabinets, and thus a large refrigerant charge is required. Even if optimizing the design and control of such refrigeration plants can improve their energy efficiency and subsequently reduce the environmental impact, their total equivalent warming impact (TEWI) is hardly affected, as it is mainly influenced by refrigerant charge and leakage. As an example, in [29, 30], a supermarket refrigeration plant with secondary loop both at the evaporation and condensation side was investigated. The system used R507 as primary refrigerant and 50% by mass potassium formate/propylene glycol and ethylene glycol/water mixtures as secondary refrigerants at the evaporation and condensation sides respectively; a 61% reduction in the primary refrigerant charge with respect to traditional Canadian multiplex systems was obtained, with a comparable or even lower energy consumption.

An alternative to the application of traditional secondary-loop refrigeration systems in supermarkets allowing to reduce the refrigerant charge is represented by "Water-Loop Self-Contained" (WLSC) systems, where each cabinet is equipped with its own vapour compression refrigerating machine, whose condensation unit (usually a double-pipe or plate heat exchanger) is connected to a common water circuit, from where heat is then rejected through a water-to-air or water-to-water chiller, [31,32]. Reduction of CO_2 emissions of 56 – 58% were calculated with respect to traditional multiplex systems, both with fixed or floating suction pressure control, mainly because of the reduction in the refrigerant charge and leakages and the decrease in indirect emissions due to the higher energy efficiency caused by modulated compressors power control, [32].

1.7 Control systems in a refrigeration plant

As reported in 1.5 and 1.6, many researchers focused on finding ways of improving the energy efficiency and the environmental impact of refrigeration systems which are mainly based on physical design and thus can usually imply significant costs. Among strategies which allow to decrease the energy consumption while containing the costs of system changes, those related to control systems have a great importance, since they ensure success of industrial processes or, like in food industry, conservation of goods, which may be damaged if particular attention in the design of suitable control strategies is not exerted [1, 5]. In addition, a proper control design can also lead to refrigerant charge reductions, thus decreasing the plant environmental impact, [33]. Indeed, a refrigeration

plant, either industrial or for residential air conditioning and heat pumping, usually works in transient conditions, which require suitable control systems to obtain the desired output from the plant or to avoid dangerous operating conditions. As reported in [34], among others, the main control levels in a refrigeration plant, considering only configurations with direct expansion evaporators, can be classified as:

- control of the cooling capacity by acting on the operating conditions of the compressors (velocity, actual displacement, refrigerant bypass);
- control of the refrigerant superheat by acting on the opening of the expansion valve, be it thermostatic or electronic;
- control of the condensation conditions through variation of the rotational speed of fans or pumps which establish the mass flow rate of the secondary fluid at the condenser;
- in secondary loop refrigeration systems, control of the cooling power available to the user by modifying the operating conditions of the heat exchangers, mainly the mass flow rates of the fluids involved by changing the opening of valves or the speed of a fan or a pump.

In addition, a pressure control (e.g. acting on the air/water mass flow rate) is often installed on the condenser side in order to avoid highs or lows, which would cause system malfunctioning.

In the following the basic principles of control systems and the most common control logics used in refrigeration systems will be described. Thereafter, the effects of control strategies on energy efficiency and on the environmental impact of refrigeration plants will be briefly reviewed.

1.7.1 Basic principles on control systems

The main purpose of each plant control level is to maintain a so-called "controlled variable" $y(\tau)$, e.g. a temperature, as close as possible to a "reference signal" $y_{ref}(\tau)$, acting on the controlled system through a "control signal" $u(\tau)$ [35]. The "controller" is therefore the device forcing the controlled variable to follow the reference signal by generating a suitable control signal, taking also into account the effects of other effects $d(\tau)$ called "disturbances", which also influence the dynamics of the controlled system. As an example, in a refrigeration plant controlled variables can be the water temperature or the refrigerant superheat at the outlet of the evaporator and the control signal can be the compressor speed or the opening of the expansion valve, whilst a variation in the thermal load or the heat exchanger fouling can be considered as disturbances. In Fig. 1.28, the generic schematic of a controlled system with the main signals involved is sketched.

Beside the reference signal $y_{ref}(\tau)$, a controller usually calculates the control signal $u(\tau)$ at a certain time on the basis of different pieces of information, among which are the actual value of the controlled variable $y(\tau)$ and the disturbance $d(\tau)$. One of the most common configuration for an industrial controller

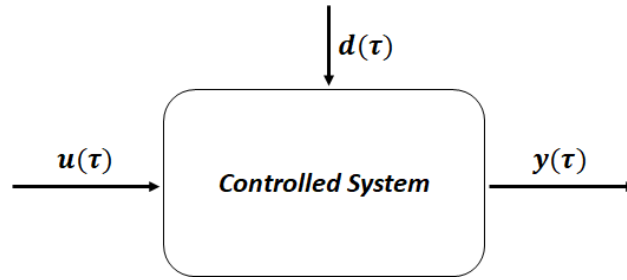


Figure 1.28: Generic schematic of a controlled system with the main signals involved.

is the "feedback control scheme" which basically calculates the control signal $u(\tau)$ on the basis of the error signal $e(\tau)$ estimated as the difference between the reference signal and the actual controlled variable. A schematic reporting the generic operating principle of such controllers is reported in Fig. 1.29.

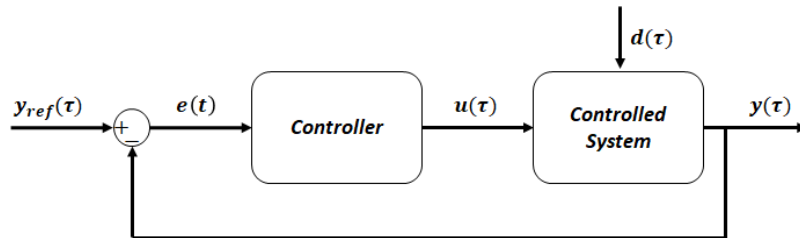


Figure 1.29: Generic schematic of a feedback control.

Among industrial controllers, two main categories can be found on the basis of the type of the action made on the controlled system: On-Off and Proportional-Integral-Derivative (PID) controllers.

On-Off controllers

On-off controllers are also called "two-positions" controllers, since the control signal can only take two values, namely a maximum u_1 and a minimum u_2 . As an example, when an on-off controller is used to control the compressor of a refrigerating system to manage the available cooling power, $y(\tau)$ is the temperature of the chilled fluid (or the suction pressure as well), y_{ref} is the temperature (or pressure) set-point, $d(\tau)$ is the thermal load and u_1 and u_2 are the compressor "on" and "off" conditions respectively. Equations 1.2 allows to determine the control signal $u(\tau)$ as a function of the error $e(\tau)$ for an ideal two-positions controller.

$$u(\tau) = \begin{cases} u_1 & \text{if } e(\tau) > 0 \\ u_2 & \text{if } e(\tau) < 0 \end{cases} \quad (1.2)$$

Looking at Eq. 1.2, it can be noticed how the ideal on-off controller modifies its action every time a change in sign of the error signal occurs, thus leading

to too high switch frequencies which may cause problems, like, in refrigeration systems, a reduction in compressors life. To overcome this, on-off controllers are generally used with hysteresis cycles, as shown in the schematic of Fig. 1.30. In this case, the switch from u_2 to u_1 occurs when the error $e(\tau)$ exceeds

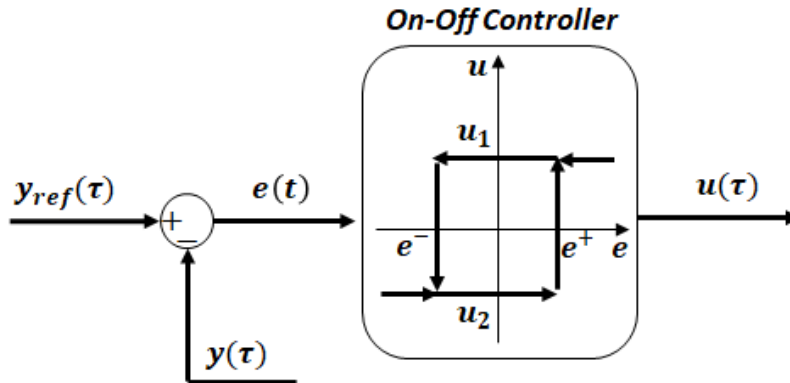


Figure 1.30: Generic schematic of an on-off controller.

the upper value e^+ of the dead band; in a very similar way, the switch from u_1 to u_2 occurs when $e(\tau)$ is lower than the bottom value $-e^-$ of the dead band. Equations 1.3-1.4 describe the behaviour of an on-off controller with hysteresis.

$$\text{if } u(\tau - 1) = u_2 \begin{cases} u(\tau) = u_2 & \text{if } u(\tau) < e^+ \\ u(\tau) = u_1 & \text{if } u(\tau) > e^+ \end{cases} \quad (1.3)$$

$$\text{if } u(\tau - 1) = u_1 \begin{cases} u(\tau) = u_1 & \text{if } u(\tau) > -e^- \\ u(\tau) = u_2 & \text{if } u(\tau) < -e^- \end{cases} \quad (1.4)$$

PID controllers

The control signal of a PID controller is generated by the sum of three contributions, namely the proportional, the integral and the derivative actions. As shown in Fig. 1.31, in a PID controller with only the proportional action, the control signal $u(\tau)$ is proportional to the error signal $e(\tau)$, and the constant of proportionality K_P is called "proportional gain". The control signal for the

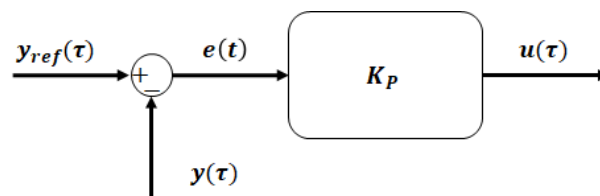


Figure 1.31: Schematic of the proportional action in a PID controller.

proportional action can be thus calculated as:

$$u(\tau) = K_P \cdot e(\tau) \quad (1.5)$$

As shown in Fig. 1.32, in the case of a PID controller with only the integral action the control signal is proportional to the integral of the error and can be evaluated through Eq. 1.6, where "integral gain" is the constant K_I .

$$u(\tau) = K_I \cdot \int e(\tau) d\tau \quad (1.6)$$

If only the derivative action is present, as reported in the operation schematic

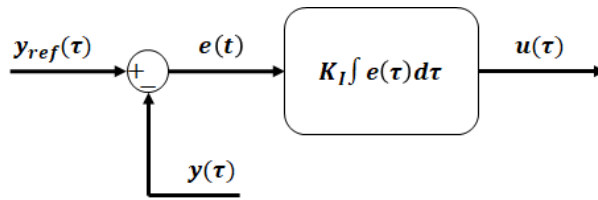


Figure 1.32: Schematic of the integral action in a PID controller.

shown in Fig. 1.33, $u(\tau)$ is proportional to the derivative of the error signal $e(\tau)$ and the proportionality constant K_D is the "derivative gain", as also reported in Eq. 1.7.

$$u(\tau) = K_D \cdot \frac{d(e(\tau))}{d\tau} \quad (1.7)$$

In a generic PID controller, all three contributions must be taken into account,

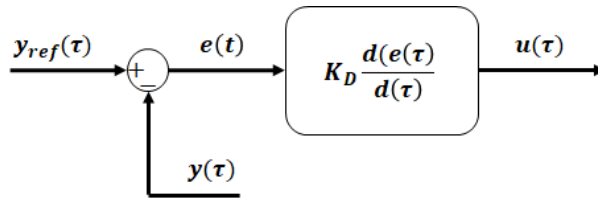


Figure 1.33: Schematic of the derivative action in a PID controller.

and the control signal can be expressed as:

$$u(\tau) = K_P \cdot e(\tau) + K_I \cdot \int e(\tau) d\tau + K_D \cdot \frac{d(e(\tau))}{d\tau} \quad (1.8)$$

However, Eq. 1.8 is usually written as:

$$u(\tau) = K_P \cdot \left[e(\tau) + \frac{1}{T_I} \cdot \int e(\tau) d\tau + T_D \cdot \frac{d(e(\tau))}{d\tau} \right] \quad (1.9)$$

where T_I and T_D are called integral and derivative times respectively.

As an example, if a PID controller is used to control the cooling power of a refrigeration plant by acting on the compressor, the control signal $u(\tau)$ would correspond to the compressor frequency, which, from a purely theoretical point of view, could take an infinite number of values. However, in real plants, upper and lower limits on the number of revolutions per minute are imposed by the manufacturers, thus limiting the values that $u(\tau)$ can assume.

1.7.2 Influence of control systems on energy efficiency of refrigeration plants

Capacity control

Regarding the cooling capacity control of a refrigeration machine, which usually acts on the compressor, the on-off strategy is still nowadays a very common solution, both in industrial refrigeration and in residential air-conditioning, in particular for low-capacity machines [34]. However, this kind of control logic is usually characterized by a series of drawbacks which affect both technical and energetic aspects. Among the former is the limitation in the allowed number of compressor starts per hour, which, if not maintained under the limit allowed by the manufacturers, could bring to a severe reduction in the life of the device. The main reason can be found in the high surge current required at each start-up to restore the operating pressures at the evaporator and at the condenser, with a consequent significant increase in the temperature of the electric coils of the driving motor. As reported in [34], the maximum number of starts suggested for a volumetric compressor is usually six per hour, which can be brought to 8-10 when scroll compressors are used.

Another drawback in the use of an on-off control strategy is related to the so-called "cycling losses", which represent the increase in the electric power demand of a refrigerating unit working intermittently when compared to the consumption of the same machine working in steady-state at the same evaporation and condensation temperatures, [31]. Basically, the decrease in the energy efficiency due to cycling losses is mainly due to the refrigerant migration from the high- to the low-pressure sides of the plant during the machine off-periods which leads to a pressure equalization and a subsequent increase in the energy demand during the machine start-up necessary to restore the steady-state operating conditions. Such a phenomenon is typical of systems equipped with capillary expansion devices, where reductions in the energy efficiency up to 25% have been highlighted in comparison to machines working continuously, [36–38]. As reported in [39] by Bagarella et al., also intermittent systems using TEVs as expansion devices are subjected to refrigerant migration during off periods, and reduction in the energy efficiency up to 13% can be attributed to the cycling losses. The same authors suggest that one way to reduce the adverse effects of cycling losses in these systems consists in the introduction of a solenoid valve in series to the TEV thus disconnecting the high-pressure from the low-pressure side during the off periods; however, the best results in terms of energy efficiency in machines operating intermittently

have been obtained using an electronic expansion valve, which allows more advanced control strategies at starts.

A technical solution to overcome the limits of an on-off control strategy is the use of refrigerating machines equipped with an inverter-driven compressor, to modulate the rotational frequency to precisely control the temperature of the chilled fluid at either inlet or outlet of the evaporator. Usually a PID control algorithm is adopted to reduce the number of starts per hour, reducing as a consequence the mechanical stress of the compressor and the effects of cycling losses. In comparison to intermittent machines a reduction in the ratio between condensation and evaporation pressure at partial loads is also granted, thus leading to an increase in the COP. In fact, since a modulating unit supplies the same amount of energy of an on-off machine but over longer time, the mean supply temperature of the chilled secondary fluid, and thus the evaporation pressure, can be higher, with subsequent increase in the efficiency [40]. As mentioned in section 1.7.1, the rotational frequency of the shaft cannot assume infinite values, since upper and lower limits are prescribed by the manufacturer to ensure good energy efficiencies and to avoid malfunctioning of the devices, with lower bounds usually set between 15 and 30 Hz [31]. In fact, especially for rotary compressors like screw, scroll and sliding vane, a reduction in the isentropic efficiency η_{is} and volumetric efficiency η_v occurs when operating at frequencies far from the rated value [41, 42]. At higher frequency, the main cause of this is the increase of pressure drops and mechanical losses in the suction chamber, whilst at lower speed larger leakages occur between the high and the low pressure sides, because of the decreasing in oil sealing [41, 42]. In reciprocating compressors, the volumetric efficiency is less affected by the revolution frequency, whilst variations in the isentropic efficiency can be highlighted when operating far from the design speed; the lowest values of η_{is} are obtained for semi-hermetic types which are more influenced by the actual superheat of the refrigerant in the suction section, caused by temperature increase when flowing around the motor windings [43]. In addition to the possible reduction of efficiencies with the variation of frequency, the presence of the inverter, which is necessary to modulate the rotational speed and characterized by electric efficiencies between 95% and 98%, represents a drawback of variable speed compressors in terms of both energy efficiency and cost [42]. Moreover, if circulation pumps and fans with no modulation are used, an increase in the energy consumption required to operate the auxiliary devices occurs, since they work longer than with an intermittent machine [44]. An alternative to reduce cycling is represented by multi-level on-off controllers, which are usually applied to multi-cylinder reciprocating compressors or machines equipped with more than one compressor, [34]. Each level of the controller follows an on-off logic, as presented in section 1.7.1, and the number of active stages depends on the supply or return temperature of the operating fluid.

Superheat control

Another controlled variable which has a great impact on the operation of a refrigeration system, both in terms of energy efficiency and components safety, is refrigerant superheat at the outlet of the evaporator. To this aim, excluding systems with capillary valves, a dry-expansion vapour-compression machine is usually equipped with thermostatic (TEV) or electronic expansion valves (EEV). Whilst TEVs allow a mechanically-driven control of the refrigerant superheat, EEVs are usually operated by a stepper motor, which can be controlled through a PID or more advanced systems. Generally speaking, the higher the superheat, the farther the cycle is from the ideal Carnot cycle, thus reducing the overall energy efficiency; on the other hand, too low values of superheat could lead to valve hunting and allow a certain amount of liquid refrigerant to enter the compressor, resulting in its failure. For some authors, the main causes behind the phenomenon of instability in thermostatic expansion valves must be sought in the evaporator characteristics [45–49]. As investigated by Huelle, [46–49], the minimum stable superheat (MSS) under which instability phenomena occur depends on the evaporator itself and is influenced by the heat transfer conditions, such as flow of the secondary fluid, temperature difference and, above all, thermal load. The closer superheat is kept to the MSS in the stable region, the higher is the COP. For others, the valve hunting has to be associated with stability of the evaporator fluid supply control system [50–53]. As demonstrated in [54], valve hunting can occur also in systems equipped with EEVs when too high PID gains are used; moreover, a MSS point exists for electronic valves as well, and the superheat set point must be higher than its value to guarantee stability [55].

Several works are focused on the analysis of the effects of superheat control on the performance of refrigerating machines. Tassou and Al-Nizari, [56], compared the performances of a TEV and an EEV through an experimental analysis carried out on a commercial chiller both in steady-state and transient conditions. Similar energy performance and control quality were identified for the two valves in steady-state conditions, whilst lower oscillations and thus a more stable control of the refrigerant superheat occurred when the EEV was used. Also, the authors investigated the effects of the superheat set point of the EEV on the energy performance of the machine, highlighting how too low set points lead to instability phenomena, whilst too high values decrease the COP. The authors also showed how setting high gains in the PID controller at the machine start-up could reduce the cycling losses typical of the on-off control, whilst low gains in steady-state operations could ensure lower oscillations in the refrigerant superheat: adaptive gains thus represent an optimum solution. As reported in the work by Yu et al. on an air-cooled reciprocating chiller, [57], thermostatic expansion valves usually require high pressure differentials (at least 690 kPa) to work properly, thus barring the possibility of reducing the condensation pressure through control of the mass flow rate of the secondary fluid when its temperature decreases. Subsequently, lower COPs are obtained with respect to EEVs, which can work with pressure differentials down to 103 kPa and thus allow condensation temperature only slightly higher

than that of the secondary fluid. Although TEVs ensure a stable control of the superheat when operating with set points higher than the MSS, the amount of superheat obtained is often inconsistent with the desired value, [58]. In fact, the type of control obtained by using a TEV can be assimilated to a proportional (P) controller, which does not allow to cancel the error in the controlled variable when the system operates far from name conditions. The EEV is unaffected by this, since PIDs can be configured in the electronic controller, and the presence of the integral action (I) ensures compensation for that error. The higher control precision and energy efficiency usually allowed by electronic expansion valves together with the high potentiality in the electronic field available nowadays contribute to make the analysis of different and more advanced control logics applied to EEVs a central field of investigation. Jolly et al., [59], analysed the impact of a fuzzy-logic control algorithm together with an adaptive control of the superheat set point of an EEV on the performance of a fin-type evaporator in a refrigeration container. In particular, the superheat set point was varied on-line in order to always work close to the minimum stable superheat (MSS), thus optimizing energy efficiency. The authors highlighted that, using such a control, a 10% increase of the COP is obtained in comparison to a fixed set-point, whilst the improvement in energy efficiency raises up to 20% when the superheat is controlled through a TEV. In [60], Qi et al. developed a new control logic for the refrigerant superheat in a direct-expansion air conditioner which had to be used with a MIMO controller acting on the compressor and evaporator fan speeds to simultaneously control air temperature and humidity. Basically, the new controller was a PID integrated with two additional inputs, namely the variations in compressor and fan speeds, to compensate the large deviation in the superheat highlighted on the same machine when using a traditional PID in combination with the MIMO, as shown in [61, 62]. The new controller showed better performance both in terms of control quality and of energy efficiency. Besides, also the application of model predictive controls (MPC) to manage the overture of an EEV can be found in literature. As an example, Dantas et al., [63], realized an ARMAX model (Auto Regressive Moving Average with eXogenous input) of a refrigeration system to predict the evaporation and condensation temperatures, T_e and T_c , and the superheat ΔT_{sh} . The work was the basis for the design of an MPC of the expansion device aimed at improving the energy efficiency in comparison to traditional PID controller.

Condensation conditions

In addition to the cooling capacity and the superheat at evaporator outlet, the conditions of the refrigerant in the condenser play a significant role in the operation of the machine and its energy performance. The condensation pressure, or the refrigerant subcooling at the outlet of the heat exchanger, is usually kept at the desired set point by acting on the fans or pumps which control the mass flow rate of the secondary fluid.

Manske et al, [64], investigated the effects of the head pressure control of an

evaporative condenser in industrial refrigeration systems, finding how values minimizing the energy consumption are a linear function of the wet-bulb outdoor temperature. In [65, 66], Yu and Chan investigated the effects of an optimum condensation temperature control on the COP of an air-cooled centrifugal chiller. The authors carried out simulations in TRNSYS showing how controlling the fans speed to keep the desired set point of the condensation temperature, which is varied as a function of the outdoor temperature, allows to significantly increase the COP, particularly at part load conditions. In comparison to the traditional condensation pressure control with constant speed fans, the use of variable speed fans with suitable control strategies allows to increase the chiller COP by 4.0 – 127.5%.

Many authors investigated the possibility of controlling the condensation conditions to optimize heat recovery in applications where both cooling and heating demands are present. For example, in [67], Arias and Lundqvist investigated through simulations the performance of a refrigeration system for a supermarket in Sweden, where both floating condensation pressure and heat recovery strategies were used reporting higher energy efficiencies in comparison adoption of either strategy. Investigation of heat recovery strategies is typical for refrigeration systems operating with carbon dioxide (R744), where the usually high temperatures reached, especially in transcritical conditions, allow to recover heat at different temperature levels. Ge and Tassou, [68], investigated through simulations the heat recovery potential of an all- CO_2 refrigeration system serving a supermarket. The authors showed how, considering the typical weather in UK, the heat recovery potential can be increased by increasing the pressure in the gas cooler/condenser up to the level which allows to satisfy all the heating demand. Also, Polzot et al., [69], compared the performance of a R744 booster refrigeration system serving a supermarket for both refrigeration and heating demand with those of a traditional R134a/ CO_2 cascade refrigeration system together with an R410a heat pump for space heating and hot water. The CO_2 system was also equipped with two additional heat exchangers at the high pressure side, in series to the gas cooler/condenser, to meet the thermal requirement. The analysis was theoretical and carried out through annual simulations in TRNSYS. In the booster system, the high pressure set-point was increased to meet the energy demand for space heating and hot water, whilst it floated dependently on the ambient temperature when no heat was required; although higher energy consumption were shown in summer with respect to the traditional plant, annual energy savings up to 6.5% were highlighted dependently on the climate because of the higher efficiency during cold periods.

Chapter 2

Dynamic model of the VCC system

Thermal systems like refrigerating machines based on vapour compression cycles (VCC) often experience unsteady conditions during real operation, because of disturbances caused by either changes in external conditions (such as load, ambient temperatures etc.) or by actions of the control system. The possibility of investigating before installation the transient behaviour of such systems through dynamic models represents a useful analysis tool and a potential source of economic savings, because it allows to choose the best control logic for a certain application and to foresee any critical situations which could lead to system failure [6]: in this chapter, the mathematical structure at the base of the models realized for the main components of a vapour compression refrigerating machine is described.

As shown in Fig. 2.1, the dynamic model of a whole vapour compression refrigerating machine can be obtained through an input-output logic, where the outputs of a single component model represent the inputs for another one. More in detail, considering a simple vapour compression system (VCS) neglecting the dynamics of the accumulator, the receiver and the pipes, the pressure at the evaporator and the condenser, P_e and P_c , and the refrigerant enthalpy at the evaporator and condenser outlets, h_{ero} and h_{cro} , represent the input to the compressor and expansion valve models, through which it is possible to calculate the refrigerant mass flow rates, \dot{m}_{rk} and \dot{m}_{rv} , and enthalpies at the inlet of the heat exchangers, h_{kro} and h_{vro} . Moreover, in order to completely determine the model, other inputs are required, like the secondary fluid mass flow rates (\dot{m}_{ef} and \dot{m}_{cf}) and inlet temperatures (T_{efi} and T_{cfi}) for the heat exchangers, the control signal to the EEV which determine the position of the pin (p), the rotation frequency (f) and the part-load condition (PL) for the reciprocating compressor.

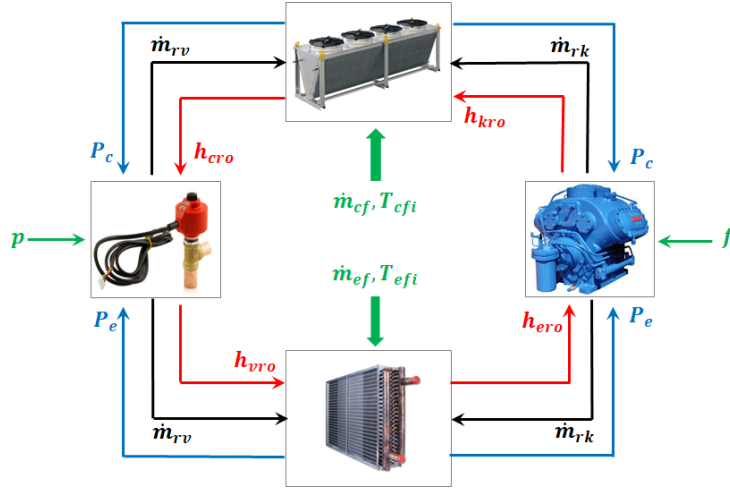


Figure 2.1: Scheme of the model of a vapour compression refrigeration system: input-output connection of the models of the single components.

2.1 General characteristics of dynamic models for VCS

As reviewed in [70], it is usual to classify dynamic models of vapour compression refrigerating machines in three main categories, namely white box, gray box and black box. White-box models, also referred to as "first principles", are obtained starting from the physical laws describing the process to be modelled, such as conservation equations. Robustness is one of their most important characteristics, since variations in the system parameters are directly managed by the governing equations, and a deep insight of the phenomenon is offered; however, a great effort is required in their creation, tuning and validation. Black-box models, also called "data-driven" models, represent the opposite approach, since they rely on experimental data for the identification of a dynamic model. They are quicker to develop than white-box models, but their validity is strictly connected to the particular system investigated. Grey-box models can be placed in-between, since they combine physical governing equations with experimental data under the form of performance maps (e.g. efficiency maps).

Another fundamental characteristic of a dynamic model is the time-scale of the transients to be investigated. In particular, on the basis of the time constant relative to the system response to a certain perturbation, the transients of a system can be classified as small-scale and large-scale. Possible causes of large transients are changes in thermal load, start-up and shut-down processes, perturbation imposed by the control system, whilst swift fluctuations in operating conditions of valve and compressor are usually responsible for small-scale transients, characterized by system responses on a smaller time scale. Thus, once the time scale of the transient to be investigated has been identified, each component of the system must be mathematically described with a sufficient degree of accuracy, allowing to obtain a model suitable for practical use, [71].

In VCC systems, the dynamics of major interest are usually those of thermal nature related to the heat exchangers, which are described by systems of ordinary differential equations, whilst the mechanical dynamics of mass flow devices like valves and positive displacement compressors are usually somewhat faster and are therefore modelled through static models using algebraic equations. In some works, lumped parameter model of the compressor shell or simple time delay in the compressor outlet enthalpy, like in [72], has also been included in order to take the thermal dynamics into account. As for the expansion device, an exception is represented by the thermostatic valve, which is described by a first order differential equation for the calculation of the bulb temperature that drives the valve opening together with the elastic force due to the spring, [70, 73].

Dynamic models of VCC systems can also be classified on the basis of the dynamic modelling approach used for the heat exchangers. As reviewed in [70, 73], three main approaches can be identified: lumped-parameter, moving-boundary (MB) and finite-control volumes (FCV) models. Lumped-parameter models usually apply conservation equations to the entire heat exchanger or to multiple control volumes within it (usually associated with different refrigerant phases) which do not change their extension in time; it is usually a simplified approach used to investigate aspects of the phenomenon different from the two-phase flows, like the coefficient of performance of the system. The MB approach can be considered as an upgrade of the lumped parameter approach: it consists in dividing the heat exchanger into volumes dependent on the refrigerant phase but with time-dependent extensions, which thus become dynamic variables. The last approach used to model the heat exchangers of a VCS is the finite-control volume (FCV), which consists in discretising the device in a number of cells for which conservation equations are written: this model describes the phenomenon in greater detail than lumped-parameter and MB models, but, on the other hand, is usually of higher order and thus more computationally expensive [73]. Bendapudi et al. carried out a comparison between performances of moving-boundary and finite-volume approaches, used for the dynamic model of a shell-and-tube heat exchanger, [74]. Results showed how the FCV formulation is more robust when simulating machine start-up and any kind of large transient, but with a three times higher computational cost than MB approach, which can manage large transients as well, but with a stability strongly dependent on the compressor and valve models. Because of its low computational cost while maintaining a certain degree of accuracy often suitable for control design, the moving boundary approach was adopted in this work.

2.2 Overview of the applications of the MB approach to VCSs

One of the earliest work on dynamic modelling of two-phase flows in the heat exchangers of a refrigeration system was carried out by Wedekind et al., [75],

who applied the moving boundary formulation to the two-phase flows in tubes evaporators and condensers, realizing how the two-phase region can be treated in a lumped form by means of the system mean void fraction instead of using the transient form of momentum equation. This work can be considered as pioneering for the MB models, since almost every researcher developing this kind of models adopts the mean void fraction assumption.

Grald and MacArthur, [76], presented a MB model of a direct expansion evaporator incorporated into an overall heat pump model, using a lumped-parameter approach for the condenser. The evaporator moving-boundary model was compared in terms of predicted cooling capacity and compressor power to a discretized model previously validated against experimental data. No information about the evaporation pressure trend were given for the moving boundary model.

He et al., [77], were among the first authors to use the MB approach to develop a multiple inputs-outputs (MIMO) control for a direct expansion vapour compression refrigeration system for air conditioning applications. The models were validated against experimental data, showing how the MIMO control system improved the performance of the system.

In [78], Leducq et al. applied the moving boundary approach to the complete dynamic model of a VCS using water as secondary fluids, and analyse the model response to sudden changes in compressor velocity and valve opening through comparison with experimental data.

Kumar et al., [79], presented a state space based multi-input multi-output model for a direct expansion air-conditioning system considering both the dynamics of the VCS and the air circuit and taking into account condensation on the evaporator's wall. The MB approach was used to model the VCS heat exchangers but convective heat transfer was neglected in the vapour region in order to reduce the number of variables. The model was validated through experimental data obtained in an air-conditioning system for a railway coach and controlled by an ON-OFF logic; however, only results obtained for the cabin temperature and humidity were presented in the validation procedure.

Rasmussen and Alleyne, [80], applied the moving boundary approach to obtain control-oriented models for a direct expansion transcritical vapour compression systems.

Lei and Zaheeruddin, [81], implemented a dynamic model of a water chiller refrigeration system but no validation results were reported. The authors investigated the effects of variations in control input such as compressor frequency and thermostatic expansion valve opening fraction and reported only the results of simulations.

Several works in literature are aimed at developing MB models which allow the appearance/disappearance of fluid phase regions, thus enabling the model to simulate large transients too. These models are often referred to as "switched moving-boundary" (SMB) and, like MB models, are of low order and often suitable for control design. The works by Willatzen, Pettit and Sorensen, [82, 83], were among the first where the switched moving-boundary approach was used to model large transients such as compressor ON-OFF cycling.

Li and Alleyne, [84], presented a complete dynamic model of an air conditioning VCS able to simulate large transients typical of shut-down and start-up operations using an advanced switch moving-boundary approach for the finned-tube evaporator and condenser models, starting from the model of an air-cooled condenser presented in [85]. In particular, the evaporator can operate with two regions (TP+V) or with the two-phase region (TP) only, whilst the condenser can have three regions (V+TP+L), two regions (V+TP,TP+L) or one single region (TP,V). Results were compared to experimental data obtained in two different tests: stop-start steps in both compressor speed and valve opening inputs and stop-start step change in the compressor speed only.

Eldredge et al., [86], presented an alternative to the SMB approach, extending the definition of mean void fraction in order to handle transients which slightly shift from saturation conditions at the outlet of the heat exchangers.

In [87], Cecchinato and Mancini developed a switched moving boundary model of a direct expansion finned coil evaporator including refrigerant mean density and superheated vapour density among the state variables in order to obtain a model which intrinsically conserved mass. The switching scheme among the two formulations presented (TP-V and TP) was driven by the superheated vapour density and the length of the superheated region, without the need of minimum threshold length. The model was validated comparing results with those obtained through a FCV model previously validated against experimental data. However, a similar formulation for the condenser was not given and simulations were carried out in "open-loop", i.e. without connections to the remaining parts of the VCS.

In the work presented by Qiao et al., [88], a switched moving-boundary model of heat exchangers was presented including refrigerant pressure drop. They also investigated the effects of the state variables chosen on refrigerant mass conservation and computational efficiency and concluded that moving boundary models can only manage non-zero flows thus becoming unsuitable for prolonged off-cycle transients of vapour compression systems.

In [89], a review of the switching schemes used for moving boundary models of evaporators and a comparison with the finite-volume approach were presented. Three different switching schemes (enthalpy-based, mean void fraction-based, density-based) were compared through numerical simulations carried out by means of a fixed-step solver and guidelines on the use of such schemes were given.

As emerges from this brief literature review, the moving boundary approach, and in particular the SMB framework, has often been adopted by researchers to investigate the dynamic behaviour of vapour compression refrigerating machines and to design suitable control strategies. However, through this approach, mainly direct expansion machines have been investigated and, in the cases where water chillers were considered, brazed-plate heat exchangers (BPHE) were not taken into account. Since BPHE represent a reasonable way to reduce the amount of refrigerant in the plant because of their high efficiency and low volume, in this work the SMB approach was used to model also their dynamic behaviour.

2.3 Modelling approach for the heat exchangers

The core of the mathematical model of a vapour compression refrigerating machine is represented by the heat exchangers, namely the evaporator and the condenser, since they have the main influence on the dynamics of the system [70]. Since the main purpose of this work is to obtain a dynamic model of a vapour compression refrigerating machine able to investigate the effects of control systems on energy efficiency, environmental impact and control quality while maintaining a low-order system of differential equations possibly for control design, the switched moving-boundary approach (SMB) was chosen, where the governing equations are obtained applying the conservation equations to the control volumes associated with each phase-dependent region of the refrigerant and the wall. The choice of the state variables to describe the thermodynamic state of each region is in fact arbitrary, but consequences in switching schemes and in model conservativeness must be evaluated. In this work, because of the large literature available, the well-established switching schemes and the extended experimental validation, the modelling technique detailed in [84,85,90,91] was adopted, where the two-phase region is described using the pressure and the mean void fraction $\bar{\gamma}$ as a dynamic variable in order to allow the simulation of large transients, which can occur under the action of certain control logics (e.g. step variations in compressor speed in multi-level control). In such large transients, the assumption of a constant mean void fraction is no longer valid, [75], since the pressure and the mass contained in the heat exchangers vary significantly. The refrigerant single-phase regions are described through pressure and enthalpy instead. Furthermore, in order for the model to be able to simulate large transients typical of on-off control strategies, since the moving-boundary approach tends to fail when considering prolonged zero flows, [88], a simplified lumped-parameter approach was adopted when simulating machine off periods so as to capture mainly the dynamic evolution of the pressure and ensuring mass conservation.

Two types of heat exchangers were investigated, namely finned-tubes and brazed-plate, and the main assumptions made were:

- one-dimensional, compressible and unsteady flow of refrigerant;
- the area of the cross-section at the refrigerant side is constant along the heat exchanger;
- uniform refrigerant pressure along the heat exchangers, so as to neglect the momentum equation;
- a suitable mean void fraction correlation was used in order to take into account its dependence on pressure and quality;
- thermal storage within the heat exchanger mass was taken into account, by means of a constant specific heat c_w ;

- axial conduction was neglected;
- the conductive thermal resistance of the heat exchanger was neglected;
- thermal storage in the secondary fluid side was neglected, both for finned-tubes and for brazed-plate heat exchangers.

The required boundary conditions for the model of the heat exchangers are:

- inlet refrigerant mass flow rate;
- inlet refrigerant enthalpy;
- outlet refrigerant mass flow rate;
- inlet secondary fluid mass flow rate;
- inlet secondary fluid temperature.

It emerges how the refrigerant pressure is not among the boundary conditions in the HEX model, since it is considered as a state variable which is dynamically evaluated during the simulations. This approach allows to use the pressure as a boundary condition for the models of the volumetric devices such as the expansion valve and the compressor, which adapt the refrigerant mass flow rate on the basis of the pressure level established in the heat exchangers. The necessary steps to obtain mass and energy balance in the SMB form will be described in detail for the evaporator only, whilst for the condenser only the final form of the equations will be reported. Equations for the refrigerant and the heat exchanger structure are independent of the heat exchanger configuration, whereas for the secondary fluid a cross-flow and a counter-current flow configuration were used for the finned-tubes and the brazed-plate heat exchangers respectively.

Before entering into details on the SMB formulation of the HEX models, a few words about the correlation used must for the mean void fraction be spent.

2.4 Mean void fraction correlation

The use of the mean void fraction $\bar{\gamma}$ is very handy in the modelling of two-phase flows, since it allows application of a lumped-parameter approach instead of the transient form of the momentum equation, [75]. Also, from knowledge of the mean void fraction an estimation of the refrigerant mass contained in the two-phase (TP) region can be made. In this work, to simulate large transients which may occur under the action of certain control strategies, the mean void fraction is considered a dynamic variable, as done in several works, e.g. [84, 85]. In fact, as explained in [85], the use of the mean void fraction among the dynamic variables grants continuity and therefore the conservation of mass in the TP region when a switch in model formulation occurs: this is a very important issue since the refrigerant mass contained in a refrigeration

plant is a quantity of fundamental interest.

The void fraction γ evaluated at a certain section of the heat exchanger in the two-phase region, which can be defined as the ratio between the area occupied by the gas and the area of the whole section, strictly depends on the local vapour quality x , the liquid and vapour densities ρ_l and ρ_v and the velocities of the two phases. On the basis of the discussion in [92], γ can be expressed through Eq. 2.1, where S is the slip ratio, defined as the ratio of the vapour and liquid velocities.

$$\gamma = \frac{1}{1 + S \frac{1-x}{x} \frac{\rho_v}{\rho_l}} \quad (2.1)$$

The slip ratio S depends on the flow pattern and it is usually determined through suitable correlations. An expression for the mean void fraction $\bar{\gamma}$ can be obtained integrating Eq. 2.1 over the length of the heat exchanger; considering an uniform heat flux in the TP region and thus a linear profile of the vapour quality, Eq. 2.1 can be integrated considering the quality x as a variable:

$$\bar{\gamma} = \frac{1}{x_o - x_i} \int_{x_i}^{x_o} \frac{x}{x + (1-x) \frac{\rho_v}{\rho_l} S} dx \quad (2.2)$$

Using the correlation suggested by Zivi, [93], like in [84, 85], and thus expressing the slip ratio through Eq. 2.3, an analytical form of the mean void fraction as a function of liquid and dry-saturated vapour densities and inlet and outlet quality can be determined, as reported in Eq. 2.4, where $A = S \frac{\rho_v}{\rho_l}$.

$$S = \left(\frac{\rho_v}{\rho_l} \right)^{-\frac{1}{3}} \quad (2.3)$$

$$\bar{\gamma} = \frac{1}{1-A} - \frac{A}{(1-A)^2(x_o - x_i)} \ln \left(\frac{(1-A)x_o + A}{(1-A)x_i + A} \right) \quad (2.4)$$

When the refrigerant at the HEX outlet is in two-phase conditions, if the actual value of the mean void fraction $\bar{\gamma}$ is known, the refrigerant outlet quality and therefore its enthalpy can be determined iteratively solving Eq. 2.4.

From Eq. 2.4, an equilibrium value of the mean void fraction $\bar{\gamma}_{TOT}$ can be defined in the cases of complete evaporation ($x_o = 1$) or condensation ($x_o = 0$), as shown in Eqs. 2.5-2.6.

$$\bar{\gamma}_{TOTe} = \bar{\gamma}(x_o = 1) \quad (2.5)$$

$$\bar{\gamma}_{TOTc} = \bar{\gamma}(x_o = 0) \quad (2.6)$$

From Eq. 2.4, the partial derivative of the mean void fraction with respect to the pressure, used in the definition of Eqs. 2.35 and 2.101, can be determined. Indeed, imposing $f_1 = \frac{1}{1-A}$, $f_2 = \frac{A}{(1-A)^2(x_{out}-x_{in})}$ and $f_3 = \ln \left(\frac{(1-A)x_{out}+A}{(1-A)x_{in}+A} \right)$, such a partial derivative can be written through Eq. 2.7,

where the derivatives of f_1, f_2, f_3 and A are calculated by means of Eqs. 2.8-2.11.

$$\frac{\partial \bar{\gamma}}{\partial P} = \frac{\partial f_1}{\partial P} - \left(\frac{\partial f_2}{\partial P} f_3 + f_2 \frac{\partial f_3}{\partial P} \right) \quad (2.7)$$

$$\frac{\partial f_1}{\partial P} = \frac{1}{(1-A)^2} \left(\frac{\partial A}{\partial P} \right) \quad (2.8)$$

$$\frac{\partial f_2}{\partial P} = \frac{(1+A)}{(1-A)^3 (x_{out} - x_{in})} \left(\frac{\partial A}{\partial P} \right) \quad (2.9)$$

$$\frac{\partial f_3}{\partial P} = \frac{(1-x_{out})[(1-A)x_{in} + A] - (1-x_{in})[(1-A)x_{out} + A]}{[(1-A)x_{in} + A][(1-A)x_{out} + A]} \left(\frac{\partial A}{\partial P} \right) \quad (2.10)$$

$$\frac{\partial A}{\partial P} = \frac{2S}{3} \frac{\rho_l \frac{\partial \rho_v}{\partial P} - \rho_v \frac{\partial \rho_l}{\partial P}}{\rho_l^2} \quad (2.11)$$

2.5 Evaporator

The evaporators considered in this work are of the direct-expansion type, with the refrigerant exiting as a superheated vapour during normal operating conditions. In this case, the heat exchanger can be discretized into two zones on the basis of the refrigerant phase: in the first one, the fluid is in two-phase (TP) conditions and exits with quality $x = 1$, whilst in the second one it is superheated vapour (V), where further heating is accompanied by an increase in temperature.

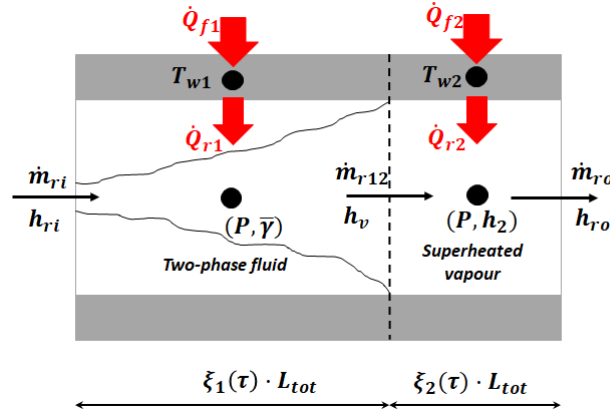


Figure 2.2: Evaporator discretization using the SMB approach: two-regions formulation.

The situation is depicted in Fig.2.2 where \dot{m}_{ri} and \dot{m}_{ro} are the refrigerant inlet and outlet mass flow rates respectively, \dot{m}_{r12} is the mass flow rate exchanged between the two regions, h_{ri} and h_{ro} the refrigerant inlet and outlet enthalpies, h_v the enthalpy of dry-saturated vapour, P the pressure, $\bar{\gamma}$ the mean

void fraction in the TP region, h_2 the mean enthalpy in the V region, T_{w1} and T_{w2} the mean wall temperatures in the two regions and L_{tot} the total length of one single refrigerant path. Moreover the time-dependent non-dimensional length ξ_j for the generic zone j , which represent a state variable, is defined as:

$$\xi_j(\tau) = \frac{L_j(\tau)}{L_{tot}} \quad (2.12)$$

The non-dimensional length ξ_j must also satisfy the condition:

$$\sum_j \xi_j(\tau) = 1 \quad (2.13)$$

In the following, the two-regions formulation (TP+V) of the evaporator, representing the normal operating mode of a dry-expansion heat exchanger, is described first, and the one-region (TP) formulation is then derived from the TP+V system of equations; after that, the equations describing the dynamic behaviour of the heat exchanger during off periods are reported.

2.5.1 Two-regions formulation: two-phase and superheated vapour

Refrigerant-side equations

The governing equations for the evaporator in the SMB formulation are obtained starting from the transient mass and energy balance for open systems applied to each region of the heat exchanger, whose extension varies in time. For the two-phase region, to which index 1 is associated, following the nomenclature of Fig. 2.2 the mass generic mass balance is:

$$\frac{dm_1}{d\tau} = \frac{d(\rho_1 A_{Cr} L_{tot} \xi_1)}{d\tau} = \dot{m}_{ri} - \dot{m}_{r12} \quad (2.14)$$

In Eq. 2.14, A_{Cr} is the refrigerant-side cross-sectional area and ρ_1 is the refrigerant mean density in the TP region. Applying the chain rule:

$$\xi_1 \frac{d\rho_1}{d\tau} + \rho_1 \frac{d\xi_1}{d\tau} = \frac{\dot{m}_{ri} - \dot{m}_{r12}}{A_{Cr} L_{tot}} \quad (2.15)$$

In order to describe the thermodynamic state of the TP region, the pressure P and the mean void fraction $\bar{\gamma}$ were chosen as state variables, on the basis of previous works, [84, 85, 90, 91]; the density of the refrigerant in the two-phase region can be expressed as a function of P and $\bar{\gamma}$ as:

$$\rho_1 = (1 - \bar{\gamma})\rho_l + \bar{\gamma}\rho_v \quad (2.16)$$

The density time derivative thus becomes:

$$\frac{d\rho_1}{d\tau} = \left. \frac{\partial \rho_1}{\partial P} \right|_{\bar{\gamma}} \frac{dP}{d\tau} + \left. \frac{\partial \rho_1}{\partial \bar{\gamma}} \right|_P \frac{d\bar{\gamma}}{d\tau} \quad (2.17)$$

Starting from Eq. 2.16, the partial derivatives of density appearing in Eq. 2.17 can be written as:

$$\left. \frac{\partial \rho_1}{\partial \bar{\gamma}} \right|_P = \rho_v - \rho_l \quad (2.18)$$

$$\left. \frac{\partial \rho_1}{\partial P} \right|_{\bar{\gamma}} = (1 - \bar{\gamma}) \frac{\partial \rho_l}{\partial P} + \bar{\gamma} \frac{\partial \rho_v}{\partial P} \quad (2.19)$$

Introducing Eqs. 2.18-2.19 in Eq. 2.15 and isolating the terms containing model inputs yields the mass balance equation for the TP region:

$$\boxed{\frac{d\xi_1}{d\tau} + \frac{\xi_1}{\rho_1} \left. \frac{\partial \rho_1}{\partial P} \right|_{\bar{\gamma}} \frac{dP}{d\tau} + \frac{\xi_1}{\rho_1} \left. \frac{\partial \rho_1}{\partial \bar{\gamma}} \right|_P \frac{d\bar{\gamma}}{d\tau} + \frac{\dot{m}_{r12}}{\rho_1 A_{Cr} L_{tot}} = \frac{\dot{m}_{ri}}{\rho_1 A_{Cr} L_{tot}}} \quad (2.20)$$

Application of the energy balance applied to the TP region, gives:

$$\frac{dU_1}{d\tau} = \dot{m}_{ri} h_{ri} - \dot{m}_{r12} h_v + \dot{Q}_{r1} - P \frac{dV_1}{d\tau} \quad (2.21)$$

In Eq. 2.21, U_1 is the refrigerant internal energy in the TP region, Q_{r1} the heat transfer rate at the wall and $P \frac{dV_1}{dt}$ is the instantaneous volume expansion work. The internal energy can be expressed as a function of enthalpy H_1 , pressure P and volume V_1 :

$$U_1 = H_1 - PV_1 = m_1 h_1 - PV_1$$

Thus the time derivative of the internal energy of Eq. 2.21 can be developed applying the chain rule and substituting Eq. 2.14 for the time derivative of m_1 , leading to:

$$\frac{dU_1}{d\tau} = m_1 \frac{dh_1}{dt} + h_1 (\dot{m}_{ri} - \dot{m}_{r12}) - P \frac{dV_1}{d\tau} - V_1 \frac{dP}{d\tau} \quad (2.22)$$

Inserting Eq. 2.22 in Eq. 2.21 and simplifying the terms related to the expansion work:

$$m_1 \frac{dh_1}{d\tau} - V_1 \frac{dP}{d\tau} + \dot{m}_{r12} (h_v - h_1) = \dot{m}_{ri} (h_{ri} - h_1) + \dot{Q}_{r1} \quad (2.23)$$

The specific enthalpy associated with the TP region can be expressed as a function of P and $\bar{\gamma}$, as shown in Eq. 2.24, and thus its time derivative can be calculated through Eq. 2.25.

$$h_1 = \frac{(1 - \bar{\gamma}) \rho_l h_l + \bar{\gamma} \rho_v h_v}{\rho_1} \quad (2.24)$$

$$\frac{dh_1}{d\tau} = \left. \frac{\partial h_1}{\partial P} \right|_{\bar{\gamma}} \frac{dP}{d\tau} + \left. \frac{\partial h_1}{\partial \bar{\gamma}} \right|_P \frac{d\bar{\gamma}}{d\tau} \quad (2.25)$$

The partial derivatives of specific enthalpy appearing in Eq. 2.25 can be obtained starting from Eq. 2.24 and applying the chain rule, leading to:

$$\left. \frac{\partial h_1}{\partial P} \right|_{\bar{\gamma}} = \{[(1 - \bar{\gamma})\left(\frac{\partial \rho_l}{\partial P} h_l + \rho_l \frac{\partial h_l}{\partial P}\right) + \bar{\gamma}\left(\frac{\partial \rho_v}{\partial P} h_v + \rho_v \frac{\partial h_v}{\partial P}\right)]\rho_1 - [(1 - \bar{\gamma})\rho_l h_l + \bar{\gamma}\rho_v h_v] \frac{\partial \rho_1}{\partial P}\} / (\rho_1^2) \quad (2.26)$$

$$\left. \frac{\partial h_1}{\partial \bar{\gamma}} \right|_P = \frac{(\rho_v h_v - \rho_l h_l)\rho_1 - [(1 - \bar{\gamma})\rho_l h_l + \bar{\gamma}\rho_v h_v] \frac{\partial \rho_1}{\partial \bar{\gamma}}}{\rho_1^2} \quad (2.27)$$

Substituting Eqs. 2.25 into Eq. 2.23 and expressing the volume and the refrigerant mass of the TP region as $V_1 = A_{Cr}\xi_1 L_{tot}$ and $m_1 = \rho_1 A_{Cr}\xi_1 L_{tot}$ yields the energy balance equation for the TP region with P and $\bar{\gamma}$ as time-dependent state variables:

$$\xi_1 \left[\left. \frac{\partial h_1}{\partial P} \right|_{\bar{\gamma}} - \frac{1}{\rho_1} \right] \frac{dP}{d\tau} + \xi_1 \left. \frac{\partial h_1}{\partial \bar{\gamma}} \right|_P \frac{d\bar{\gamma}}{d\tau} + \frac{(h_v - h_l)}{\rho_1 A_{Cr} L_{tot}} \dot{m}_{r12} = \frac{\dot{Q}_{r1} - \dot{m}_{ri}(h_1 - h_{ri})}{\rho_1 A_{Cr} L_{tot}} \quad (2.28)$$

The same approach can be applied to the superheated vapour region, to which index 2 is associated; the generic mass balance is:

$$\frac{dm_2}{d\tau} = \frac{d(\rho_2 A_{Cr} L_{tot} \xi_2)}{d\tau} = \dot{m}_{r12} - \dot{m}_{ro} \quad (2.29)$$

Applying the chain rule and noticing that $\xi_2 = 1 - \xi_1$ and thus $\frac{d\xi_2}{d\tau} = -\frac{d\xi_1}{d\tau}$:

$$\xi_2 \frac{d\rho_2}{d\tau} - \rho_2 \frac{d\xi_1}{d\tau} = \frac{\dot{m}_{r12} - \dot{m}_{ro}}{A_{Cr} L_{tot}} \quad (2.30)$$

The mean density of the superheated vapour ρ_2 can be determined as a function of pressure and enthalpy through the tables of refrigerant properties and its time derivative can be expressed as:

$$\frac{d\rho_2}{d\tau} = \left. \frac{\partial \rho_2}{\partial P} \right|_{h_2} \frac{dP}{d\tau} + \left. \frac{\partial \rho_2}{\partial h_2} \right|_P \frac{dh_2}{d\tau} \quad (2.31)$$

The mass balance equation for the V region becomes:

$$\frac{d\xi_1}{d\tau} - \frac{\xi_2}{\rho_2} \left. \frac{\partial \rho_2}{\partial P} \right|_{h_2} \frac{dP}{d\tau} - \frac{\xi_2}{\rho_2} \left. \frac{\partial \rho_2}{\partial h_2} \right|_P \frac{dh_2}{d\tau} + \frac{\dot{m}_{r12}}{\rho_2 A_{Cr} L_{tot}} = \frac{\dot{m}_{ro}}{\rho_2 A_{Cr} L_{tot}} \quad (2.32)$$

The generic energy balance for the superheated vapour region is:

$$\frac{dU_2}{d\tau} = \dot{m}_{r12} h_v - \dot{m}_{ro} h_{ro} + \dot{Q}_{r2} - P \frac{dV_2}{d\tau} \quad (2.33)$$

Expressing the internal energy as a function of enthalpy, pressure and volume leads to the final form of the energy balance for the V region, shown in Eq. 2.34:

$$\boxed{-\frac{\xi_2}{\rho_2} \frac{dP}{d\tau} + \xi_2 \frac{dh_2}{d\tau} + \frac{(h_2 - h_v)}{\rho_2 A_{Cr} L_{tot}} \dot{m}_{r12} = \frac{\dot{Q}_{r2} - \dot{m}_{ro}(h_{ro} - h_2)}{\rho_2 A_{Cr} L_{tot}}} \quad (2.34)$$

As emerges from Eqs. 2.20-2.28-2.32-2.34, five unknowns (namely the time derivatives and the intermediate mass flow rate) are present in just four equations. Thus, Equation 2.35 is added to make the mean void fraction track an equilibrium value, which depends on the flow regime established, [85]. Equation 2.35 also ensures continuity and thus conservation for refrigerant mass in the two-phase region when switches among model formulations occur.

$$\boxed{\frac{\partial \bar{\gamma}}{\partial P} \frac{dP}{d\tau} - \frac{d\bar{\gamma}}{d\tau} = K_{\bar{\gamma}}(\bar{\gamma} - \bar{\gamma}_{TOT})} \quad (2.35)$$

$\bar{\gamma}_{TOT}$ represents the mean void fraction equilibrium value when the refrigerant outlet quality equals 1 and depends on the operating pressure and the inlet and outlet conditions. The calculation of $\bar{\gamma}_{TOT}$ and $\frac{\partial \bar{\gamma}}{\partial P}$ can be carried out through the use of suitable correlations, as discussed in section 2.4. $K_{\bar{\gamma}}$ is a tunable relaxation gain which depends on the application, and was set to a value of 5, equivalent to a relaxation time of 200 ms, as done in [85].

In addition to Eqs. 2.20-2.28-2.32-2.34-2.35, Eq. 2.36 representing a global mass balance of the heat exchanger is considered, in order to track the value of the refrigerant mean density ρ_m which is used in the off-duty formulation, as detailed in section 2.5.3.

$$\boxed{\frac{d\rho_m}{d\tau} = \frac{\dot{m}_{ri} - \dot{m}_{ro}}{A_{Cr} L_{tot}}} \quad (2.36)$$

The system of ordinary differential equations (ODEs) describing the dynamics of the refrigerant is thus composed by six equations with the six unknowns $\xi_1, P, \bar{\gamma}, h_2, m_{r12}$.

Wall-side equations

To determine the wall mean temperatures, the energy balance must be applied to each wall region, considering the so-called *wall rezoning* to ensure integral energy conservation at the wall. If \dot{Q}_{rj} and \dot{Q}_{fj} are the heat transfer rates between wall and refrigerant and wall and secondary fluid in the region j , the energy balance at the wall region can be written as:

$$\frac{dU_{w1}}{dt} = \dot{Q}_{f1} - \dot{Q}_{r1} + m_w c_w T_{int} \frac{d\xi_1}{dt} \quad (2.37)$$

$$\frac{dU_{w2}}{dt} = \dot{Q}_{f2} - \dot{Q}_{r2} - m_w c_w T_{int} \frac{d\xi_1}{dt} \quad (2.38)$$

The terms with the time derivative of the non-dimensional length ξ_1 in Eqs. 2.37-2.38 represent the energy transport through the moving interface and allow the time derivative of the wall mean internal energy (calculated as

the weighted average of the internal energy of the single regions) to be equal to the total net heat transfer rate, thus satisfying the integral energy conservation requirement, [85]. T_{int} is a temperature transported by the moving interface, and several alternative ways to describe it can be found in literature [89]. In this work, an upwind scheme based on the interface velocity has been chosen, as presented in [85]. In particular, if the interface is moving rightward, the interface temperature is equal to the temperature of region on the right; in the same way if it is moving leftward the interface temperature is equal to the temperature on of the region on the left side. This behaviour is described by Eqs. 2.39-2.40.

$$\frac{d\xi_1}{d\tau} > 0 \implies T_{int} = T_{w2} \quad (2.39)$$

$$\frac{d\xi_1}{d\tau} < 0 \implies T_{int} = T_{w1} \quad (2.40)$$

Expressing the internal energy of the generic region j as $U_{wj} = m_w c_w \xi_j T_{wj}$, the equations for wall energy balance become:

$$\boxed{\frac{dT_{w1}}{d\tau} = \frac{1}{\xi_1} \left(\frac{\dot{Q}_{f1} - \dot{Q}_{r1}}{m_w c_w} - (T_{w1} - T_{int}) \frac{d\xi_1}{d\tau} \right)} \quad (2.41)$$

$$\boxed{\frac{dT_{w2}}{d\tau} = \frac{1}{\xi_2} \left(\frac{\dot{Q}_{f2} - \dot{Q}_{r2}}{m_w c_w} - (T_{int} - T_{w2}) \frac{d\xi_1}{d\tau} \right)} \quad (2.42)$$

At each time-step, the value of the mean wall temperature T_{wm} is calculated through Eq. 2.43 and stored to be used in the off-duty formulation to calculate the heat transfer rates.

$$T_{wm} = \xi_1 T_{w1} + \xi_2 T_{w2} \quad (2.43)$$

2.5.2 One-region formulation: two-phase

Under certain operating conditions, such as when control acts to vary the compressor speed stepwise trying to track the thermal load in multi-level control, the superheated vapour region may disappear. However, to prevent numerical failure of the model, a switch from a two-regions to a one-region formulation must be provided. Under these circumstances, the variables associated with the V region (h_2 and T_{w2}) are inactive and thus are forced to track suitable values which allow the model, if necessary, to revert unflinchingly to the two-regions formulation.

Refrigerant-side equations

The first equation is obtained imposing that non-dimensional length of the two-phase region does not vary in time:

$$\boxed{\frac{d\xi_1}{d\tau} = 0} \quad (2.44)$$

The mass and energy balance for the two-phase region can be obtained substituting Eq. 2.44 into Eqs. 2.20 and 2.28, and considering that the intermediate mass flow rate \dot{m}_{r12} is equal to the outlet mass flow rate m_{ro} :

$$\boxed{\xi_1 \left. \frac{\partial \rho_1}{\partial P} \right|_{\bar{\gamma}} \frac{dP}{d\tau} + \xi_1 \left. \frac{\partial \rho_1}{\partial \bar{\gamma}} \right|_P \frac{d\bar{\gamma}}{d\tau} = \frac{\dot{m}_{ri} - \dot{m}_{ro}}{A_{Cr} L_{tot}}} \quad (2.45)$$

$$\boxed{\xi_1 \left[\left. \frac{\partial h_1}{\partial P} \right|_{\bar{\gamma}} - \frac{1}{\rho_1} \right] \frac{dP}{d\tau} + \xi_1 \left. \frac{\partial h_1}{\partial \bar{\gamma}} \right|_P \frac{d\bar{\gamma}}{d\tau} = \frac{\dot{Q}_{r1} - \dot{m}_{ri}(h_1 - h_{ri}) - \dot{m}_{ro}(h_{ro} - h_1)}{\rho_1 A_{Cr} L_{tot}}} \quad (2.46)$$

For switching purposes, the mean enthalpy h_2 in the V region is forced to track the enthalpy of the dry-saturated vapour h_v , as shown in Eq. 2.47, where K_h is a tunable tracking constant set here to 5 s^{-1} , to guarantee that the tracking is sufficiently fast.

$$\boxed{\frac{dh_2}{dt} = K_h(h_v - h_2)} \quad (2.47)$$

It can be noticed how in the one-region formulation, Eq. 2.35 is no longer necessary, since the value of the mean void fraction can be completely determined by the mass and energy balance. Also in this case, the value of the refrigerant mean density ρ_m is tracked; even if it is possible to make ρ_m track the value of ρ_1 (one single region active), the global mass balance described in Eq. 2.36 was preferred, since allows to check the mass conservativeness of the pure SMB approach.

$$\frac{d\rho_m}{d\tau} = \frac{\dot{m}_{ri} - \dot{m}_{ro}}{A_{Cr} L_{tot}}$$

Wall-side equations

In the one-region formulation, the first wall-side equation is the energy balance for the two-phase region imposing the constance of the non-dimensional length ξ_1 (which is ≈ 1 , to avoid numerical issues in the case of switching):

$$\boxed{\frac{dT_{w1}}{d\tau} = \frac{1}{\xi_1} \left(\frac{\dot{Q}_{f1} - \dot{Q}_{R1}}{m_w c_w} \right)} \quad (2.48)$$

For the region associated with the superheated vapour, which is inactive, the temperature T_{w2} is forced to track the value of T_{w1} , as highlighted in Eq. 2.49, where K_T is a tunable tracking constant set here to 5 s^{-1} to guarantee a sufficiently fast tracking.

$$\boxed{\frac{dT_{w2}}{d\tau} = K_T(T_{w1} - T_{w2})} \quad (2.49)$$

Also in this situation the mean wall temperature T_{wm} is calculated through 2.43 and stored for use in the off-duty formulation.

2.5.3 Off-duty formulation

During machine off periods, that is when at least one between the inlet and outlet mass flow rate is zero, the aim of the model is to mainly capture the evolution of the pressure and ensure mass conservation. The refrigerant in the heat exchanger is therefore described through a single value of the pressure P and of the mean density ρ_m . The first governing equation coincides with the global mass balance, Eq. 2.36, which is repeated here:

$$\frac{d\rho_m}{d\tau} = \frac{\dot{m}_{ri} - \dot{m}_{ro}}{A_{Cr}L_{tot}}$$

The second governing equation is the global energy balance, where the mean enthalpy h_m is expressed as a function of pressure and density:

$$\left(\frac{\partial h_m}{\partial P} \Big|_{\rho_m} - \frac{1}{\rho_m} \right) \frac{dP}{d\tau} + \frac{\partial h_m}{\partial \rho_m} \Big|_P \frac{d\rho_m}{d\tau} = \frac{\dot{Q}_{rtot} + \dot{m}_{ri}(h_{ri} - h_m) - \dot{m}_{ro}(h_{ro} - h_m)}{\rho_m A_{Cr} L_{tot}} \quad (2.50)$$

Since the calculation of the partial derivative of enthalpy with respect to density is numerically cost-intensive and in order to obtain all the thermodynamic variables and their derivatives as a function of pressure and enthalpy, Eq. 2.50 is analytically manipulated as illustrated in [72]. First of all, both members of Eq. 2.50 are multiplied by $\frac{\partial \rho_m}{\partial h_m} \Big|_P$:

$$\frac{\partial \rho_m}{\partial h_m} \Big|_P \left(\frac{\partial h_m}{\partial P} \Big|_{\rho_m} - \frac{1}{\rho_m} \right) \frac{dP}{d\tau} + \frac{\partial \rho_m}{\partial h_m} \Big|_P \frac{\partial h_m}{\partial \rho_m} \Big|_P \frac{d\rho_m}{d\tau} = \frac{\partial \rho_m}{\partial h_m} \Big|_P \left(\frac{\dot{Q}_{rtot} + \dot{m}_{ri}(h_{ri} - h_m) - \dot{m}_{ro}(h_{ro} - h_m)}{\rho_m A_{Cr} L_{tot}} \right)$$

Then, the double and triple product rule of calculus is applied:

$$\frac{\partial x}{\partial y} \Big|_z \cdot \frac{\partial y}{\partial x} \Big|_z = 1$$

$$\frac{\partial x}{\partial y} \Big|_z \cdot \frac{\partial y}{\partial z} \Big|_x \cdot \frac{\partial z}{\partial x} \Big|_y = -1$$

The final form of the global energy balance is thus obtained, Eq. 2.51:

$$\boxed{-\left(\frac{\partial \rho_m}{\partial P}\bigg|_{h_m} + \frac{1}{\rho_m} \frac{\partial \rho_m}{\partial h_m}\bigg|_P\right) \frac{dP}{d\tau} + \frac{d\rho_m}{d\tau} = \frac{\partial \rho_m}{\partial h_m}\bigg|_P \left(\frac{\dot{Q}_{rtot} + \dot{m}_{ri}(h_{ri} - h_m) - \dot{m}_{ro}(h_{ro} - h_m)}{\rho_m A_{Cr} L_{tot}} \right)}
\tag{2.51}$$

From Eqs. 2.36 and 2.51, the time derivative of during off-duty periods the inactive variables ξ_1 , $\bar{\gamma}$ e h_2 are forced to track suitable values on the basis of the mean void fraction in the whole heat exchanger, $\bar{\gamma}_{off}$, which can be determined as shown in Eq. 2.52.

$$\boxed{\bar{\gamma}_{off} = \frac{\rho_m - \rho_l}{\rho_v - \rho_l}}
\tag{2.52}$$

In the evaporator, during machine stops, the refrigerant may be in two-phase conditions ($0 \leq \bar{\gamma}_{off} \leq 1$) or, possibly, superheated vapour ($\bar{\gamma}_{off} > 1$), since when using direct expansion evaporators, it is desired to keep the liquid refrigerant in the high-pressure side of the loop by closing the EEV or a solenoid valve when using a TEV, [31]. Under these considerations, the tracking values chosen for the inactive variables are summarised in Tab. 2.1.

Table 2.1: Tracking values for the evaporator inactive variables during machine stops as a function of the whole mean void fraction $\bar{\gamma}_{off}$.

	$0 \leq \bar{\gamma}_{off} \leq 1$	$\bar{\gamma}_{off} > 1$
ξ_{track}	0.999	0.001
$\bar{\gamma}_{track}$	$\bar{\gamma}_{off}$	0.999
h_{2track}	h_v	h_m

The tracking equations are:

$$\boxed{\frac{d\bar{\gamma}}{d\tau} = K_{\bar{\gamma}}(\bar{\gamma}_{track} - \bar{\gamma})}
\tag{2.53}$$

$$\boxed{\frac{d\xi_1}{d\tau} = K_{\xi}(\xi_{1track} - \xi_1)}
\tag{2.54}$$

$$\boxed{\frac{dh_2}{d\tau} = K_h(h_{2track} - h_2)}
\tag{2.55}$$

The relaxation factors $K_{\bar{\gamma}}$, K_{ξ} e K_h are tunable by the user and have been set to $5 s^{-1}$ in this work.

Similarly to the refrigerant, the wall is considered as a single entity characterized by its mean temperature T_{wm} during machine off periods. The wall energy balance is thus described by Eq. 2.56, where \dot{Q}_{ftot} and \dot{Q}_{rtot} are the total heat transfer rate with the secondary fluid and the refrigerant respectively.

$$\boxed{\frac{dT_{wm}}{d\tau} = \frac{\dot{Q}_{ftot} - \dot{Q}_{rtot}}{m_w c_w}} \quad (2.56)$$

The inactive variables T_{w1} and T_{w2} are forced to track T_{wm} in order to allow the model to start again with the SMB formulation, as shown in Eqs. 2.57-2.58.

$$\boxed{\frac{dT_{w1}}{d\tau} = K_T(T_{wm} - T_{w1})} \quad (2.57)$$

$$\boxed{\frac{dT_{w2}}{d\tau} = K_T(T_{wm} - T_{w2})} \quad (2.58)$$

2.5.4 Calculation of the refrigerant outlet conditions

Whilst the refrigerant mass flow rate at the outlet is a model input, the refrigerant outlet enthalpy h_{ro} must be determined on the basis of the number of active regions.

Two-regions formulation

In the two-regions formulation, the refrigerant at the outlet section is superheated vapour and the outlet enthalpy must be determined considering some temperature profile within the V region. In this work an exponential temperature profile on the form presented by Eq 2.59 was assumed.

$$T(\xi) = T_{w2} - (T_{w2} - T_{r1})e^{-\alpha\xi} \quad (2.59)$$

In Eq. 2.59, T_{w2} is the wall mean temperature in the superheated vapour region, T_{r1} is refrigerant temperature at saturation and α a parameter obtained by imposing the temperature boundary condition at the outlet $T(\xi = \xi_2) = T_{ro}$, leading to:

$$\alpha = -\frac{1}{\xi_2} \ln\left(\frac{T_{ro} - T_{w2}}{T_{r1} - T_{w2}}\right)$$

Integrating Eq. 2.59 between $\xi = 0$ and $\xi = \xi_2$ yields Eq. 2.60, which expresses the mean temperature T_{r2} , uniquely defined by h_2 and P_2 and allows calculation of T_{ro} once T_{r1} , T_{r2} and T_{w2} are known.

$$T_{r2} = T_{w2} - (T_{w2} - T_{r1}) \left[\frac{\frac{T_{w2} - T_{ro}}{T_{w2} - T_{r1}} - 1}{\ln\left(\frac{T_{w2} - T_{ro}}{T_{w2} - T_{r1}}\right)} \right] \quad (2.60)$$

Due to its non-linearity, Eq. 2.60 is solved through linear interpolation by means of a pre-generated table generated in which the temperature difference between the wall and the refrigerant at the outlet $\Delta T_o = T_{w2} - T_{ro}$ is given as a function of the temperature difference at the inlet of the region,

$\Delta T_i = T_{w2} - T_{r1}$, and the mean temperature difference, $\Delta T_m = T_{w2} - T_{r2}$.

One-region formulation

In the one-region formulation, the refrigerant at the outlet has a vapour quality lower than or equal to 1; thus the outlet enthalpy of the refrigerant can be calculated as:

$$h_{ro} = x_o h_v + (1 - x_o) h_l \quad (2.61)$$

The outlet quality x_o can be calculated from the actual values of the mean void fraction $\bar{\gamma}$, the pressure P and the inlet enthalpy h_{ri} by means of the Zivi correlation presented in section 2.4, which leads to the solution of a non-linear equation.

Off-period formulation

During the off-duty periods, the outlet enthalpy has often no impact on the dynamics of the heat exchanger, since the inlet and outlet mass flow rates are usually zero. However, in the case the outlet mass flow rate has a non-zero value (e.g. because of the presence of a relatively long pipe which delays the effect of the compressor shut-down on the evaporator), the refrigerant outlet enthalpy has been considered equal to the mean enthalpy h_m .

2.5.5 Calculation of the refrigerant-side heat transfer rate

Neglecting the thermal resistance due to thermal conduction in the wall, the heat transfer rate between wall and refrigerant in the generic region j in the SMB formulation can be expressed through Eqs. 2.62, where A_{Sr} is the total refrigerant heat transfer area and α_{rj} is the convective heat transfer coefficient between the refrigerant and the generic wall region j , which is updated at each time-step.

$$\dot{Q}_{rj} = \alpha_{rj} \xi_j A_{Sr} (T_{wj} - T_{rj}) \quad (2.62)$$

The heat transfer coefficient for evaporation in the brazed-plate heat exchanger is calculated through the correlation presented by Longo et al. in, [94], whilst for the evaporation in the finned-tube heat exchanger the Wattlelet correlation [95] was used.

For the superheated vapour region in the brazed-plate heat exchanger a specific correlation reported in [94] was chosen, whilst the Gnielinski correlation was used for the superheated vapour in the finned-tube heat exchanger, [96]. During the machine off periods, the calculation of the total heat transfer rate on the refrigerant side is carried out through Eq. 2.63.

$$\dot{Q}_{rtot} = \alpha_r A_{Sr} (T_{wm} - T_{rm}) \quad (2.63)$$

In both HEX configurations investigated, the heat transfer coefficient α_r is calculated on the basis of the actual value of $\bar{\gamma}_{off}$. As reported in Eq. 2.64, if $0 \leq \bar{\gamma}_{off} \leq 1$, the heat transfer coefficient is calculated as a weighted mean between the pool boiling heat transfer coefficient α_{pool} in circular tubes, [96], and the purely conductive heat transfer coefficient, dependent on the dry-saturated vapour thermal conductivity λ_v and the hydraulic diameter d_h , where the weights are based on the mean void fraction $\bar{\gamma}_{off}$, which gives an estimate of the amount of gas and liquid within a certain volume.

$$\alpha_{r\ off} = (1 - \bar{\gamma}_{tot})\alpha_{pool} + \bar{\gamma}_{off} \frac{\lambda_v}{d_h} \quad (2.64)$$

If $\bar{\gamma}_{off} > 1$, the heat transfer coefficient is calculate considering pure conduction through a superheated vapour, as per Eq. 2.65, λ_{sh} is the thermal conductivity of the superheated vapour.

$$\alpha_r = \frac{\lambda_{sh}}{d_h} \quad (2.65)$$

Thermophysical properties of the refrigerant for the calculation of the heat transfer coefficients are evaluated using the mean values in each region.

2.5.6 Calculation of the secondary fluid heat transfer rate

In this section the method used for the calculation of the heat transfer rate on the secondary-fluid side is reported, on the basis of the HEX configuration. For both configurations considered the thermophysical properties of the secondary fluid are evaluated at its inlet temperature T_{fi} .

Finned-tubes heat exchanger

In finned-tube heat exchangers the secondary fluid is air. In this work, only dry air will be treated. Considering uniform pressure, temperature and velocity for the air at the inlet of the heat exchanger, the heat transfer rate between the fluid and the wall in the SMB framework can be calculated as:

$$\dot{Q}_{f1} = \xi_1 \dot{m}_f c_{pf} (T_{fi} - T_{fo1}) \quad (2.66)$$

$$\dot{Q}_{f2} = \xi_2 \dot{m}_f c_{pf} (T_{fi} - T_{fo2}) \quad (2.67)$$

In Eq 2.66-2.67, T_{fo1} and T_{fo2} are the air temperatures at the outlet of the TP and V regions respectively, which can be computed through the $\varepsilon - NTU$ method, assuming an efficiency $\varepsilon = 1 - \exp(-NTU_f)$; for a generic region j :

$$T_{foj} = T_{wj} + (T_{fi} - T_{wj}) \exp(-NTU_f) \quad (2.68)$$

The number of thermal units is obtained as:

$$NTU_f = \frac{A_{Sf}\alpha_f}{\dot{m}_f c_{pf}} \quad (2.69)$$

In Eq. 2.69, A_{Sf} is the air-side heat transfer area, α_f is the air convective heat transfer coefficient, calculated through correlations for finned-tubes compact heat exchangers as suggested by Kays and London, [97], \dot{m}_f the air mass flow rate and c_{pf} the specific heat at constant pressure.

Air outlet temperature is then obtained considering a perfect mixing between the air flows across the HEX regions, as shown in Eq. 2.70.

$$T_{fo} = \xi_1 T_{fo1} + \xi_2 T_{fo2} \quad (2.70)$$

During the machine off-periods, the total heat transfer rate on the secondary fluid side for the wall global energy balance is calculated as:

$$\dot{Q}_{ftot} = \dot{m}_f c_{pf} (T_{fi} - T_{fo}) \quad (2.71)$$

Where air outlet temperature is:

$$T_{fo} = T_{wm} + (T_{fi} - T_{wm}) \exp(-NTU_f) \quad (2.72)$$

In the case of zero airflow, the heat transfer coefficient α_f is calculated through the correlation for natural convection on a horizontal cylinder available in [96], and the air is supposed to exit the heat exchanger at the mean wall temperature. The heat transfer rate in SMB framework and zero airflow can be calculated through Eqs. 2.73-2.74, whilst for the off-period formulation Eq. 2.75 is used.

$$\dot{Q}_{f1} = \alpha_f A_{Sf} (T_{fi} - T_{w1}) \quad (2.73)$$

$$\dot{Q}_{f2} = \alpha_f A_{Sf} (T_{fi} - T_{w2}) \quad (2.74)$$

$$\dot{Q}_{ftot} = \alpha_f A_{Sf} (T_{fi} - T_{wm}) \quad (2.75)$$

Brazed-plate heat exchanger

In the case of the brazed-plate heat exchanger, a counterflow configuration has been considered; thus, the temperature of the secondary fluid at outlet of the V region (index 2) represents the inlet temperature for the TP region (index 1). The heat transfer rate exchanged in region 2 between the secondary fluid and the wall is:

$$\dot{Q}_{f2} = \dot{m}_f c_{pf} (T_{fi} - T_{w2}) (1 - \exp(-NTU_{f2})) \quad (2.76)$$

The number of thermal units in region 2, NTU_{f2} , can be calculated through Eq. 2.77, where α_{f2} is the heat transfer coefficient between fluid and wall, A_{Sf}

is the total heat transfer area on the secondary fluid side, \dot{m}_f the secondary fluid mass flow rate and c_{pf} its specific heat at constant pressure.

$$NTU_{f2} = \frac{\alpha_f \xi_2 A_{Sf}}{\dot{m}_f c_{pf}} \quad (2.77)$$

The fluid temperature at the outlet of region 2, T_{f12} , which is now entering region 1 is calculated as:

$$T_{f12} = T_{fi} - \frac{\dot{Q}_{f2}}{\dot{m}_f c_{pf}} \quad (2.78)$$

The heat transfer rate in region 1 and the secondary fluid outlet temperature can be now calculated through Eqs. 2.79-2.81.

$$\dot{Q}_{f1} = \dot{m}_f c_{pf} (T_{f12} - T_{w1}) (1 - \exp(-NTU_{f1})) \quad (2.79)$$

$$NTU_{f1} = \frac{\alpha_f \xi_1 A_{Sf}}{\dot{m}_f c_{pf}} \quad (2.80)$$

$$T_{fo} = T_{f12} - \frac{\dot{Q}_{f1}}{\dot{m}_f c_{pf}} \quad (2.81)$$

In the off-period formulation, the wall mean temperature T_{wm} is considered for the calculation of the secondary fluid outlet temperature and the heat transfer rate used in the wall-side energy balance, according to Eqs. 2.82-2.84.

$$\dot{Q}_{ftot} = \dot{m}_f c_{pf} (T_{fi} - T_{wm}) (1 - \exp(-NTU_f)) \quad (2.82)$$

$$NTU_f = \frac{\alpha_f A_{Sf}}{\dot{m}_f c_{pf}} \quad (2.83)$$

$$T_{fo} = T_{fi} - \frac{\dot{Q}_{ftot}}{\dot{m}_f c_{pf}} \quad (2.84)$$

The heat transfer coefficient α_f for the secondary fluid is calculated through the Martin correlation presented in [98].

When no flow occurs, a purely conductive heat transfer coefficient is considered, which is calculated through Eq. 2.85, where λ_f is the thermal conductivity of the secondary fluid and d_h the hydraulic diameter.

$$\alpha_f = \frac{\lambda_f}{d_h} \quad (2.85)$$

The heat transfer rate in SMB framework and zero-flow of the secondary fluid can be calculated through Eqs. 2.86-2.87, whilst for the off-period formulation Eq. 2.88 is used.

$$\dot{Q}_{f1} = \alpha_f A_{Sf} (T_{fi} - T_{w1}) \quad (2.86)$$

$$\dot{Q}_{f2} = \alpha_f A_{Sf} (T_{fi} - T_{w2}) \quad (2.87)$$

$$\dot{Q}_{ftot} = \alpha_f A_{Sf} (T_{fi} - T_{wm}) \quad (2.88)$$

2.5.7 Correction factors for heat transfer coefficients

The heat transfer coefficients calculated through the correlations presented in the previous sections are then multiplied by the correction factors C_{TP} , C_V , C_{Off} and C_f , as shown in Eqs. 2.89-2.92, in order to allow the user to tune the model to better match experimental data in the validation process.

$$\alpha_{r1} = C_{TP} \cdot \alpha_{r1} \quad (2.89)$$

$$\alpha_{r2} = C_V \cdot \alpha_{r2} \quad (2.90)$$

$$\alpha_{r_{off}} = C_{off} \cdot \alpha_{r_{off}} \quad (2.91)$$

$$\alpha_f = C_f \cdot \alpha_f \quad (2.92)$$

2.5.8 Switching criteria

In this section, the switching criteria adopted for SMB modelling of the evaporator are presented. Figure 2.3 summarises all the possible switches which can occur in the evaporator model, distinguishing the switches between model formulations within the SMB framework and the switches between the SMB and the off-periods frameworks. The switching scheme within the SMB framework is based on the works presented in [84] and [85].

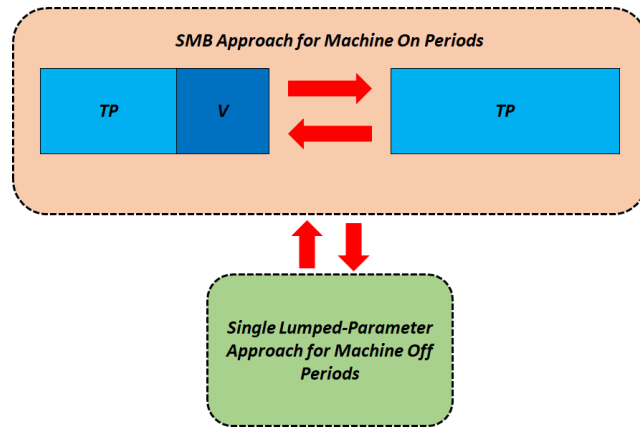


Figure 2.3: Possible switches for the evaporator model.

SMB switches: from two-regions (TP-V) to one region (V)

The switch from the two-regions formulation to the one-region formulation within the SMB framework occurs on the basis of the non-dimensional length ξ_1 and its time derivative: when the extension of the superheated vapour region

ξ_2 is sufficiently small and continues to decrease, then the switch to the one-region formulation must occur; in particular, the switching condition can be resumed as follows:

- $\xi_2 \leq \xi_{2min}$
- $\frac{d\xi_1}{d\tau} > 0$

After tuning to obtain the minimum threshold value, ξ_{2min} has been set to 0.001, which prevents numerical failure of the model.

SMB switches: from one region (V) to two-regions (TP-V)

The switch from the one-region (TP) formulation to the two-region (TP-V) formulation occurs on the basis of the content of refrigerant in vapour phase within the heat exchanger; in particular, if the amount of vapour in the heat exchanger exceeds the amount of vapour in the case of complete evaporation and continues to increase, then the switch must occur. This condition can be summarised as:

- $\xi_1(\bar{\gamma} - \bar{\gamma}_{TOT}) \geq \varepsilon$
- $\frac{d\bar{\gamma}}{d\tau} > 0$

ε has been set to 0.001.

Switch from the SMB to the off-duty formulation

When the inlet or outlet refrigerant mass flow rate goes to zero, the model switches from the SMB to the off-duty framework. Mathematically, the switch occurs when $\dot{m}_{ri} < 0.0001 \text{ kg} \cdot \text{s}^{-1}$ or $\dot{m}_{ro} < 0.0001 \text{ kg} \cdot \text{s}^{-1}$. The reactivation of the SMB framework occurs when both the inlet and outlet mass flow rates have non-zero values, i.e. $\dot{m}_{ri} > 0.0001 \text{ kg} \cdot \text{s}^{-1}$ and $\dot{m}_{ro} > 0.0001 \text{ kg} \cdot \text{s}^{-1}$. On the basis of the actual value of $\bar{\gamma}_{off}$, the model prepares for the next switch to the SMB framework: since in the operating conditions considered in this work (compressor on-off cycling together with a simultaneous opening and closing of the EEV thus avoiding evaporator pump-down, and variations in the secondary fluid temperature contained within the limits imposed by the control system) $\bar{\gamma}_{off}$ is usually between 0 and 1, the model will restart in the SMB framework with the one-region (TP) formulation. In the near future, the model will be integrated in order to tackle also system pump-down and a condition of complete superheating in the heat exchanger.

2.6 Condenser

As for the evaporator, the dynamic model of the condenser is likewise based on the SMB framework. During normal operating conditions, the refrigerant enters the condenser as superheated vapour and then it is cooled down till it

exits the heat exchanger in two-phase conditions or slightly subcooled; thus, up to three regions can exist simultaneously, as depicted in Fig. 2.4. For the non-dimensional lengths ξ_1, ξ_2 and ξ_3 the same definitions and properties highlighted in Eqs. 2.12-2.13 apply.

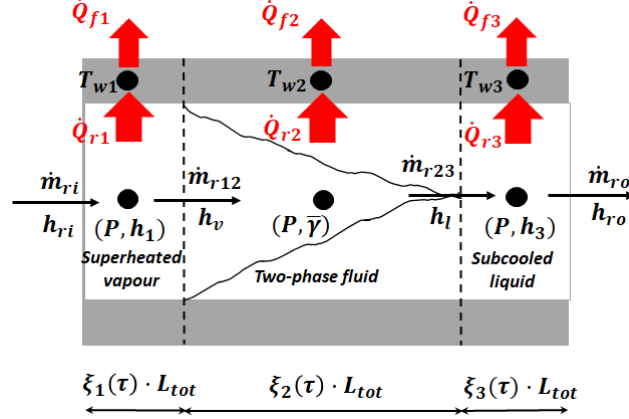


Figure 2.4: Condenser discretization using the SMB approach: three-region formulation.

The model formulations considered in this work, described in detail in the following sections, are:

- three-region formulation: superheated vapour, two-phase and subcooled liquid (V+TP+L);
- two-region formulation: superheated vapour and two-phase (V+TP);
- two-region formulation: two-phase and subcooled liquid (TP+L);
- one-region formulation: two-phase condition (TP);
- off-duty formulation (Off).

The condition of uniform superheated vapour in the condenser was neglected, since it usually happens when the condenser is subject to a strong decrease in pressure, which is typical of long off periods in refrigerating machines equipped with a capillary tube and no solenoid valves for shut-off between high and low pressure parts of the circuit.

Since the mathematical procedure used is the same applied to the evaporator, only the final form of the equations describing the various formulation will be reported.

2.6.1 Three-region formulation: superheated vapour, two-phase and subcooled liquid

Refrigerant-side equations

The first six equations for the SMB model of the condenser in the three regions formulation, Eqs. 2.93-2.98, are obtained applying the mass and energy balances to the three control volumes in the same way discussed in section 2.5.1.

Also in this case, the variables chosen for the single-phase regions are pressure and enthalpy, whilst the TP region is described through the pressure P and the mean void fraction $\bar{\gamma}$, with the density ρ_2 and enthalpy h_2 and their partial derivatives with respect to the pressure and the mean void fraction determined through Eqs. 2.16-2.19 and Eqs. 2.24-2.27.

$$\boxed{\frac{d\xi_1}{d\tau} + \frac{\xi_1}{\rho_1} \frac{\partial \rho_1}{\partial P} \Big|_{h_1} \frac{dP}{d\tau} + \frac{\xi_1}{\rho_1} \frac{\partial \rho_1}{\partial h_1} \Big|_P \frac{dh_1}{d\tau} + \frac{\dot{m}_{r12}}{\rho_1 A_{Cr} L_{tot}} = \frac{\dot{m}_{ri}}{\rho_1 A_{Cr} L_{tot}}} \quad (2.93)$$

$$\boxed{\frac{\xi_1}{\rho_1} \frac{dP}{d\tau} - \xi_1 \frac{dh_1}{d\tau} + \frac{(h_1 - h_v)}{\rho_1 A_{Cr} L_{tot}} \dot{m}_{r12} = \frac{\dot{Q}_{r1} - \dot{m}_{ri}(h_{ri} - h_1)}{\rho_1 A_{Cr} L_{tot}}} \quad (2.94)$$

$$\boxed{\frac{d\xi_2}{d\tau} + \frac{\xi_2}{\rho_2} \frac{\partial \rho_2}{\partial P} \Big|_{\bar{\gamma}} \frac{dP}{d\tau} + \frac{\xi_2}{\rho_2} \frac{\partial \rho_2}{\partial \bar{\gamma}} \Big|_P \frac{d\bar{\gamma}}{d\tau} - \frac{\dot{m}_{r12}}{\rho_2 A_{Cr} L_{tot}} + \frac{\dot{m}_{r23}}{\rho_2 A_{Cr} L_{tot}} = 0} \quad (2.95)$$

$$\boxed{\xi_2 \left[\frac{1}{\rho_2} - \frac{\partial h_2}{\partial P} \Big|_{\bar{\gamma}} \right] \frac{dP}{d\tau} - \xi_2 \frac{\partial h_2}{\partial \bar{\gamma}} \frac{d\bar{\gamma}}{d\tau} + \frac{(h_v - h_2)}{\rho_2 A_{Cr} L_{tot}} \dot{m}_{r12} + \frac{(h_2 - h_l)}{\rho_2 A_{Cr} L_{tot}} \dot{m}_{r23} = \frac{\dot{Q}_{r2}}{\rho_2 A_{Cr} L_{tot}}} \quad (2.96)$$

$$\boxed{\frac{d\xi_1}{d\tau} + \frac{d\xi_2}{d\tau} - \frac{\xi_3}{\rho_3} \frac{\partial \rho_3}{\partial P} \Big|_{h_3} \frac{dP}{d\tau} - \frac{\xi_3}{\rho_3} \frac{\partial \rho_3}{\partial h_3} \Big|_P \frac{dh_3}{d\tau} + \frac{\dot{m}_{r23}}{\rho_3 A_{Cr} L_{tot}} = \frac{\dot{m}_{ro}}{\rho_3 A_{Cr} L_{tot}}} \quad (2.97)$$

$$\boxed{\frac{\xi_3}{\rho_3} \frac{dP}{d\tau} - \xi_3 \frac{dh_3}{d\tau} + \frac{(h_l - h_3)}{\rho_3 A_{Cr} L_{tot}} \dot{m}_{r23} = \frac{\dot{Q}_{r3} - \dot{m}_{ro}(h_3 - h_{ro})}{\rho_3 A_{Cr} L_{tot}}} \quad (2.98)$$

In this case, the set of unknowns consists of the non-dimensional length ξ_1 and ξ_2 , the pressure P , the enthalpies h_1 and h_3 , the mean void fraction $\bar{\gamma}$ and the intermediate mass flow rates \dot{m}_{r12} and \dot{m}_{r23} . Thus, two more equations are needed. Since the refrigerant inlet and outlet enthalpies for the superheated vapour region are known, the first one is obtained forcing h_1 to track the mean value defined by Eq. 2.99, as highlighted by Eq. 2.100. The term K_h is a tracking coefficient, set here to 5 s^{-1} to make h_2 track fast the value of h_{track} while keeping the computational cost to a minimum.

$$h_{track} = \frac{h_{ri} + h_v}{2} \quad (2.99)$$

$$\boxed{\frac{dh_1}{d\tau} = K_h (h_{track} - h_1)} \quad (2.100)$$

As done for the evaporator, Eq. 2.101 is introduced to ensure the continuity in the mean void fraction $\bar{\gamma}$ and thus conservation for refrigerant mass in the two-phase regions when switches among model formulations occur.

$$\boxed{\frac{\partial \bar{\gamma}}{\partial P} \frac{dP}{d\tau} - \frac{d\bar{\gamma}}{d\tau} = K_{\gamma}(\bar{\gamma} - \bar{\gamma}_{TOT})} \quad (2.101)$$

In addition, the global energy balance described by Eq. 2.102 is also solved in order to track the value of the mean density ρ_m used for the off-duty formulation, where the heat exchanger is modelled with a lumped-parameter approach.

$$\boxed{\frac{d\rho_m}{d\tau} = \frac{\dot{m}_{ri} - \dot{m}_{ro}}{A_{Cr}L_{tot}}} \quad (2.102)$$

Wall-side equations

Energy balances for the HEX structure are derived as explained in section 2.5.1; also for the condenser, the intermediate temperatures must be defined in order to account for energy re-distribution during the moving of the volumes boundaries, and their values are established on the basis of the boundary velocity, [85].

$$\frac{d\xi_1}{d\tau} \geq 0 \implies T_{int12} = T_{w2} \quad (2.103)$$

$$\frac{d\xi_1}{d\tau} < 0 \implies T_{int12} = T_{w1} \quad (2.104)$$

$$\frac{d\xi_1}{d\tau} + \frac{d\xi_2}{d\tau} \geq 0 \implies T_{int23} = T_{w3} \quad (2.105)$$

$$\frac{d\xi_1}{d\tau} + \frac{d\xi_2}{d\tau} < 0 \implies T_{int23} = T_{w2} \quad (2.106)$$

The equations describing the transient behaviour of the HEX wall are thus Eqs. 2.107-2.109.

$$\boxed{\frac{dT_{w1}}{d\tau} = \frac{1}{\xi_1} \left[\frac{\dot{Q}_{R1} - \dot{Q}_{f1}}{m_w c_w} - (T_{w1} - T_{int12}) \frac{d\xi_1}{d\tau} \right]} \quad (2.107)$$

$$\boxed{\frac{dT_{w2}}{d\tau} = \frac{1}{\xi_2} \left[\frac{\dot{Q}_{R2} - \dot{Q}_{f2}}{m_w c_w} + T_{int23} \left(\frac{d\xi_1}{d\tau} + \frac{d\xi_2}{d\tau} \right) - T_{int12} \frac{d\xi_1}{d\tau} - T_{w2} \frac{d\xi_2}{d\tau} \right]} \quad (2.108)$$

$$\boxed{\frac{dT_{w3}}{d\tau} = \frac{1}{\xi_3} \left[\frac{\dot{Q}_{R3} - \dot{Q}_{f3}}{m_w c_w} + (T_{w3} - T_{int23}) \left(\frac{d\xi_1}{d\tau} + \frac{d\xi_2}{d\tau} \right) \right]} \quad (2.109)$$

As for the evaporator, the mean wall temperature is calculated through Eq. 2.110 and stored for its use in the off-period formulation.

$$T_{wm} = \xi_1 T_{w1} + \xi_2 T_{w2} + \xi_3 T_{w3} \quad (2.110)$$

2.6.2 Two-region formulation: superheated vapour and two-phase

Refrigerant-side equations

In many events the refrigerant can exit the heat exchanger in two-phase conditions and thus the subcooled liquid region disappears. The model must therefore switch to the two-region formulation with the superheated vapour and two-phase regions (V+TP). The non-dimensional length ξ_3 tends to zero (it is given a very low value in order to prevent matrix singularity), and its extension does not vary in time. Thus, since $d\xi_3/d\tau = 0$ with $\xi_3 = 1 - \xi_1 - \xi_2$:

$$\boxed{\frac{d\xi_1}{d\tau} + \frac{d\xi_2}{d\tau} = 0} \quad (2.111)$$

Starting from Eqs. 2.93 and 2.96 and considering that $\dot{m}_{r23} = \dot{m}_{ro}$, the mass and energy balance for the superheated vapour and the two-phase regions become:

$$\boxed{\frac{d\xi_1}{d\tau} + \frac{\xi_1}{\rho_1} \frac{\partial \rho_1}{\partial P} \Big|_{h_1} \frac{dP}{d\tau} + \frac{\xi_1}{\rho_1} \frac{\partial \rho_1}{\partial h_1} \Big|_P \frac{dh_1}{d\tau} + \frac{\dot{m}_{r12}}{\rho_1 A_{Cr} L_{tot}} = \frac{\dot{m}_{ri}}{\rho_1 A_{Cr} L_{tot}}} \quad (2.112)$$

$$\boxed{\frac{\xi_1}{\rho_1} \frac{dP}{d\tau} - \xi_1 \frac{dh_1}{d\tau} + \frac{(h_1 - h_v)}{\rho_1 A_{Cr} L_{tot}} \dot{m}_{r12} = \frac{\dot{Q}_{r1} - \dot{m}_{ri}(h_{ri} - h_1)}{\rho_1 A_{Cr} L_{tot}}} \quad (2.113)$$

$$\boxed{\frac{d\xi_2}{d\tau} + \frac{\xi_2}{\rho_2} \frac{\partial \rho_2}{\partial P} \Big|_{\bar{\gamma}} \frac{dP}{d\tau} + \frac{\xi_2}{\rho_2} \frac{\partial \rho_2}{\partial \bar{\gamma}} \Big|_P \frac{d\bar{\gamma}}{d\tau} - \frac{\dot{m}_{r12}}{\rho_2 A_{Cr} L_{tot}} = -\frac{\dot{m}_{ro}}{\rho_2 A_{Cr} L_{tot}}} \quad (2.114)$$

$$\boxed{\xi_2 \left[\frac{1}{\rho_2} - \frac{\partial h_2}{\partial P} \Big|_{\bar{\gamma}} \right] \frac{dP}{d\tau} - \xi_2 \frac{\partial h_2}{\partial \bar{\gamma}} \frac{d\bar{\gamma}}{d\tau} + \frac{(h_v - h_2)}{\rho_2 A_{Cr} L_{tot}} \dot{m}_{r12} = \frac{\dot{Q}_{r2} - \dot{m}_{ro}(h_2 - h_{ro})}{\rho_2 A_{Cr} L_{tot}}} \quad (2.115)$$

As highlighted in Eq. 2.116, the inactive variable h_3 is forced to track the saturated liquid enthalpy, ensuring the model to be able to face the reappearance of the subcooled liquid region.

$$\boxed{\frac{dh_3}{dt} = K_h(h_l - h_3)} \quad (2.116)$$

With the same approach used for the three-region formulation, the enthalpy in the superheated vapour region is forced to track the mean value between the inlet and the dry-saturated vapour enthalpies, as shown in Eq. 2.100, and the global mass balance described by 2.102 is solved to track the value of the mean density ρ_m . For both Eqs. 2.116 and 2.100, the tracking value K_h was set to 5 s^{-1} .

$$\boxed{\frac{dh_1}{d\tau} = K_h(h_{track} - h_1)}$$

$$\boxed{\frac{d\rho_m}{dt} = \frac{\dot{m}_{rin} - \dot{m}_{rout}}{A_{CR}L_{tot}}}$$

Wall-side equations

In the V-TP formulation, only the intermediate temperature T_{int12} must be determined, since the boundary between the TP and L regions is fixed. Also in this case, Eqs. 2.103-2.104 are used.

$$\frac{d\xi_1}{dt} \geq 0 \implies T_{int12} = T_{w2}$$

$$\frac{d\xi_1}{dt} < 0 \implies T_{int12} = T_{w1}$$

Considering Eq. 2.111, the energy balances for the wall regions associated to the superheated vapour and two-phase refrigerant are described by Eqs. 2.117-2.118, whilst Eq. 2.119 is introduced with a tracking coefficient $K_T = 5 \text{ s}^{-1}$ in order to make the inactive variable T_{w3} track the temperature T_{w2} of the near region.

$$\boxed{\frac{dT_{w1}}{d\tau} = \frac{1}{\xi_1} \left[\frac{\dot{Q}_{r1} - \dot{Q}_{f1}}{m_w c_w} - (T_{w1} - T_{int12}) \frac{d\xi_1}{d\tau} \right]} \quad (2.117)$$

$$\boxed{\frac{dT_{w2}}{d\tau} = \frac{1}{\xi_2} \left[\frac{\dot{Q}_{r2} - \dot{Q}_{f2}}{m_w c_w} - T_{int12} \frac{d\xi_1}{d\tau} - T_{w2} \frac{d\xi_2}{d\tau} \right]} \quad (2.118)$$

$$\boxed{\frac{dT_{w3}}{d\tau} = K_T(T_{w2} - T_{w3})} \quad (2.119)$$

As for the three-region formulations, the mean wall temperature is updated by means of Eq. 2.110 and stored for its use in the off-period formulation.

2.6.3 Two-region formulation: two-phase and subcooled liquid

Refrigerant-side equations

In large plants, when the compressor switches on again after a machine off period, there can be transients where the refrigerant at the inlet of the condenser is in two-phase conditions and thus no superheated vapour region is present in the heat exchanger, while a certain degree of subcooling is kept at the outlet. In such a condition, the extension of the V region tends to zero and its derivative is null, as shown in Eq. 2.120, the enthalpy h_1 is forced

to track the dry-saturated vapour enthalpy h_v , which is a good initialization point when the V region reappears, see Eq. 2.121.

$$\boxed{\frac{d\xi_1}{d\tau} = 0} \quad (2.120)$$

$$\boxed{\frac{dh_1}{d\tau} = K_h(h_v - h_1)} \quad (2.121)$$

To completely define the model in these circumstances, the mass and energy balances for TP and L regions are rewritten, starting from Eqs. 2.95-2.98 and considering that $\dot{m}_{r12} = \dot{m}_{ri}$, leading to Eqs. 2.122-2.125.

$$\boxed{\frac{d\xi_2}{d\tau} + \frac{\xi_2}{\rho_2} \frac{\partial \rho_2}{\partial P} \Big|_{\bar{\gamma}} \frac{dP}{d\tau} + \frac{\xi_2}{\rho_2} \frac{\partial \rho_2}{\partial \bar{\gamma}} \Big|_P \frac{d\bar{\gamma}}{d\tau} + \frac{\dot{m}_{r23}}{\rho_2 A_{Cr} L_{tot}} = \frac{\dot{m}_{ri}}{\rho_2 A_{Cr} L_{tot}}} \quad (2.122)$$

$$\boxed{\xi_2 \left[\frac{1}{\rho_2} - \frac{\partial h_2}{\partial P} \Big|_{\bar{\gamma}} \right] \frac{dP}{d\tau} - \xi_2 \frac{\partial h_2}{\partial \bar{\gamma}} \frac{d\bar{\gamma}}{d\tau} + \frac{(h_2 - h_l)}{\rho_2 A_{Cr} L_{tot}} \dot{m}_{r23} = \frac{\dot{Q}_{r2} - \dot{m}_{ri}(h_{ri} - h_2)}{\rho_2 A_{Cr} L_{tot}}} \quad (2.123)$$

$$\boxed{\frac{d\xi_3}{d\tau} - \frac{\xi_3}{\rho_3} \frac{\partial \rho_3}{\partial P} \Big|_{h_3} \frac{dP}{d\tau} - \frac{\xi_3}{\rho_3} \frac{\partial \rho_3}{\partial h_3} \Big|_P \frac{dh_3}{d\tau} + \frac{\dot{m}_{r23}}{\rho_3 A_{Cr} L_{tot}} = \frac{\dot{m}_{ro}}{\rho_3 A_{Cr} L_{tot}}} \quad (2.124)$$

$$\boxed{\frac{\xi_3}{\rho_3} \frac{dP}{d\tau} - \xi_3 \frac{dh_3}{d\tau} + \frac{(h_l - h_3)}{\rho_3 A_{Cr} L_{tot}} \dot{m}_{r23} = \frac{\dot{Q}_{r3} - \dot{m}_{ro}(h_3 - h_{ro})}{\rho_3 A_{Cr} L_{tot}}} \quad (2.125)$$

To ensure mass conservation during model switches involving the appearance and disappearance of the subcooled liquid region and to track the value of the mean density used in off-period formulation, Eqs. 2.101 and 2.102 are used.

$$\boxed{\frac{\partial \bar{\gamma}}{\partial P} \frac{dP}{d\tau} - \frac{d\bar{\gamma}}{d\tau} = K_\gamma(\bar{\gamma} - \bar{\gamma}_{TOT})}$$

$$\boxed{\frac{d\rho_m}{d\tau} = \frac{\dot{m}_{ri} - \dot{m}_{ro}}{A_{Cr} L_{tot}}}$$

Wall-side equations

In this formulation, only the intermediate temperature T_{int23} is necessary, and its calculation is carried out through Eqs. 2.126-2.127, obtained substituting Eq. 2.120 into Eq. 2.105-2.106.

$$\frac{d\xi_2}{d\tau} \geq 0 \implies T_{int23} = T_{w3} \quad (2.126)$$

$$\frac{d\xi_2}{d\tau} < 0 \implies T_{int23} = T_{w2} \quad (2.127)$$

Since the V region is inactive, the wall temperature T_{w1} is forced to track T_{w2} for switching purposes, as shown in Eq. 2.128, whilst the energy balances on TP and L regions are obtained substituting Eq. 2.120 into Eqs. 2.108-2.109, leading to Eqs. 2.129-2.130.

$$\boxed{\frac{dT_{w1}}{d\tau} = K_T(T_{w2} - T_{w1})} \quad (2.128)$$

$$\boxed{\frac{dT_{w2}}{d\tau} = \frac{1}{\xi_2} \left[\frac{\dot{Q}_{r2} - \dot{Q}_{f2}}{m_w c_w} + T_{int23} \frac{d\xi_2}{d\tau} - T_{w2} \frac{d\xi_2}{d\tau} \right]} \quad (2.129)$$

$$\boxed{\frac{dT_{w3}}{d\tau} = \frac{1}{\xi_3} \left[\frac{\dot{Q}_{r3} - \dot{Q}_{f3}}{m_w c_w} + (T_{w3} - T_{int23}) \frac{d\xi_2}{d\tau} \right]} \quad (2.130)$$

Like for the three-region formulation, the mean wall temperature is updated by means of Eq. 2.110 and stored for its use in the off-period formulation.

2.6.4 One-region formulation: two-phase

Refrigerant-side equations

As explained for the two-region (TP-L) formulation, under certain transient conditions the refrigerant can enter the HEX as two-phase mixture and, if the heat transfer rate is not sufficient, the fluid can exit the condenser with a vapour quality x larger than zero, thus leading to the disappearance of the superheated vapour and the subcooled liquid regions and the presence of the two-phase region only. In such a condition, the extensions of the non-dimensional lengths ξ_1 and ξ_2 are constant, as highlighted in Eqs. 2.131-2.132. Moreover, for switching purposes, the enthalpies h_1 and h_3 are forced to track the values of the enthalpies of the dry-saturated vapour h_v and saturated liquid h_l respectively, as shown in Eqs. 2.133-2.134, where $K_h = 5 \text{ s}^{-1}$.

$$\boxed{\frac{d\xi_1}{d\tau} = 0} \quad (2.131)$$

$$\boxed{\frac{d\xi_2}{d\tau} = 0} \quad (2.132)$$

$$\boxed{\frac{dh_1}{d\tau} = K_h(h_v - h_1)} \quad (2.133)$$

$$\boxed{\frac{dh_3}{d\tau} = K_h(h_l - h_3)} \quad (2.134)$$

To complete the set of equations for the refrigerant side, the mass and energy balances are applied to the TP region, as shown in Eqs. 2.135-2.136, and the mean value of the refrigerant density is tracked through Eq. 2.102. It has to be underlined that in this situation the mean density ρ_m must be equal to the the mean density in the TP region ρ_2 : the use of Eq. 2.102 allows one again to verify the mass conservativeness of the model in the SMB framework.

$$\boxed{\frac{\xi_2}{\rho_2} \frac{\partial \rho_2}{\partial P} \Big|_{\bar{\gamma}} \frac{dP}{d\tau} + \frac{\xi_2}{\rho_2} \frac{\partial \rho_2}{\partial \bar{\gamma}} \Big|_P \frac{d\bar{\gamma}}{d\tau} = \frac{\dot{m}_{ri} - \dot{m}_{ro}}{\rho_2 A_{Cr} L_{tot}}} \quad (2.135)$$

$$\boxed{\xi_2 \left[\frac{1}{\rho_2} - \frac{\partial h_2}{\partial P} \Big|_{\bar{\gamma}} \right] \frac{dP}{d\tau} - \xi_2 \frac{\partial h_2}{\partial \bar{\gamma}} \frac{d\bar{\gamma}}{d\tau} = \frac{\dot{Q}_{r2} - \dot{m}_{ri}(h_{ri} - h_2) - \dot{m}_{ro}(h_2 - h_{ro})}{\rho_2 A_{Cr} L_{tot}}} \quad (2.136)$$

Wall-side equations

In this case, no intermediate temperatures are calculated, since the extension of the TP region is constant. Thus the equations describing the wall-side one-region moving boundary model are Eqs. 2.137-2.139, namely the tracking equations for inactive variables T_{w1} and T_{w3} , with a tracking gain $K_T = 5 \text{ s}^{-1}$, and the wall energy balance on the TP region.

$$\boxed{\frac{dT_{w1}}{d\tau} = K_T(T_{w2} - T_{w1})} \quad (2.137)$$

$$\boxed{\frac{dT_{w2}}{d\tau} = \frac{1}{\xi_2} \left[\frac{\dot{Q}_{R2} - \dot{Q}_{A2}}{m_w c_w} \right]} \quad (2.138)$$

$$\boxed{\frac{dT_{w3}}{d\tau} = K_T(T_{w2} - T_{w3})} \quad (2.139)$$

Once again, the mean wall temperature is updated by means of Eq. 2.110 and stored for its use in the off-duty formulation.

2.6.5 Off-duty formulation

Similarly to what done for the evaporator, during the machine off periods the condenser is modelled as a single lumped parameter, thus assuming uniform conditions of the thermodynamic variables. Indeed, the main aim of the model here is to correctly predict the pressure and ensure mass conservation, regardless of the actual refrigerant outlet conditions. The global mass balance is described by the here-reported Eq. 2.102, whilst Eq. 2.140 expresses the global energy balance after the same analytical manipulations described in section 2.5.3.

$$\boxed{\frac{d\rho_m}{d\tau} = \frac{\dot{m}_{ri} - \dot{m}_{ro}}{A_{Cr}L_{tot}}}$$

$$\boxed{-\left(\frac{\partial\rho_m}{\partial P}\Big|_{h_m} + \frac{1}{\rho_m}\frac{\partial\rho_m}{\partial h_m}\Big|_P\right)\frac{dP}{d\tau} + \frac{d\rho_m}{d\tau} = \frac{\partial\rho_m}{\partial h_m}\Big|_P\left(\frac{\dot{m}_{ri}(h_{ri} - h_m) - \dot{m}_{ro}(h_{ro} - h_m) - \dot{Q}_{rtot}}{\rho_m A_{Cr} L_{tot}}\right)}$$

(2.140)

As for the evaporator, the inactive variables are forced to track suitable values on the basis of the value taken by the mean void fraction in the whole heat exchanger $\bar{\gamma}_{off}$, expressed through Eq. 2.52. Since to preserve the liquid refrigerant on the high pressure side of the plant the EEV is kept closed during machine stops, the condition of uniform superheated vapour in the condenser was neglected. Typically, it has been noticed that $\bar{\gamma}_{off}$ is usually between 0 and 1, leading to a two-phase condition of the refrigerant in the condenser; therefore, the tracking values are $\xi_{1track} = 0.005$, $\xi_{2track} = 0.995$, $h_{1track} = h_v$, $h_{3track} = h_l$ and the tracking equations become Eqs. 2.141-2.145, where the tracking gains $K_{\bar{\gamma}}$, K_{ξ} e K_h take again the value of $5 s^{-1}$.

$$\boxed{\frac{d\bar{\gamma}}{d\tau} = K_{\bar{\gamma}}(\bar{\gamma}_{off} - \bar{\gamma})}$$

(2.141)

$$\boxed{\frac{d\xi_1}{d\tau} = K_{\xi}(\xi_{1track} - \xi_1)}$$

(2.142)

$$\boxed{\frac{d\xi_2}{d\tau} = K_{\xi}(\xi_{2track} - \xi_2)}$$

(2.143)

$$\boxed{\frac{dh_1}{d\tau} = K_h(h_{1track} - h_1)}$$

(2.144)

$$\boxed{\frac{dh_3}{d\tau} = K_h(h_{3track} - h_3)}$$

(2.145)

During the machine off periods, also the HEX wall is modelled through a single lumped parameter, and a global energy balance, written as highlighted in Eq. 2.146, is solved.

$$\boxed{\frac{dT_{wm}}{d\tau} = \frac{\dot{Q}_{rtot} - \dot{Q}_{ftot}}{m_w c_w}}$$

(2.146)

The inactive variables T_{w1} , T_{w2} and T_{w3} are forced to track T_{wm} in order to allow the model to start again with the SMB formulation, as shown in Eqs. 2.147-2.149.

$$\boxed{\frac{dT_{w1}}{d\tau} = K_T(T_{wm} - T_{w1})} \quad (2.147)$$

$$\boxed{\frac{dT_{w2}}{d\tau} = K_T(T_{wm} - T_{w2})} \quad (2.148)$$

$$\boxed{\frac{dT_{w3}}{d\tau} = K_T(T_{wm} - T_{w3})} \quad (2.149)$$

2.6.6 Calculation of the refrigerant outlet conditions

The method used to determine the refrigerant outlet conditions is the same adopted for the evaporator and presented in section 2.5.4.

In the SMB framework, when the refrigerant at the condenser outlet is in single-phase conditions, the outlet enthalpy h_{ro} is calculated from the pressure P and the outlet temperature T_{ro} , evaluated assuming an exponential temperature profile in the subcooled region and solving Eq. 2.60. When two-phase refrigerant exits the HEX instead, the outlet enthalpy is calculated through Eq. 2.61, where the outlet quality is obtained from the actual values of the mean void fraction $\bar{\gamma}$, the pressure P and the inlet enthalpy to the TP region by means of the Zivi correlation presented in section 2.4.

In the off-duty formulation, the mean enthalpy h_m is considered as the refrigerant outlet condition.

2.6.7 Calculation of the refrigerant-side heat transfer rate

Similarly to the evaporator, the heat transfer rate between wall and refrigerant in the generic region j in the SMB formulation is expressed through Eq. 2.150:

$$\dot{Q}_{rj} = \alpha_{rj}\xi_j A_{Sr}(T_{rj} - T_{wj}) \quad (2.150)$$

The heat transfer coefficient for condensation in the brazed-plate heat exchanger is calculated through the correlation presented by Longo et al. in [99], whilst for the finned-tubes heat exchangers the Dobson and Chato correlation for condensation in circular tubes and presented in [96] was used.

For the superheated vapour and subcooled liquid regions in the brazed-plate heat exchangers, the Martin correlation, [98], was chosen, whilst the Gnielinski correlation was used for the finned-tubes heat exchanger, [96].

During off periods, the calculation of the total heat transfer rate on the refrigerant side is carried out through Eq. 2.151, where, for both HEX configurations, the heat transfer coefficient α_r is calculated on the basis of the actual value of $\bar{\gamma}_{off}$: since $\bar{\gamma}_{off}$ is usually between 0 and 1, the correlations for condensation heat transfer are used again.

$$\dot{Q}_{rtot} = \alpha_r A_{Sr}(T_{rm} - T_{wm}) \quad (2.151)$$

2.6.8 Calculation of the secondary fluid heat transfer rate

Finned-tubes heat exchanger

In the finned-tubes condenser, the fluid flows assume a cross-flow configuration; thus, the heat transfer rate exchanged on the secondary fluid side can be calculated as:

$$\dot{Q}_{f1} = \xi_1 \dot{m}_f c_{pf} (T_{fo1} - T_{fi}) \quad (2.152)$$

$$\dot{Q}_{f2} = \xi_2 \dot{m}_f c_{pf} (T_{fo2} - T_{fi}) \quad (2.153)$$

$$\dot{Q}_{f3} = \xi_3 \dot{m}_f c_{pf} (T_{fo3} - T_{fi}) \quad (2.154)$$

The temperature of the secondary fluid at the outlet of each region T_{foj} can be evaluated by means of Eq. 2.155, which applies the $\varepsilon - NTU$ method with an efficiency $\varepsilon_f = 1 - \exp(-NTU_f)$.

$$T_{foj} = T_{wj} - (T_{wj} - T_{fi}) \exp(-NTU_f) \quad (2.155)$$

The number of heat transfer units is computed through Eq. 2.69, where the heat transfer coefficient α_f is calculated according to the correlations for finned-tubes compact heat exchangers suggested by Kays and London, [97].

$$NTU_f = \frac{A_{sf} \alpha_f}{\dot{m}_f c_{pf}}$$

Air outlet temperature is then obtained considering a perfect mixing between the air flows across the HEX regions, as shown in Eq. 2.156.

$$T_{fo} = \xi_1 T_{fo1} + \xi_2 T_{fo2} + \xi_3 T_{fo3} \quad (2.156)$$

During the machine off periods, the total heat transfer rate on the secondary fluid side for the wall global energy balance is calculated through Eqs. 2.157-2.158.

$$\dot{Q}_{ftot} = \dot{m}_f c_{pf} (T_{fo} - T_{fi}) \quad (2.157)$$

Where air outlet temperature is:

$$T_{fo} = T_{wm} - (T_{wm} - T_{fi}) \exp(-NTU_f) \quad (2.158)$$

As done for the finned-tubes evaporator, when \dot{m}_f approaches zero, the heat transfer coefficient α_f is calculated through the correlation for natural convection on a horizontal cylinder available in [96], and the air is supposed to exit the heat exchanger at the mean wall temperature. The heat transfer rate

in SMB framework and zero-air flow can be calculated through Eqs. 2.159-2.161, whilst for the off-period formulation Eq. 2.162 is used.

$$\dot{Q}_{f1} = \alpha_f A_{Sf} (T_{w1} - T_{fi}) \quad (2.159)$$

$$\dot{Q}_{f2} = \alpha_f A_{Sf} (T_{w2} - T_{fi}) \quad (2.160)$$

$$\dot{Q}_{f3} = \alpha_f A_{Sf} (T_{w3} - T_{fi}) \quad (2.161)$$

$$\dot{Q}_{ftot} = \alpha_f A_{Sf} (T_{wm} - T_{fi}) \quad (2.162)$$

Brazed-plate heat exchanger

Similarly to the evaporator, a counter-current configuration was adopted for the brazed-plate heat exchangers, and the temperature of the secondary fluid at the outlet of one region represents the inlet for the subsequent. In the general case of the three-region formulation in the SMB framework, starting from the subcooled region, the heat transfer rate and the secondary fluid outlet temperature can be calculated through Eqs. 2.163-2.171.

$$\dot{Q}_{f3} = \dot{m}_f c_{pf} (T_{w3} - T_{fi}) (1 - \exp(-NTU_{f3})) \quad (2.163)$$

$$NTU_{f3} = \frac{\alpha_f \xi_3 A_{Sf}}{\dot{m}_f c_{pf}} \quad (2.164)$$

$$T_{f23} = T_{fin} + \frac{\dot{Q}_{f3}}{\dot{m}_f c_{pf}} \quad (2.165)$$

$$\dot{Q}_{f2} = \dot{m}_f c_{pf} (T_{w2} - T_{f23}) (1 - \exp(-NTU_{f2})) \quad (2.166)$$

$$NTU_{f2} = \frac{\alpha_f \xi_2 A_{Sf}}{\dot{m}_f c_{pf}} \quad (2.167)$$

$$T_{f12} = T_{f23} + \frac{\dot{Q}_{f2}}{\dot{m}_f c_{pf}} \quad (2.168)$$

$$\dot{Q}_{f1} = \dot{m}_f c_{pf} (T_{w1} - T_{f12}) (1 - \exp(-NTU_{f1})) \quad (2.169)$$

$$NTU_{f1} = \frac{\alpha_f \xi_1 A_{Sf}}{\dot{m}_f c_{pf}} \quad (2.170)$$

$$T_{fo} = T_{f12} + \frac{\dot{Q}_{f1}}{\dot{m}_f c_{pf}} \quad (2.171)$$

In the off-duty formulation, the wall mean temperature T_{wm} is considered for the calculation of the secondary fluid outlet temperature and the heat transfer rate used in the wall-side energy balance, as highlighted in Eqs. 2.172-2.174. As for the brazed-plate evaporator, α_f is calculated through the Martin correlation, [98].

$$\dot{Q}_{ftot} = \dot{m}_f c_{pf} (T_{wm} - T_{fi}) (1 - \exp(-NTU_f)) \quad (2.172)$$

$$NTU_f = \frac{\alpha_f A_{Sf}}{\dot{m}_f c_{pf}} \quad (2.173)$$

$$T_{fo} = T_{fi} + \frac{\dot{Q}_{ftot}}{\dot{m}_f c_{pf}} \quad (2.174)$$

When \dot{m}_f approaches zero, a purely conductive heat transfer coefficient is considered, and calculated through Eq. 2.85; in such a condition, the heat transfer rates in the SMB framework are computed through Eqs. 2.175-2.177, whilst for the off-duty formulation Eq. 2.178 applies.

$$\dot{Q}_{f1} = \alpha_f A_{Sf} (T_{w1} - T_{fi}) \quad (2.175)$$

$$\dot{Q}_{f2} = \alpha_f A_{Sf} (T_{w2} - T_{fi}) \quad (2.176)$$

$$\dot{Q}_{f3} = \alpha_f A_{Sf} (T_{w3} - T_{fi}) \quad (2.177)$$

$$\dot{Q}_{ftot} = \alpha_f A_{Sf} (T_{wm} - T_{fi}) \quad (2.178)$$

2.6.9 Correction factors for the heat transfer coefficients

With the same approach used for the evaporator model, the heat transfer coefficients obtained through correlations are multiplied by correction factors which allow to tune the model when validation of experimental data is carried out. In addition to the correction factors C_{TP} , C_V , C_{Off} and C_f presented for the evaporator in section 2.5.7, the coefficient C_L is added to correct the heat transfer coefficient in the subcooled liquid region, as shown by Eq. 2.179.

$$\alpha_{r3} = C_L \cdot \alpha_{r3} \quad (2.179)$$

2.6.10 Switching criteria

Figure 2.5 summarizes all the possible switches which can occur in the condenser model, distinguishing them between model formulations within the SMB framework and between the SMB and the off-duty frameworks. The switching scheme within the SMB framework is based on the works presented in [84] and [85].

SMB switches: disappearance of the subcooled liquid region (L)

In the SMB framework, when the model is in the three-region (V-TP-L) or in the two-region (TP-L) formulation, under certain operating conditions the region associated with the subcooled refrigerant may disappear. In this case, the switching scheme is based on the non-dimensional length ξ_3 and its derivative; in particular, if ξ_3 is lower than a certain threshold and is continuing to

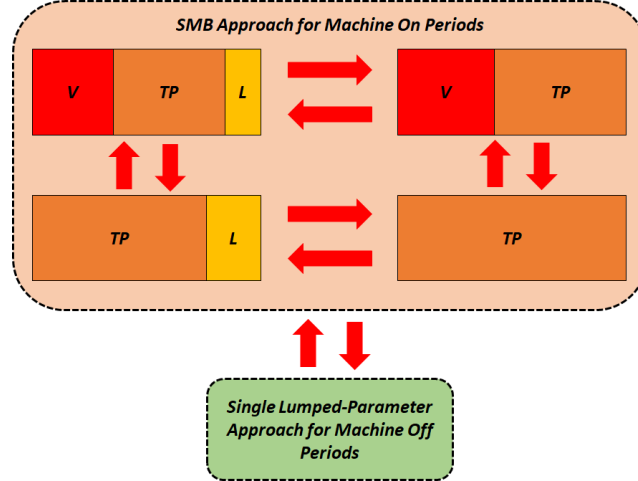


Figure 2.5: Possible switches for the condenser model.

decrease, then the switch to the two-region (V-TP) or one-region (TP) formulations must occur, depending on the previous condition. The scheme can be summarised as:

- $\xi_3 \leq \xi_{3min}$
- $\frac{d\xi_3}{d\tau} = -\frac{d\xi_1}{d\tau} - \frac{d\xi_2}{d\tau} < 0$

After a calibration process aimed at finding the minimum threshold ensuring numerical stability, the value of ξ_{3min} was set to 0.005.

SMB switches: reappearance of the subcooled liquid region (L)

An opposite condition is represented by the possible reappearance of the subcooled liquid region when the model is in the two-region (V-TP) or one-region (TP) formulations. In such cases, the switch is based on the mean void fraction $\bar{\gamma}$ and its time derivative. In particular, when the amount of liquid in the TP region exceeds the equilibrium value associated to an outlet quality $x_o = 0$ and is increasing, then the model must switch to three regions (V-TP-L) or two-region (TP-L) formulations. The condition can be summarised as follows:

- $\xi_2(\bar{\gamma}_{TOT} - \bar{\gamma}) \geq \varepsilon$
- $\frac{d\bar{\gamma}}{d\tau} < 0$

After the calibration procedure, ε was set to 0.001.

SMB switches: disappearance of the superheated vapour region (V)

When the model is in the three-region (V-TP-L) or two-region (V-TP) formulations, disappearance of the superheated vapour region (V) may occur (e.g. because of the presence of a desuperheater), and a switch to the two-region (TP-L) or one-region (TP) formulations must take place. In this case, the

switch is based on the non-dimensional extension of the superheated vapour region, ξ_1 , and its time derivative: when ξ_1 is lower than a certain threshold and is decreasing, then the model must switch to the two-region (TP-L) or one-region (TP) formulations. The condition can be summarised as:

- $\xi_1 \leq \xi_{1min}$
- $\frac{d\xi_1}{d\tau} < 0$

After the calibration process, the threshold value ξ_{1min} was set to 0.005.

SMB switches: reappearance of the superheated vapour region (V)

The switching scheme allowing the model to manage the reappearance of the superheated vapour region (V) when it is in its two-region (TP-L) or one-region (TP) formulations is simply based on the value of the refrigerant inlet enthalpy h_{ri} ; in particular:

- $h_{ri} \geq h_v$

Switch from the SMB to the off-duty formulation

The switching scheme between the SMB and off-period frameworks is managed in the same way presented for the evaporator in section 2.5.8. In particular, the switch from the SMB to off-period formulation occurs when $\dot{m}_{ri} < 0.0001 \text{ kg} \cdot \text{s}^{-1}$ or $\dot{m}_{ro} < 0.0001 \text{ kg} \cdot \text{s}^{-1}$, whilst reactivation begins when both the inlet and outlet mass flow rates have non-zero values, i.e. $\dot{m}_{ri} > 0.0001 \text{ kg} \cdot \text{s}^{-1}$ and $\dot{m}_{ro} > 0.0001 \text{ kg} \cdot \text{s}^{-1}$.

Whilst the model is in the off-period framework, on the basis of $\bar{\gamma}_{off}$, it selects the right SMB formulation in the case the refrigerant mass flow rates takes non-zero values suitable for the switch; since $\bar{\gamma}_{off}$ is usually between 0 and 1, the model will restart in the SMB framework with the one-region (TP) formulation, but code improvements are foreseen to enhance its flexibility.

2.7 Compressor

As already seen in Chapter 1, the compressor, together with the expansion device, provides a certain refrigerant mass flow rate in the refrigeration plant, on the basis of the operating pressures, P_i and P_o , the refrigerant enthalpy at the evaporator outlet, h_{ero} , and the rotational frequency f , which represent the compressor model inputs, as previously seen in Fig. 2.1. In addition to the mass flow rate \dot{m}_{rk} , the model of the compressor also provides the refrigerant outlet enthalpy h_{ro} and the electric power consumption \dot{W}_{el} .

The calculation of the outputs is based on the polynomials usually given by the compressor manufacturer, whose coefficients are dependent on the frequency f and on the degree of superheating ΔT_{sh} at the inlet of the compressor, whilst their independent variables are the saturation temperatures T_{sati} and $T_{sat o}$ at

the inlet and outlet pressures. The values obtained through the polynomials are then multiplied by the correction factors $C_{\dot{m}_r}$, C_T and $C_{\dot{W}_{el}}$, to improve the match with experimental data. In fact, the polynomials are calculated by the manufacturer in steady-state conditions and inaccuracies may be significant when used during transients.

Since the mechanical and electrical dynamics of a positive-displacement compressor are usually faster than the thermal evolution, the mass flow rate through the compressor and the electric power consumption are directly computed through algebraic expressions, Eqs. 2.180-2.181.

$$\dot{m}_{rk} = C_{\dot{m}_r} \cdot (z_{m1} + z_{m2}T_{sat i} + z_{m3}T_{sat o} + z_{m4}T_{sat i}^2 + z_{m5}T_{sat i}T_{sat o} + z_{m6}T_{sat o}^2 + z_{m7}T_{sat i}^3 + z_{m8}T_{sat i}^2T_{sat o} + z_{m9}T_{sat i}T_{sat o}^2 + z_{m10}T_{sat o}^3)$$
(2.180)

$$\dot{W}_{el} = C_{\dot{W}_{el}} \cdot (z_{W1} + z_{W2}T_{sat i} + z_{W3}T_{sat o} + z_{W4}T_{sat i}^2 + z_{W5}T_{sat i}T_{sat o} + z_{W6}T_{sat o}^2 + z_{W7}T_{sat i}^3 + z_{W8}T_{sat i}^2T_{sat o} + z_{W9}T_{sat i}T_{sat o}^2 + z_{W10}T_{sat o}^3)$$
(2.181)

Similarly to what described in [72], the compressor outlet enthalpy is calculated through a first-order differential equation to take into account the thermal dynamics of the shell in a simplified way, as expressed in Eq. 2.182, where τ_k is a time constant tunable by the user on the basis of compressor dimensions and experimental data, h_{ro} is the actual value of the compressor outlet enthalpy and $h_{ro static}$ is the instantaneous outlet enthalpy considering the compressor as a quasi-static component, evaluable as a function of the outlet pressure P_o and the outlet temperature $T_{ro static}$ computed through polynomials, as shown in Eq. 2.183 .

$$\frac{dh_{ro}}{d\tau} = \frac{h_{ro static} - h_{ro}}{\tau_k}$$
(2.182)

$$T_{ro static} = C_T \cdot (z_{T1} + z_{T2}T_{sat i} + z_{T3}T_{sat o} + z_{T4}T_{sat i}^2 + z_{T5}T_{sat i}T_{sat o} + z_{T6}T_{sat o}^2 + z_{T7}T_{sat i}^3 + z_{T8}T_{sat i}^2T_{sat o} + z_{T9}T_{sat i}T_{sat o}^2 + z_{T10}T_{sat o}^3)$$
(2.183)

2.8 Electronic expansion valve

The electronic expansion valve (EEV) is considered as a static component and, like for the compressor, the model inputs are inlet and outlet pressures, P_i and P_o , the inlet enthalpy, h_{ri} and a control signal p which controls its opening through the position of the shutter. Since the heat exchange to the surrounding is negligible and no work is extracted, the transformation can be considered as isenthalpic and thus the outlet enthalpy can be calculated as:

$$\boxed{h_{ro} = h_{ri}} \quad (2.184)$$

The mass flow rate is calculated through Bernoulli's equation:

$$\boxed{\dot{m}_{rv} = C_{D0}g(p)\sqrt{\rho_{ri}(P_i - P_o)}} \quad (2.185)$$

In Eq. 2.185, ρ_{ri} is the density of the refrigerant at the inlet, C_{D0} is the wide-open discharge coefficient, and $g(p)$ is a function of the non-dimensional position of the shutter p which allows to calculate the actual valve discharge coefficient and can be specified by the user.

Chapter 3

Model implementation

The choice of the software implementation platform is fundamental to keep the computational cost of a dynamic model at its minimum. Many software available on the market, like TRNSYS[®], Modelica[®], EnergyPlus[®], ESP-r[®], GT-SUITE[®] and Matlab/Simulink[®], can be used to simulate transients in refrigeration systems.

In a first attempt, the mathematical model presented in Chapter 2 was implemented in TRNSYS[®], since it is a well-established software used to carry out transient energy analyses of a large variety of plants coupled with buildings, [100], and characterized by a rich library of functions, called “Types”. However, the numerical complexity of the heat exchanger models and the large transients occurring when certain control system are applied make the software unsuitable to perform such simulations at low computational costs.

The in-house library of components has therefore been implemented in Simulink, since it represents a widespread tool for the simulation of dynamic systems and its input-output architecture, together with the large variety of numerical solvers available, is very suitable for the kind of model of this work. In addition to being endowed with a large library of standard block-functions, one of the most important feature is the possibility for the user to write customized functions in different programming languages like C, C++, Ada, Matlab and Fortran. In this work, the Matlab-Level 2 S-Function framework was used as a basis whereon to build the mathematical models presented in Chapter 2. In fact, using Matlab, it is possible to obtain subroutines which have an interaction with the Simulink engine very similar to that of the built-in Simulink blocks and are suitable for continuous, discrete and hybrid systems [101].

In this chapter, the architecture of a generic Matlab Level 2 S-Function is presented at first. Then, the S-Functions related to each of the components of the VCS are described in detail, also discussing the initialization procedure of the code and the management of the thermodynamic properties of the fluids involved.

3.1 Structure of a Matlab Level 2 S-Function

The basic principle behind the behaviour of a Matlab-Level 2 S-Function is illustrated in Fig. 3.1: the customized block takes the input variables, which can be obtained through other blocks in the model, and possibly user-defined parameters to evaluate the continuous state variables (if present), described by a system of ordinary differential equations (ODEs), and the block outputs.

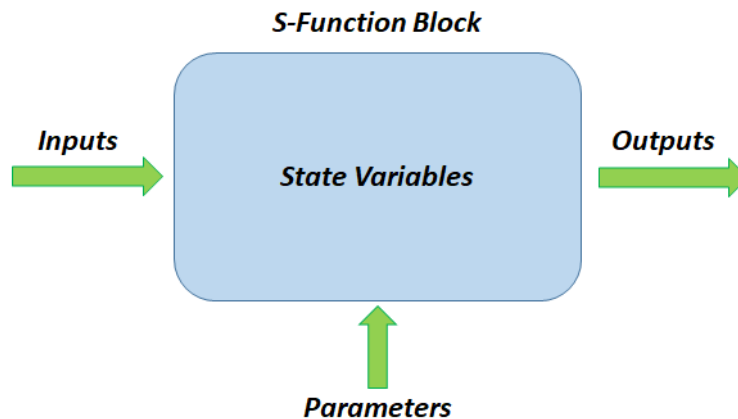


Figure 3.1: Scheme of the basic operating principle of an S-Function.

To better understand the structure of a generic Matlab-Level 2 S-Function, in Fig. 3.2 the main stages of a dynamic simulation in Simulink are reported. After an initialization procedure, the Simulink engine starts a simulation loop lasting until simulation ends, and punctuated by the simulation time-step; in such a loop each block of the model is called in the order chosen during the initialization phase, and its state variables, derivatives and outputs are computed. If a block contains continuous state variables, thus described by ODEs, an inner integration loop starts too.

Before the first simulation loop, the Simulink engine initialize the so-called *SimStruct*, which contains the main information about the S-Functions (number of inputs, outputs, continuous states, discrete states and parameters), defined in the *setup* section of the customized blocks. Then, the Matlab-Level 2 S-Functions call a set of so-called *callback methods* which are called by the Simulink engine at a given stage and perform user-defined tasks. The most important callback methods for a Matlab-Level 2 S-Function are:

- *PostPropagationSetup*: allows to allocate memory for variables and data storage during simulation.
- *Start*: allows the user to initialize the continuous and discrete states and to store useful data in the pre-allocated memory.
- *Outputs*: in this section, the necessary tasks for the calculation of the final values of outputs in a time-step are implemented.

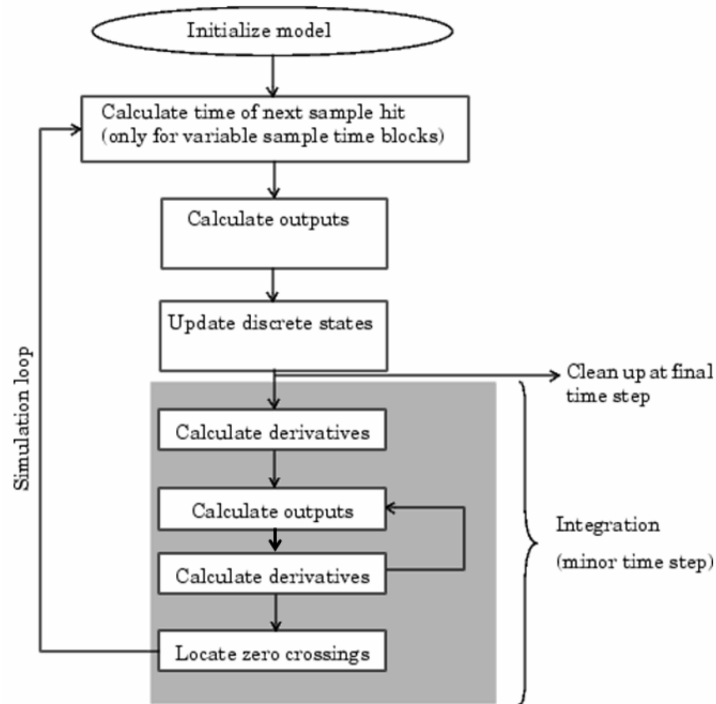


Figure 3.2: Main stages of a dynamic simulation carried out in Simulink environment [101].

- *Update*: in this callback method, the discrete variables are updated once-per-time-step.
- *Derivative*: if the S-Function contains continuous states, the Derivative and Outputs callback methods are called in the inner loop shown in Fig. 3.2 in order to calculate the continuous state variables.

In the following sections the inputs, outputs and parameters for the Matlab-Level 2 S-Functions realized are reported.

3.2 S-Function for the heat exchanger models

As discussed in Chapter 2, two configurations of heat exchangers are considered: finned-tube and brazed-plate heat exchangers. In Fig. 3.3, the S-Function block associated to the brazed-plate evaporator is shown, since its inputs and outputs are the same for the finned-tube type. As explained in Chapter 2, the inputs required for the heat exchanger models, on the left side of Fig. 3.3, are the refrigerant inlet and outlet mass flow rates, \dot{m}_{ri} and \dot{m}_{ro} , the refrigerant inlet enthalpy h_{ri} and the secondary fluid inlet mass flow rate \dot{m}_{fi} and temperature T_{fi} ; the model outputs are located on the right side instead and include the refrigerant pressure P , the outlet enthalpy h_{ro} , the main refrigerant temperatures like the saturation temperature T_{sat} and the outlet temperature T_{ro} , the non-dimensional lengths of regions ξ_j , the wall temperatures T_{wj} , the model operating mode, the secondary fluid intermediate and

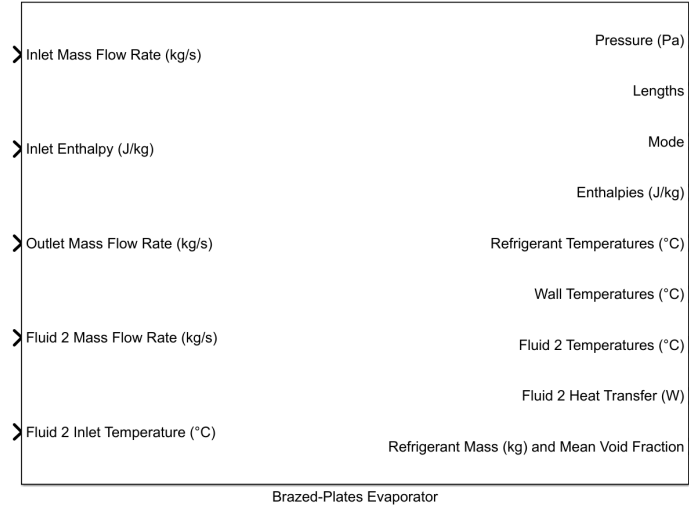


Figure 3.3: S-Function block of the brazed-plate evaporator: inputs and outputs on the left and right end sides respectively.

outlet temperature T_{fo} and the heat transfer rates on the secondary fluid side \dot{Q}_{fj} .

As illustrated in Fig. 3.1, in addition to the inputs a certain number of parameters might be necessary for the model definition. In Fig. 3.4, a part of the block mask where to define the model parameters is shown as an example.

In Tab 3.1, all the parameters required for the definition of the model of the BPHEs, valid for both evaporator and condenser, are reported. From the parameters values it is possible to evaluate the main quantities necessary to define the system of ODEs described in Chapter 2, as highlighted in Eqs. 3.1-3.5, which allow the calculation of the refrigerant and secondary fluid sides cross section area, A_{Crr} and A_{Crf} , the hydraulic diameter d_h , the heat transfer areas A_{Sr} and A_{Sf} , the total length of the refrigerant path L_{tot} and the total wall mass m_w . Moreover, specifying the type of refrigerant and secondary fluid at the beginning of the simulation makes possible to upload the tables fluids' properties compiled as described in section 3.5.

$$A_{Crr} = A_{Crf} = w \cdot b \quad (3.1)$$

$$d_h = 2b \quad (3.2)$$

$$A_{Sr} = A_{Sf} = (N_{channel r} + N_{channel f} - 1) \cdot \Phi \cdot w \cdot l \quad (3.3)$$

$$L_{tot} = l \quad (3.4)$$

$$m_w = (N_{channel r} + N_{channel f} - 1) \cdot m_{plate} \quad (3.5)$$

In Tab. 3.2, all the parameters required for the definition of the model of the finned-tube heat exchangers, valid for both evaporator and condenser, are reported. In this case, the variables needed to define the system of ODEs are already given by the user.

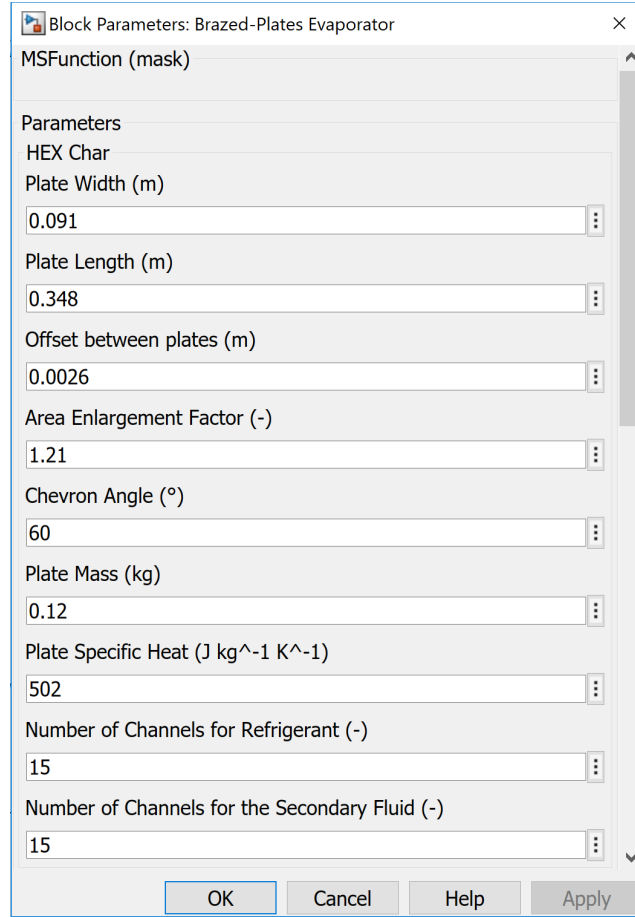


Figure 3.4: View of the parameters mask for the brazed-plate evaporator.

As highlighted in Tabs. 3.1-3.2, in addition to the parameters required to define the structural characteristics of the heat exchangers, a set of conditions must be given in order to correctly initialize the model. To determine the initial values of all the state variables (non-dimensional lengths, mean-void fraction, enthalpies, mean density wall temperatures) a steady-state condition with compressor switched on is superimposed at the beginning of the simulation. Future code improvements are needed to allow the user to initialize the model also with the compressor turned off. In the following two subsections, the initialization procedure adopted for the evaporator and the condenser is described.

3.2.1 Evaporator initialization

Since the value of the pressure when $\tau = 0$ s is already given in the parameters list, the left variables to be initialized are the non-dimensional length of the TP region ξ_1 , the mean void fraction $\bar{\gamma}$, the enthalpy in the superheated vapour region h_2 , the mean density ρ_m and the wall temperatures T_{w1} .

On the basis of the values of the outlet enthalpy h_{ro0} and the dry-saturated vapour h_v at pressure P_0 , it is immediate to establish the SMB formulation at

Table 3.1: Parameters for the brazed-plate heat exchangers.

w	Plate width (m)
l	Plate length (m)
b	Offset between plates (m)
Φ	Area enlargement factor ($-$)
θ	Chevron angle ($^\circ$)
m_{plate}	Mass of a plate (kg)
c_{plate}	Plate specific heat capacity ($J \cdot kg^{-1}K^{-1}$)
$N_{channel r}$	Number of channels for the refrigerant ($-$)
$N_{channel f}$	Number of channels for the secondary fluid ($-$)
$-$	Type of refrigerant
$-$	Type of secondary fluid
C_V	Heat transfer correction factor for the superheated refrigerant region ($-$)
C_{TP}	Heat transfer correction factor for the two-phase refrigerant region ($-$)
C_L	Heat transfer correction factor for the subcooled refrigerant region, valid for the condenser only ($-$)
C_{off}	Heat transfer correction factor for the refrigerant in the off-period formulation ($-$)
C_f	Heat transfer correction factor for the secondary fluid ($-$)
P_0	Pressure at the beginning of the simulation (Pa)
h_{ri0}	Refrigerant inlet enthalpy at the beginning of the simulation ($J \cdot kg^{-1}$)
h_{ro0}	Refrigerant outlet enthalpy at the beginning of the simulation ($J \cdot kg^{-1}$)
\dot{m}_{r0}	Refrigerant mass flow rate at the beginning of the simulation, assuming a steady-state condition ($kg \cdot s^{-1}$)
\dot{m}_{f0}	Secondary fluid mass flow rate at the beginning of the simulation ($kg \cdot s^{-1}$)
T_{fi0}	Secondary fluid inlet temperature at the beginning of the simulation ($^\circ C$)

the beginning of the simulation, as resumed in Tab. 3.3.

Initialization in the two-region formulation

In the case $h_{ro0} > h_v$, the mean void fraction $\bar{\gamma}$ is evaluated through Eq. 2.4, once the refrigerant inlet quality is known from its enthalpy h_{ri0} and pressure P_0 and imposing an outlet quality $x_o = 1$.

A linear profile is assumed for the enthalpy in the superheated vapour region, so that the mean enthalpy h_2 is easily estimated as:

$$h_{20} = \frac{h_{v0} + h_{ro0}}{2} \quad (3.6)$$

To determine ξ_1 , T_{w1} and T_{w2} at $\tau = 0 s$ a distinction must be made between the two HEX configurations.

Table 3.2: Parameters for the finned-tube heat exchangers.

d_h	Hydraulic diameter (m)
L_{tot}	Total length of one pass (m)
A_{Crf}	Secondary fluid side cross section (m^2)
A_{Sf}	Secondary fluid side heat transfer area (m^2)
A_{Crr}	Refrigerant side cross section (m^2)
A_{Sr}	Refrigerant side heat transfer area (m^2)
m_w	Wall mass (kg)
c_w	Wall specific heat capacity ($J \cdot kg^{-1} K^{-1}$)
–	Type of refrigerant
–	Type of secondary fluid
C_V	Heat transfer correction factor for the superheated refrigerant region (–)
C_{TP}	Heat transfer correction factor for the two-phase refrigerant region (–)
C_L	Heat transfer correction factor for the subcooled refrigerant region, valid only for the condenser (–)
C_{off}	Heat transfer correction factor for the refrigerant in the off-period formulation (–)
C_f	Heat transfer correction factor for the secondary fluid (–)
P_0	Pressure at the beginning of the simulation (Pa)
h_{ri0}	Refrigerant inlet enthalpy at the beginning of the simulation ($J \cdot kg^{-1}$)
h_{ro0}	Refrigerant outlet enthalpy at the beginning of the simulation ($J \cdot kg^{-1}$)
\dot{m}_{r0}	Refrigerant mass flow rate at the beginning of the simulation, assuming a steady-state condition ($kg \cdot s^{-1}$)
\dot{m}_{f0}	Secondary fluid mass flow rate at the beginning of the simulation ($kg \cdot s^{-1}$)
T_{fi0}	Secondary fluid inlet temperature at the beginning of the simulation ($^{\circ}C$)

Table 3.3: Initialization of the SMB framework for the evaporator model

$h_{ro0} > h_v$	Two-region formulation TP-V
$h_{ro0} \leq h_v$	One-region formulation TP

Finned-tube heat exchanger

In the case of the finned-tube heat exchanger, a cross-flow configuration is adopted and thus, after an estimation of the heat transfer coefficients at the beginning of the simulation α_{r10} , α_{r20} and α_{f0} , to determine the wall temperatures is sufficient to apply the wall energy balances, as shown in Eqs. 3.7-3.8:

$$\alpha_{r10} \xi_{10} A_{Sr} (T_{w10} - T_{r10}) = \xi_{10} \dot{m}_{f0} c_{pf} (T_{fi0} - T_{w10}) \left(1 - \exp\left(-\frac{\alpha_{f0} A_{Sf}}{\dot{m}_{f0} c_{pf}}\right) \right) \quad (3.7)$$

$$\alpha_{r20} \xi_{20} A_{Sr} (T_{w20} - T_{r20}) = \xi_{20} \dot{m}_{f0} c_{pf} (T_{fi0} - T_{w20}) \left(1 - \exp\left(-\frac{\alpha_{f0} A_{Sf}}{\dot{m}_{f0} c_{pf}}\right) \right) \quad (3.8)$$

From Eqs. 3.7-3.8 it can be noticed how the non-dimensional lengths appear on both sides and can thus be simplified, leading to the formulation of the initial wall temperatures T_{w10} and T_{w20} expressed in Eqs. 3.9-3.10:

$$T_{w10} = \frac{\alpha_{r10}A_{Sr}T_{r10} + \dot{m}_{f0}c_{pf}T_{fi0} \left(1 - \exp\left(-\frac{\alpha_{f0}A_{Sf}}{\dot{m}_{f0}c_{pf}}\right)\right)}{\alpha_{r10}A_{Sr} + \dot{m}_{f0}c_{pf} \left(1 - \exp\left(-\frac{\alpha_{f0}A_{Sf}}{\dot{m}_{f0}c_{pf}}\right)\right)} \quad (3.9)$$

$$T_{w20} = \frac{\alpha_{r20}A_{Sr}T_{r20} + \dot{m}_{f0}c_{pf}T_{fi0} \left(1 - \exp\left(-\frac{\alpha_{f0}A_{Sf}}{\dot{m}_{f0}c_{pf}}\right)\right)}{\alpha_{r20}A_{Sr} + \dot{m}_{f0}c_{pf} \left(1 - \exp\left(-\frac{\alpha_{f0}A_{Sf}}{\dot{m}_{f0}c_{pf}}\right)\right)} \quad (3.10)$$

To determine the value of ξ_{10} , a first-principle balance must be applied to the two refrigerant regions as highlighted in Eqs. 3.11-3.12:

$$\alpha_{r10}\xi_{10}A_{Sr}(T_{w10} - T_{r10}) = \dot{m}_{r0}(h_{v0} - h_{ri0}) \quad (3.11)$$

$$\alpha_{r20}\xi_{20}A_{Sr}(T_{w20} - T_{r20}) = \dot{m}_{r0}(h_{ro0} - h_{v0}) \quad (3.12)$$

Calling $\dot{Q}_{r10} = \dot{m}_{r0}(h_{v0} - h_{ri0})$, $\dot{Q}_{r20} = \dot{m}_{r0}(h_{ro0} - h_{v0})$, remembering that $\xi_{20} = 1 - \xi_{10}$ and dividing Eq. 3.11 by Eq. 3.12, an expression for ξ_{10} is obtained:

$$\xi_{10} = \frac{\frac{\dot{Q}_{r10}}{\dot{Q}_{r20}}}{\frac{\dot{Q}_{r10}}{\dot{Q}_{r20}} + \frac{\alpha_{r10}}{\alpha_{r20}} \left(\frac{T_{w10} - T_{r10}}{T_{w20} - T_{r20}}\right)} \quad (3.13)$$

Calculating the density ρ_{10} in the two-phase region by means of Eq. 2.16 and the density ρ_{20} through properties table as a function of P_0 and h_{20} , the initial mean density ρ_{m0} can be evaluated:

$$\rho_{m0} = \xi_{10}\rho_{10} + \xi_{20}\rho_{20} \quad (3.14)$$

Brazed-plate heat exchanger

For the brazed-plate heat exchangers, the non-dimensional length ξ_1 contributes to the definition of the secondary fluid side efficiencies ε_{fj} and thus separate computation of the wall temperatures T_{w10} and T_{w20} and of the non-dimensional length ξ_{10} cannot be accomplished. In this case, the system of non-linear equations composed by Eq. 3.13 and Eqs. 3.15-3.16 must be solved, and the *fsolve* routine available in Matlab is used to this purpose. The first guess values for ξ_{10} , T_{w10} and T_{w20} are those obtained for a cross-flow configuration.

$$\alpha_{r10}\xi_{10}A_{Sr}(T_{w10} - T_{r10}) = \dot{m}_{f0}c_{pf}(T_{f120} - T_{w10}) \left(1 - \exp\left(-\frac{\alpha_{f0}\xi_{10}A_{Sf}}{\dot{m}_{f0}c_{pf}}\right)\right) \quad (3.15)$$

$$\alpha_{r20}\xi_{20}A_{Sr}(T_{w20} - T_{r20}) = \dot{m}_{f0}c_{pf}(T_{fi0} - T_{w20}) \left(1 - \exp\left(-\frac{\alpha_{f0}\xi_{20}A_{Sf}}{\dot{m}_{f0}c_{pf}}\right)\right) \quad (3.16)$$

The initial secondary fluid intermediate temperature T_{f120} appearing in Eqs. 3.15-3.16 can be calculated through Eq. 3.17 once the heat transfer rate exchanged in the superheated vapour region $\dot{Q}_{r20} = \dot{m}_{r0}(h_{ro0} - h_{v0})$ has been evaluated.

$$T_{f120} = T_{fi0} - \frac{\dot{Q}_{r20}}{\dot{m}_{f0}c_{pf}} \quad (3.17)$$

Once ξ_{10} is known, Eq. 3.14 can be used again to determine ρ_{m0} .

Initialization in the one-region formulation

If $h_{ro0} \leq h_{v0}$, then the evaporator model is initialized in the one-region (TP) formulation of the SMB framework. In this case, since the superheated vapour region is not active, the following values are chosen to initialize h_2 and ξ_1 , in order to prevent model failure in the case of a model switch to the two-region formulation:

$$h_{20} = h_{v0} \quad (3.18)$$

$$\xi_{10} = 0.999 \quad (3.19)$$

The mean void fraction $\bar{\gamma}$ is still evaluated through Eq. 2.4, once the refrigerant inlet quality is known from its enthalpy h_{ri0} and pressure P_0 and calculating the outlet quality as:

$$x_o = \frac{h_{ro0} - h_{l0}}{h_{v0} - h_{l0}} \quad (3.20)$$

Independently from the HEX configuration, the wall temperature T_{w10} in the TP region can be evaluated through Eq. 3.9 and the same initialization value is assumed for T_{w20} .

In this case, the mean density coincides with the density in the two-phase region:

$$\rho_{m0} = \rho_{10} \quad (3.21)$$

3.2.2 Condenser initialization

Similarly to the evaporator model, the initial value of pressure P_0 is given as a model parameter, and thus the variables to be initialized are the non-dimensional lengths ξ_1 , ξ_2 , the superheated vapour enthalpy h_1 , the mean void fraction $\bar{\gamma}$, the subcooled liquid enthalpy h_3 , the mean density ρ_m and the wall temperatures T_{w1} , T_{w2} and T_{w3} . Also in this case, the starting SMB formulation and thus the initialization procedure depends on the value of the initial refrigerant outlet enthalpy, as summarised in Tab. 3.4.

Table 3.4: Initialization of the SMB framework for the condenser model

$h_{ro0} < h_l$	Three-region formulation V-TP-L
$h_{ro0} \geq h_v$	Two-region formulation V-TP

A refrigerant inlet enthalpy in the superheated vapour region is required at the beginning of the simulation, and the initialization of the refrigerant enthalpy in the superheated vapour region is obtained as:

$$h_{10} = \frac{h_{ri0} + h_{v0}}{2} \quad (3.22)$$

Initialization in the three-region formulation

If $h_{r00} \leq h_l$, the model is initialized in the three-region (V-TP-L) formulation, and the initial value of the mean void fraction $\bar{\gamma}_0$ can be evaluated through Eq. 2.4, considering a unitary inlet quality and complete condensation.

As for the enthalpy in the subcooled region h_{30} , a mean value between the saturated liquid and the outlet enthalpies is used:

$$h_{30} = \frac{h_{l0} + h_{r00}}{2} \quad (3.23)$$

Similarly to the evaporator, for the initialization of ξ_1 , ξ_2 and the wall temperatures T_{w1} , T_{w2} and T_{w3} a distinction must be made among HEX configurations.

Finned-tube heat exchanger

In the finned-tube condenser, like for the evaporator, it is immediate to calculate the initial values of the wall temperatures starting from the wall energy balances, see Eqs. 3.24-3.26, where the heat transfer coefficients α_{r10} , α_{r20} , α_{r30} and α_{f0} are evaluated at the beginning of the simulation. T_{w10} , T_{w20} and T_{w30} are thus calculated through Eqs. 3.27-3.29.

$$\alpha_{r10}\xi_{10}A_{Sr}(T_{r10}-T_{w10}) = \xi_{10}\dot{m}_{f0}c_{pf}(T_{w10}-T_{fi0})\left(1-\exp\left(-\frac{\alpha_{f0}A_{Sf}}{\dot{m}_{f0}c_{pf}}\right)\right) \quad (3.24)$$

$$\alpha_{r20}\xi_{20}A_{Sr}(T_{r20}-T_{w20}) = \xi_{20}\dot{m}_{f0}c_{pf}(T_{w20}-T_{fi0})\left(1-\exp\left(-\frac{\alpha_{f0}A_{Sf}}{\dot{m}_{f0}c_{pf}}\right)\right) \quad (3.25)$$

$$\alpha_{r30}\xi_{30}A_{Sr}(T_{r30}-T_{w30}) = \xi_{30}\dot{m}_{f0}c_{pf}(T_{w30}-T_{fi0})\left(1-\exp\left(-\frac{\alpha_{f0}A_{Sf}}{\dot{m}_{f0}c_{pf}}\right)\right) \quad (3.26)$$

$$T_{w10} = \frac{\alpha_{r10}A_{Sr}T_{r10} + \dot{m}_{f0}c_{pf}T_{fi0}\left(1 - \exp\left(-\frac{\alpha_{f0}A_{Sf}}{\dot{m}_{f0}c_{pf}}\right)\right)}{\alpha_{r10}A_{Sr} + \dot{m}_{f0}c_{pf}\left(1 - \exp\left(-\frac{\alpha_{f0}A_{Sf}}{\dot{m}_{f0}c_{pf}}\right)\right)} \quad (3.27)$$

$$T_{w20} = \frac{\alpha_{r20}A_{Sr}T_{r20} + \dot{m}_{f0}c_{pf}T_{fi0}\left(1 - \exp\left(-\frac{\alpha_{f0}A_{Sf}}{\dot{m}_{f0}c_{pf}}\right)\right)}{\alpha_{r20}A_{Sr} + \dot{m}_{f0}c_{pf}\left(1 - \exp\left(-\frac{\alpha_{f0}A_{Sf}}{\dot{m}_{f0}c_{pf}}\right)\right)} \quad (3.28)$$

$$T_{w30} = \frac{\alpha_{r30}A_{Sr}T_{r30} + \dot{m}_{f0}c_{pf}T_{fi0}\left(1 - \exp\left(-\frac{\alpha_{f0}A_{Sf}}{\dot{m}_{f0}c_{pf}}\right)\right)}{\alpha_{r30}A_{Sr} + \dot{m}_{f0}c_{pf}\left(1 - \exp\left(-\frac{\alpha_{f0}A_{Sf}}{\dot{m}_{f0}c_{pf}}\right)\right)} \quad (3.29)$$

To determine the value of ξ_{10} and ξ_{20} , a first-principle balance must be applied to the three refrigerant regions as highlighted in Eqs. 3.30-3.32:

$$\alpha_{r10}\xi_{10}A_{Sr}(T_{r10} - T_{w10}) = \dot{m}_{r0}(h_{ri0} - h_{v0}) \quad (3.30)$$

$$\alpha_{r20}\xi_{20}A_{Sr}(T_{r20} - T_{w20}) = \dot{m}_{r0}(h_{v0} - h_{l0}) \quad (3.31)$$

$$\alpha_{r30}\xi_{30}A_{Sr}(T_{r30} - T_{w30}) = \dot{m}_{r0}(h_{l0} - h_{ro0}) \quad (3.32)$$

Dividing Eq. 3.30 by Eqs. 3.31 and 3.32 leads to Eqs. 3.33-3.34, which allow to evaluate ξ_{10} and ξ_{20} , since $\xi_{30} = 1 - \xi_{10} - \xi_{20}$.

$$\frac{\alpha_{r10}\xi_{10}(T_{r10} - T_{w10})}{\alpha_{r20}\xi_{20}(T_{r20} - T_{w20})} = \frac{(h_{ri0} - h_{v0})}{(h_{v0} - h_{l0})} \quad (3.33)$$

$$\frac{\alpha_{r10}\xi_{10}(T_{r10} - T_{w10})}{\alpha_{r30}\xi_{30}(T_{r30} - T_{w30})} = \frac{(h_{ri0} - h_{v0})}{(h_{l0} - h_{ro0})} \quad (3.34)$$

The calculation of the mean density ρ_{m0} through Eq. 3.35 is now straightforward, once the density ρ_{20} in the two-phase region is calculated by means of Eq. 2.16 and the density in the single-phase regions, ρ_{10} and ρ_{30} , through properties table as a function of pressure and enthalpy.

$$\rho_{m0} = \xi_{10}\rho_{10} + \xi_{20}\rho_{20} + \xi_{30}\rho_{30} \quad (3.35)$$

Brazed-plate heat exchanger

Similarly to the evaporator, also in the condenser the non-dimensional lengths contribute to the definition of the secondary fluid side efficiency and thus a system of non-linear equations must be solved in order to obtain ξ_{10} , ξ_{20} , T_{w10} , T_{w20} and T_{w30} . In particular, the system is composed of Eqs. 3.33-3.34 and Eqs. 3.36-3.38, and the *fsolve* Matlab routine is used, with the values obtained for a cross-flow configuration as initial guess. Once the non-dimensional lengths at the beginning of the simulation are known, the mean density ρ_{m0} can be initialized too through Eq. 3.35.

$$\alpha_{r10}\xi_{10}A_{Sr}(T_{r10} - T_{w10}) = \dot{m}_{f0}c_{pf}(T_{w10} - T_{f120}) \left(1 - \exp\left(- \frac{\alpha_{f0}\xi_{10}A_{Sf}}{\dot{m}_{f0}c_{pf}} \right) \right) \quad (3.36)$$

$$\alpha_{r20}\xi_{20}A_{Sr}(T_{r20} - T_{w20}) = \dot{m}_{f0}c_{pf}(T_{w20} - T_{f230}) \left(1 - \exp\left(- \frac{\alpha_{f0}\xi_{20}A_{Sf}}{\dot{m}_{f0}c_{pf}} \right) \right) \quad (3.37)$$

$$\alpha_{r30}\xi_{30}A_{Sr}(T_{r30} - T_{w30}) = \dot{m}_{f0}c_{pf}(T_{w30} - T_{f30}) \left(1 - \exp\left(- \frac{\alpha_{f0}\xi_{30}A_{Sf}}{\dot{m}_{f0}c_{pf}} \right) \right) \quad (3.38)$$

Initialization in the two-region formulation

If $h_{ro0} \geq h_{l0}$, then the condenser model is initialized in the two-region (V-TP) formulation of the SMB framework. In this case, the subcooled liquid region does not exist, and the initial value of the mean enthalpy h_{30} is set to h_l , whilst the non-dimensional extension ξ_3 is initialized to a value of 0.005 to prevent

numerical failure in the case the subcooled liquid reappears. The mean void fraction $\bar{\gamma}$ is still evaluated through Eq. 2.4, calculating the outlet quality through Eq. 3.20, and the initial value of the enthalpy in the superheated vapour region h_{10} is calculated by means of Eq. 3.22.

Finned-tube heat exchanger

In the finned-tube configuration, the initial values of the wall temperatures T_{w10} and T_{w20} are evaluated through Eqs. 3.27-3.28; since no subcooled region exist, the value of T_{w30} is set equal to T_{w20} .

As for the non-dimensional lengths, ξ_{10} is calculated by means of Eq. 3.33, whilst ξ_{20} is evaluated applying the summation of Eq. 2.13 as a function of ξ_{10} and ξ_{30} . The mean density ρ_m can then be initialized through Eq. 3.35.

Brazed-plate heat exchanger

For the brazed-plate condenser, the initialization of ξ_1 , T_{w1} and T_{w2} is carried out solving a non-linear system of three equations, considering that ξ_{20} can be expressed through summation (Eq. 2.13) as a function of ξ_{10} and ξ_{30} . The first equation is obtained applying the energy balance to the superheated vapour and two-phase regions of the refrigerant and dividing them, leading to:

$$\frac{\alpha_{r10}\xi_{10}(T_{r10} - T_{w10})}{\alpha_{r20}\xi_{20}(T_{r20} - T_{w20})} = \frac{(h_{ri0} - h_{v0})}{(h_{v0} - h_{ro0})} \quad (3.39)$$

The second equation coincides with Eq. 3.36, whereas the third is derived from Eq. 3.37 assuming the secondary fluid inlet temperature T_{fi0} instead of the intermediate temperature T_{f230} , so that:

$$\alpha_{r20}\xi_{20}A_{Sr}(T_{r20} - T_{w20}) = \dot{m}_{f0}c_{pf}(T_{w20} - T_{fi0}) \left(1 - \exp\left(-\frac{\alpha_{f0}\xi_{20}A_{Sf}}{\dot{m}_{f0}c_{pf}}\right) \right) \quad (3.40)$$

As done for the finned-tube condenser, T_{w30} is set equal to T_{w20} and the mean density ρ_m is initialized through Eq. 3.35.

3.3 S-Function for the compressor model

In Fig- 3.5, a picture of the compressor S-Function is shown, highlighting the model inputs and outputs on the left and right sides respectively. As already explained in section 2.7, the inlet and outlet pressure (P_i and P_o), the inlet enthalpy (h_{ri}) and the rotational frequency (f) are needed to evaluate the refrigerant mass flow rate (\dot{m}_r), the outlet enthalpy (h_{ro}) and the electric power consumption (\dot{W}_{el}).

Table 3.5 lists all the parameters required for the compressor model. It can be noticed how a file containing the polynomials of the compressor is needed; in particular, the file contains the values of the polynomial coefficients for different values of the rotational frequency and the superheating at the compressor inlet. Moreover, the time constant for the calculation of the refrigerant outlet enthalpy is required and values for the initialization of the mass flow rate and the enthalpy must be given.

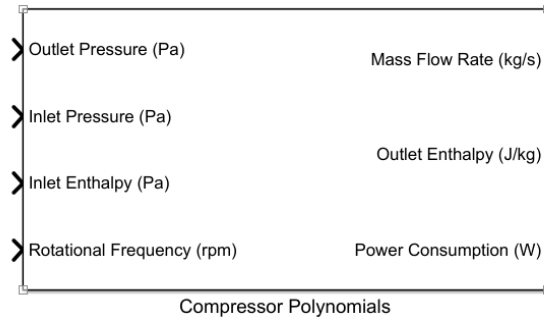


Figure 3.5: S-Function block of the compressor: inputs and outputs on the left and right end sides respectively.

Table 3.5: Parameters for the compressor.

–	Type of refrigerant
–	Performance maps
τ_k	Compressor time constant for outlet enthalpy calculation (s)
\dot{m}_{r0}	Initial refrigerant mass flow rate ($kg \cdot s^{-1}$)
h_{ro0}	Initial outlet enthalpy ($J \cdot kg$)

3.4 S-Function for the EEV model

In Fig- 3.6, a picture of the EEV S-Function is shown, highlighting the model inputs and outputs on the left and right sides respectively. Similarly to the compressor, the inlet and outlet pressure (P_i and P_o) and the inlet enthalpy (h_{ri}) are required to determine the refrigerant mass flow rate (\dot{m}_r) and the outlet enthalpy (h_{ro}). Moreover, the on-off signal, taking into account valve closure during off periods, and the non-dimensional position of the pin must be considered to correctly evaluate the mass flow rate.

Among the parameters required to define the EEV model, there are the type of refrigerant, the wide-open discharge coefficient C_{D0} and the function $g(p)$ which allows to calculate the actual valve discharge coefficient depending on the non-dimensional position of the shutter p .

3.5 Fluid properties

In order to make simulations as fast as possible, tables of thermodynamic properties are generated before running the models using the CoolProp and REFPROP libraries, [102, 103]; linear interpolation is then performed during simulation on the basis of the known variables.

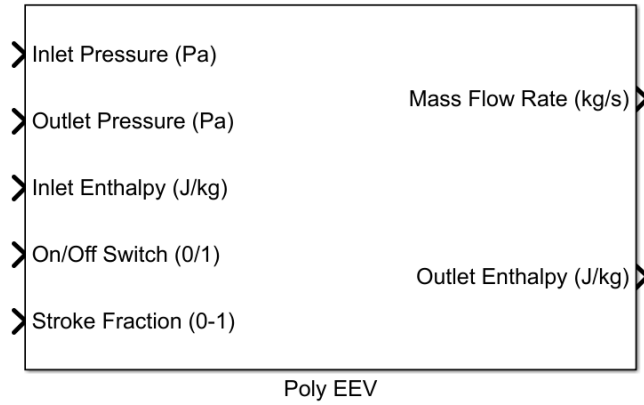


Figure 3.6: S-Function block of the electronic expansion valve: inputs and outputs on the left and right end sides respectively.

Table 3.6: List of the look-up tables implemented for the refrigerant side.

Two-phase	Single-phase
$T_{sat}(P), \rho_l(P), \rho_v(P), h_l(P), h_v(P),$ $\mu_l(P), \mu_v(P), c_{pl}(P), c_{pv}(P), \lambda_l(P),$ $\lambda_v(P)$	$T(P, h), \rho(P, h), h(P, s), s(P, h),$ $c_p(P, h), \lambda(P, T), \mu(P, T)$

3.5.1 Refrigerant

Table 3.6 reports the look-up tables implemented in order to let the model run properly, classifying them on the basis of the refrigerant phase. Calculation of the partial derivatives necessary to define the model are carried out during interpolation, using a forward linearization in order to reduce the number of interpolations. In particular, with reference to Fig. 3.7, calling x and y two generic independent variables, and the value of a generic dependent variable z and its partial derivatives can be calculated as:

$$z(x, y) = z_{j,k} + \left. \frac{\partial z_{j,k}}{\partial x} \right|_y \cdot (x - x_k) + \left. \frac{\partial z_{j,k}}{\partial y} \right|_x \cdot (y - y_j) \quad (3.41)$$

$$\left. \frac{\partial z_{j,k}}{\partial x} \right|_y = \frac{\Delta z_{j,k} \Big|_y}{\Delta x_k} = \frac{z_{k+1,j} - z_{k,j}}{x_{k+1} - x_k} \approx \left. \frac{\partial z(x, y)}{\partial x} \right|_y \quad (3.42)$$

$$\left. \frac{\partial z_{j,k}}{\partial y} \right|_x = \frac{\Delta z_{j,k} \Big|_x}{\Delta y_j} = \frac{z_{k,j+1} - z_{k,j}}{y_{j+1} - y_j} \approx \left. \frac{\partial z(x, y)}{\partial y} \right|_x \quad (3.43)$$

3.5.2 Secondary fluids

Thermophysical properties for secondary fluids tables are generated for density ρ , viscosity μ , thermal conductivity λ and specific heat capacity at constant

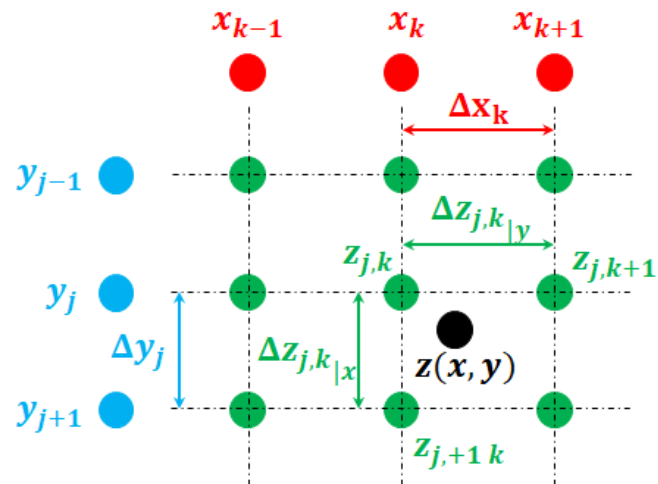


Figure 3.7: Scheme for the calculation of partial derivatives in the interpolation procedure.

pressure c_p as a function of temperature, once the pressure has been chosen.

Chapter 4

Numerical Verification

Before the library of models presented in Chapter 3 can be used for transient energy analysis of refrigeration systems, a validation procedure of the code should be carried out, both numerically and experimentally. In this chapter, the reliability of the in-house code (referred as "Unibo") is numerically verified comparing its predictions to those obtained through Thermosys[®], a Matlab/SIMULINK[®] toolbox developed at the University of Illinois, Urbana-Champaign (UIUC), [104, 105], which makes use of the SMB approach for the models of the heat exchangers, includes the models of the main components of a VCS (finned-tube evaporator and condenser, brazed-plate evaporator and condenser, compressor, electronic and thermostatic expansion valve, receiver and accumulator) and it has a very low computational cost which makes it suitable for control design.

Nevertheless, some shortcomings limit its usefulness in the analysis of the effects of control system on the energy efficiency of refrigerating machines, thus justifying the development of an in-house library. The first drawback is related to the absence of an output for the electric power in the compressor model, thus making the estimation of the COP impossible. Moreover, the compressor model is linearised and very sensitive to the initial conditions set for the refrigerant mass flow rate in the configuration mask. Besides, when inserting a liquid receiver in the model, the refrigerant conditions at the outlet of the condenser are forced to be two-phase, thus preventing the existence of a certain degree of subcooling, which is what often happens in practice. Another drawback was highlighted when trying to simulate an off period with Thermosys, shutting the compressor down and closing the EEV: the condensation pressure is forced to take an equilibrium value following a certain dynamic evolution, and becomes insensitive to variations of the boundary conditions (e.g. changes in the temperature of the secondary fluid). This aspect prevents the use of the library to investigate the effects of control strategies like on-off controls on the energy efficiency of the machine.

The results obtained in the numerical verification presented in this chapter has been obtained simulating the transient behaviour of an air-to-air vapour compression refrigerating machine (whose characteristics will be described first), focusing on the behaviour of the finned-tubes heat exchangers and of the EEV.

The in-house models of the EEV, the finned-tube evaporator and condenser were firstly verified separately, replacing one by one the corresponding component in the Thermosys[®] model. After that, a verification of the three components together, which were connected to the Thermosys[®] compressor model, was carried out. An attempt to verify also the compressor model presented in Chapter 2 obtaining the characteristic polynomials of the compressor modelled in Thermosys[®] was made; in particular, the suction and discharge pressures, the refrigerant superheating at the compressor inlet and the rotational frequency were varied in order to obtain a cloud of values for the refrigerant mass flow rate and the outlet enthalpy to use in a regression analysis. The outputs turned out to be strongly dependent on the initial conditions, so no reliable polynomials could be obtained. Only an experimental validation of the compressor model has therefore been carried out, as presented in Chapter 5.

4.1 Description of the system

The characteristics of the system were taken from a demonstrative model available in Thermosys[®], using R134a as a refrigerant. Table 4.1 shows the geometrical parameters of the heat exchangers and the correction factors used for the heat transfer coefficients both in the Thermosys[®] and the Unibo models. The reciprocating compressor available in the Thermosys[®] library has a displacement of 3.042 cm^3 and a time-constant of 25 s to take into account of the thermal inertia of the structure in the calculation of the outlet enthalpy. As for the valve, a wide-open discharge coefficient $C_{D0} = 1.2649 \cdot 10^{-5}$ was used and the valve characteristic $g(p)$ was quadratic as reported in Eq. 4.1. The air mass flow rates at the evaporator, \dot{m}_{fe} and condenser \dot{m}_{fc} were set to 0.105 and $0.294 \text{ kg} \cdot \text{s}^{-1}$ respectively. The inlet temperature of the air was 30°C at the condenser and 25°C at the evaporator.

$$g(p) = 2p - p^2 \quad (4.1)$$

4.2 Verification of the EEV model

To numerically verify the EEV model, a test imposing sudden variations in the valve opening was carried out, as described in greater detail in Tab. 4.2. The rotational speed of the compressor was maintained at 1500 rpm.

Figure 4.1 shows a comparison between the refrigerant mass flow rate across the EEV predicted by the Thermosys[®] and Unibo models. The qualitative trend of \dot{m}_{rv} is the same for the two models. In particular, when decreasing the valve opening the refrigerant mass flow rate decreases as well, whilst an opposite behaviour is obtained when the opening is increased. From a quan-

Table 4.1: Characteristics of the finned-tube heat exchangers.

	Finned-tube condenser	Finned-tube evaporator
D_h (mm)	8.103	8.126
L_{tot} (m)	10.690	11.458
A_{Cf} (m ²)	0.0898	0.0584
A_{Sf} (m ²)	2.79266	3.068019
A_{Cr} (m ²)	$5.156 \cdot 10^{-5}$	$5.156 \cdot 10^{-5}$
A_{Sr} (m ²)	0.2750	0.2916
m_w (kg)	4.656	2.744
c_w (J · kg ⁻¹ K ⁻¹)	467	487
C_{TP} (-)	1	1
C_V (-)	0.5	2
C_L (-)	1	-
C_f (-)	1.2	1.1

Table 4.2: Characteristics of the test.

Time period (s)	Position of the pin p (-)
0-500	0.120
501-1500	0.096
1501-3000	0.120

titative point of view, a maximum deviation of about 5% is shown. The EEV model is therefore considered to be numerically verified.

4.3 Verification of the finned-tube evaporator model

The numerical verification of the finned-tube evaporator was carried out through two tests, called Test 1 and Test 2, which were characterized by sudden variations in the valve opening and compressor speed respectively. In Test 1, the valve opening is subjected to an increase of 20% at $\tau = 500$ s (p varies from 0.12 to 0.144) and then returns to its initial value at $\tau = 1500$ s whilst the compressor speed is maintained constant at 1500 rpm; in this way it is possible to investigate the evaporator flooding with a subsequent disappearance of the superheating region. In Test 2 the position of the valve pin is kept constant at 0.12 and the compressor speed gets a 20% increase at $\tau = 500$ s (the rotational frequency varies from 1500 to 1800 rpm) and then gets back to its initial value at $\tau = 1500$ s, in order to investigate the effects of depletion at the evaporator.

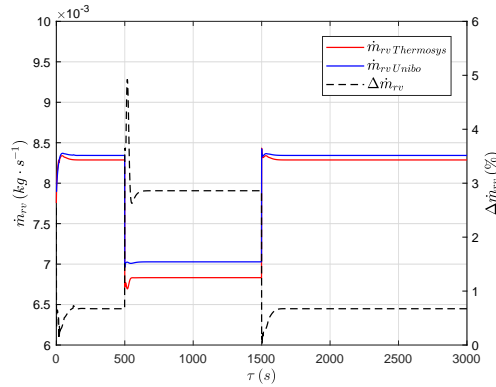


Figure 4.1: Refrigerant mass flow rate through the valve in the EEV model verification: comparison between Thermosys[®] and Unibo

4.3.1 Results for Test 1

Figure 4.2 (a) and (b) respectively show the evaporation pressure P_e and the refrigerant mass m_e contained in the evaporator predicted by the Unibo and Thermosys[®] models in Test 1. The increase in the valve opening whilst maintaining the compressor speed constant induces an increase in the evaporation pressure due to the higher amount of refrigerant contained in the heat exchanger. The maxima percentage deviations between the Unibo and Thermosys[®] predictions are lower than 2.5% for both the pressure and the refrigerant mass. However, it can be noticed how the steady state values of the refrigerant mass predicted by the Thermosys[®] evaporator before $\tau = 500$ s and after $\tau = 1500$ s are different, in spite of equal boundary conditions. This behaviour does not appear in the Unibo evaporator because of the presence of the global mass balance based on the mean density ρ_m , which ensures mass conservativeness. This anomaly may be due to the presence of linearisation processes in the Thermosys[®] code.

As can be seen from Fig. 4.3, once the valve opening is increased, the evaporator gets flooded and the superheated vapour region disappears. The non-dimensional length of the two-phase region ξ_{e1} tends to the unity.

Figure 4.4 reports the trends of the refrigerant superheating at the evaporator outlet (a) and the air outlet temperature (b). The trends predicted by the in-house code and by Thermosys[®] are qualitatively the same. The maximum deviation in the prediction of the superheating is lower than 1.5 K which may be due to differences in the heat transfer correlations used for the air side. As for the air outlet temperature, there is a very low quantitative difference, with a maximum deviation lower than 0.5 K. Similarly to the refrigerant mass, also the steady state values returned by Thermosys[®] for ξ_{e1} , ΔT_{sh} and T_{efo} are different before $\tau = 500$ s and after $\tau = 1500$ s.

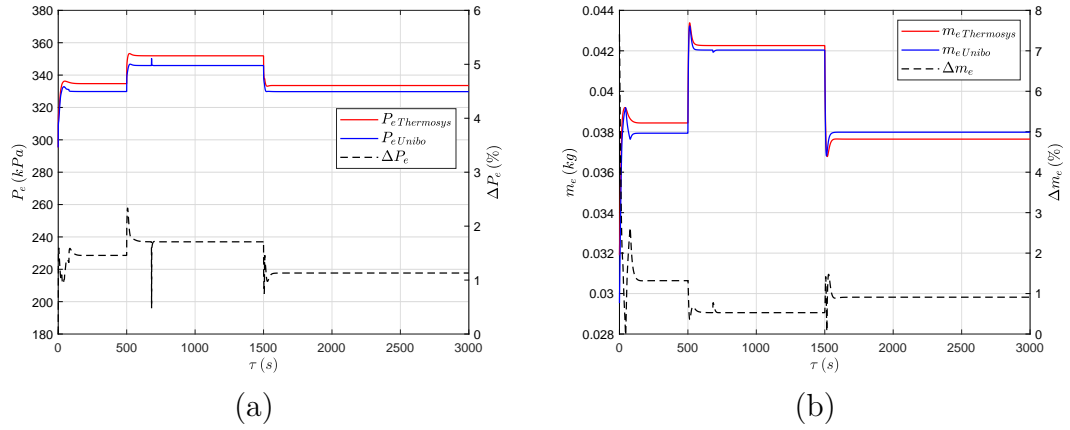


Figure 4.2: Evaporation pressure (a) and refrigerant mass (b) in the finned-tube evaporator model verification: comparison between Thermosys® and Unibo in Test1.

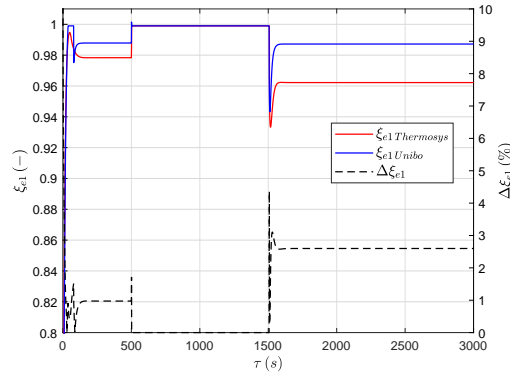


Figure 4.3: Non-dimensional extension of the TP region in the finned-tube evaporator model: comparison between Thermosys® and Unibo in Test 1.

4.3.2 Results for Test 2

Also in Test 2, the results given by the in-house code are very similar to those obtained through Thermosys®. As shown in Fig. 4.5, the maxima percentage deviations in the prediction of pressure and refrigerant mass are lower than 3%.

The non-dimensional length of the two-phase region ξ_{e1} is reported in Fig. 4.6, with percentage deviations lower than 2%, if the spikes in correspondence of the steps are neglected.

As shown in Fig. 4.7 (a), the refrigerant superheating increases when increasing the compressor speed, keeping the valve opening constant. This is due to the reduction in the evaporation pressure (lower saturation temperature) which increases the vapour content in the heat exchanger together with the increase in the the cooling power. The deviation between the values predicted by Unibo and Thermosys® for the superheating is lower than 3 K, and takes its maximum when the compressor runs at higher speed. This may be due

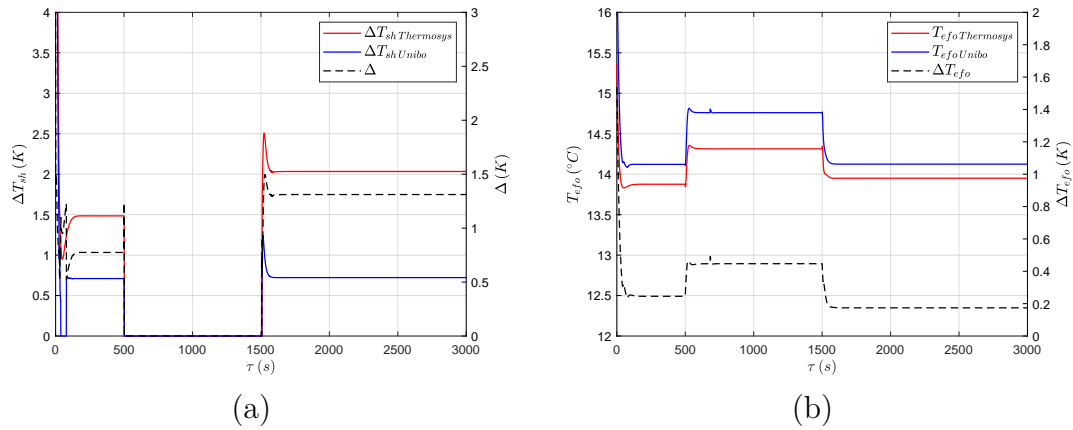


Figure 4.4: Refrigerant superheating (a) and air outlet temperature (b) in the finned-tube evaporator model verification: comparison between Thermosys[®] and Unibo in Test 1.

to differences in the heat transfer correlations, which can have different sensitivities to variations in the refrigerant mass flow rate. As for the air outlet temperature, the two models return almost the same values, as shown in Fig. 4.7 (b).

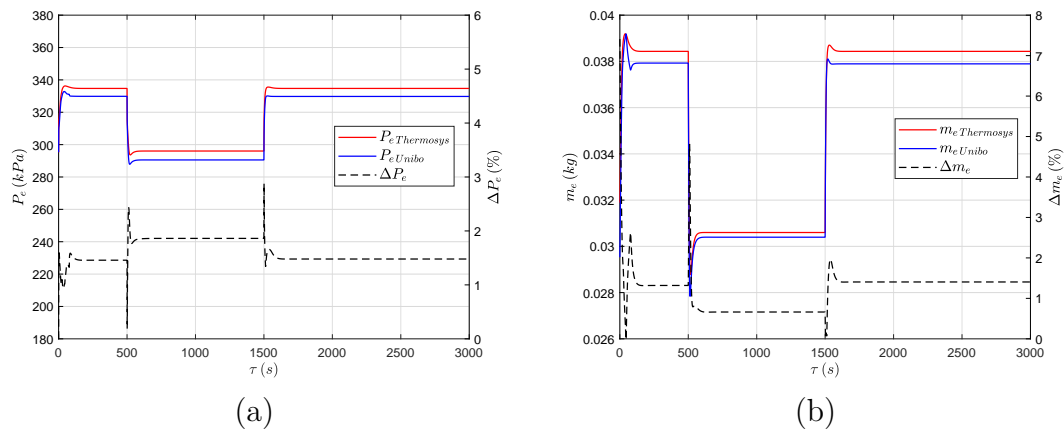


Figure 4.5: Evaporation pressure (a) and refrigerant mass (b) in the finned-tube evaporator model verification: comparison between Thermosys[®] and Unibo in Test 2.

4.4 Verification of the finned-tube condenser model

In the individual verification of the finned-tube condenser, the same tests (namely Test 1 and Test 2) presented in section 4.3 were used.

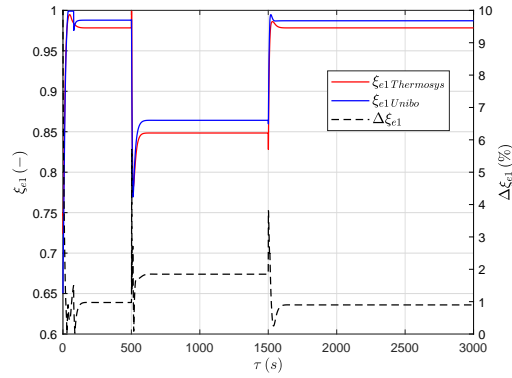


Figure 4.6: Non-dimensional extension of the TP region in the finned-tube evaporator model: comparison between Thermosys[®] and Unibo in Test2.

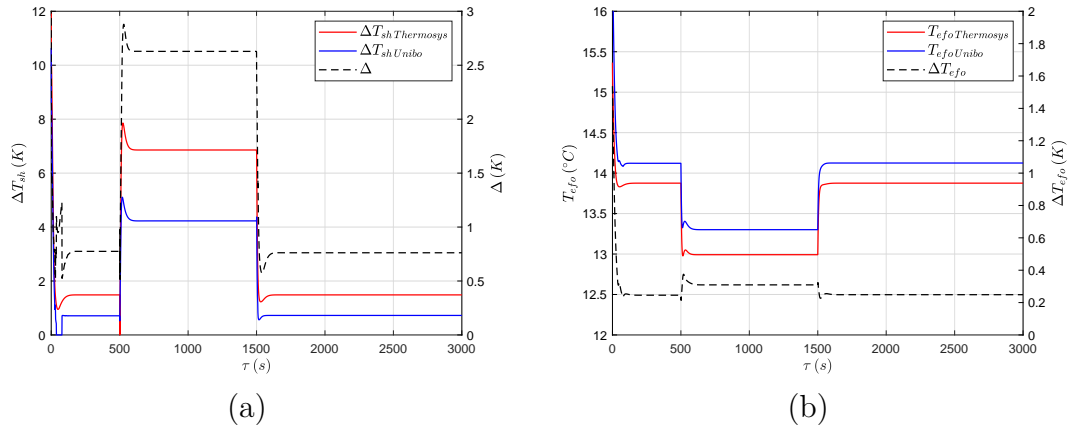


Figure 4.7: Refrigerant superheating (a) and air outlet temperature (b) in the finned-tube evaporator model verification: comparison between Thermosys[®] and Unibo in Test 2.

4.4.1 Results for Test 1

Figure 4.8 shows the trends of the condensation pressure and the refrigerant mass contained in the condenser. As can be seen from Fig. 4.8 (a), the value of P_c predicted by the Thermosys[®] model slightly increases when the valve opening increases, whilst an opposite behaviour is underlined for the Unibo model. The behaviour predicted by the Unibo model seems more consistent with results related to the refrigerant mass in the condenser, as shown in Fig. 4.8 (b). In fact, increasing the valve opening while keeping the same compressor velocity entails a mass reduction in the heat exchanger which should decrease the refrigerant pressure. However, the pressure level at the condenser is also influenced by the operating conditions of both the evaporator and the compressor: since the evaporation pressure increases due to the increased refrigerant mass at the low-pressure side and the reciprocating compressor works with an almost constant pressure ratio across the valves, at the condenser the pressure may increase too. Thus, depending on the dominant effect between

mass reduction and evaporation pressure increase, both pressure trends predicted by the Unibo and Thermosys[®] models have physical meaning. This will be discussed further in section 4.5.1.

From Fig. 4.8 (b), it can be also noticed how the Thermosys[®] model returns a different value of refrigerant mass once the boundary conditions return to the initial values.

Figure 4.9 reports the results obtained for the non-dimensional lengths of

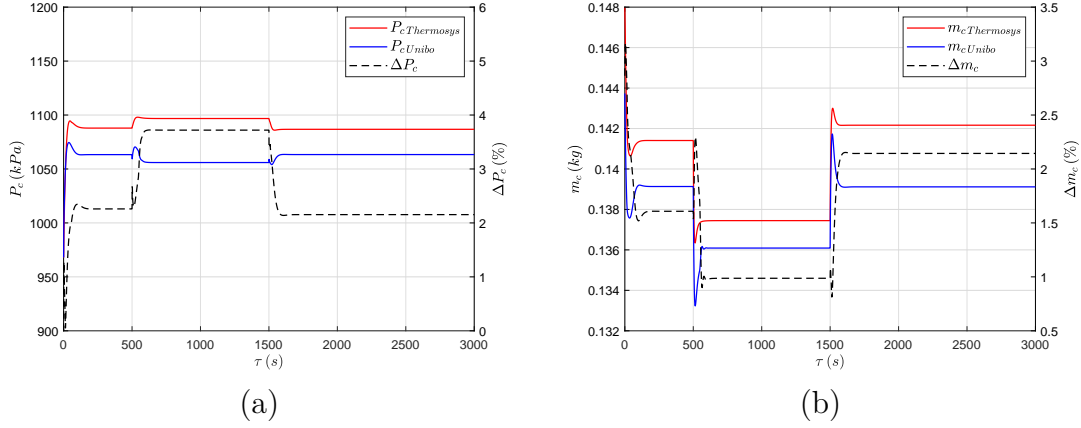


Figure 4.8: Condensation pressure (a) and refrigerant mass (b) in the finned-tube condenser model verification: comparison between Thermosys[®] and Unibo in Test1.

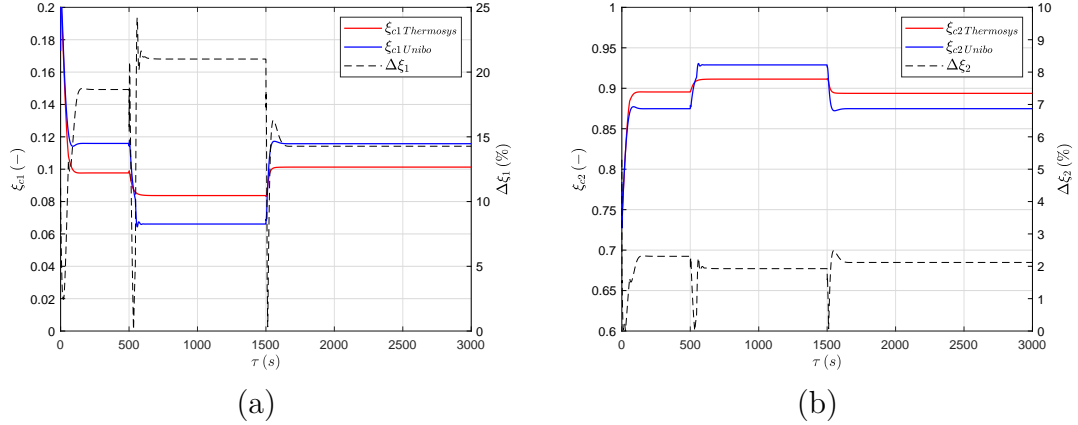


Figure 4.9: Non-dimensional extension of the V (a) and TP (b) regions in the finned-tube condenser model verification: comparison between Thermosys[®] and Unibo in Test 1.

the V and TP regions in the condenser. The qualitative trends are basically the same for the Thermosys[®] and Unibo models, with the last one which appears more sensitive to the variation in the valve opening. A possible cause can be found in differences in the heat transfer coefficients calculation. The V region decreases when the valve opening is increased, because the enthalpy of

the refrigerant at the outlet of the compressor decreases as a subsequence of the reduction in the pressure ratio, and the heat transfer coefficients increase because of the enhancement of the refrigerant mass flow rate. Moreover, the length of the TP region increases, because of the enhancement of the condensation heat transfer rate, due to the higher refrigerant mass flow rate.

As shown in Fig. 4.10 (a), the extension of the TP region makes the subcooling disappear when the valve opening is increased. Also, it can be noticed how the Thermosys[®] model does not return the same value of ΔT_{sc} when the valve returns to its initial value, whilst the results obtained through the Unibo model showed better repeatability. Fig. 4.10 (b) shows the air temperature at the outlet of the condenser: the results obtained by the two models are practically the same.

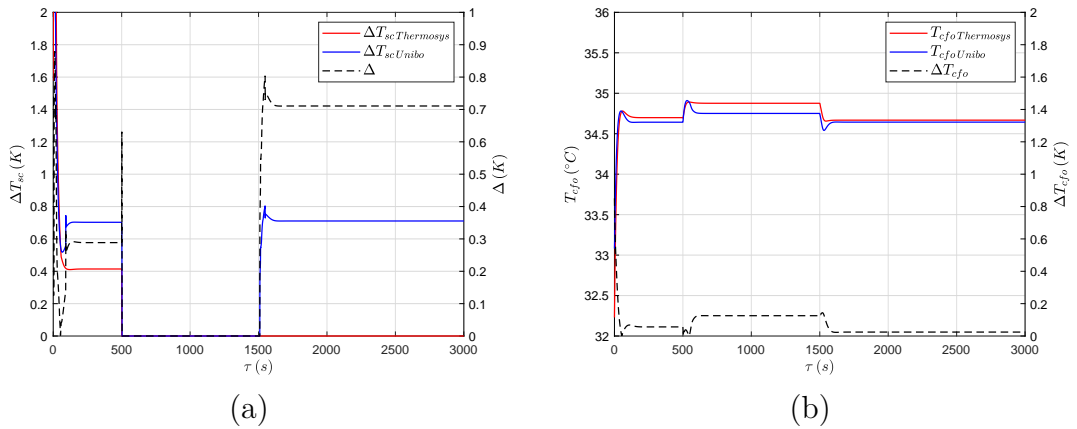


Figure 4.10: Refrigerant subcooling (a) and air outlet temperature (b) in the finned-tube condenser model verification: comparison between Thermosys[®] and Unibo in Test 1.

4.4.2 Results for Test 2

In this subsection the results obtained for the condenser in Test 2 are presented. Figure 4.11 reports the trends of the condensation pressure (a) and the refrigerant mass (b). The higher speed of the compressor in the central part of the simulation produces an increase of the pressure and the refrigerant content. Percentage deviations below 2.5% are highlighted between the pressure and the refrigerant mass predicted by the two models. The results for the non-dimensional lengths are reported in Fig. 4.12, which highlight an increase in the extension of the V region and a decrease of the TP region for both models. This behaviour is caused by the increase in the compression ratio which makes the isentropic efficiency of the compressor decrease; subsequently the refrigerant enthalpy at the inlet of the condenser increases. The length of the TP region diminishes as a consequence, also because of the improvement in the heat transfer conditions due to the higher mass flow rate and temperature difference between the refrigerant and the secondary fluid.

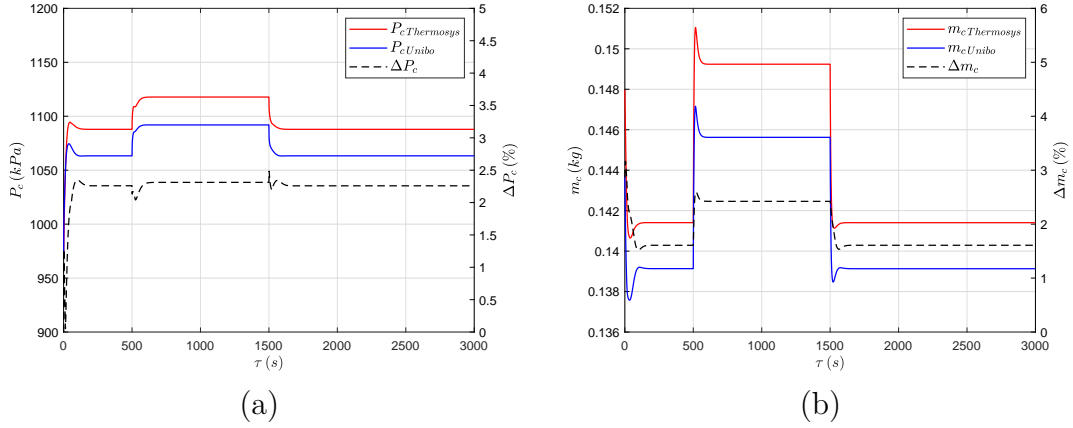


Figure 4.11: Condensation pressure (a) and refrigerant mass (b) in the finned-tube condenser model verification: comparison between Thermosys® and Unibo in Test2.

As shown in Fig. 4.13 (a) both models predict a higher degree of subcooling when the compressor speed gets its higher values. Indeed, the existence of the liquid phase is facilitated by the higher values of the condensation pressure. Figure 4.13 (b) shows the trend of the air outlet temperature, which slightly increases when the compressor speed steps from 1500 to 1800 rpm, because a higher thermal power must be released from the condenser. The response of the two models is practically identical.

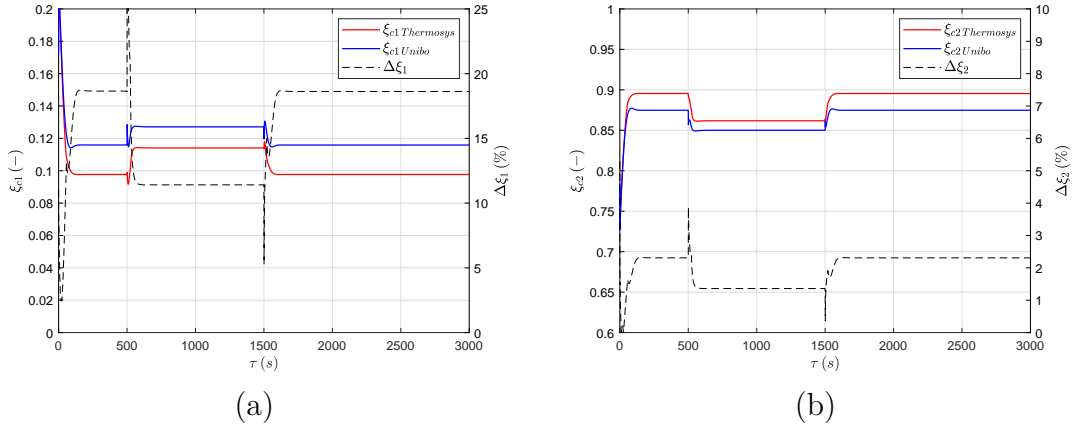


Figure 4.12: Non-dimensional extension of the V (a) and TP (b) regions in the finned-tube condenser model: comparison between Thermosys® and Unibo in Test 2.

4.5 Verification of the air-to-air machine model

In this section the results obtained for the in-house models of the EEV and heat exchangers connected to the Thermosys® compressor model will be presented.

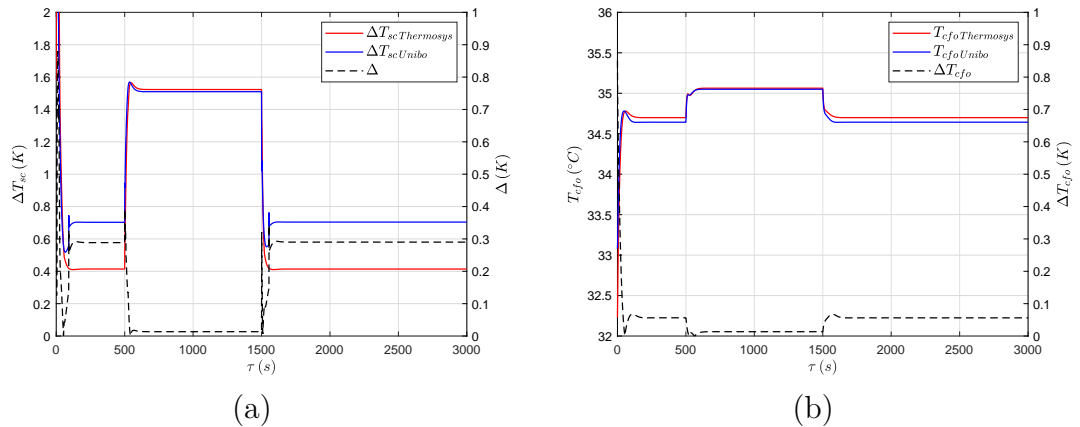


Figure 4.13: Refrigerant subcooling (a) and air outlet temperature (b) in the finned-tube condenser model verification: comparison between Thermosys® and Unibo in Test 2.

The results are based on the same tests presented in section 4.3.

4.5.1 Results for Test 1

Figure 4.14 shows the trends of the evaporation and condensation pressure in the heat exchangers obtained with the Unibo and Thermosys® models, highlighting a good match between the two responses. The percentage deviation between the two models is indeed below 3.5% and 6.5% for the condensation and evaporation pressure respectively. In this case, as shown in Fig. 4.14 (a), both the Unibo and the Thermosys® models predict a pressure increase at the condenser, differently to the results obtained in the stand-alone verification of the finned-tubes condenser (see section 4.4.1). This can be due to the higher pressure increase at the evaporator shown by the Unibo model (see Fig. 4.14 (b)) together with the almost constant pressure ratio across the reciprocating compressor valves, consistently to what discussed in section 4.4.1.

The refrigerant mass flow rate across the EEV is reported in Fig. 4.15 (a). As expected, increasing the opening degree of the valve leads to an increase of the refrigerant mass flow rate. The Unibo model appears more sensitive than Thermosys®, but the qualitative trend of the two is very similar. The maximum deviation is about 8%. Figure 4.15 (b) depicts the trend of the refrigerant mass m_{tot} contained in the evaporator and the condenser, showing how it is not conserved by Thermosys® once the sudden step valve opening occurs, although the variation of the total mass is small. The percentage deviation in the prediction of the refrigerant mass is below 2%.

The refrigerant subcooling ΔT_{sc} and superheating ΔT_{sh} at the outlet of the heat exchangers are shown in Fig. 4.16. It can be seen how the Unibo model predicts a null subcooling during the whole simulation, proving a better repeatability than Thermosys®, whose value of ΔT_{sc} drops to zero when the valve opens and never reverts to the initial value once the valve resumes its

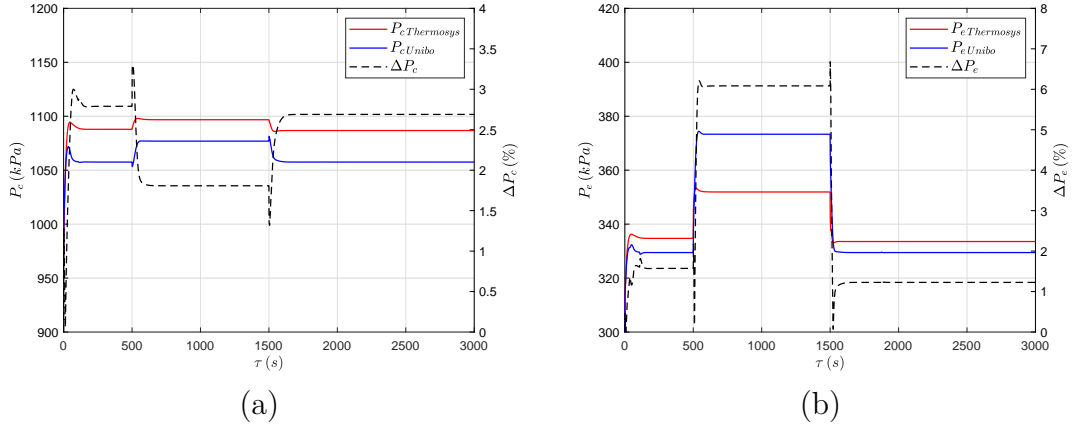


Figure 4.14: Condensation (a) and evaporation (b) pressure in the verification of the air-to-air machine: comparison between Thermosys[®] and Unibo in Test1.

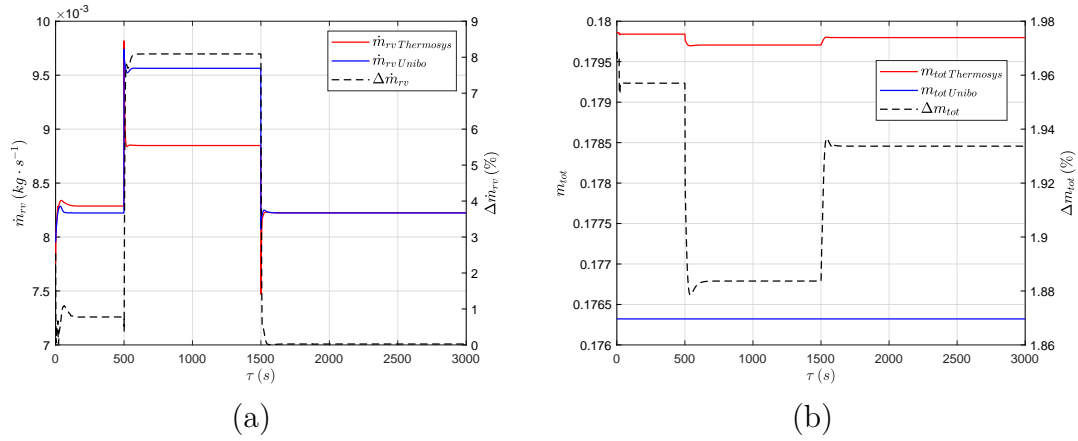


Figure 4.15: Refrigerant mass flow rate through the EEV (a) and global refrigerant mass (b) in the verification of the air-to-air machine: comparison between Thermosys[®] and Unibo in Test1.

initial opening. Similar considerations hold for superheating; contrary to the Unibo model, Thermosys[®] gives different values of ΔT_{sh} before $\tau = 500$ s and after $\tau = 1500$ s although boundary conditions are the same. Neglecting the spikes in correspondence of the sudden variations, deviations lower than 0.5 K and 1.5 K are highlighted for ΔT_{sc} and ΔT_{sh} respectively.

Figure 4.17 shows the results for the air outlet temperatures T_{cfo} and T_{efo} . Both at the condenser and at the evaporator an increase in the outlet temperature is shown once the valve opens ; indeed, the higher pressures obtained between $\tau = 500$ s and $\tau = 1500$ s involve higher saturation temperatures of the refrigerant and thus higher mean wall temperatures.

4.5.2 Results for Test 2

Figure 4.18 shows the trends of the refrigerant mass flow rate across the EEV (a) and the total refrigerant charge (b) in the two heat exchangers obtained

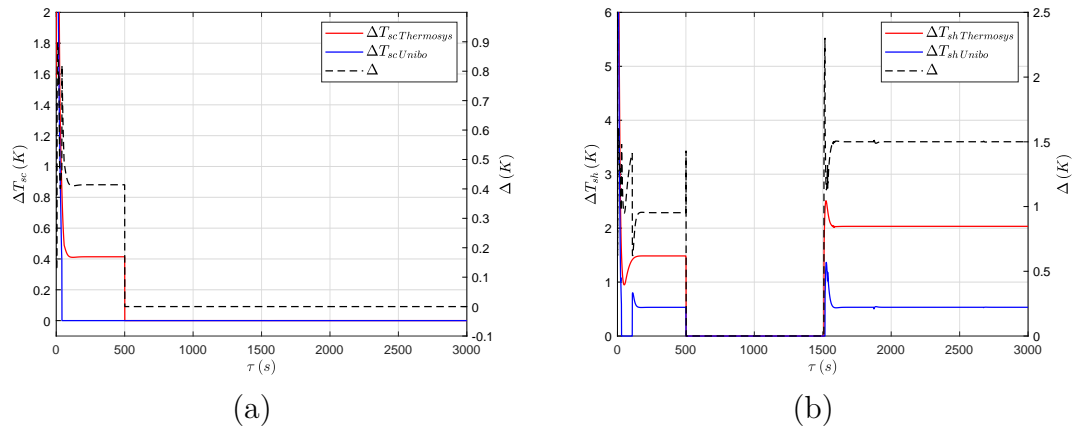


Figure 4.16: Refrigerant subcooling (a) and superheating (b) in the verification of the air-to-air machine: comparison between Thermosys[®] and Unibo in Test1.

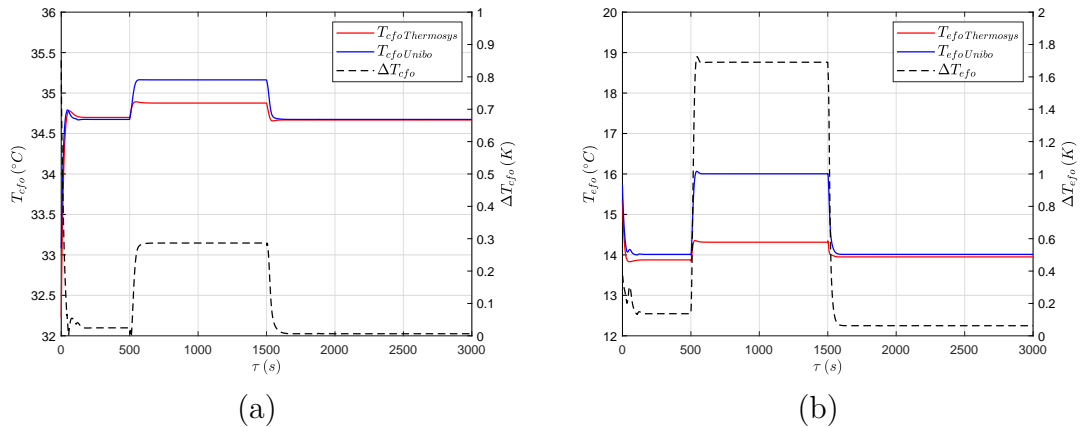


Figure 4.17: Air outlet temperatures at the condenser (a) and at the evaporator (b) in the verification of the air-to-air machine: comparison between Thermosys[®] and Unibo in Test1.

in Test 2. As expected, increasing the rotational speed leads to an increase in the refrigerant mass flow rate. The response of the two models is very similar, with deviations below 1.7%. As for the total refrigerant charge, the deviation between the Unibo and Thermosys[®] model is below 2%. In this case, also the Thermosys[®] model is conservative, since no zones disappearance occurs during the simulation carried out using the library developed by the University of Illinois.

The results obtained for the condensation and evaporation pressure are shown in Fig. 4.19. The higher rotational speed of the compressor involves a higher heat transfer rate at the condenser, thus making the condensation pressure increase. At the evaporator the pressure decreases because part of the refrigerant is circulated to the high-pressure side of the loop. This leads to an increase of the pressure ratio which in turn increases the refrigerant mass flow rate across the valve, whose opening is kept fixed. The deviation between the two models

is below 3% for both the condenser and the evaporator.

Figure 4.20 shows the values of ΔT_{sc} and ΔT_{sh} . The increase in the con-

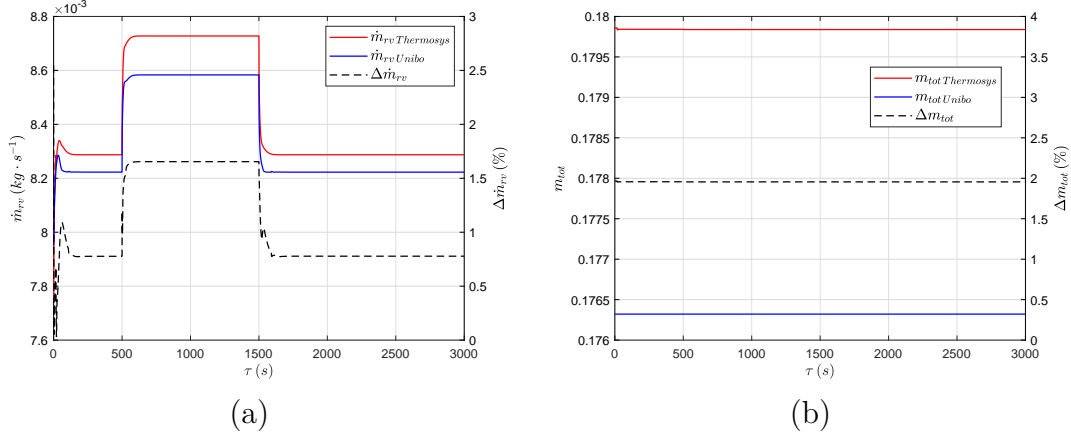


Figure 4.18: Refrigerant mass flow rate through the EEV (a) and global refrigerant mass (b) in the verification of the air-to-air machine: comparison between Thermosys[®] and Unibo in Test2.

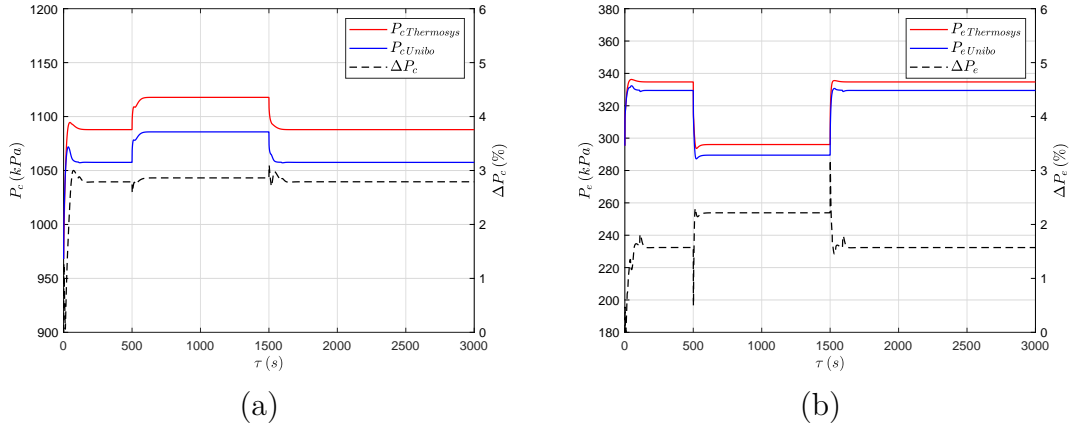


Figure 4.19: Condensation (a) and evaporation (b) pressure in the verification of the air-to-air machine: comparison between Thermosys[®] and Unibo in Test2.

condensation pressure and in the heat transfer rate involves higher degrees of subcooling, as shown in Fig. 4.20 (a); similarly, the lower amount of refrigerant charge at the evaporator between $\tau = 500$ s and $\tau = 1500$ s makes the superheating increase as reported in Fig. 4.20 (b). The maximum deviation between the two models is below 0.6 K for ΔT_{sc} and below 1.5 K for ΔT_{sh} . The results obtained for the air outlet temperature are reported in Fig. 4.21. Since the condensation heat transfer rate is higher at high rotational speed, the air outlet temperature at the condenser increases. Also at the evaporator the heat transfer rate increases between $\tau = 500$ s and $\tau = 1500$ s, thus cooling the air exiting the heat exchanger. The dynamic response of the two models is practically identical both at the condenser and the evaporator.

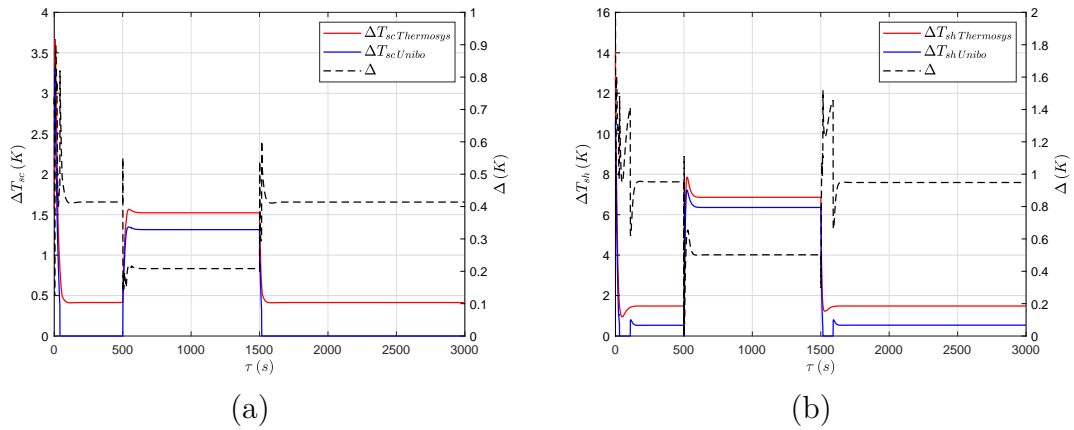


Figure 4.20: Refrigerant subcooling (a) and superheating (b) in the verification of the air-to-air machine: comparison between Thermosys[®] and Unibo in Test2.

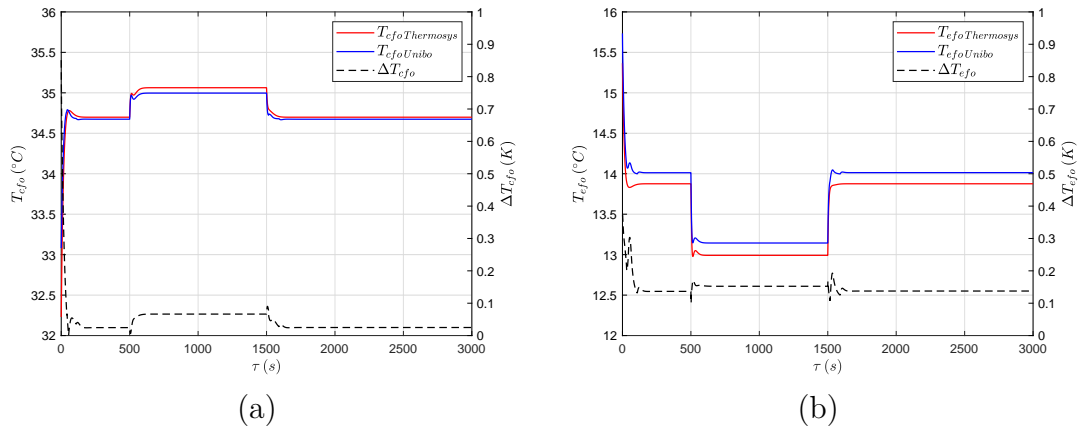


Figure 4.21: Air outlet temperatures at the condenser (a) and at the evaporator (b) in the verification of the air-to-air machine: comparison between Thermosys[®] and Unibo in Test2.

4.6 Conclusions

A numerical verification of the in-house models of the finned-tube heat exchangers and the EEV was carried out using the library Thermosys[®] as a benchmark software. Although the library developed by the University of Illinois at Urbana-Champaign includes all the fundamental components of a vapour-compression refrigerating machine, some drawbacks (e.g. no electric power consumption available in the compressor model, numerically forced behaviour of the heat exchangers under certain conditions like machine off-duty) limit its use in transient energy analysis. The models of the EEV and the finned-tube heat exchangers were verified as stand-alone components at first. As for the electronic valve, the Unibo and Thermosys[®] models give a very similar responses, with deviations below 5% in the prediction of the refrigerant mass flow rate.

The individual verification of the evaporator and the condenser and the veri-

fication of the air-to-air machine (with the exception of the compressor) were carried out through two numerical tests characterized by sudden variations in the valve opening and the compressor speed, since these are among the most important controlled variable in refrigerating machines. The response of the Unibo and Thermosys[®] models was very similar. The main differences were highlighted in the prediction of the refrigerant superheating and subcooling at the outlet of the heat exchangers, since different heat transfer correlations may have been used in Thermosys[®], especially on the air side. The Unibo models proved more repeatability in the prediction of ΔT_{sc} and ΔT_{sh} and of the refrigerant charge.

The results obtained give a first proof of the in-house code reliability for the prediction of the main physical variables of a vapour-compression cycle and of its behaviour in transient conditions.

Chapter 5

Experimental Validation

In Chapter 4, the numerical verification of the models was presented, focusing on the main components of an air-to-air refrigerating machine, whose transient behaviour is often simulated through dynamic models using the SMB approach for the heat exchangers, as anticipated in section 2.2. From the literature review reported in the same section, it also emerges that the SMB approach is rarely used to simulate water chillers and that there is a lack of literature on the application of the SMB on the dynamic behaviour of brazed-plates heat exchangers (BPHE), which are of high interest because of their low volume which allows to contain the refrigerant charge. Moving from these considerations, the experimental validation of the models described in Chapter 2 was conducted considering a refrigerating machine which uses BPHEs as evaporator and condenser.

In this chapter, a comparison between experimental data measured on an existent water-to-water vapour-compression refrigerating machine and the numerical predictions of the in-house model is carried out to validate all the main components of a VCS (brazed-plate evaporator and condenser, EEV and compressor). In particular, the response of the model was analysed in terms of evaporation and condensation pressure, refrigerant outlet temperature, degrees of superheating and subcooling, secondary fluid outlet temperatures and COP.

In the first step the fully-open discharge coefficient C_{D0} in the valve model, the coefficients $C_{\dot{m}_r}$, $C_{\dot{W}_{el}}$, C_T and the time constant τ_k in the compressor model were tuned to match the experimental refrigerant mass flow rate, the compressor outlet enthalpy and the electric power consumption. Then, the evaporator, the EEV and the compressor were validated together and the correction parameters for the heat transfer coefficients C_{TP} , C_V and C_f in the evaporator were tuned to match the experimental evaporation pressure and the outlet conditions of the refrigerant and secondary fluid. Finally, the model of the whole machine with neither refrigerant receiver nor suction accumulator was validated and the correction parameters for the heat transfer coefficients C_V, C_{TP} , C_L and C_f in the condenser were tuned to improve the match with experimental data.

5.1 The machine and the experimental setup

The experimental facility used to validate the model is a heat pump located at the Polytechnic of Milan, shown in Fig. 5.1, and it is used to test low GWP refrigerants which represent alternatives to the widespread R134a [106, 107].



Figure 5.1: Experimental facility located at the Polytechnic of Milan.

The plant layout is shown in Fig. 5.2; it can be noticed how in addition to the four main elements required by the thermodynamic cycle, components are present which prevent system failure. In the suction line, an accumulator ensures a gas phase at the compressor inlet, whilst a liquid receiver placed at the outlet of the condenser prevents gas bubbles to enter the electronic expansion valve. Moreover, an oil separator is located between the compressor and the condenser, to remove the lubricant from the refrigerant flow and send it back to the compressor case.

Two auxiliary circuits are coupled with the refrigerating machine. In the hot circuit, the water is heated in the condenser and is then partly recirculated to the inlet, where it is possible to control the water outlet temperature through a three-way valve which mixes the flow with the water coming from a 500-litre tank. The main flow is then sent to the recuperator, where it exchanges heat with the cold circuit, and is further cooled down in an auxiliary heat exchanger, which through a chiller allows to counterbalance the electric power absorbed by the compressor. The water is then sent back to the tank. The configuration of the cold circuit is the same of the hot circuit except for the absence of the chiller. The fluid is a mixture of water and glycol ethylene with a glycol volume concentration of 25.4% and a freezing temperature of -12.6°C .

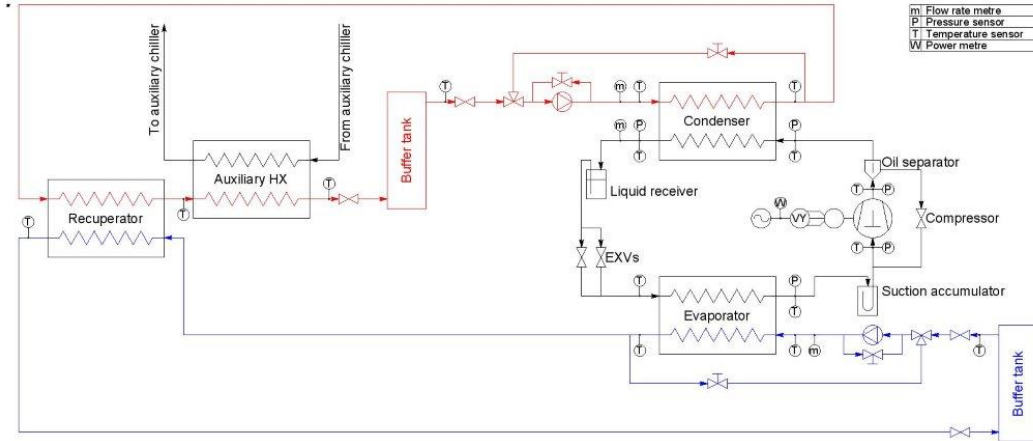


Figure 5.2: Layout of the experimental facility.

5.1.1 Components of the refrigerating machine

What follow is a brief description of the main components of the machine, namely the compressor, the evaporator, the condenser, the expansion device, the liquid receiver and the suction accumulator.

Compressor

The compressor is a Frascold D3-13.1Y VS semi-hermetic reciprocating compressor equipped with an inverter. The main compressor data are reported in Tab. 5.1. The polynomials z_m , z_W and z_T required for the compressor model can be easily obtained through the Frascold software available in the company web site.

Table 5.1: Frascold D3-13.1Y VS data.

Model	N of cylinders	Displacement at 50 Hz ($m^3 \cdot h^{-1}$)	Frequency (Hz)
D3-13.1Y VS	2	13.15	30-87

Evaporator and condenser

The evaporator and the condenser are brazed plate heat exchangers manufactured by Swep and their main characteristics are reported in Tab. 5.2.

Table 5.2: Evaporator and condenser data.

Model	No. of plates	Dimension (mm)	Max flow ($m^3 \cdot h^{-1}$)
B16Hx30	30	376 x 119	16.9
B10THx40	40	289 x 119	9

Expansion valve

In the facility two EEVs were installed in parallel, to ensure the safety of the cycle even with low refrigerant mass flow rates and cooling capacity. In particular, if the mass flow rate measured by the flow meter is smaller than the lower limit of the larger valve, the refrigerant is redirected to the smaller valve. The opening of the valves is controlled on the basis of the actual refrigerant superheating at the outlet of the evaporator, which is measured through temperature and pressure sensors at the outlet of the heat exchanger. The valves are E2V05 and E2V24 models manufactured by Carel, characterized by a cooling capacity of 1.4 kW and 16.9 kW respectively and by a maximum operating pressure of 45 bar. In the experiments, only the E2V24 valve was operated. The refrigerant mass flow rate across the EEV can be evaluated through Eq. 5.1, which was supplied by the manufacturer and implemented into the valve model. C_{D0} is the full-aperture discharge coefficient whose value was tuned to match experimental data, L is a valve parameter which in this case was equal to 0.9, and p is the actual valve opening fraction, ranging from 0.1 to 1. Equation 5.1 can be easily cast into the form of Eq. 2.185.

$$\dot{m}_{r\ valve} = \frac{\rho_{ri} C_{D0} 0.1^{\frac{L-(p-0.1)}{L}} \sqrt{1000 \rho_{ri} (P_i - P_o)}}{3600^2} \quad (5.1)$$

Liquid receiver

The liquid receiver is installed to face conditions different from those of design. In this facility a 2.8 liters Frigomec product was chosen.

Suction accumulator

Between the evaporator and the compressor a suction accumulator is installed to prevent liquid refrigerant to enter the compressor. On the machine at the Polytechnic of Milan, an Emerson accumulator with a capacity of 2.33 liters was installed.

5.1.2 Measurement instrumentation

In the following, the measurement instruments used in the facility will be described.

Refrigerant mass flow rate

The refrigerant mass flow rate is measured at the outlet of the condenser through an Endress-Hauser Proline Promass E300 flow meter based on the Coriolis effect. The location of the sensor was chosen to prevent loss of accuracy when in contact with two-phase fluids and to avoid contact with refrigerant at maximum temperature and with oil. Table 5.3 reports the main characteristics of the refrigerant flow meter.

Table 5.3: Data of the Endress-Hauser mass flow meter for the refrigerant.

Model	Range ($kg \cdot h^{-1}$)	Uncertainty	Output (mA)
Proline Promass E300	0-300	$\pm 0.15\% r.v.$	4-20

Refrigerant pressure

The pressure of the refrigerant is measured at the inlet/outlet of the compressor and the condenser through Huba Control 520 sensors, whose characteristics are reported in Tab. 5.4.

Table 5.4: Data of the Huba sensors for the refrigerant pressure.

Model	Pressure	Range (bar)	Uncertainty	Output (mA)
Huba Control 520	High	0-40	$\pm 0.3\% r.v.$	4-20
Huba Control 520	Low	0-9	$\pm 0.3\% r.v.$	4-20

Temperature

Temperature measurements are carried out at the inlet/outlet of each heat exchanger, both on the refrigerant and secondary fluid side, and at the suction/discharge of the compressor. The sensors installed are RTD Pt100 produced by Carel and calibrated through a thermostatic bath. Table 5.5 shows the main characteristics of the temperature sensors.

Table 5.5: Data of the Huba sensors for the refrigerant pressure.

Model	Range ($^{\circ}C$)	Uncertainty	Output (mA)
Carel Pt100	-10 - 110	$\pm 0.15\% r.v.$	Auto

Compressor electric power absorption

The power absorbed by the compressor is measured by means of a CEWE power transducer, whose characteristics are reported in Tab. 5.6.

Table 5.6: Data of the Huba sensors for the refrigerant pressure.

Model	Uncertainty	Output (mA)
CEWE DPT221-401	$\pm 0.2\% r.v.$	4-20

Secondary fluid mass flow rate

The mass flow rate of the secondary fluids is measured through Huba Control instruments placed at the discharge section of each pump, measuring the volumetric flow rate and the temperature. The characteristics of the instruments are reported in Tab. 5.7

Table 5.7: Data of the Endress-Hauser mass flow meter for the refrigerant.

Model	Range ($l \cdot \text{min}^{-1}$)	Uncertainty	Output (mA)
Huba Control 210	3.5-50	$\pm 0.2\%$ <i>r.v.</i>	4-20

Data acquisition

National Instrument data acquisition boards were used to collect data with a sampling rate of 1 s.

Table 5.8: National Instrument boards for data acquisition.

Signal	Board
4-20 mA in	cDAQ-9208
RTD in	cDAQ-9217
0-10 V in	cDAQ-9205
0-10 V out	cDAQ-9264

5.2 Experimental campaign

In the experimental campaign, the zeotropic mixture R450a was used as a refrigerant in substitution of R134a. Two types of transients were investigated through two different tests, characterized by imposing a sudden variation in the EEV opening (Test 1) and in the compressor speed (Test 2) respectively, since they represent the main controlled variables in a vapour compression refrigerating machine. The perturbations in both tests were applied once the system had reached steady state. Moreover, in both tests the electronic expansion valve and the three-way valves on the secondary fluid circuits were manually controlled, thus letting the degree of superheating at the outlet of the evaporator and the secondary fluid outlet temperatures vary on the basis of the working conditions.

5.2.1 Test 1: steps in the valve opening

Table 5.9 reports the characteristics of Test 1. The values of the percentage valve opening were chosen to ensure a gas phase at the inlet of the compressor.

Table 5.9: Characteristics of Test 1.

Time period (s)	Valve Opening (%)
0-1420	39.6%
1421-3450	33.3%
3451-5000	39.6%

Figure 5.3 shows the refrigerant mass flow rate measured at the condenser outlet $\dot{m}_{r\,exp}$. It can be noticed how a sudden decrease of the valve opening from 39.6% to 33.3% causes a reduction in the refrigerant mass flow rate of about 12.5%.

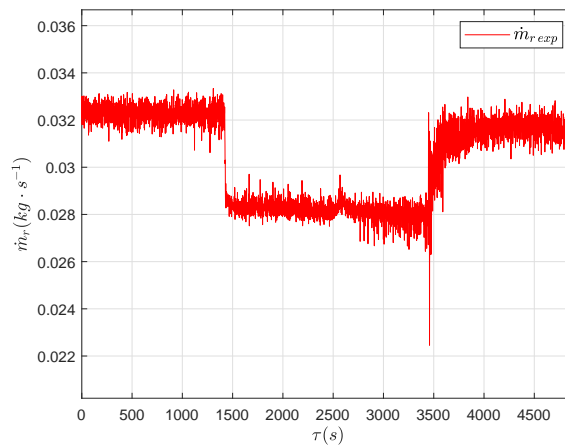


Figure 5.3: Measured refrigerant mass flow rate during Test 1.

As shown in Fig. 5.4 (a), when the refrigerant mass flow rate is reduced, the pressure in the evaporator decreases, mainly because of the smaller amount of mass flowing through the heat exchanger. In Fig. 5.4 (b) the pressure at the compressor outlet and condenser inlet and outlet is plotted. Also in this case, a pressure reduction can be noticed, since the power to be discharged through the condenser decreases. The first reason for this is the reduction in the electric power absorbed by the compressor shown in Fig. 5.5, due to the lower mass flow rate to circulate. Moreover, the reduction in the temperature drop for the water-glycol mixture at the evaporator underlined in Fig. 5.6 (a) contributes to reduce the cooling load and thus the energy to dissipate at the high pressure side. In addition, the temperature of the water at the condenser inlet decreases because of the mixing process in the three-ways valve, subsequently reducing the condensation pressure (see Fig. 5.6 (b)). As expected, the pressure decreases when moving from the compressor discharge section to the condenser outlet. Since the models of the heat exchangers are devised with the assumption of isobaric transformations, the pressure at the compressor suction and discharge sections will be taken as a reference in the

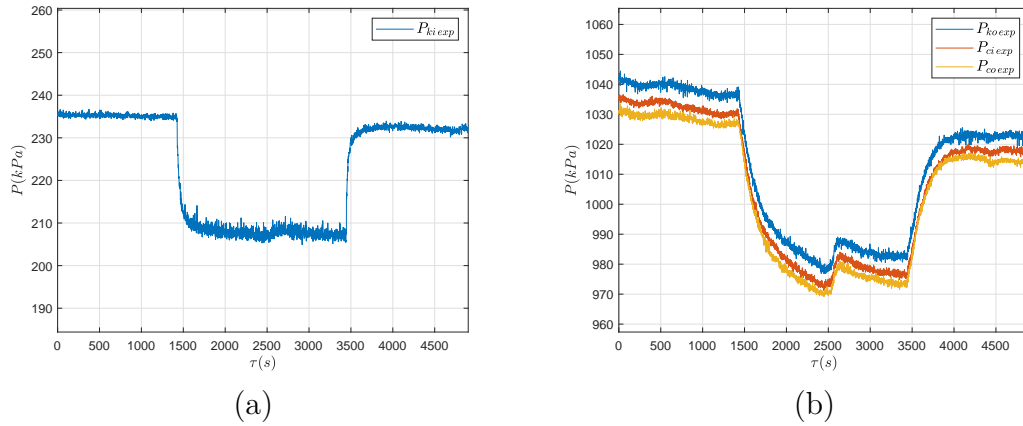


Figure 5.4: Measured pressures during Test 1. (a) Compressor Inlet. (b) Compressor outlet, condenser inlet and outlet.

comparison between numerical and experimental data.

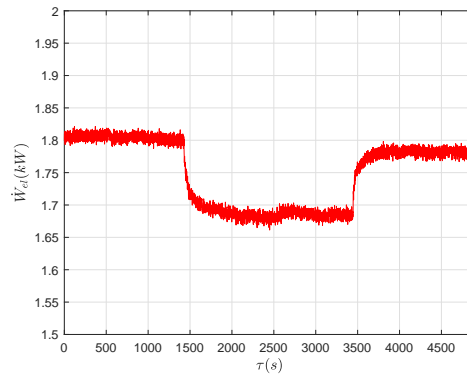


Figure 5.5: Electric power absorbed by the compressor during Test 1.

The temperatures of the refrigerant at the outlet of the heat exchangers and the degrees of superheating and subcooling are reported in Fig. 5.7. The reduction of the evaporation pressure and of the refrigerant mass flow rate, together with the increase in the water-glycol inlet temperature cause a significant increase in the superheating (from 10.5 K to 16.5 K). As for the subcooling, a slight increase of about 0.5 K is underlined.

Figure 5.8 shows the experimental mass flow rate of the secondary fluids in the evaporator (a) and the condenser (b), \dot{m}_{fe} and \dot{m}_{fc} . The average of the measured data, $\dot{m}_{fe,smooth}$ and $\dot{m}_{fc,smooth}$, will be used as inputs for the models of heat exchangers.

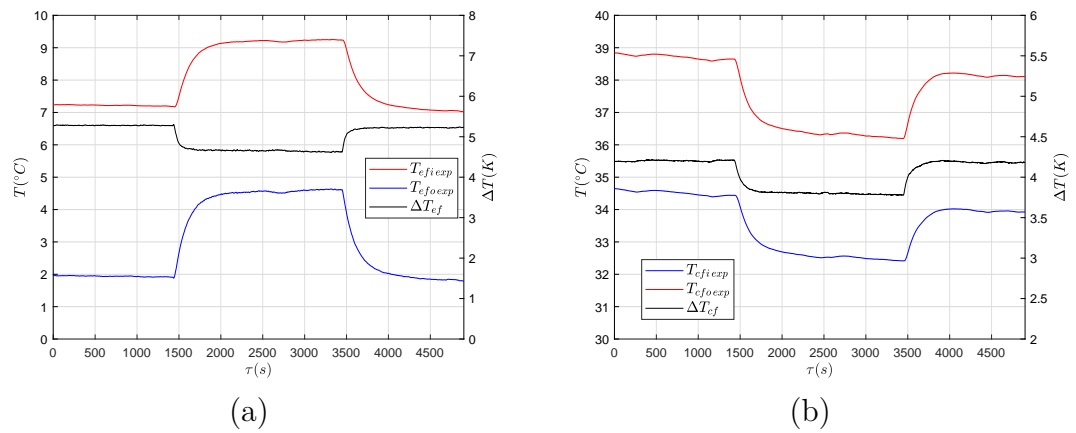


Figure 5.6: Inlet and outlet temperatures of the water-glycol mixture at the evaporator (a) and of the water at the condenser (b) during Test 1.

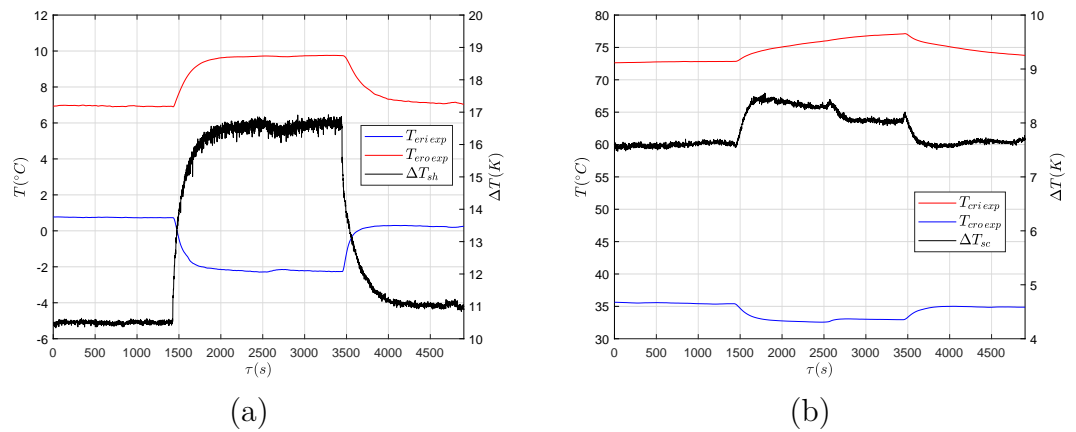


Figure 5.7: Measured refrigerant temperatures, superheating and subcooling during Test 1. (a) Evaporator. (b) Condenser.

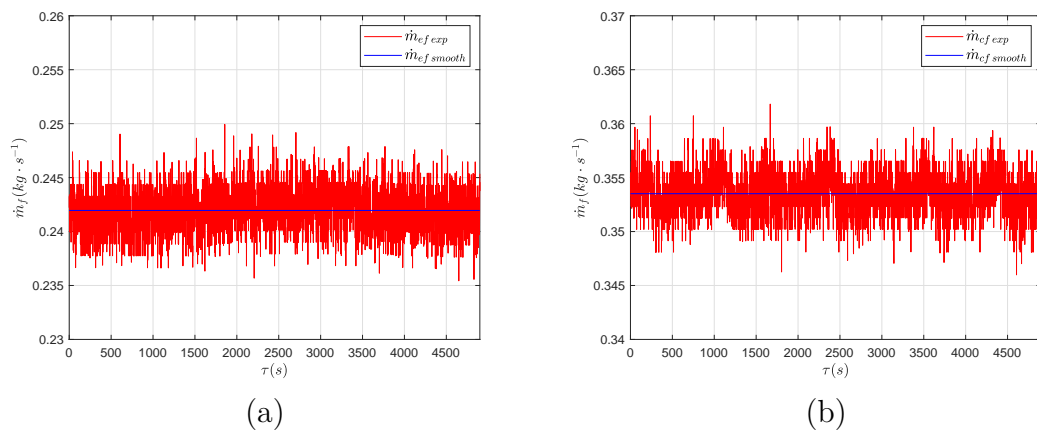


Figure 5.8: Measured mass flow rate of water-glycol mixture at the evaporator (a) and of the water at the condenser (b) during Test 1.

5.2.2 Test 2: steps in the compressor frequency

Table 5.10 reports the characteristics of Test 2, where steps in the compressor frequency were imposed. The variations in the measured mass flow rate of the

Table 5.10: Characteristics of Test 2.

Time period (s)	Compressor Frequency (Hz)
0-1220	50
1221-3334	65
3335-5100	50

refrigerant is shown in Fig. 5.9: with a 30% increase in the frequency, the mass flow rate increases 2.1% only. Indeed, the effects due to the frequency increase are counterbalanced by the strong decrease in the evaporation pressure shown in Fig. 5.10 (a), and by the increase in the superheating at the outlet of the evaporator, Fig. 5.13, which cause a strong reduction in the refrigerant density at the compressor inlet. Whilst the pressure at evaporator decreases, the condensation pressure increases (see Fig. 5.10 (b)); this is mainly due to the transfer of refrigerant mass from the low to the high pressure side and to the increase in the thermal power to be exchanged at the condenser. In fact, the increase in the compressor frequency involves both an increase in the electric power absorbed (see Fig. 5.11) and a slight increase in the cooling power exchanged at the evaporator (see the temperature drop for the water-glycol mixture in Fig. 5.12 (a)). Moreover, the inlet temperature of water at the condenser increases thus contributing to the raise of pressure (see Fig. 5.12 (b)).

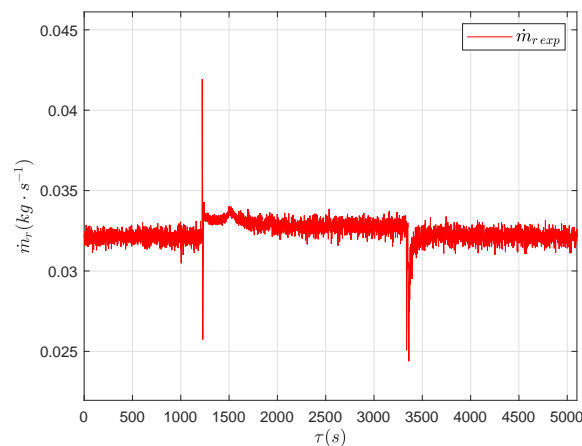


Figure 5.9: Measured refrigerant mass flow rate during Test 2.

As for the outlet conditions of the refrigerant, Fig. 5.13 shows the temporal trend of the outlet temperatures and of the degree of superheating and

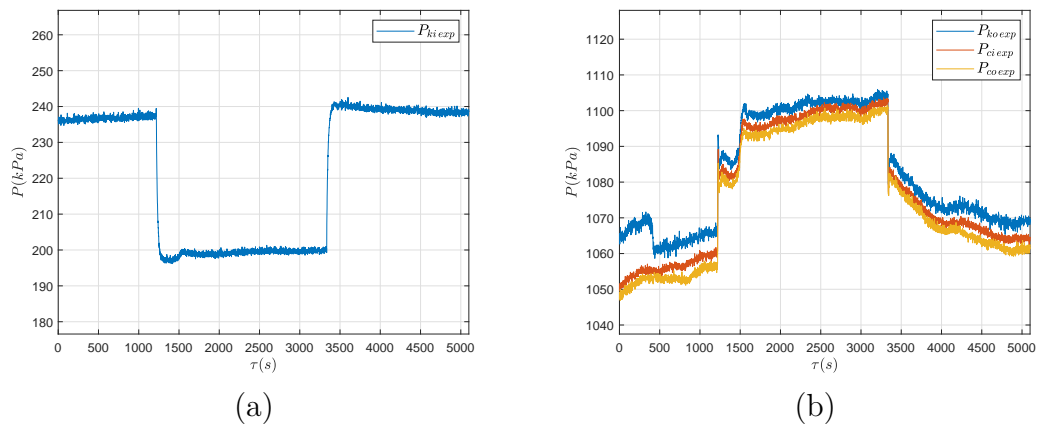


Figure 5.10: Measured pressures during Test 2. (a) Compressor Inlet. (b) Compressor outlet, condenser inlet and outlet.

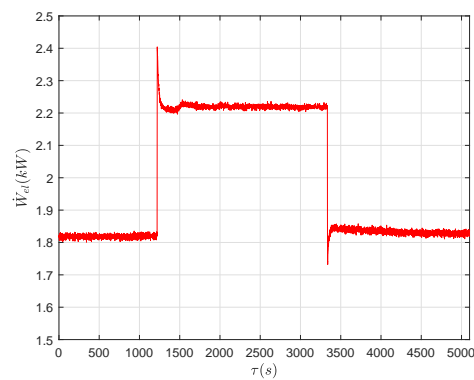


Figure 5.11: Electric power absorbed by the compressor during Test 2.

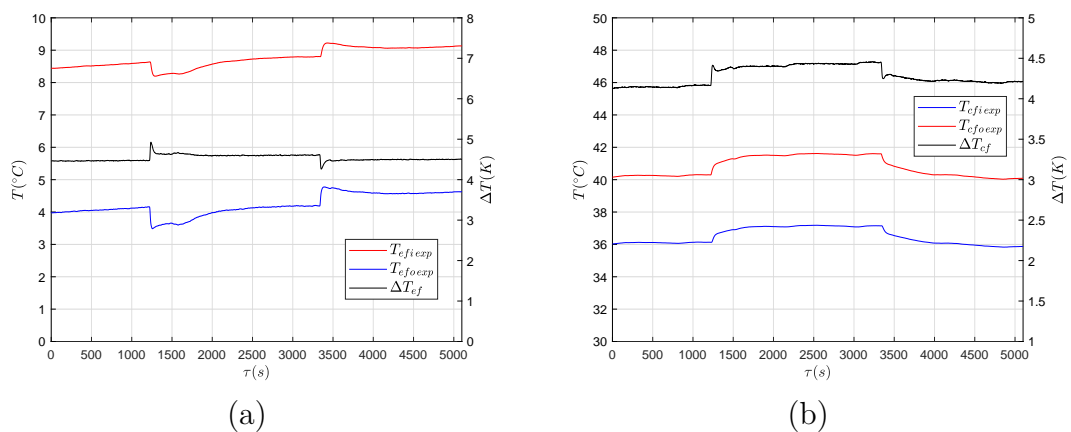


Figure 5.12: Inlet and outlet temperatures of the water-glycol mixture at the evaporator (a) and of the water at the condenser (b) during Test 2.

subcooling. The rise of the degree of superheating from 12 K to 17 K is mainly due to the slight increase in the cooling power and the decrease in the evaporation pressure that widens the temperature difference between the refrigerant

and the secondary fluid. As for the subcooling, sudden variations, yet within 1 K , are highlighted when steps in frequency occur.

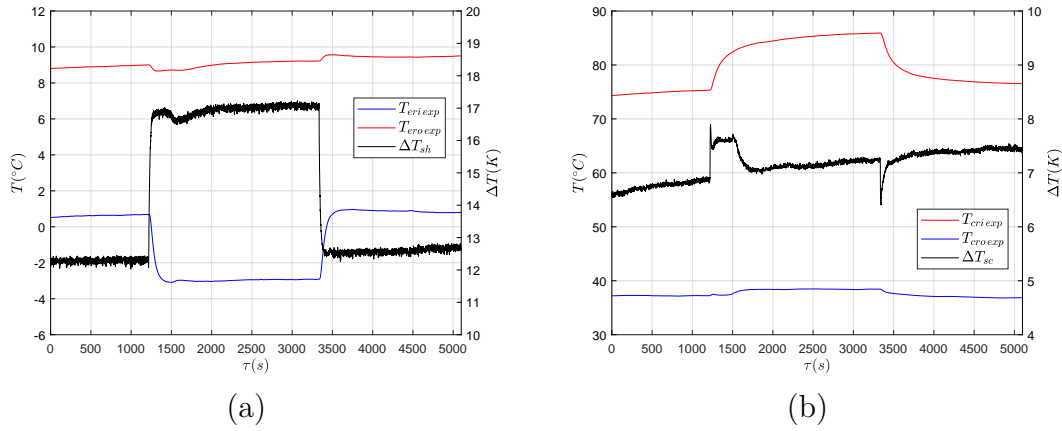


Figure 5.13: Measured refrigerant temperatures, superheating and subcooling during Test 2. (a) Evaporator. (b) Condenser.

Figure 5.14 shows the trends of the secondary fluids mass flow rates; also in this case, the average of the experimental values was calculated to be used as model input in the validation procedure.

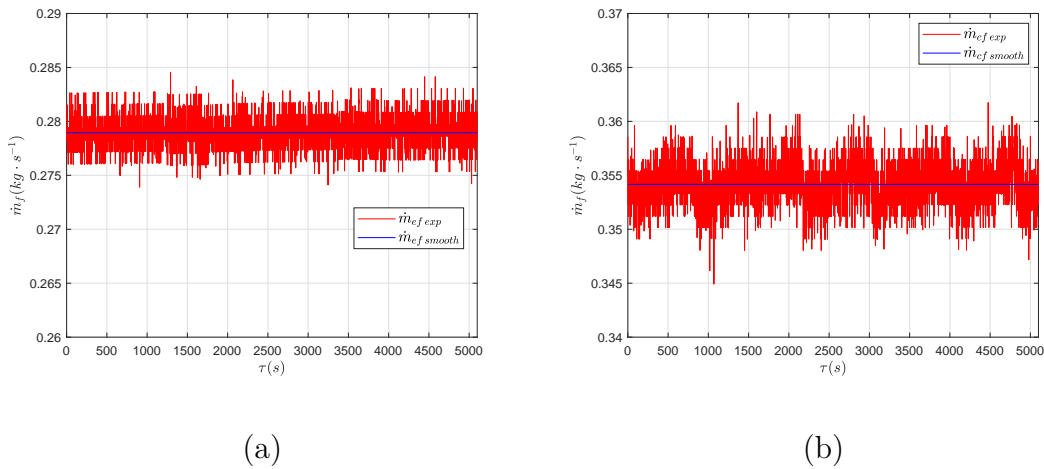


Figure 5.14: Measured mass flow rate of water-glycol mixture at the evaporator (a) and of the water at the condenser (b) during Test 2.

5.3 Valve tuning and validation

The first step in the validation procedure of the vapour compression refrigerating machine was the tuning of the EEV model. In particular, the fully-open discharge coefficient C_{D0} was manually adjusted to optimize the match between the numerical and the experimental mass flow rate of the refrigerant, using Test 1 as a reference, since it directly involves variations in the valve

opening. The starting value of C_{D0} was set to 0.25, as suggested by the manufacturer.

5.3.1 Validation under Test 1 conditions

Figure 5.15 shows a comparison between the experimental and predicted refrigerant mass flow rate across the valve and the percentage deviation under Test 1 conditions and with $C_{D0} = 0.25$. Although the qualitative trend of the predicted mass flow rate reflects the experimental one, it can be noticed how the numerical values grossly underestimate the experimental ones, with percentage deviations slightly below 60%, thus mandating some tuning.

Figure 5.16 shows the results obtained for the validation under Test 1 condi-

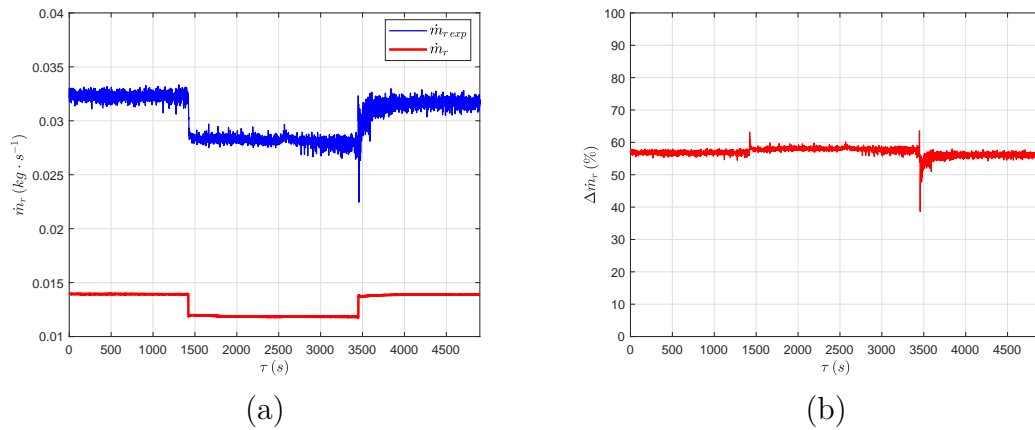


Figure 5.15: Validation of the valve model. Comparison between the experimental mass flow rate and the value predicted by the valve model (a) and percentage deviation (b) with $C_{D0} = 0.25$ under Test 1 conditions.

tions after manual tuning with $C_{D0} = 0.58$, highlighting a good correspondence between numerical and experimental data under both test conditions. In particular, with the exception of the spikes in correspondence of the sudden steps, the maximum percentage deviation is always below 7.5%.

5.3.2 Validation under Test 2 conditions

Figure 5.17 shows the results obtained for the mass flow rate through the valve under Test 2 conditions and with $C_{D0} = 0.25$. As already seen for Test 1, the qualitative trend of the mass flow rate is captured by the model with significant deviations.

After the tuning procedure ($C_{D0} = 0.58$), the results shown in Fig. 5.18 are obtained, with a percentage deviation always lower than 7%, with the exceptions of the spikes highlighted when the steps in the compressor frequency occur.

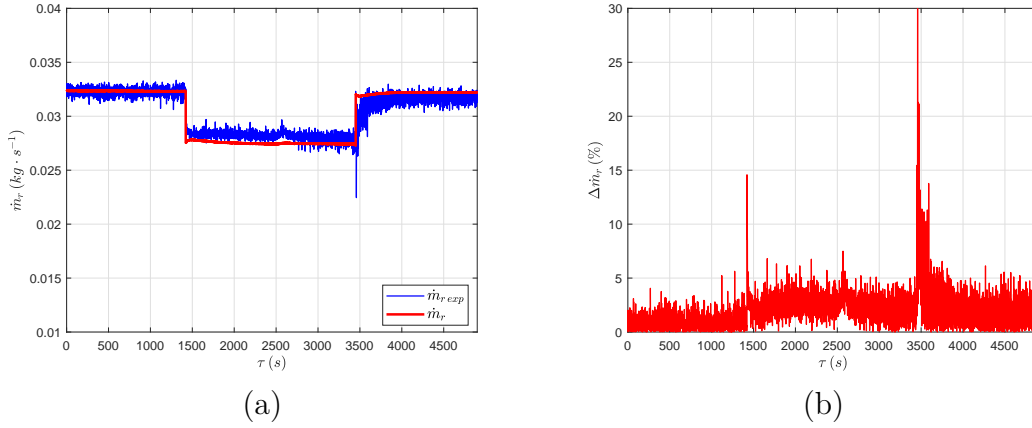


Figure 5.16: Validation of the valve model. Comparison between the experimental mass flow rate and the value predicted by the valve model (a) and percentage deviation (b) with $C_{D0} = 0.58$ under Test 1 conditions.

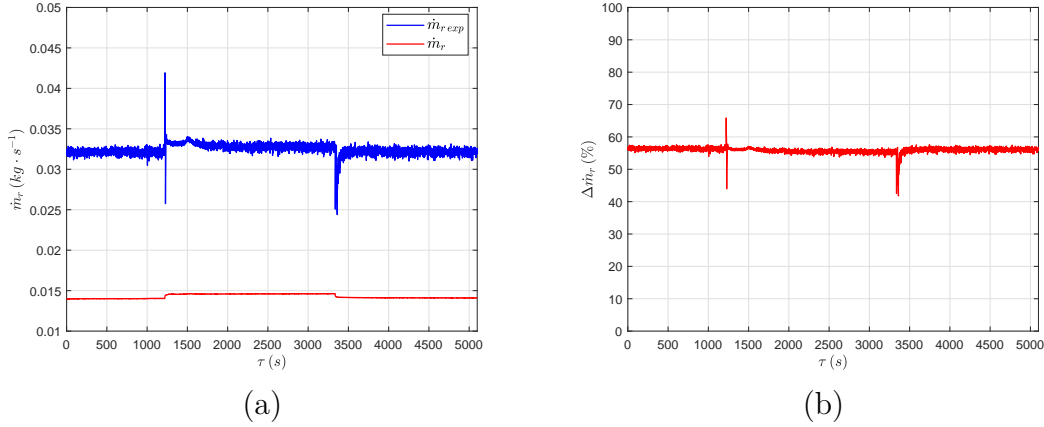


Figure 5.17: Validation of the valve model. Comparison between the experimental mass flow rate and the value predicted by the valve model (a) and percentage deviation (b) with $C_{D0} = 0.25$ under Test 2 conditions.

5.4 Compressor tuning and validation

The second step in the experimental validation consisted of the tuning of the compressor time constant τ_k required in the determination of the outlet enthalpy through the approximation of a first-order dynamic system. To this aim, the experimental temperature at the discharge section of the compressor during Test 2 was used, thus calculating the time constant for a step variation in the rotational frequency. The value obtained was then employed to validate the model under Test 1 too.

With reference to Fig. 5.19, where τ_i and τ_f are the times corresponding the first and second frequency step respectively, the time constant τ_k was determined on the basis of the definition given for first-order dynamic systems [35]. In particular, τ_k can be defined as the time required to reach the 63% of the steady state value, which in this case has been assumed equal to the temper-

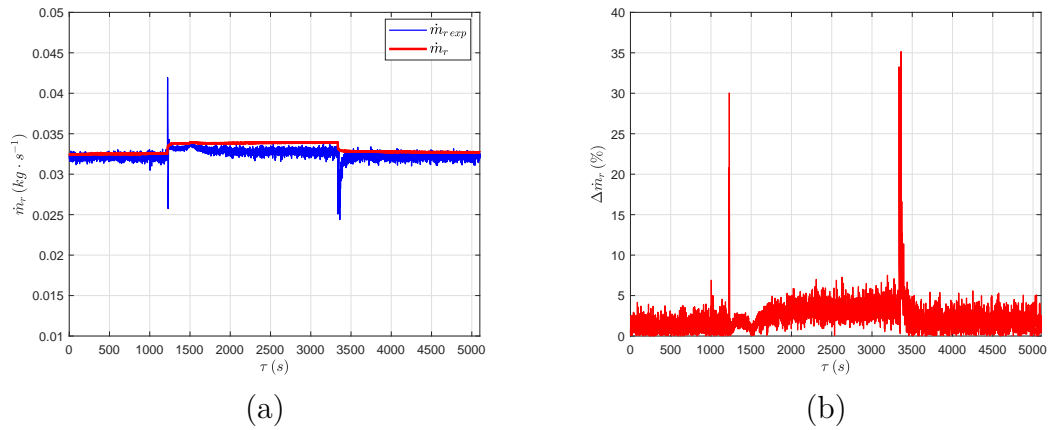


Figure 5.18: Validation of the valve model. Comparison between the experimental mass flow rate and the value predicted by the valve model (a) and percentage deviation (b) with $C_{D0} = 0.58$ under Test 2 conditions.

ature at τ_f . The value obtained for τ_k was 170 s.

After the determination of τ_k , the model of the compressor presented in

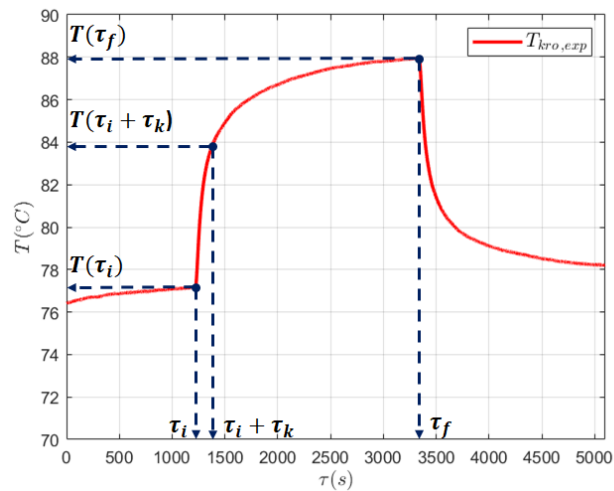


Figure 5.19: Refrigerant temperature at the compressor discharge section in Test 2. The steps in frequency occur at τ_i and τ_f ; the time constant τ_k is evaluated when the the temperature reaches the 63% of its value at τ_f .

Chapter 2 was validated. The experimental values of the pressure at the inlet and outlet sections, $P_{ki\,exp}$ and $P_{ko\,exp}$, of the refrigerant inlet enthalpy (calculated on the basis of the measured pressure $P_{ki\,exp}$ and temperature $T_{kri\,exp}$) and of the rotational frequency were used as model inputs. Moreover, the correction coefficients $C_{\dot{m}_r}$, C_T and $C_{\dot{W}_{el}}$ were manually tuned to improve the correspondence between numerical and experimental data. In particular, the tuning procedure was carried out considering Test 2 conditions, since it is characterized by steps in the rotational frequency which thus allows to test the compressor model for sudden transients.

5.4.1 Validation under Test 2 conditions

Figure 5.20 reports a comparison between the numerical and experimental refrigerant mass flow rate \dot{m}_r under Test 2 conditions when $C_{\dot{m}_r} = 1$. The correspondence between numerical and experimental data for the refrigerant mass flow rate is already satisfactory; indeed, excluding the two spikes which appear when the steps in the frequency occur, the percentage deviations always lie below 8%.

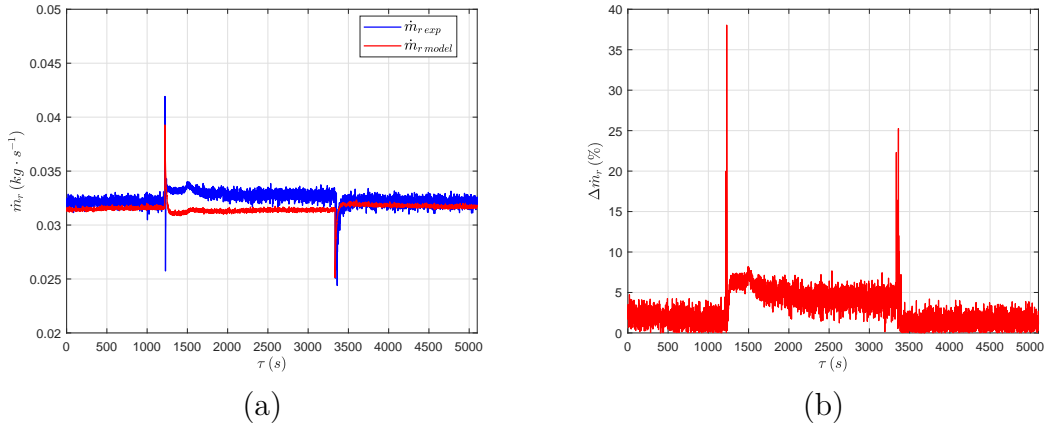


Figure 5.20: Validation of the compressor model. Comparison between the predicted and experimental refrigerant mass flow rate (a) and percentage deviation (b) with $C_{\dot{m}_r} = 1$ under Test 2 conditions.

Tuning the correction factor $C_{\dot{m}_r}$ to 1.02, the results shown in Fig. 5.21 were obtained. In this case, apart from the two spikes, the percentage deviation is always lower than 6%. Although the deviation between numerical and experimental data is acceptable considering the simplified nature of the compressor model, it can be noticed how the model predicts a decrease in the refrigerant mass flow rate when the frequency steps from 50 Hz to 65 Hz, contradicting the experimental measurements. This can be due to an overestimation of the effects of the refrigerant density reduction and to inaccuracies in the compressor polynomials at frequencies different from the nominal value of 50 Hz; the accuracy in the prediction of the mass flow rate across the compressor can be improved introducing a more detailed model of the compressor, allowing to better simulate the thermal dynamics of this machine.

Figure 5.22 shows the results obtained for the electric power absorbed by the compressor in Test 2 when $C_{\dot{W}_{el}} = 1$, with a percentage deviation between numerical and experimental data always lying below 6%. As reported in Fig. 5.23, if $C_{\dot{W}_{el}}$ is set to 1.05, the results are improved and the percentage deviation is always lower than 4%.

The results obtained for the compressor outlet temperature are reported in Figs. 5.24 and 5.25 when $C_T = 1$ and $C_T = 0.95$ respectively, showing how

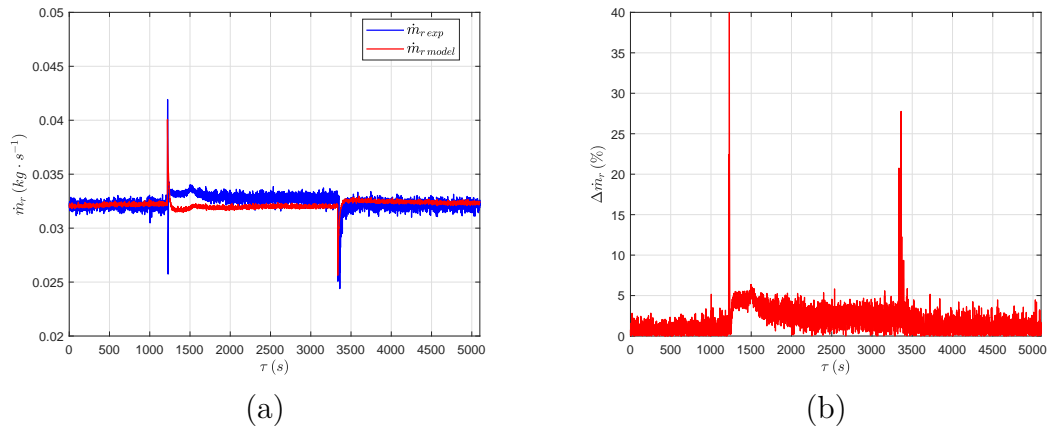


Figure 5.21: Validation of the compressor model. Comparison between the predicted and experimental refrigerant mass flow rate (a) and percentage deviation (b) with $C_{\dot{m}_r} = 1.02$ under Test 2 conditions.

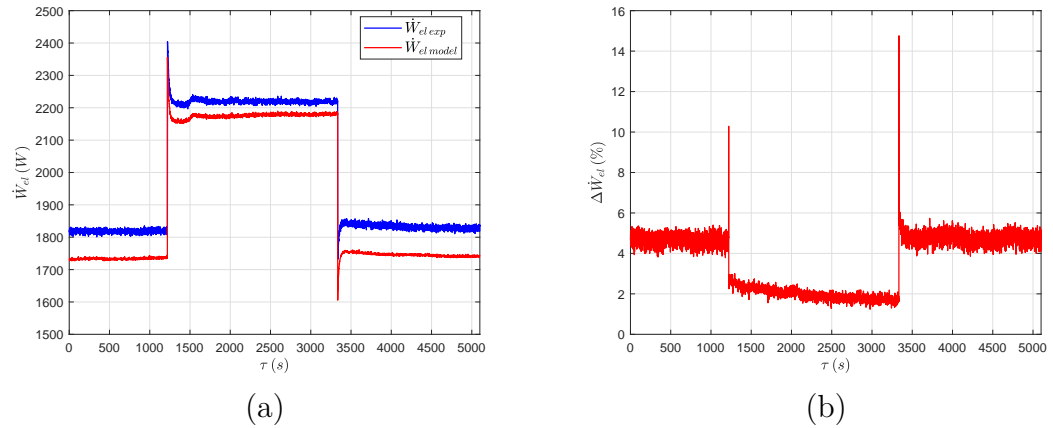


Figure 5.22: Validation of the compressor model. Comparison between the predicted and experimental electric power absorbed (a) and percentage deviation (b) with $C_{\dot{W}_{el}} = 1$ under Test 2 conditions.

the maximum deviation with respect to experimental data drops from 8.5 K to 3.7 K when correcting the value obtained through the polynomials.

5.4.2 Validation under Test 1 conditions

The results obtained for the refrigerant mass flow rate under Test 1 conditions when $C_{\dot{m}_r} = 1$ are reported in Fig. 5.26. Except for the spikes corresponding to the steps in the valve opening, the percentage deviation between numerical and experimental data always lies below 7%. When introducing a correction factor $C_{\dot{m}_r} = 1.02$, the percentage deviation is below 5% for most of the time, as shown in Fig. 5.27.

The results obtained for the electric power absorbed by the compressor under Test 1 conditions are reported in Figs. 5.28-5.29, in the cases of $C_{\dot{W}_{el}} = 1$ and $C_{\dot{W}_{el}} = 1.05$ respectively. It can be noticed how the maximum percent-

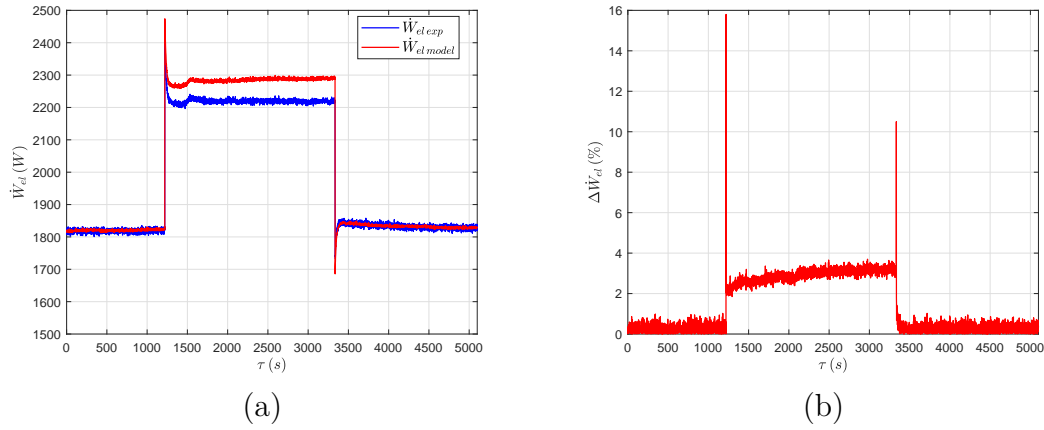


Figure 5.23: Validation of the compressor model. Comparison between the predicted and experimental electric power absorbed (a) and percentage deviation (b) with $C_{\dot{W}_{el}} = 1.05$ under Test 2 conditions.

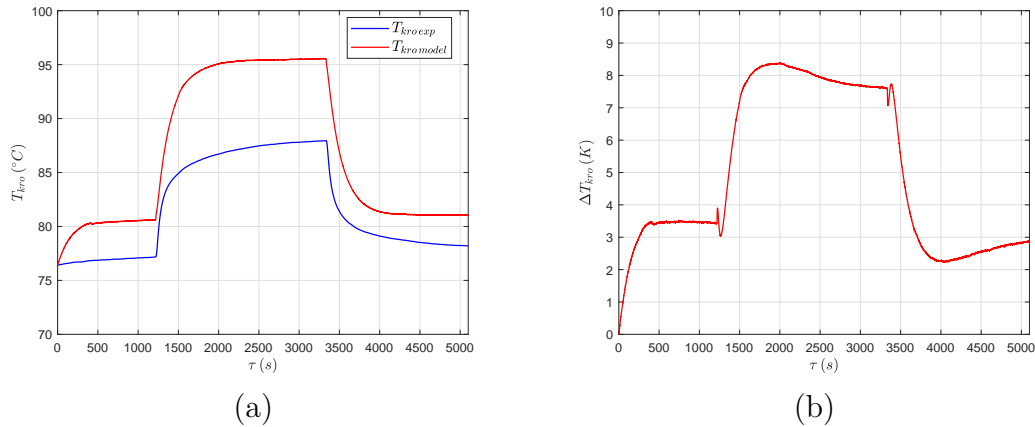


Figure 5.24: Validation of the compressor model. Comparison between the predicted and experimental refrigerant temperature at the compressor outlet (a) and absolute deviation (b) with $C_T = 1$ under Test 2 conditions.

age deviation drops from values around 6% to values lower than 1.5% when introducing a correction factor $C_{\dot{W}_{el}} = 1.05$.

Figures 5.30-5.31 report the results obtained for the refrigerant outlet temperature. The maximum deviation between numerical and experimental data is about 6.5 K when $C_T = 1$ and lower than 2.5 K when $C_T = 0.95$, thus showing how the model has good predictive capabilities. However, it can be noticed how the numerical trend is slightly different from the experimental one, suggesting that a more detailed model of the compressor instead of a simplified first-order model is required to accurately reproduce the transient thermal behaviour of this machine.

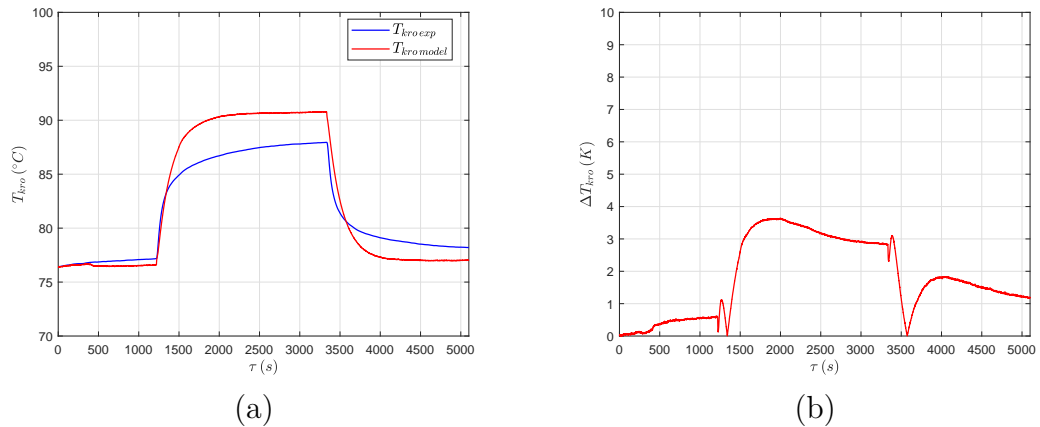


Figure 5.25: Validation of the compressor model. Comparison between the predicted and experimental refrigerant temperature at the compressor outlet (a) and absolute deviation (b) with $C_T = 0.95$ under Test 2 conditions.

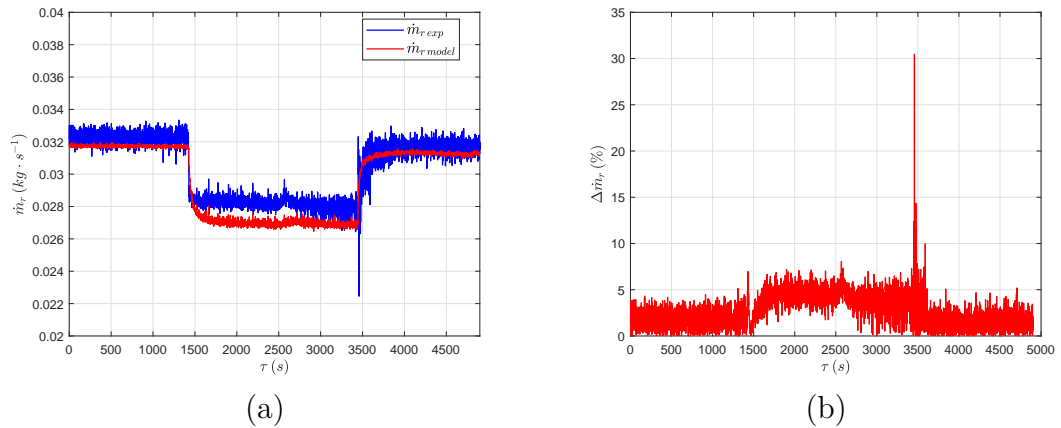


Figure 5.26: Validation of the compressor model. Comparison between the predicted and experimental refrigerant mass flow rate (a) and percentage deviation (b) with $C_{\dot{m}_r} = 1$ under Test 1 conditions.

5.5 Evaporator tuning and validation

After the models of the compressor and the expansion valve were tuned, an open-circuit model including the compressor, the valve and the evaporator was developed in order to investigate the accuracy of the evaporator model and to adjust the tuning factors C_{TP} , C_V and C_f for the heat transfer coefficients. Test 1 conditions were used for model tuning. In particular, the experimental condensation pressure and the refrigerant enthalpy at the outlet of the condenser were used as model inputs for the valve and the compressor.

5.5.1 Validation under Test 1 conditions

Results obtained with unitary tuning coefficients will be reported first. Figure 5.32 shows a comparison between the predicted and experimental pressure at

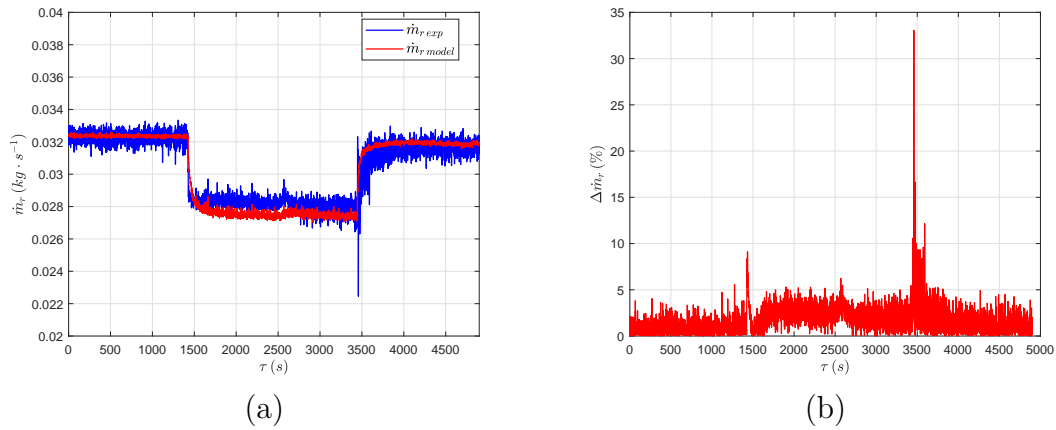


Figure 5.27: Validation of the compressor model. Comparison between the predicted and experimental refrigerant mass flow rate (a) and percentage deviation (b) with $C_{\dot{m}_r} = 1.02$ under Test 1 conditions.

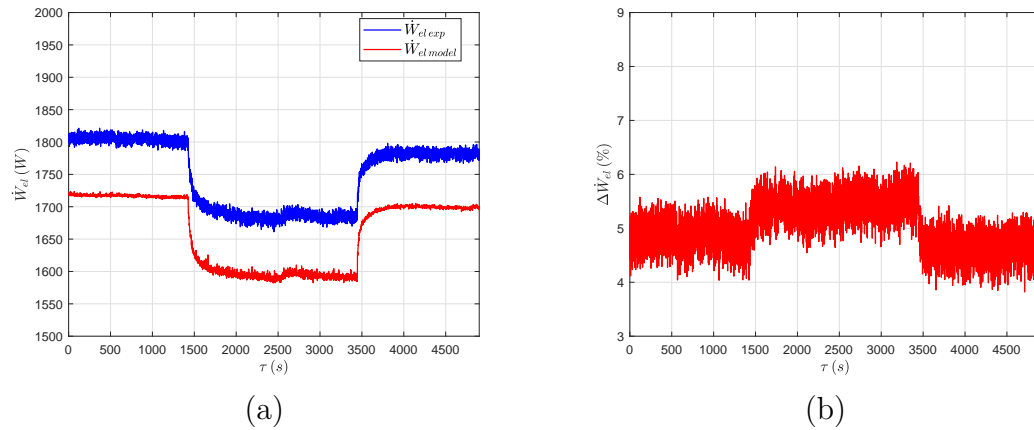


Figure 5.28: Validation of the compressor model. Comparison between the predicted and experimental electric power absorbed (a) and percentage deviation (b) with $C_{\dot{W}_{el}} = 1$ under Test 1 conditions.

the evaporator under Test 1 conditions. The numerical trend faithfully reproduces the experimental one, with percentage deviations always lower than 3%, with the exception of the two spikes of about 8.2% and 5.2% highlighted when the sudden steps in the valve opening occur.

The results related to the refrigerant temperature at the evaporator outlet are shown in Fig. 5.33. The qualitative trend of the numerical prediction is very similar to the experimental one, with a maximum absolute deviation of about 2 K, which can be improved by tuning the coefficient C_V related to the heat transfer coefficient in the superheated vapour region.

Figure 5.34 shows the evolution in time of the refrigerant superheating at the evaporator outlet, whose deviation with respect to the experimental data is influenced by the deviation in the refrigerant pressure and outlet temperature. The maximum deviation with unitary tuning coefficients is thus about 2.3 K.

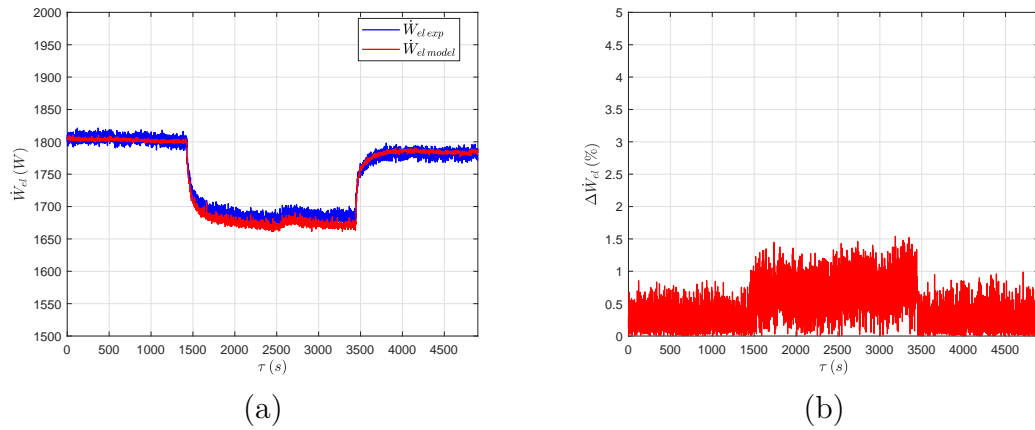


Figure 5.29: Validation of the compressor model. Comparison between the predicted and experimental electric power absorbed (a) and percentage deviation (b) with $C_{\dot{W}_{el}} = 1.05$ under Test 1 conditions.

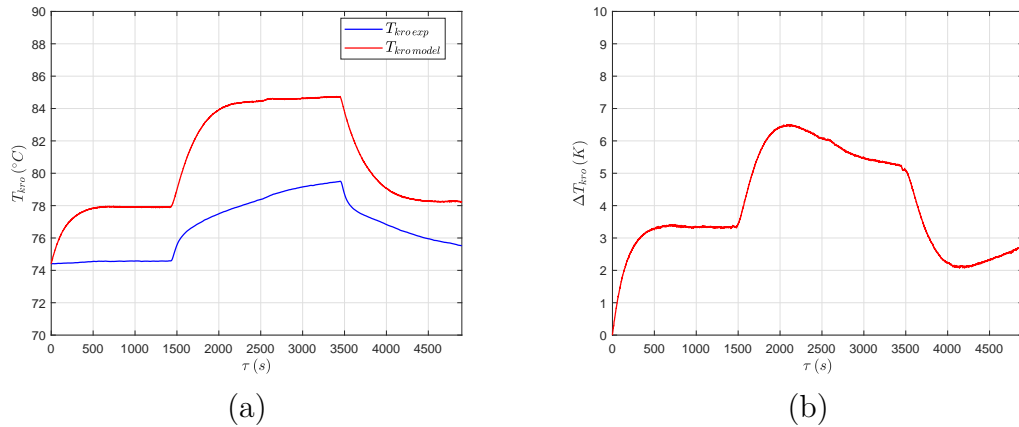


Figure 5.30: Validation of the compressor model. Comparison between the predicted and experimental refrigerant temperature at the compressor outlet (a) and absolute deviation (b) with $C_T = 1$ under Test 1 conditions.

As for the temperature of the water-glycol mixture at the outlet of the evaporator, a very good match between experimental data and numerical predictions was highlighted, as shown in Fig. 5.35. In particular, the absolute deviation is always lower than 0.1 K, except for the two spikes around 0.8 K and 0.5 K which occur in correspondence of the steps in the valve opening.

To reduce the deviation in the prediction of the refrigerant outlet temperature and superheating, the tuning coefficient for the superheated vapour region C_V was set to 2. In the following, the results obtained are reported.

The prediction of the refrigerant pressure is not particularly affected by the tuning coefficient C_V as can be seen in Fig. 5.36, with a slight decrease in the deviation when the valve opening is at 39.6%.

As for the refrigerant temperature at the evaporator outlet shown in Fig.

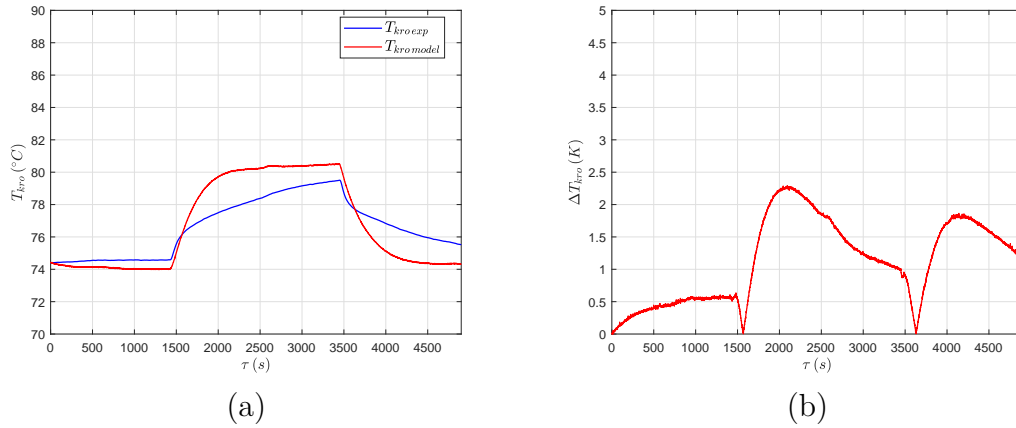


Figure 5.31: Validation of the compressor model. Comparison between the and experimental refrigerant temperature at the compressor outlet (a) and absolute deviation (b) with $C_T = 0.95$ under Test 1 conditions.

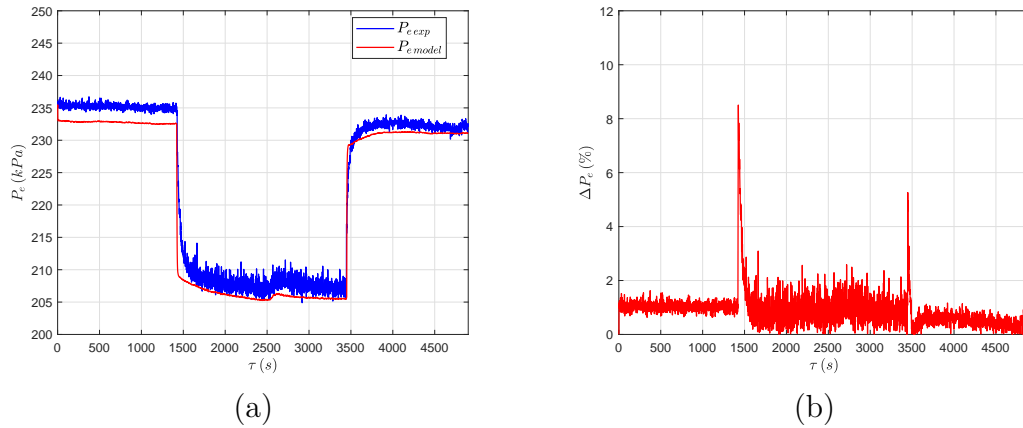


Figure 5.32: Validation of the evaporator model. Comparison between the predicted and experimental evaporation pressure (a) and percentage deviation (b) with $C_{TP} = 1$, $C_V = 1$ and $C_f = 1$ under Test 1 conditions.

5.37, it can be noticed how setting $C_V = 2$ allows to bring the deviation to values lower than 1.2 K, which is more than acceptable considering the lumped-parameter nature of the model.

Also the superheating at the evaporator outlet is significantly improved by correcting the value of C_V . In particular, as shown in Fig. 5.38, the deviation between the predicted and experimental superheating is always lower than 0.7 K, with the exception of the two spikes when the steps in the valve opening occur. As for the secondary fluid outlet temperature, no significant variations in the deviation was highlighted after the modification of C_V .

5.5.2 Validation under Test 2 conditions

The SMB model of the brazed-plate evaporator showed a good agreement with experimental data also under Test 2 conditions when using unitary tuning co-

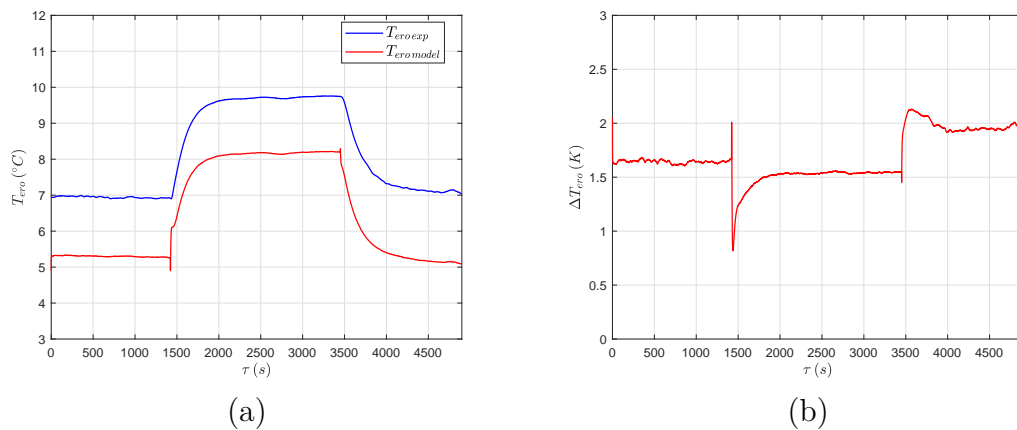


Figure 5.33: Validation of the evaporator model. Comparison between the predicted and experimental refrigerant temperature at the evaporator outlet (a) and absolute deviation (b) with $C_{TP} = 1$, $C_V = 1$ and $C_f = 1$ under Test 1 conditions.

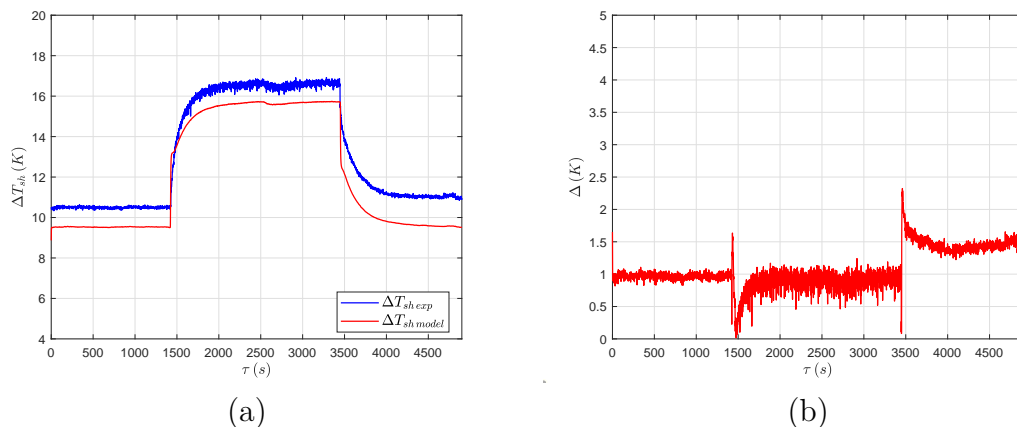


Figure 5.34: Validation of the evaporator model. Comparison between the predicted and experimental refrigerant superheating at the evaporator outlet (a) and absolute deviation (b) with $C_{TP} = 1$, $C_V = 1$ and $C_f = 1$ under Test 1 conditions.

efficients. Figure 5.39 shows the results obtained for the evaporation pressure P_e . The numerical trend of the pressure reproduces the experimental one well, with a percentage deviation which always lies below 4%. The highest deviations are obtained when the rotational frequency of the compressor is 65 Hz, when the compressor model underestimates the refrigerant mass flow rate as shown in Fig. 5.21. Indeed, when coupling the valve and compressor models together with the SMB model of the evaporator, the model-predicted refrigerant mass flow rate takes values very similar to the experimental ones, as shown in Fig. 5.40. Thus, in order for the compressor model to be able to guarantee such a mass flow rate, a higher inlet pressure and density of the refrigerant is required. A possible way to reduce the deviation in the prediction of the

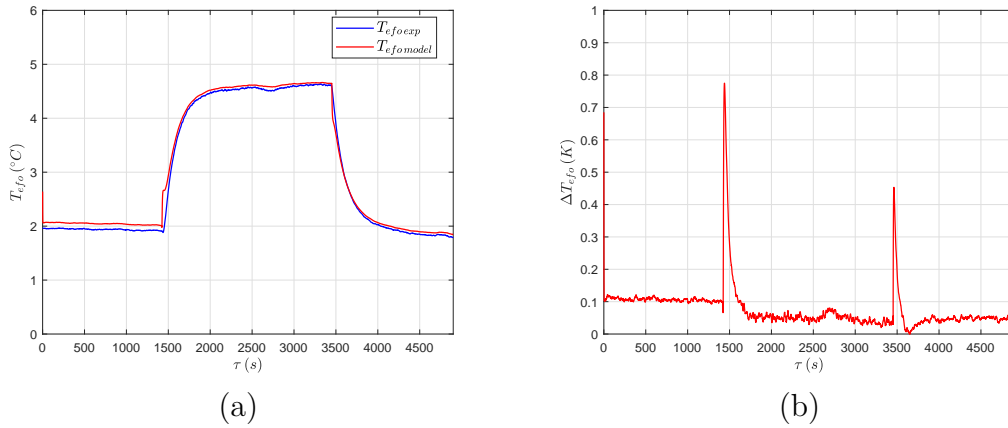


Figure 5.35: Validation of the evaporator model. Comparison between the predicted and experimental water-glycol temperature at the evaporator outlet (a) and absolute deviation (b) with $C_{TP} = 1$, $C_V = 1$ and $C_f = 1$ under Test 1 conditions.

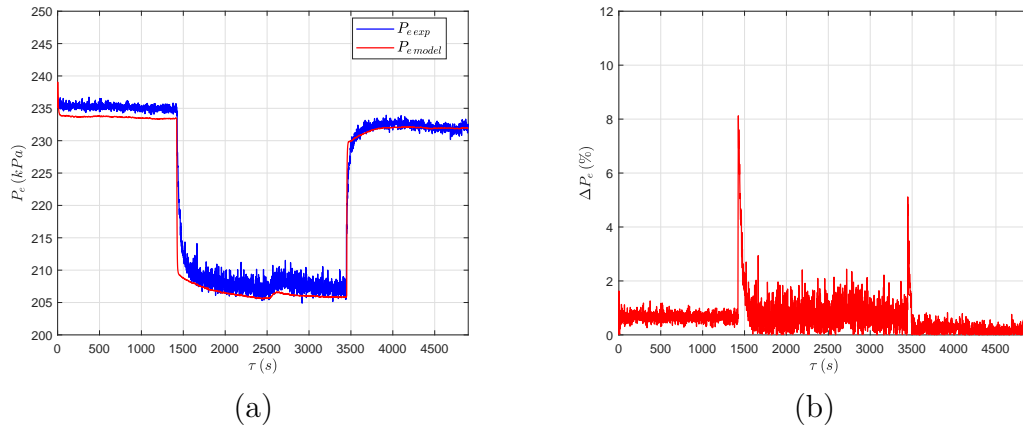


Figure 5.36: Validation of the evaporator model. Comparison between the predicted and experimental evaporation pressure (a) and percentage deviation (b) with $C_{TP} = 1$, $C_V = 2$ and $C_f = 1$ under Test 1 conditions.

pressure is to realize a more detailed and accurate model of the compressor.

The refrigerant temperature at the evaporator outlet is reported in Fig. 5.41. Also in this case the model is able to predict the temperature dynamics of the refrigerant, with a deviation always lower than 1.7 K. The spikes obtained when the sudden variations in the frequency occur are caused by considering instantaneous steps, which can lead to numerical inaccuracies.

The refrigerant superheating is shown in Fig. 5.42. It can be noticed how the absolute value of the deviation with respect to experimental data is slightly higher than that of the refrigerant outlet temperature. This is mainly due to the overestimation of the pressure and, as a consequence, of the saturation temperature.

The temperature of the water-glycol mixture at the evaporator outlet, showed

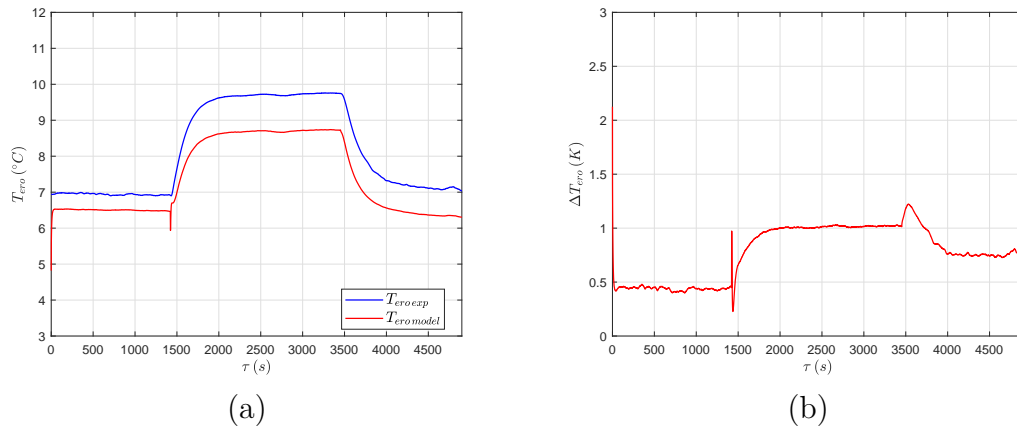


Figure 5.37: Validation of the evaporator model. Comparison between the predicted and experimental refrigerant temperature at the evaporator outlet (a) and absolute deviation (b) with $C_{TP} = 1$, $C_V = 2$ and $C_f = 1$ under Test 1 conditions.

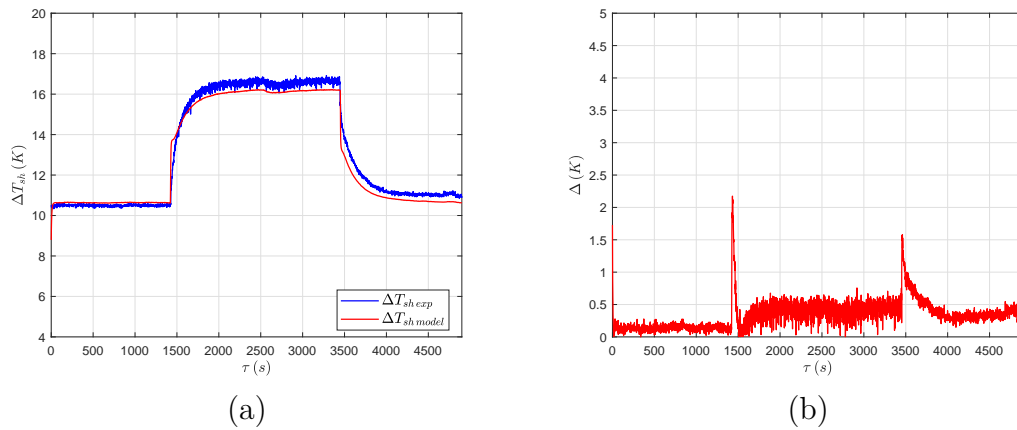


Figure 5.38: Validation of the evaporator model. Comparison between the predicted and experimental refrigerant superheating at the evaporator outlet (a) and absolute deviation (b) with $C_{TP} = 1$, $C_V = 2$ and $C_f = 1$ under Test 1 conditions.

a good level of between numerical and experimental data, as shown in Fig. 5.43, with almost negligible values of the absolute deviation, similarly to what already seen for the validation under Test 1 conditions.

When introducing a tuning factor $C_V = 2$ to improve the model predictive properties in terms of refrigerant outlet temperature and superheating at the evaporator outlet, the deviation between the model-predicted and the experimental pressure is almost unaffected, especially when $f = 65 \text{ Hz}$, since it is mainly influenced by the accuracy of the compressor model.

Introducing a non-zero tuning factor for the heat transfer coefficient in the vapour-phase region, the deviation for the refrigerant outlet temperature lies below 1 K, as shown in Fig. 5.45, with a 41% reduction with respect to the

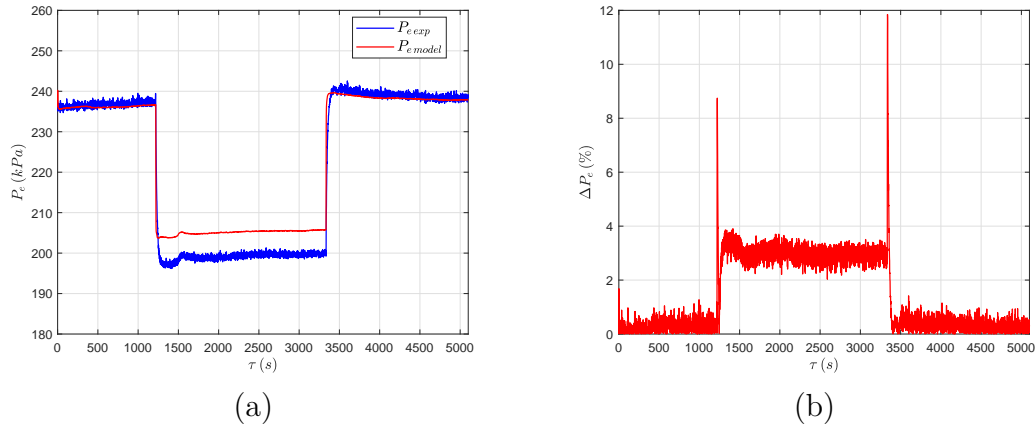


Figure 5.39: Validation of the evaporator model. Comparison between the predicted and experimental evaporation pressure (a) and percentage deviation (b) with $C_{TP} = 1$, $C_V = 1$ and $C_f = 1$ under Test 2 conditions.

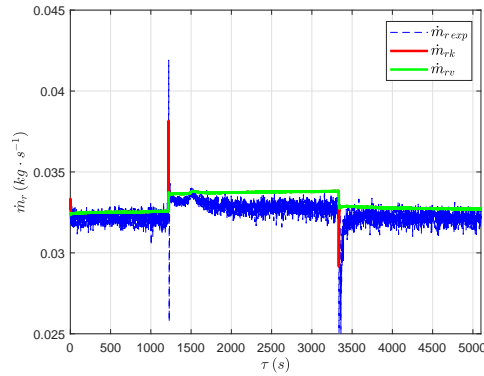


Figure 5.40: Validation of the evaporator model. Comparison between the experimental and numerical refrigerant mass flow rate predicted by the valve and the compressor models, with $C_{TP} = 1$, $C_V = 1$ and $C_f = 1$ under Test 2 conditions.

deviation obtained with unitary tuning coefficients. As for the superheating, the deviation drops from 1.2 K to 0.5 K and from 2.1 K to 1.5 K when the frequency is 50 Hz and 65 Hz respectively. The outlet temperature of the water-glycol mixture is not significantly affected by the introduction of a non-zero C_V , as already seen for the validation under Test 1 conditions.

5.6 Condenser tuning and validation of the machine model

The tuned models of the evaporator, of the compressor and of the expansion valve were connected to the condenser model in order to simulate the whole vapour compression refrigerating machine neglecting the effects of the receiver,

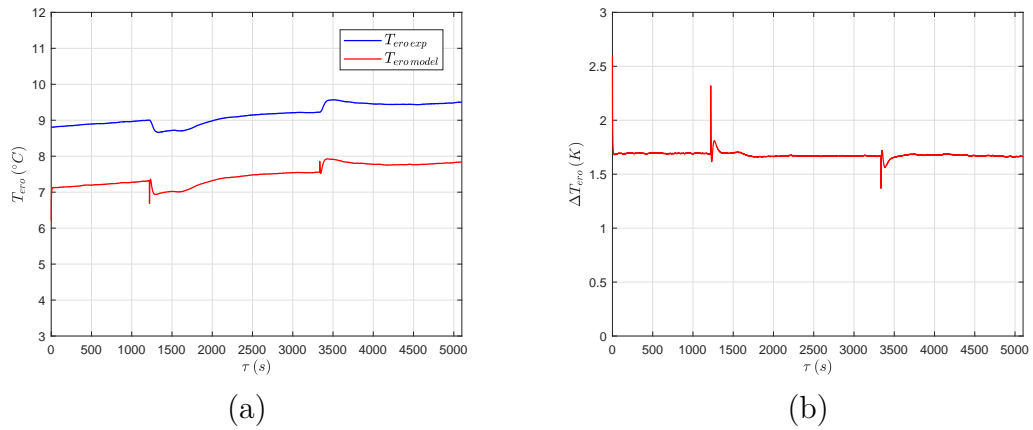


Figure 5.41: Validation of the evaporator model. Comparison between the predicted and experimental refrigerant temperature at the evaporator outlet (a) and absolute deviation (b) with $C_{TP} = 1$, $C_V = 1$ and $C_f = 1$ under Test 2 conditions.

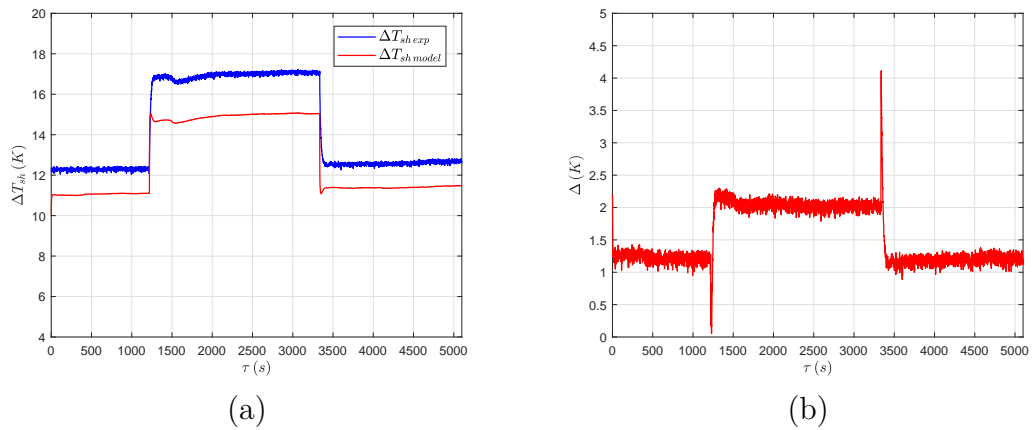


Figure 5.42: Validation of the evaporator model. Comparison between the predicted and experimental refrigerant superheating at the evaporator outlet (a) and absolute deviation (b) with $C_{TP} = 1$, $C_V = 1$ and $C_f = 1$ under Test 2 conditions.

of the suction accumulator and of the pipes. The correction factors for the heat transfer coefficient in the condenser were subsequently tuned to improve the match between numerical and experimental data.

5.6.1 Validation under Test 1 conditions

The results obtained with unitary tuning coefficients in the condenser model will be presented first. Figure 5.47 shows the results obtained for the refrigerant pressure in the heat exchangers. The condensation pressure is slightly overestimated by the model (see Fig. 5.47 (a) and (b)), with percentage deviations below 7%. Since the valve opening is maintained at the experimental value, this overestimation also affects the evaporation pressure (see Fig. 5.47

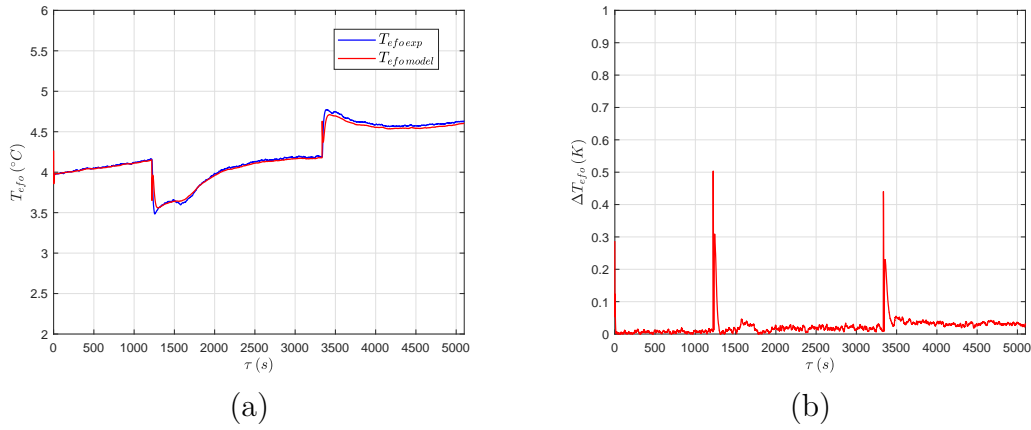


Figure 5.43: Validation of the evaporator model. Comparison between the predicted and experimental water-glycol temperature at the evaporator outlet (a) and absolute deviation (b) with $C_{TP} = 1$, $C_V = 1$ and $C_f = 1$ under Test 2 conditions.

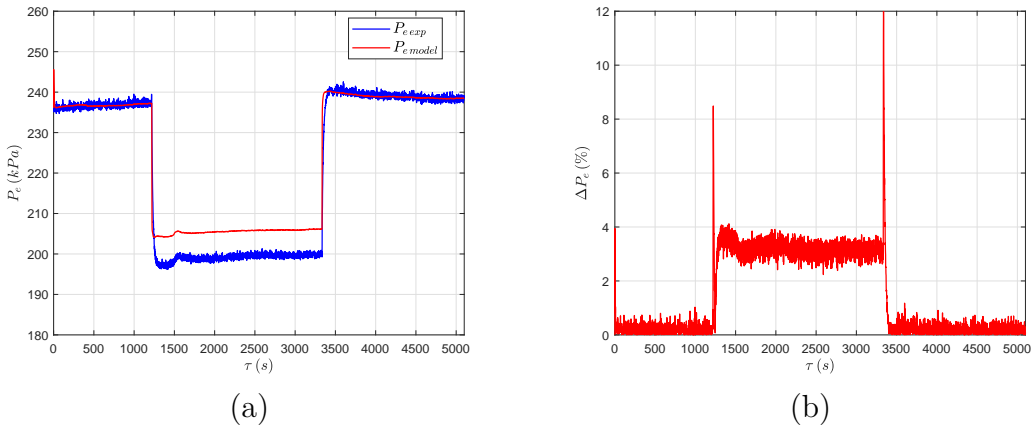


Figure 5.44: Validation of the evaporator model. Comparison between the predicted and experimental evaporation pressure (a) and percentage deviation (b) with $C_{TP} = 1$, $C_V = 2$ and $C_f = 1$ under Test 2 conditions.

(c) and (d)), whose percentage deviation lies below 4%, if the spikes in correspondence of the sudden steps are neglected.

Figure 5.48 shows how the refrigerant mass flow rates predicted by the valve and the compressor, \dot{m}_{rv} and \dot{m}_{rk} respectively, replicate the experimental data quite well, since both condensation and evaporation pressure increase.

The refrigerant temperature at the outlet of the heat exchangers is shown in Fig. 5.49, confirming how the model correctly reproduces the dynamics of the system. As for the condenser, a maximum deviation of about 2.7 K is highlighted in Figs. 5.49 (a) and (b), whilst for the already-tuned evaporator the deviation is always below 1.02 K.

As shown in Figs. 5.50 (a), the transient caused by a sudden variation in the

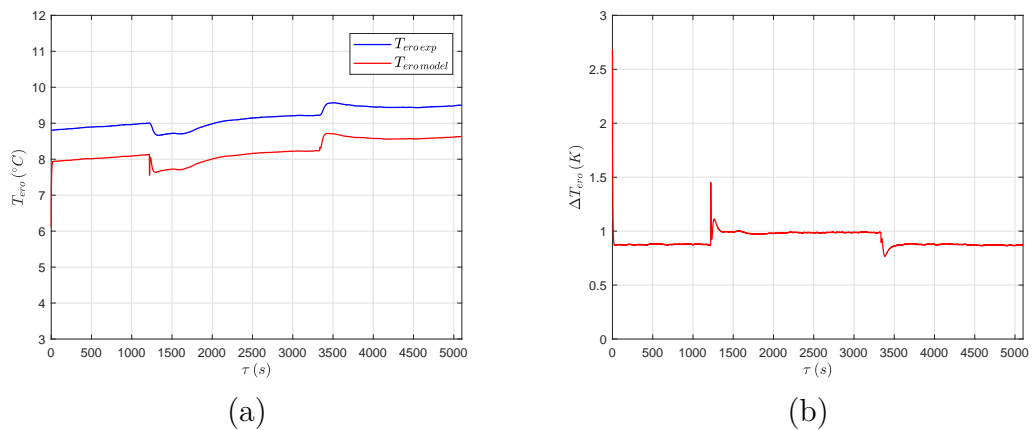


Figure 5.45: Validation of the evaporator model. Comparison between the predicted and experimental refrigerant temperature at the evaporator outlet (a) and absolute deviation (b) with $C_{TP} = 1$, $C_V = 2$ and $C_f = 1$ under Test 2 conditions.

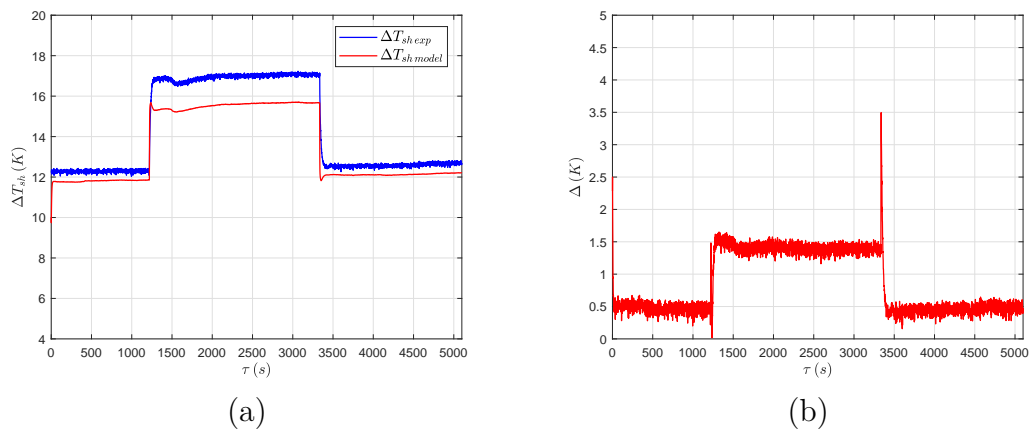


Figure 5.46: Validation of the evaporator model. Comparison between the predicted and experimental refrigerant superheating at the evaporator outlet (a) and absolute deviation (b) with $C_{TP} = 1$, $C_V = 2$ and $C_f = 1$ under Test 2 conditions.

valve opening does not involve meaningful variations in the refrigerant sub-cooling. The values predicted by the condenser model are very similar to the experimental data (deviations lower than 1 K), but mainly because it overestimates the refrigerant mean saturation temperature thus compensating the overestimation of the outlet temperature shown in Fig. 5.49 (a) and (b). The predicted refrigerant superheating at the evaporator outlet is in good agreement with the experimental values, as shown in Fig. 5.50 (c) and (d), with deviations lower than 1.5 K for most of the time and with a peak of about 2.4 K.

The temperature of the secondary fluids at the outlet of the heat exchangers

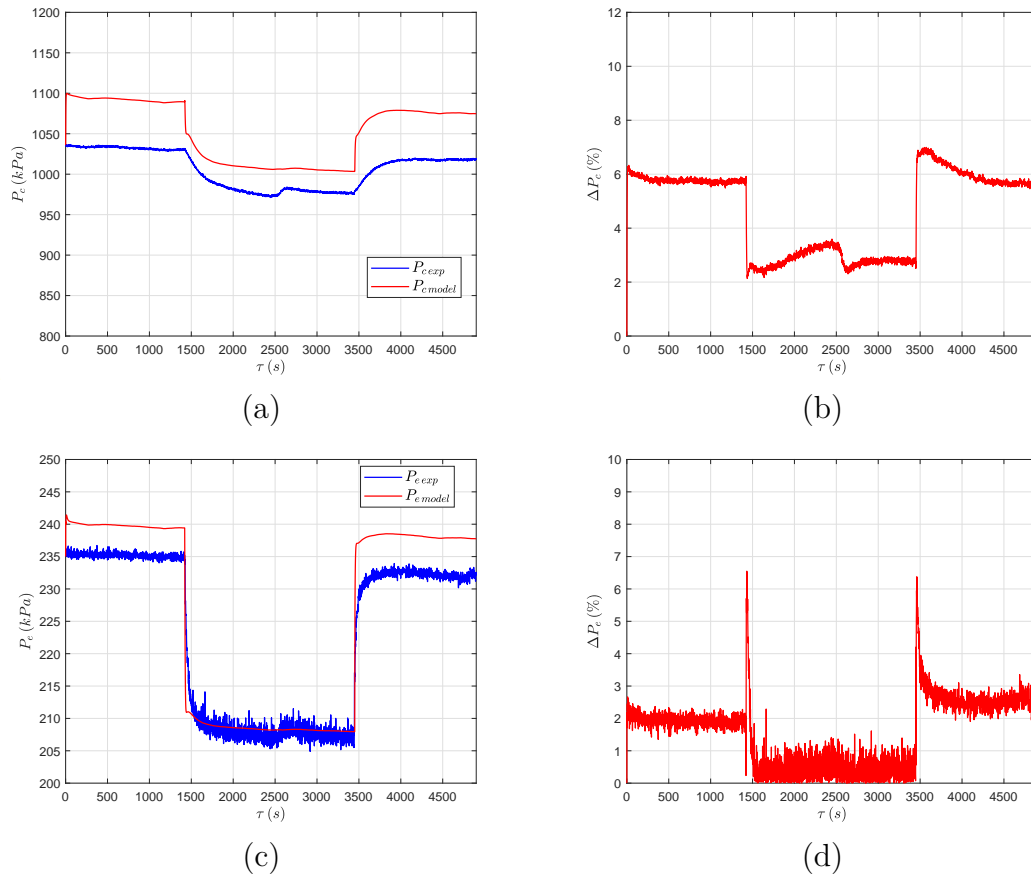


Figure 5.47: Validation of the complete model with the main system components. Comparison between the predicted and experimental pressure at the condenser ((a) and (b)) and at the evaporator ((c) and (d)), with $C_V = 1$, $C_{TP} = 1$, $C_L = 1$ and $C_f = 1$ under Test 1 conditions.

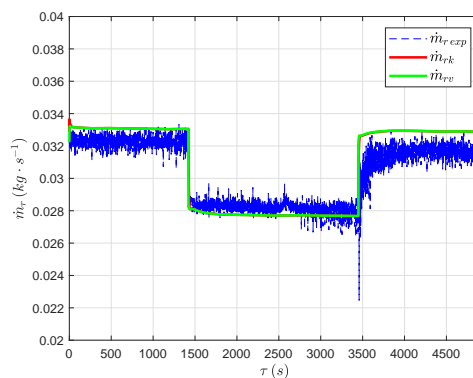


Figure 5.48: Validation of the complete model with the main system components. Model-predicted and experimental refrigerant mass flow rate, with $C_V = 1$, $C_{TP} = 1$, $C_L = 1$ and $C_f = 1$ under Test 1 conditions.

are shown in Fig. 5.51. The agreement with experimental data are good for both the water at the condenser (deviation lower than 1 K) and the water-

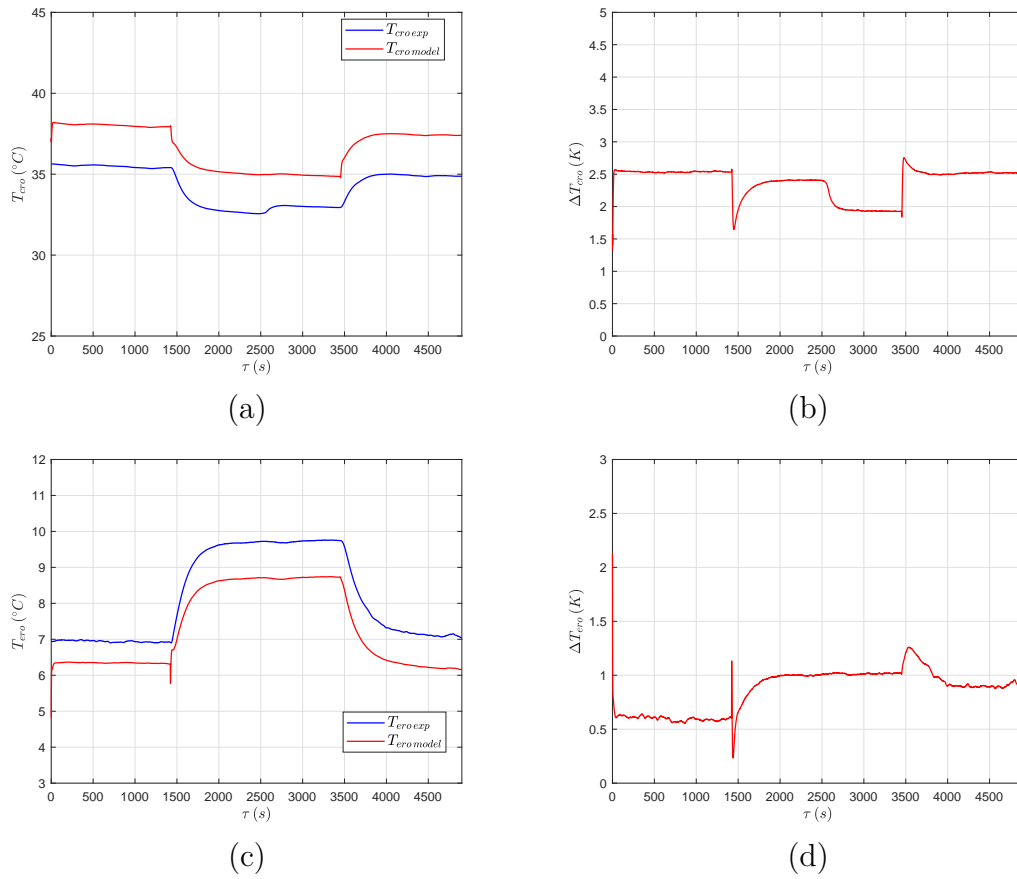


Figure 5.49: Validation of the complete model with the main system components. Comparison between the predicted and experimental temperature of the refrigerant at the outlet of the condenser ((a) and (b)) and the evaporator ((c) and (d)), with $C_V = 1$, $C_{TP} = 1$, $C_L = 1$ and $C_f = 1$ under Test 1 conditions.

glycol mixture at the evaporator (deviation lower than 0.8 K).

To investigate the effects of the transients in the energy performance of a VCS, it is important that the model correctly predicts the electric power absorption of the compressor and the thermal power removed from the secondary fluid at the evaporator. The good predictive capabilities of the model in terms of water-glycol outlet temperature shown in Fig. 5.51 (c) and (d) ensures *per se* a good prediction of the thermal power exchanged at the evaporator. As for the electric power absorption, Fig. 5.52 (a) and (b) reports a comparison between numerical and experimental data, highlighting how the percentage deviation is always lower than 5%. The COP predicted by the model is reported in Fig. 5.53 and compared to the values obtained experimentally, showing a good agreement (the percentage deviation is always lower 7%).

The correction factors C_V , C_{TP} , C_L and C_f in the condenser model were subsequently tuned in order to improve the agreement between numerical and

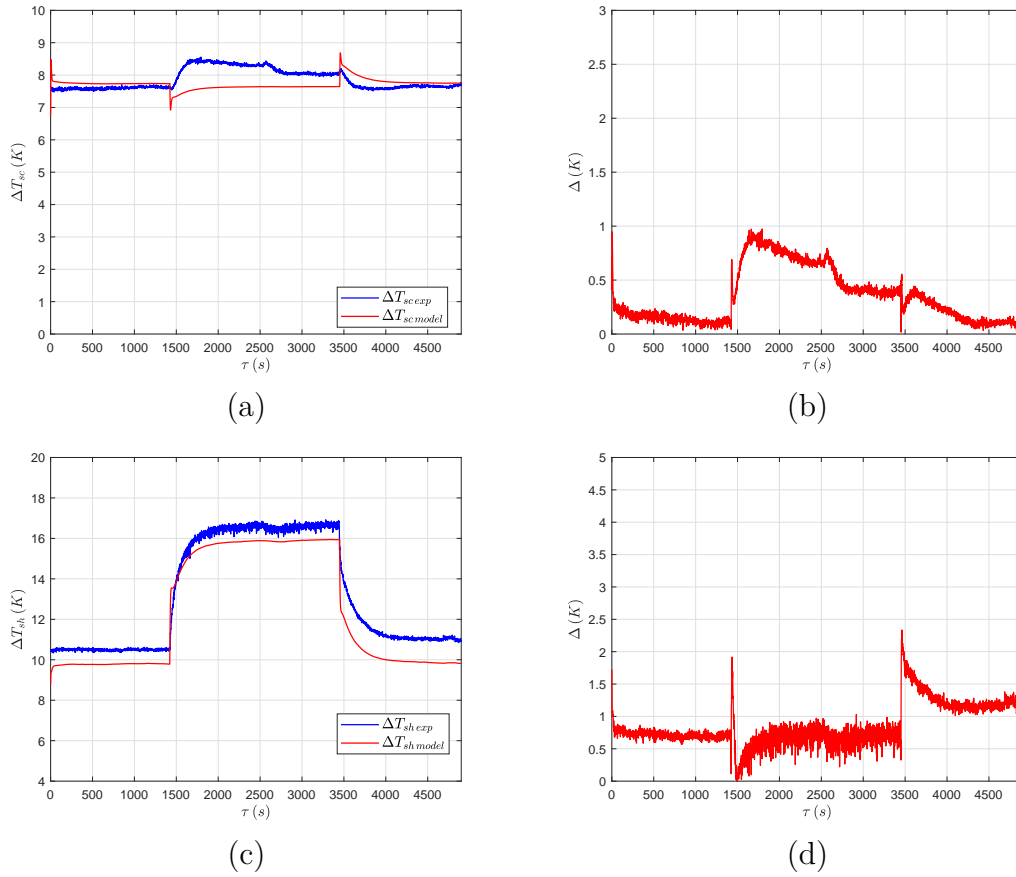


Figure 5.50: Validation of the complete model with the main system components. Comparison between the predicted and experimental subcooling and superheating of the refrigerant at the outlet of the condenser ((a) and (b)) and the evaporator ((c) and (d)), with $C_V = 1$, $C_{TP} = 1$, $C_L = 1$ and $C_f = 1$ under Test 1 conditions.

experimental data, in particular in the prediction of the refrigerant pressure at the condenser. As reported in [108], a large number of correlations is available for the calculation of the single-phase heat transfer coefficients, whose values can vary significantly. As an example, Figure 5.54 reports the Nusselt number Nu as a function of the Reynolds number Re calculated through different correlations for the single-phase refrigerant (a) and the secondary fluid (b). Percentage deviations with respect to the Martin correlation higher than 150% are highlighted.

Thus, since the Martin correlation was used for the single-phase heat transfer coefficients in the brazed-plate condenser both on the refrigerant and on the water side, as explained in sections 2.6.7 and 2.6.8, the correction factors C_V , C_L and C_f were all tuned together. In particular, a value of 1.35 was finally chosen for the three coefficients.

Figure 5.55 shows the results obtained for the refrigerant pressure in the heat exchangers. The tuning procedure significantly improves the agreement between the numerical and experimental condensation pressure, with a percent-

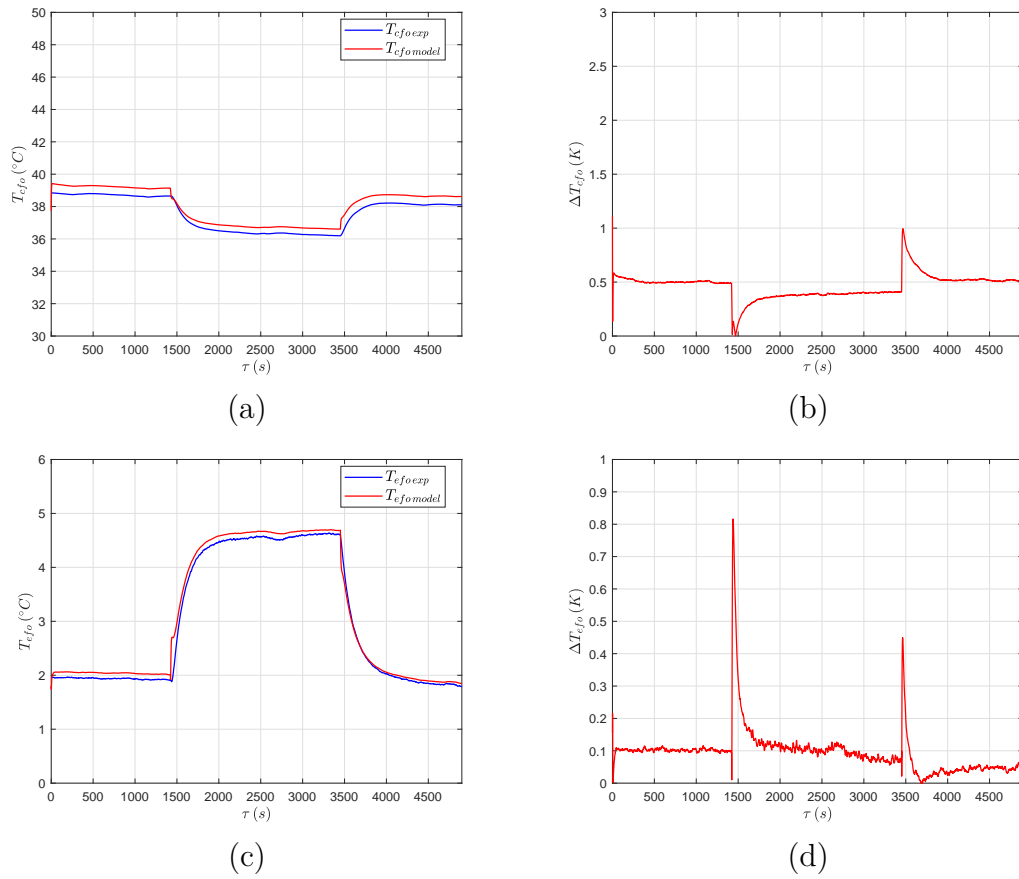


Figure 5.51: Validation of the complete model with the main system components. Comparison between the predicted and experimental temperature of the secondary fluids at the outlet of the condenser ((a) and (b)) and the evaporator ((c) and (d)), with $C_V = 1$, $C_{TP} = 1$, $C_L = 1$ and $C_f = 1$ under Test 1 conditions.

age deviation which is always below 4% (see Fig. 5.55 (a) and (b)). As for the evaporation pressure, a decrease in the values predicted by the model is highlighted in Fig. 5.55 (c) and (d); the percentage deviation thus drops to values below 1.5% when the valve is at its maximum opening whilst a slight increase with respect to the non-tuned results is shown when the opening is at its minimum. As a consequence, the prediction in the refrigerant mass flow rate improves in the first and in the last part of the simulation where the prediction of the evaporation pressure is more accurate, as demonstrated in Fig. 5.56.

Introducing corrective factors at the condenser brings a significant improvement in the prediction of the refrigerant outlet temperature at the condenser, as shown in Fig. 5.57 (a) and (b), where the deviation drops down to below 1.5 K. At the evaporator outlet, no significant improvements are highlighted, as can be noticed in Fig. 5.57 (c) and (d).

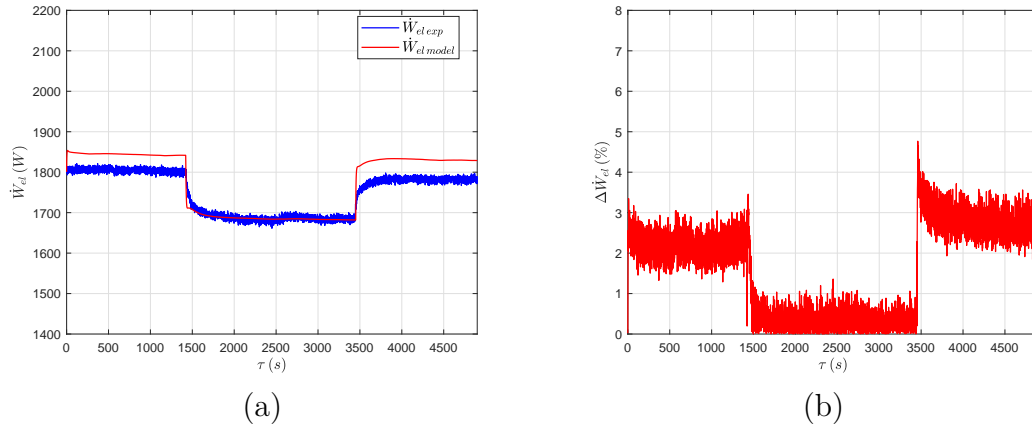


Figure 5.52: Validation of the complete model with the main system components. Comparison between the predicted and experimental electric power absorbed by the compressor (a) and percentage deviation (b), with $C_V = 1$, $C_{TP} = 1$, $C_L = 1$ and $C_f = 1$ under Test 1 conditions.

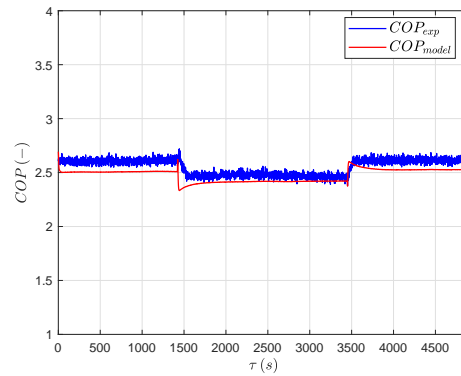


Figure 5.53: Validation of the complete model with the main system components. Comparison between the predicted and experimental COP (a) and percentage deviation (b), with $C_V = 1$, $C_{TP} = 1$, $C_L = 1$ and $C_f = 1$ under Test 1 conditions.

The effects of tuning on the predicted superheating and subcooling at the outlet of the heat exchangers are reported in Fig. 5.58. The deviation in the prediction of the refrigerant subcooling worsens, with a maximum overestimation of about 2.2 K (see Fig. 5.58 (a) and (b)), because the predicted refrigerant saturation pressure and temperature at the condenser drop sharper than the predicted outlet refrigerant temperature. Different correlations for the calculation of the single-phase heat transfer coefficients in the condenser will be tested in the near future in order to improve the capability of the model to correctly predict refrigerant outlet temperature and subcooling. On the other hand, a better estimation of the refrigerant superheating is obtained after the tuning procedure, as highlighted in Fig. 5.58 (c) and (d). No significant improvements were highlighted concerning the outlet temperatures of the secondary fluids.

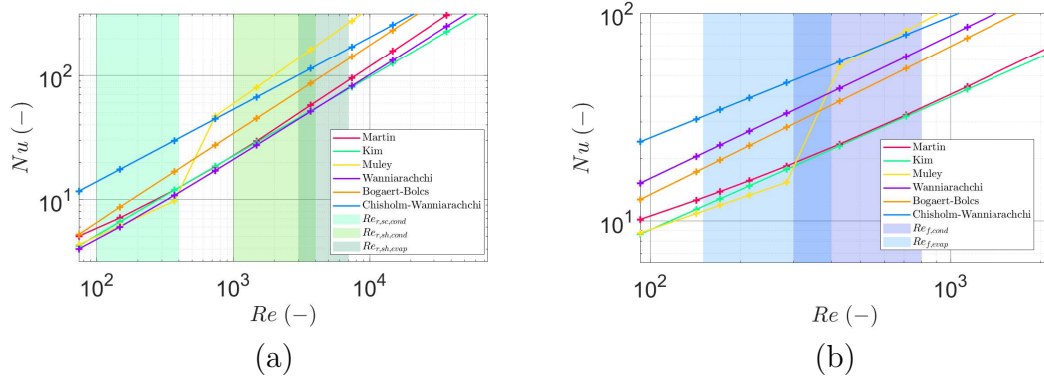


Figure 5.54: Nusselt number for the calculation of the single-phase heat transfer coefficients in brazed-plate heat exchangers using different correlations. (a) Refrigerant side. (b) Secondary fluid side.

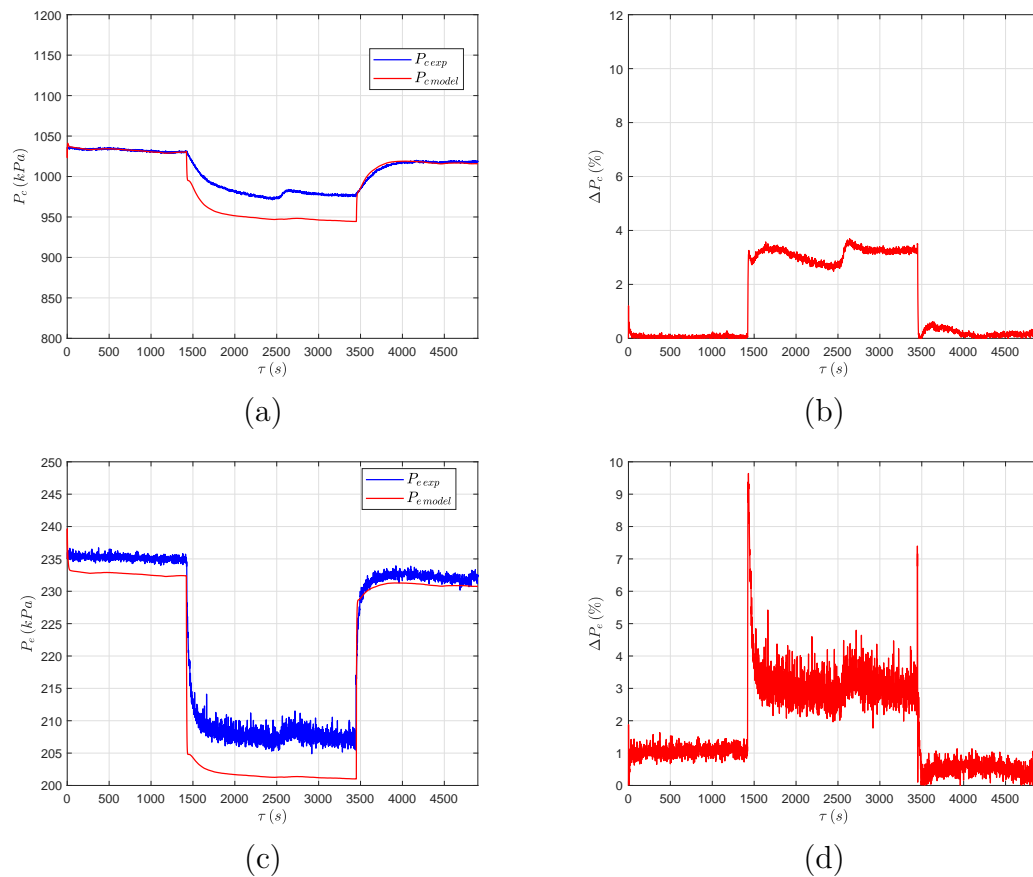


Figure 5.55: Validation of the complete model with the main system components. Comparison between the predicted and experimental pressure at the condenser ((a) and (b)) and at the evaporator ((c) and (d)), with $C_V = 1.35$, $C_{TP} = 1$, $C_L = 1.35$ and $C_f = 1.35$ under Test 1 conditions.

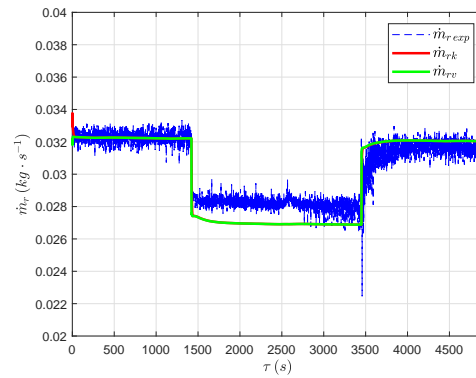


Figure 5.56: Validation of the complete model with the main system components. Model-predicted and experimental refrigerant mass flow rate, with $C_V = 1.35$, $C_{TP} = 1$, $C_L = 1.35$ and $C_f = 1.35$ under Test 1 conditions.

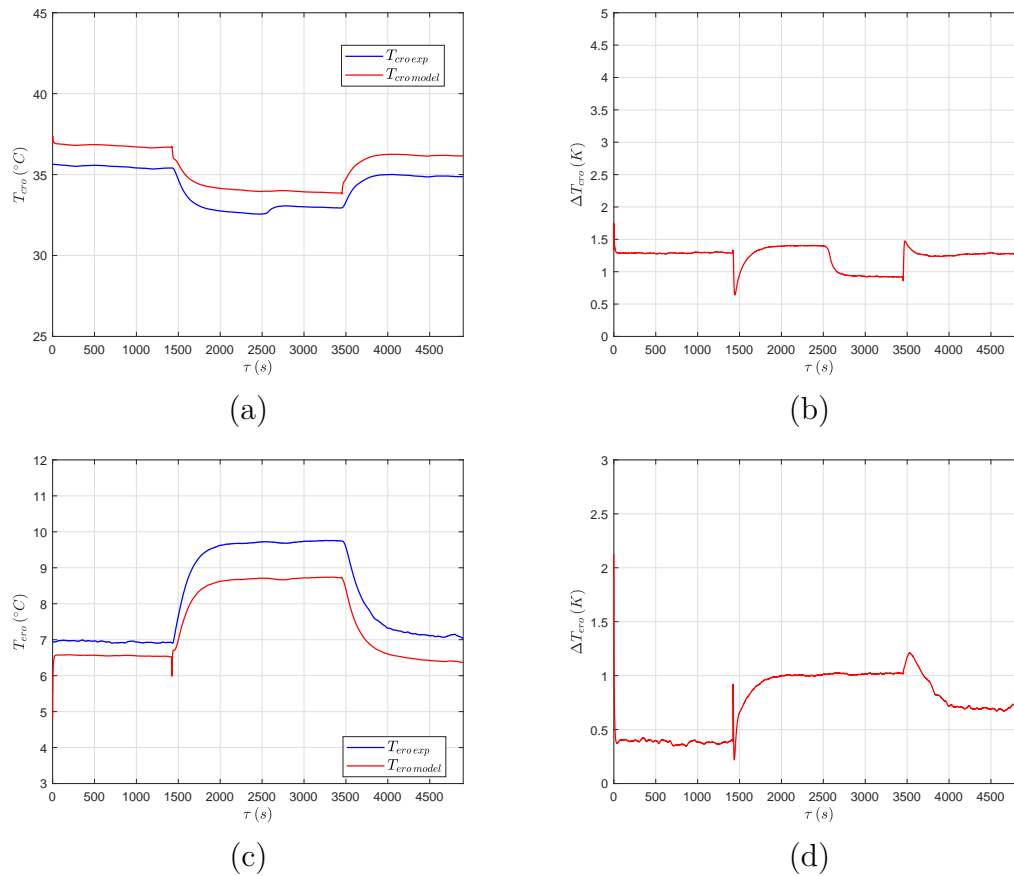


Figure 5.57: Validation of the complete model with the main system components. Comparison between the predicted and experimental temperature of the refrigerant at the outlet of the condenser ((a) and (b)) and the evaporator ((c) and (d)), with $C_V = 1.35$, $C_{TP} = 1$, $C_L = 1.35$ and $C_f = 1.35$ under Test 1 conditions.

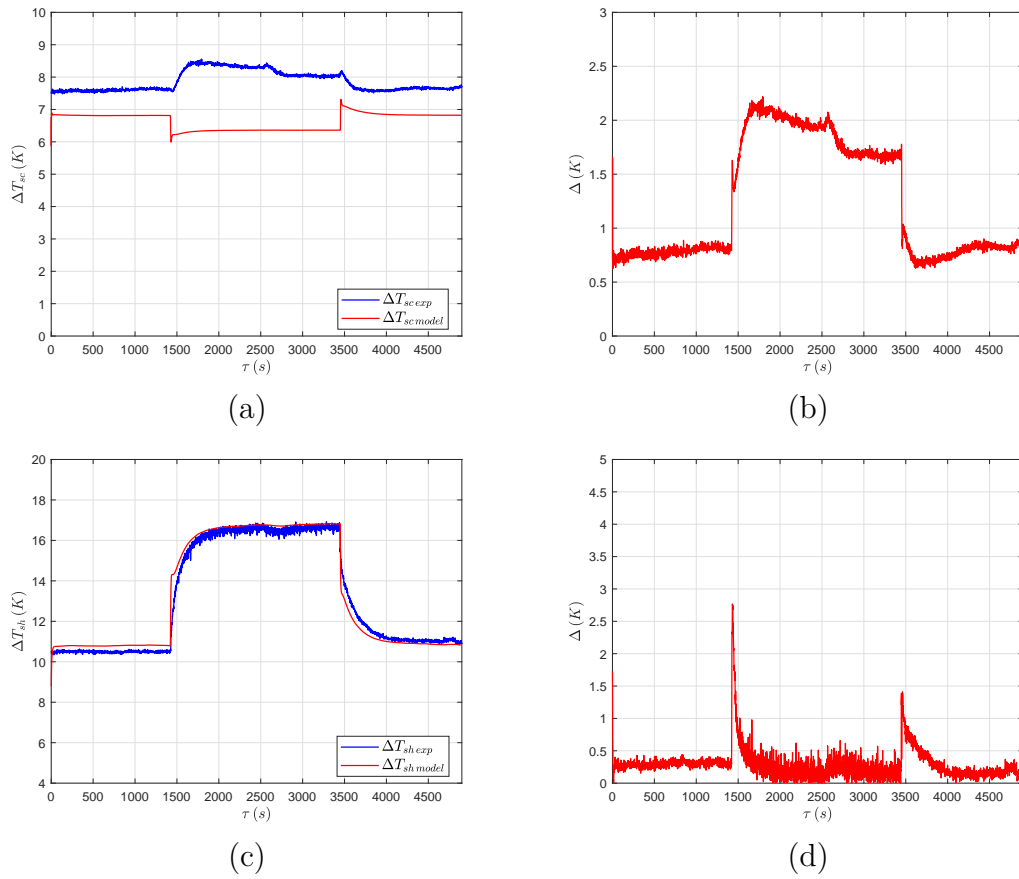


Figure 5.58: Validation of the complete model with the main system components. Comparison between the predicted and experimental subcooling and superheating of the refrigerant at the outlet of the condenser ((a) and (b)) and the evaporator ((c) and (d)), with $C_V = 1.35$, $C_{TP} = 1$, $C_L = 1.35$ and $C_f = 1.35$ under Test 1 conditions.

As shown in Fig. 5.59 the power absorbed by the compressor is predicted very accurately when the valve is at its maximum opening (deviations lower than 1.5%), whilst a higher deviation is underlined in the central part of Test 1, where the maximum deviation in the evaporation and condensation pressures occurs. As can be seen in Fig. 5.60, the numerical COP reproduces the experimental one with excellent accuracy, thus making the model suitable for transient energy analysis.

5.6.2 Validation under Test 2 conditions

In this section the results obtained in the validation under Test 2 conditions will be presented, starting from the case with unitary correction factors for the heat transfer coefficients in the condenser. The refrigerant pressure in both heat exchangers is overestimated, with a maximum deviation of 8.5% in the condenser and 8% in the evaporator, as shown in Fig. 5.61. As a main consequence of the overestimation of the evaporation pressure, the predicted

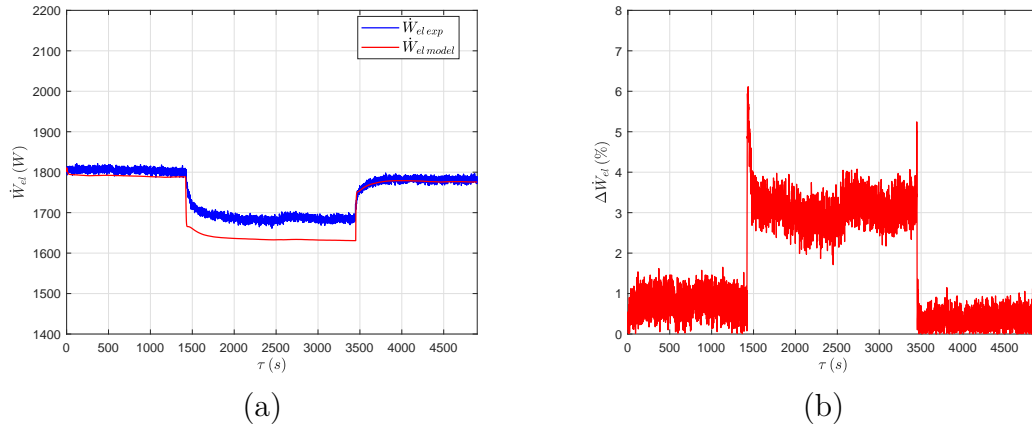


Figure 5.59: Validation of the complete model with the main system components. Comparison between the predicted and experimental electric power absorbed by the compressor (a) and percentage deviation (b), with $C_V = 1.35$, $C_{TP} = 1$, $C_L = 1.35$ and $C_f = 1.35$ under Test 1 conditions.

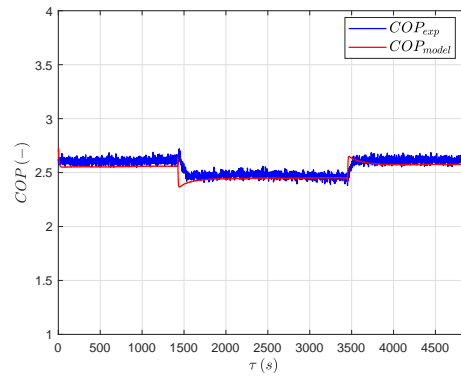


Figure 5.60: Validation of the complete model with the main system components. Comparison between the predicted and experimental COP (a) and percentage deviation (b), with $C_V = 1.35$, $C_{TP} = 1$, $C_L = 1.35$ and $C_f = 1.35$ under Test 1 conditions.

refrigerant mass flow rate slightly exceeds the experimental data, as shown in Fig. 5.62.

As already seen for the validation under Test 1 conditions, the refrigerant temperature at the outlet of the condenser is overestimated by the model, with a maximum deviation of about 3.5 K, as shown in Fig. 5.63 (a) and (b). A more accurate prediction of the refrigerant outlet temperature is obtained at the evaporator where the maximum deviation is always below 1.5 K, as can be noticed in Fig. 5.63 (c) and (d).

With unitary tuning coefficients in the condenser model, the subcooling and the superheating of the refrigerant at the outlet of the heat exchangers are predicted by the model with absolute deviations below 1 K and 2.6 K respectively, as shown in Fig. 5.64.

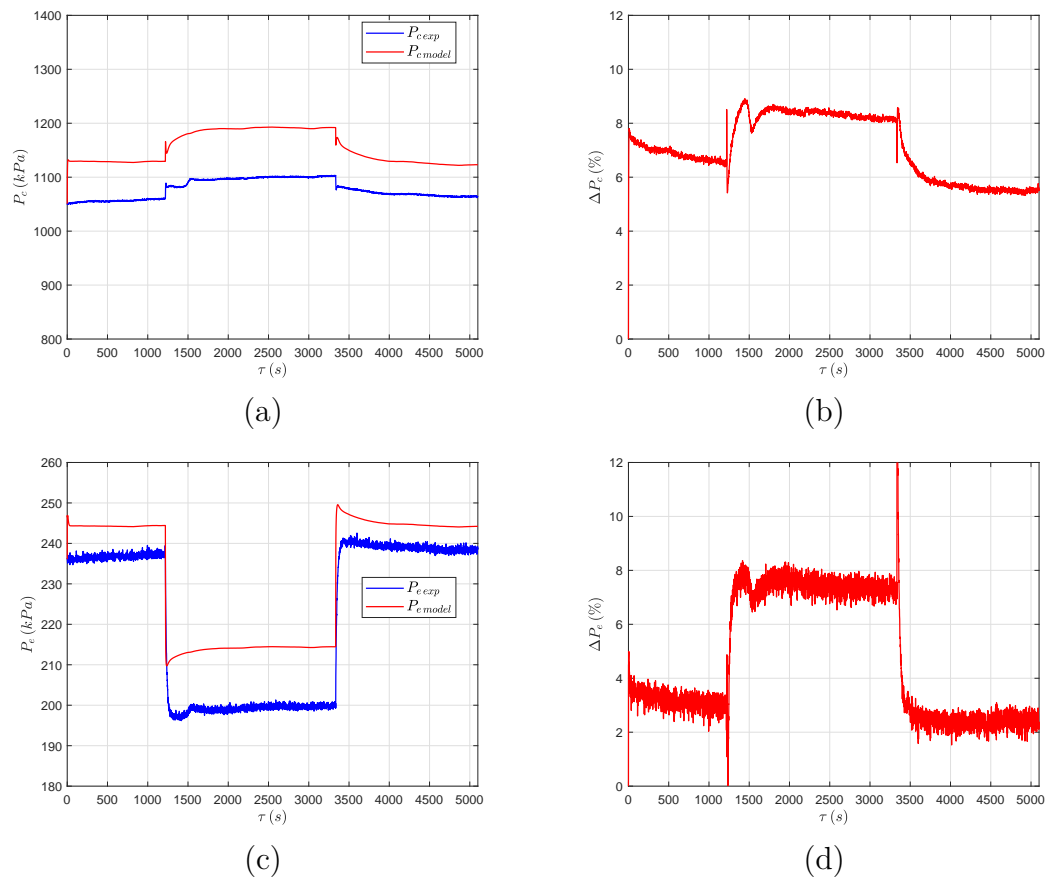


Figure 5.61: Validation of the complete model with the main system components. Comparison between the predicted and experimental pressure at the condenser ((a) and (b)) and at the evaporator ((c) and (d)), with $C_V = 1$, $C_{TP} = 1$, $C_L = 1$ and $C_f = 1$ under Test 2 conditions.

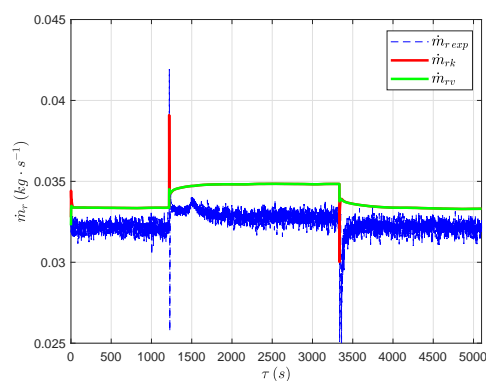


Figure 5.62: Validation of the complete model with the main system components. Model-predicted and experimental refrigerant mass flow rate, with $C_V = 1$, $C_{TP} = 1$, $C_L = 1$ and $C_f = 1$ under Test 2 conditions.

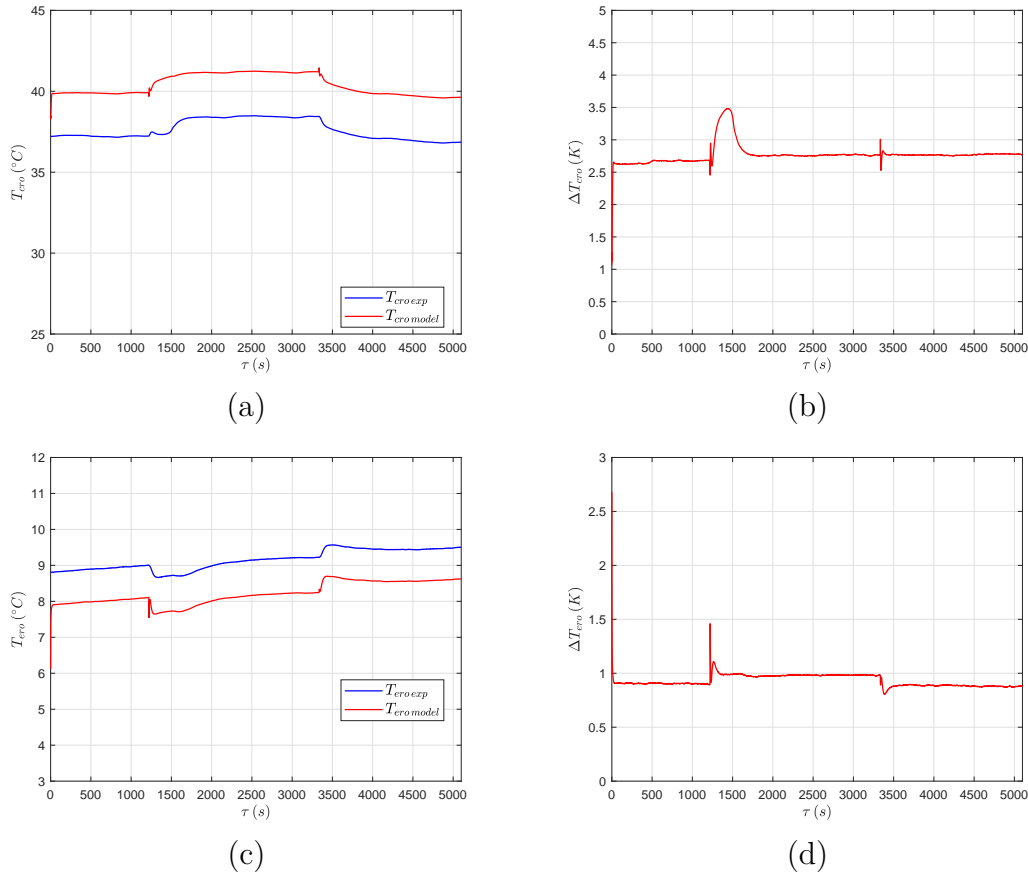


Figure 5.63: Validation of the complete model with the main system components. Comparison between the predicted and experimental temperature of the refrigerant at the outlet of the condenser ((a) and (b)) and the evaporator ((c) and (d)), with $C_V = 1$, $C_{TP} = 1$, $C_L = 1$ and $C_f = 1$ under Test 2 conditions.

The reliability of the model in predicting the outlet temperatures of the secondary fluids is confirmed also in the validation under Test 2 conditions. Indeed, as shown in Fig. 5.65, the maximum deviation between numerical and experimental data is below 0.8 K and 0.1 K (neglecting the spikes) for the condenser and the evaporator respectively.

The percentage deviation obtained for the electric power absorbed by the compressor under Test 2 conditions is below 4% and 10% when the rotational frequencies are 50 Hz and 65 Hz respectively, as shown in Fig. 5.66. The larger discrepancy at the higher rotational speed is mainly due to the deviations in the predicted pressures highlighted in Fig. 5.61 and to inaccuracies in the polynomials employed to model the compressor. As for the COP, Fig. 5.67 shows how the numerical trend reproduces fairly well the experimental one, with maximum deviations of about 8.3% highlighted at 65 Hz.

When setting the tuning coefficients in the condenser to $C_V = 1.35$, $C_{TP} = 1$, $C_L = 1.35$ and $C_f = 1.35$, the results obtained for the pressure in the heat

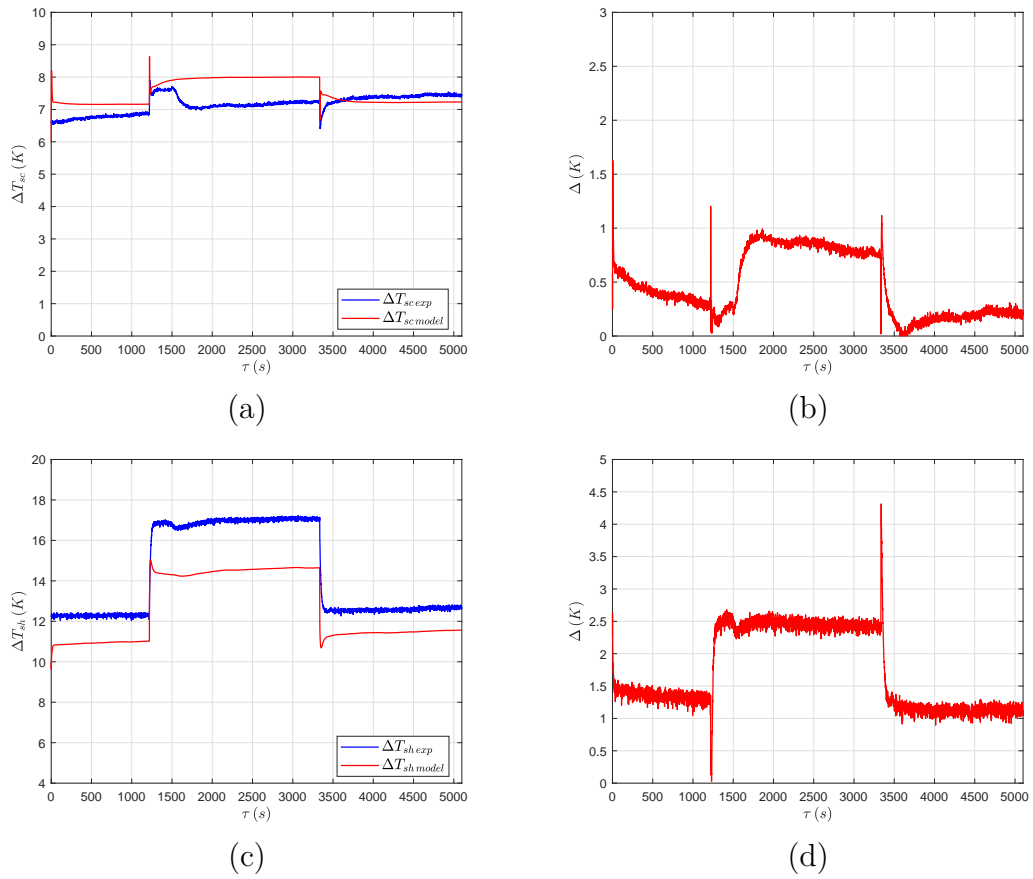


Figure 5.64: Validation of the complete model with the main system components. Comparison between the predicted and experimental subcooling and superheating of the refrigerant at the outlet of the condenser ((a) and (b)) and the evaporator ((c) and (d)), with $C_V = 1$, $C_{TP} = 1$, $C_L = 1$ and $C_f = 1$ under Test 2 conditions.

exchangers are those reported in Fig. 5.68. The relative deviation between numerical and experimental data is very low for both the condenser and the evaporator, always below 2.1% for the former and below 4.5% for the latter. The improvement in the prediction of the refrigerant pressure also allows to better estimate the mass flow rate through the valve and the compressor, as shown in Fig. 5.69.

The effects on the refrigerant temperature at the outlet of the heat exchangers are reported in Fig. 5.70; in particular a significant improvement can be noticed at the condenser, where the maximum deviation drops to a value slightly above 2 K. As for the refrigerant subcooling, reported in Fig. 5.71 (a) and (b), no significant improvements were noticed after introducing the non-unitary tuning coefficients, because of the simultaneous decrease in the condensation pressure and refrigerant outlet temperature. On the other hand, improvements in the prediction of the evaporation pressure reduce the maximum deviation in the superheating from 2.5 K to 1.7 K (see Fig. 5.71 (c)

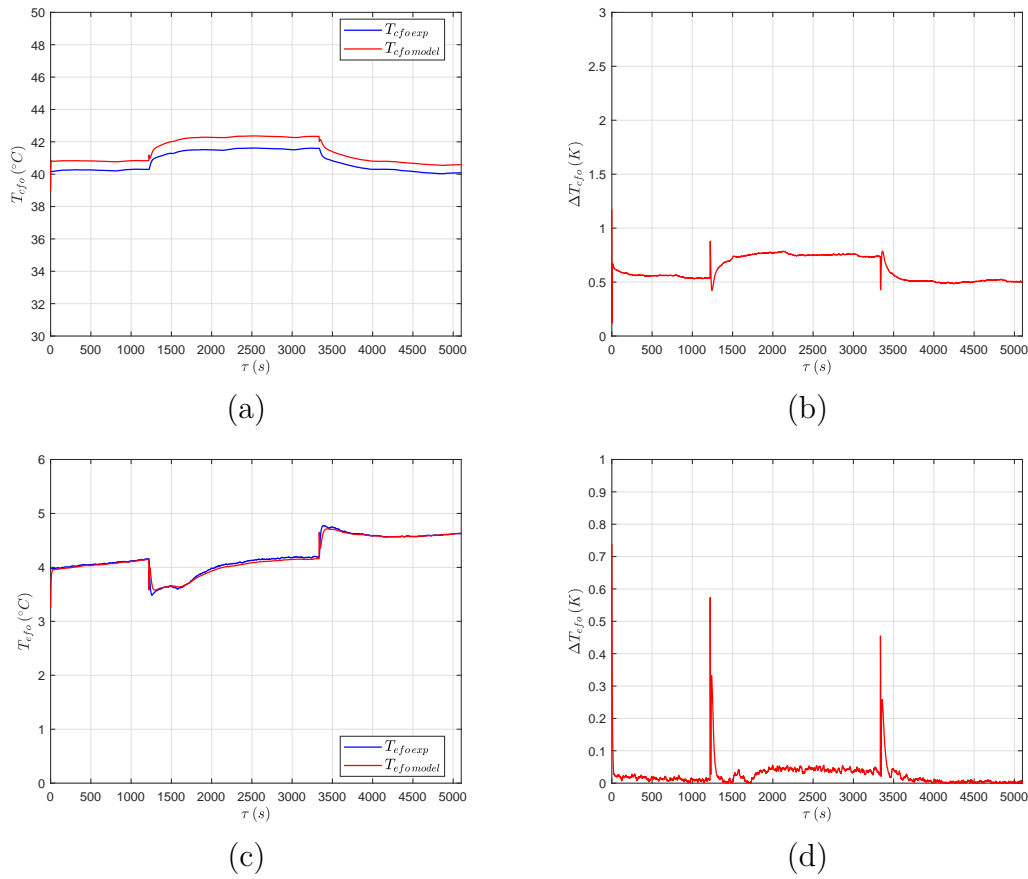


Figure 5.65: Validation of the complete model with the main system components. Comparison between the predicted and experimental temperature of the secondary fluids at the outlet of the condenser ((a) and (b)) and the evaporator ((c) and (d)), with $C_V = 1$, $C_{TP} = 1$, $C_L = 1$ and $C_f = 1$ under Test 2 conditions.

and (d)).

Tuning of the condenser also yields a better prediction of the electric power absorbed by the compressor, as shown in Fig. 5.72, where maximum deviations below 1% and 6% are highlighted at 50 Hz and 65 Hz respectively. As a consequence, prediction of the COP is also improved, as shown in Fig. 5.73.

5.7 Conclusions

In this section the experimental validation of the brazed-plate heat exchangers, of the compressor and of the EEV models was presented. In particular, the numerical predictions in terms of refrigerant pressure and outlet conditions for the heat exchangers (temperature, superheating and subcooling), secondary fluids outlet temperature, electric power consumption and COP were compared to the experimental data obtained during tests carried out on a water-to-water machine installed in the laboratories of the Polytechnic of Milan. Two tests

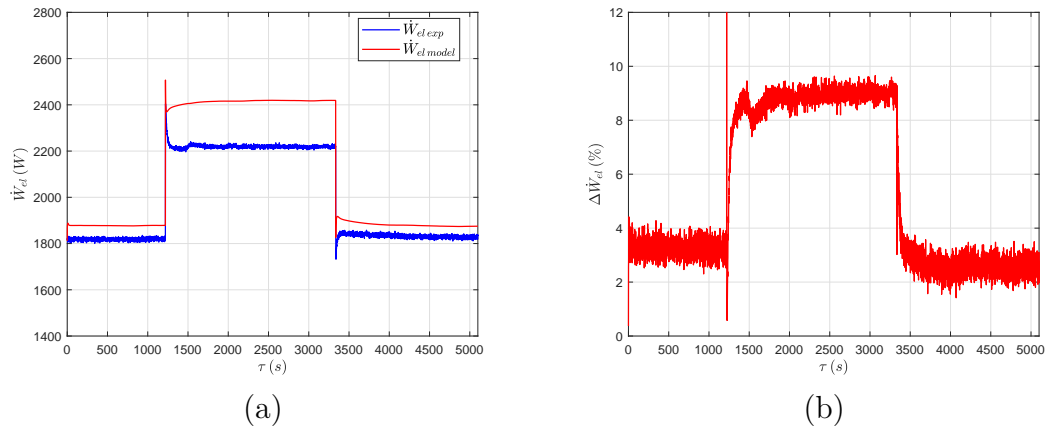


Figure 5.66: Validation of the complete model with the main system components. Comparison between the predicted and experimental electric power absorbed by the compressor (a) and percentage deviation (b), with $C_V = 1$, $C_{TP} = 1$, $C_L = 1$ and $C_f = 1$ under Test 2 conditions.

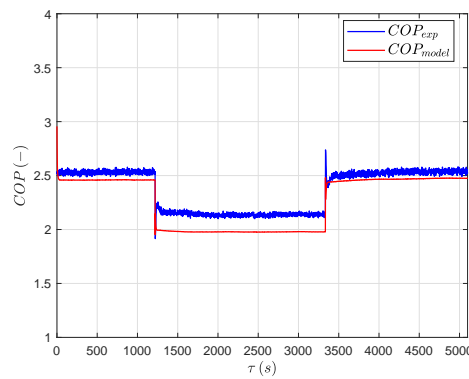


Figure 5.67: Validation of the complete model with the main system components. Comparison between the predicted and experimental COP (a) and percentage deviation (b), with $C_V = 1$, $C_{TP} = 1$, $C_L = 1$ and $C_f = 1$ under Test 2 conditions.

were conducted imposing sudden variations in the valve opening (Test 1) and in the rotational frequency of the compressor (Test 2), since they are among the main controlled variables in a vapour-compression refrigerating machine. Firstly, the fully-open discharge coefficient C_{D0} of the EEV was manually tuned to correctly reproduce the experimental trend of the refrigerant mass flow rate using the experimental pressures and refrigerant outlet conditions from the condenser as boundary conditions. Maximum percentage deviations between numerical and experimental data below 7.5% and 7% were obtained in Test 1 and Test 2 respectively after tuning.

Subsequently, the time-constant τ_k and the tuning coefficients C_{m_r} , $C_{\dot{W}_{el}}$ and C_T of the reciprocating compressor were determined to allow the compressor model to estimate the refrigerant outlet temperature, the refrigerant mass flow rate and the electric power absorbed. Considering both tests, the percentage

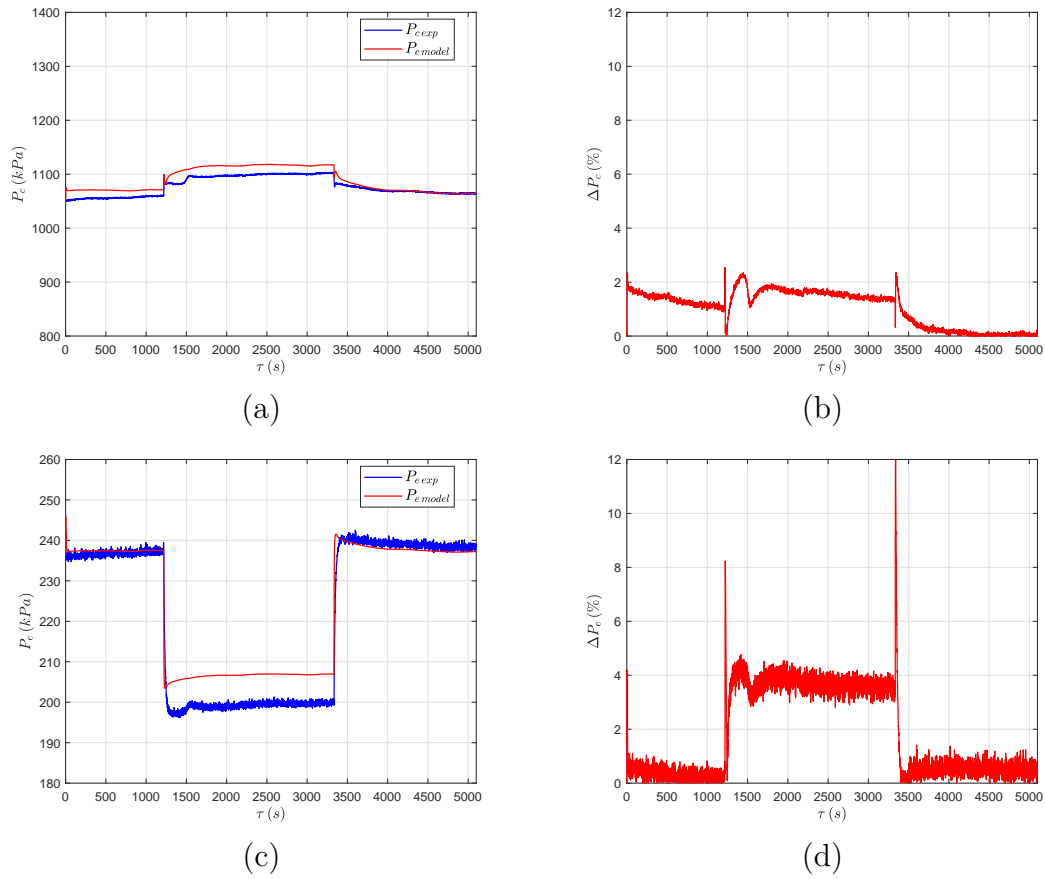


Figure 5.68: Validation of the complete model with the main system components. Comparison between the predicted and experimental pressure at the condenser ((a) and (b)) and at the evaporator ((c) and (d)), with $C_V = 1.35$, $C_{TP} = 1$, $C_L = 1.35$ and $C_f = 1.35$ under Test 2 conditions.

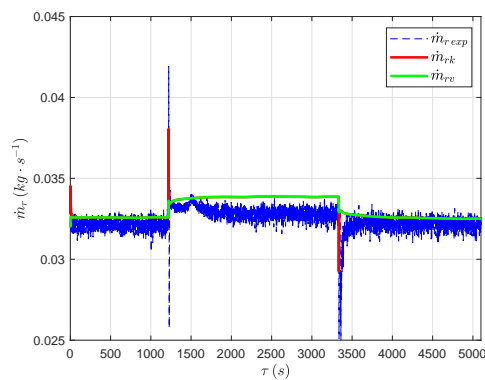


Figure 5.69: Validation of the complete model with the main system components. Model-predicted and experimental refrigerant mass flow rate, with $C_V = 1.35$, $C_{TP} = 1$, $C_L = 1.35$ and $C_f = 1.35$ under Test 2 conditions.

deviations obtained for \dot{m}_r and \dot{W}_{el} after the tuning procedure were below 6% and 4% respectively. As for T_{kro} , the maximum absolute deviation was 3.7

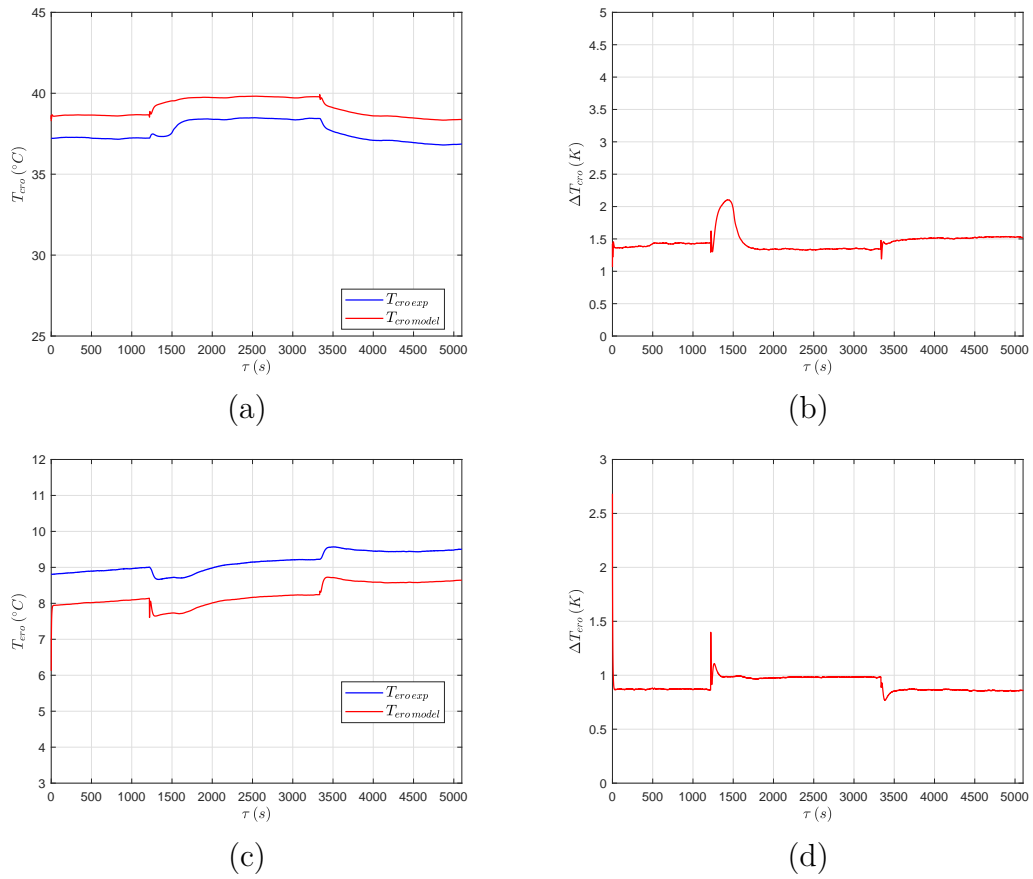


Figure 5.70: Validation of the complete model with the main system components. Comparison between the predicted and experimental temperature of the refrigerant at the outlet of the condenser ((a) and (b)) and the evaporator ((c) and (d)), with $C_V = 1.35$, $C_{TP} = 1$, $C_L = 1.35$ and $C_f = 1.35$ under Test 2 conditions.

K. The deviations may be ascribed to possible inaccuracies in the polynomials used at frequencies different from the nominal value of 50 Hz and in the simplified nature of the model. In particular, increasing the order of the compressor model by introducing a more detailed discretization to capture energy flows ought to lead to more precise results.

An open-loop model composed by the brazed-plate evaporator, the EEV and the compressor was set-up to validate the evaporator SMB model. The experimental condensation pressure and refrigerant outlet enthalpy from the condenser were used as inputs for the EEV and compressor models. A good match between numerical and experimental data was already obtained when the tuning coefficients C_{TP} , C_V and C_f were set to 1, with the highest deviations (about 2 K) highlighted for the refrigerant outlet temperature and superheating. To improve the model reliability, the value of C_V was manually tuned and a value of 2 was finally chosen; as a consequence, the maximum deviation for the refrigerant outlet temperature and superheating dropped to 1.5 K. The maximum deviation in the evaporation pressure was about 4%, corresponding

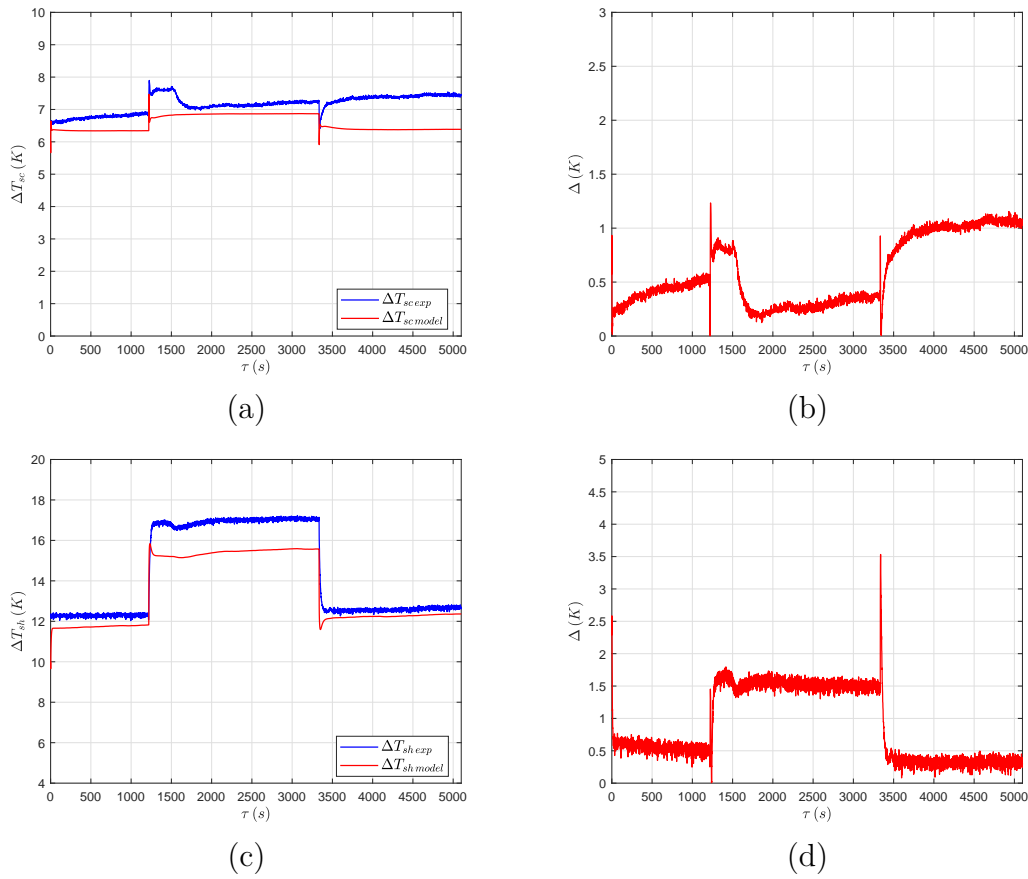


Figure 5.71: Validation of the complete model with the main system components. Comparison between the predicted and experimental subcooling and superheating of the refrigerant at the outlet of the condenser ((a) and (b)) and the evaporator ((c) and (d)), with $C_V = 1.35$, $C_{TP} = 1$, $C_L = 1.35$ and $C_f = 1.35$ under Test 2 conditions.

to the conditions of Test 2 at high compressor rotational speed, when the compressor model has the largest inaccuracies.

Finally, the model of the brazed-plate condenser was validated connecting it to the EEV, the compressor and the evaporator in a closed-loop model to simulate the dynamics of the whole machine. The liquid receiver, the suction accumulator and the pipes were not considered. In this case, the correction factors for the heat transfer coefficients in the single-phase regions in the condenser, C_V , C_L and C_f were tuned, markedly reducing the percentage deviations of the main variables of the cycle. The model also showed good predictive capability for the electric power absorbed by the compressor and for the COP, thus proving its usefulness in the energy analysis of vapour-compression cycles in transient conditions.

In the near future, experimental tests will be carried out imposing machine shut down in order to validate the model also as regards the machine off phase.

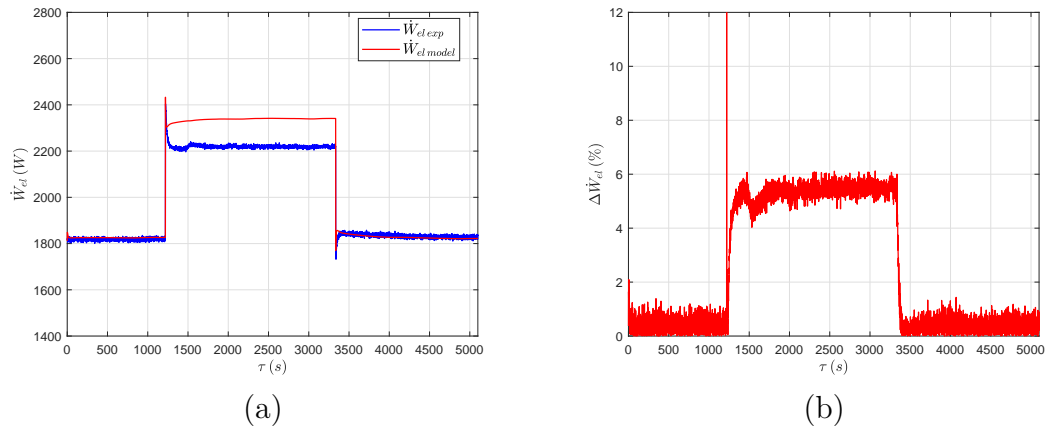


Figure 5.72: Validation of the complete model with the main system components. Comparison between the predicted and experimental electric power absorbed by the compressor (a) and percentage deviation (b), with $C_V = 1.35$, $C_{TP} = 1$, $C_L = 1.35$ and $C_f = 1.35$ under Test 2 conditions.

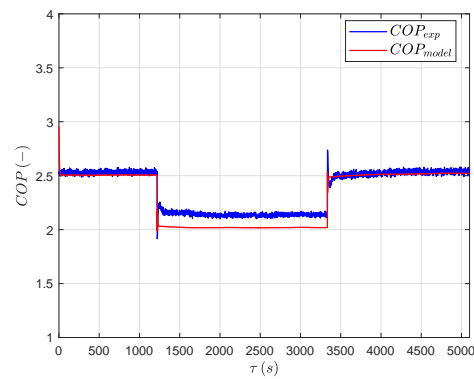


Figure 5.73: Validation of the complete model with the main system components. Comparison between the predicted and experimental COP (a) and percentage deviation (b), with $C_V = 1.35$, $C_{TP} = 1$, $C_L = 1.35$ and $C_f = 1.35$ under Test 2 conditions.

Chapter 6

Effects of the refrigerant accumulators on the dynamics of the VCS

As reported in Chapter 1, beside the four main elements of a VCS (evaporator, condenser, EEV and compressor), additional components are installed to prevent system failure. Among these, the suction accumulator and the liquid receiver have a great importance in the correct operation of such a system, since the former prevents liquid refrigerant to enter the compressor which is detrimental to the machine and the latter ensures the right amount of refrigerant mass in the circuit to cover varying thermal load conditions.

In this chapter the effects of the liquid receiver and the suction accumulator on the dynamics of the vapour-compression refrigerating machine are discussed, using the experimental data (Test 1 and Test 2) acquired from the water-to-water refrigerating machine presented in Chapter 5 as a benchmark. Indeed, Test 1 and Test 2 involve typical transients caused by the intervention of the control systems in a VCS. Two models combining the dynamics of the brazed-plate evaporator and suction accumulator in one case and that of the brazed-plate condenser and liquid receiver in the other were defined, similarly to what presented in [91]. Particular care was exerted in modelling the liquid receiver allowing the coexistence of a non-zero degree of subcooling at the outlet of the condenser and a partial filling condition of the receiver.

In sections 6.1 and 6.2 the governing equations of the combined models are presented, whilst in section 6.3 the results obtained are compared to the experimental data and to the numerical predictions of the model without accumulators.

6.1 Brazed-plate evaporator and suction accumulator model

The model of the brazed-plate evaporator and the suction accumulator combines the equations describing the SMB formulation of the evaporator pre-

sented in sections 2.5.1 and 2.5.2 (the off period is currently neglected) and the mass and energy balance at the suction accumulator (neglecting the dynamics of the shell), which is considered as a single lumped parameter described by the pressure P , which is the same as the evaporator (under the assumption of negligible pressure drop along the pipe), and the mean density ρ_{ac} . Figure 6.1 shows the inputs and the outputs to the suction accumulator model: \dot{m}_{rint} is the intermediate refrigerant mass flow rate which goes from the evaporator to the accumulator and is dynamically calculated during the simulation (thus in the equations presented in sections 2.5.1 and 2.5.2 \dot{m}_{rint} takes the place of \dot{m}_{ro}), h_{ero} is the refrigerant outlet enthalpy from the evaporator, calculated as discussed in section 2.5.4, \dot{m}_{ro} is the refrigerant mass flow rate at the outlet, coming from the compressor model, and h_{acro} is the refrigerant outlet enthalpy from the accumulator.

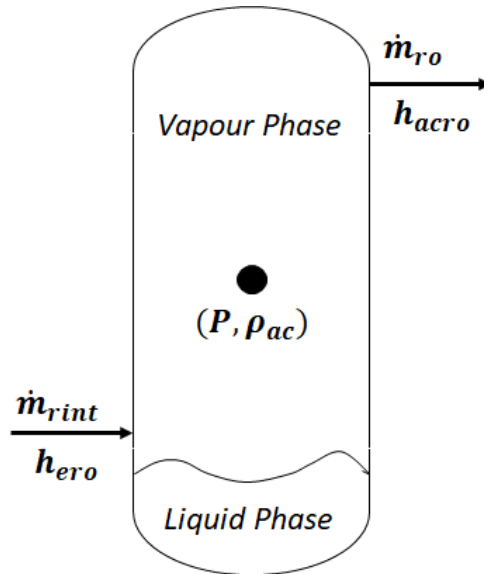


Figure 6.1: Inputs and outputs to the suction accumulator model.

The mass balance of the accumulator can be written as shown in Eq. 6.1, where V_{ac} is the accumulator total volume.

$$\boxed{V_{ac} \frac{d\rho_{ac}}{d\tau} - \dot{m}_{rint} = -\dot{m}_{ro}} \quad (6.1)$$

Equation 6.1 considers the pressure P and the refrigerant's mean density ρ_{ac} as independent variables and the analytical manipulation presented in [72] and already used to model the heat exchangers off-periods (see section 2.5.3) lead to Eq. 6.2. h_{ac} is the refrigerant mean enthalpy within the accumulator and can be calculated from property tables as a function of P and ρ_{ac} , whilst \dot{Q}_{acc} is the heat transfer rate between the refrigerant at temperature T_{ac} and the

surrounding ambient at temperature T_{amb} .

$$\boxed{-\left(\frac{\partial \rho_{ac}}{\partial P}\bigg|_{h_{ac}} + \frac{1}{\rho_{ac}} \frac{\partial \rho_{ac}}{\partial h_{ac}}\bigg|_P\right) \frac{dP}{d\tau} + \frac{d\rho_{ac}}{d\tau} - \frac{\partial \rho_{ac}}{\partial h_{ac}}\bigg|_P \frac{(h_{ero} - h_{ac})}{\rho_{ac} V_{ac}} \dot{m}_{rint} = \frac{\partial \rho_{ac}}{\partial h_{ac}}\bigg|_P \left(\frac{\dot{Q}_{acc} - \dot{m}_{ro}(h_{acro} - h_{ac})}{\rho_{ac} V_{ac}}\right)} \quad (6.2)$$

\dot{Q}_{acc} is calculated through Eq. 6.3, where A_{ac} is the total outer surface of the accumulator and α_{ac} is the global heat transfer coefficient, set constant and manually tuned to better match the refrigerant temperature at the compressor inlet.

$$\dot{Q}_{ac} = \alpha_{ac} A_{ac} (T_{amb} - T_{ac}) \quad (6.3)$$

Knowing the total volume of the accumulator V_{ac} , the void fraction $\bar{\gamma}_{ac}$ can also be calculated as a function of the mean density ρ_{ac} and of the saturated liquid and vapour densities ρ_l and ρ_v , as shown in Eq 6.4.

$$\bar{\gamma}_{ac} = \frac{\rho_{ac} - \rho_l}{\rho_v - \rho_l} \quad (6.4)$$

The enthalpy of the refrigerant at the outlet of the accumulator depends on the value of $\bar{\gamma}_{ac}$. In particular, if $0 < \bar{\gamma}_{ac} < 1$, i.e. a two-phase condition occurs within the accumulator (the evaporator is working in the single-region formulation, with a two-phase outlet condition), the refrigerant outlet enthalpy h_{acro} is equal to h_v . On the other hand, if the accumulator is filled with superheated vapour ($\bar{\gamma}_{ac} = 1$), an assumption of uniform condition throughout the accumulator is made and the outlet enthalpy h_{acro} equals the mean enthalpy h_{ac} . To ensure mass conservation and also to lay the foundation for the off-duty formulation of the combined evaporator-accumulator model, a global mass balance is introduced for a thermodynamic system including both the evaporator and the accumulator, leading to Eq. 6.5, where \dot{m}_{ri} is the inlet refrigerant mass flow rate coming from the EEV model which enters the combined evaporator-accumulator system, \dot{m}_{ro} is the outlet refrigerant mass flow rate obtained from the compressor model, ρ_m is the refrigerant mean density in the evaporator and A_{Cr} and L_{tot} are respectively the refrigerant-side cross-section area and total path length in the brazed-plate evaporator.

$$\boxed{A_{Cr} L_{tot} \frac{d\rho_m}{d\tau} + V_{ac} \frac{d\rho_{ac}}{d\tau} = \dot{m}_{ri} - \dot{m}_{ro}} \quad (6.5)$$

The state-variables can thus be determined at each time-step solving Eqs. 6.1, 6.2, 6.5 together with Eqs. 2.20, 2.28, 2.32, 2.34, 2.35, 2.41, 2.42 if the evaporator is working with the two-region formulation or with Eqs. 2.44-2.49 if the evaporator works with the one-region formulation.

6.2 Brazed-plate condenser and liquid receiver model

To develop the combined model of the brazed-plate condenser and the liquid receiver, an approach different from that presented in section 6.1 was chosen. Indeed, if a single lumped parameter is considered as done for the evaporator-accumulator model, when the degree of subcooling at the outlet of the condenser is non-zero and no expansion valves are placed between the two components (like in the experimental facility used for the tests), neglecting the heat exchanged with the surrounding, would cause the receiver to reach a condition of thermodynamic equilibrium where it is completely filled with liquid refrigerant. However, it is common in practice for the receiver to be fed with subcooled refrigerant from the condenser without being completely full of liquid [109]. Moreover, numerical issues, especially for the calculation of pressure, can arise when the receiver is completely filled with an incompressible fluid. Differently from Thermosys[®], [104, 105], whose models force the refrigerant at the condenser outlet to be in two-phase conditions when it is connected to the receiver, a combined model of the brazed-plate condenser and the receiver was realised to allow the coexistence of subcooled conditions at the condenser outlet and a partial filling condition of the receiver. To this aim, the receiver was discretized into two regions, associated to the liquid and gas phases, as shown in Fig. 6.2, where V_v and V_{sc} are the volumes of the dry-saturated vapour and the subcooled liquid respectively, whose sum is equal to the total volume of the receiver V_{rec} , ρ_{sc} is the density of the subcooled liquid phase, \dot{m}_{rint} is the intermediate refrigerant mass flow rate from the condenser, h_{cro} is the refrigerant enthalpy at the condenser outlet, \dot{m}_{ro} is the refrigerant mass flow rate at the receiver outlet, calculated by the EEV model, and h_{recro} is the refrigerant outlet enthalpy from the receiver.

The main modelling simplifications are:

- the refrigerant pressure in the receiver is the same as the condenser, thus neglecting the pressure drop along the pipe;
- the vapour phase has the properties of the dry-saturated vapour at pressure P ;
- the heat and mass transfer between the dry-saturated vapour and the liquid phase is neglected, thus considering the gas phase as an incompressible fluid;
- the refrigerant leaves the receiver at the conditions of the liquid phase ($h_{recro} = h_{sc}$);
- the receiver is considered as adiabatic.

Depending on the refrigerant conditions at the condenser outlet, the mass and energy balance of the liquid phase, the mass balance of the vapour phase and

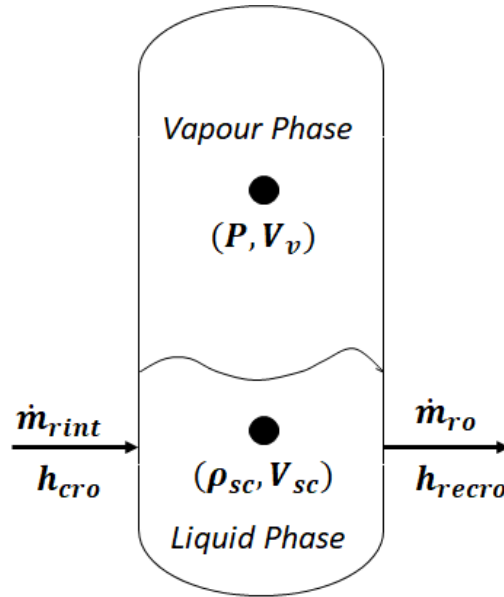


Figure 6.2: Inputs and outputs to the liquid receiver model.

the conservation of the receiver total volume are combined with the equations presented in sections 2.6.1-2.6.4 (the machine off condition is currently neglected), where \dot{m}_{rint} takes the place of \dot{m}_{ro} .

6.2.1 Subcooled liquid at the condenser outlet

When the refrigerant at the condenser outlet is subcooled liquid, all the intermediate mass flow rate \dot{m}_{rint} contributes to the mass balance of the liquid phase, which can be written as a function of the liquid density ρ_{sc} and volume V_{sc} as shown in Eq. 6.6.

$$\boxed{V_{sc} \frac{d\rho_{sc}}{d\tau} + \rho_{sc} \frac{dV_{sc}}{d\tau} - \dot{m}_{rint} = -\dot{m}_{ro}} \quad (6.6)$$

Equation 6.7 describes the energy balance of the liquid phase considering the condition of adiabaticity and the equality between the refrigerant outlet enthalpy h_{reCro} and the enthalpy h_{sc} of the liquid phase within the receiver, which can be calculated from property tables as a function of P and ρ_{sc} . The equation was written using the pressure P and the liquid density ρ_{sc} , by means of the same analytical manipulation presented in [72] and already used for the accumulator and the heat exchangers off-periods (see section 2.5.3).

$$\boxed{-\left(\frac{\partial \rho_{sc}}{\partial P}\bigg|_{h_{sc}} + \frac{1}{\rho_{sc}} \frac{\partial \rho_{sc}}{\partial h_{sc}}\bigg|_P\right) \frac{dP}{d\tau} + \frac{d\rho_{sc}}{d\tau} - \frac{\partial \rho_{sc}}{\partial h_{sc}}\bigg|_P \frac{(h_{cro} - h_{sc})}{\rho_{sc} V_{sc}} \dot{m}_{rint} = 0} \quad (6.7)$$

Since the refrigerant enters and leaves the receiver in subcooled liquid conditions, the mass balance for the vapour phase can be written as shown in Eq. 6.8.

$$\boxed{V_v \frac{\partial \rho_v}{\partial P} \frac{dP}{d\tau} + \rho_v \frac{dV_v}{d\tau} = 0} \quad (6.8)$$

To allow the conservation of the receiver total volume, Eq. 6.9 is introduced.

$$\boxed{\frac{dV_{sc}}{d\tau} + \frac{dV_v}{d\tau} = 0} \quad (6.9)$$

As done for the combined model of the brazed-plate evaporator and accumulator, a global mass balance is introduced to ensure mass conservation and to lay the foundations for the off-duty formulation, as shown in Eq. 6.10, where ρ_m is the refrigerant mean density in the condenser, A_{Cr} and L_{tot} are the refrigerant-side cross-section area and total path length in the brazed-plate condenser and m_{rec} is the total refrigerant mass in the receiver respectively.

$$A_{Cr} L_{tot} \frac{d\rho_m}{d\tau} + \frac{dm_{rec}}{d\tau} = \dot{m}_{ri} - \dot{m}_{ro} \quad (6.10)$$

Recognizing that $\frac{dm_{rec}}{d\tau} = \dot{m}_{rint} - \dot{m}_{ro}$, the global mass balance can be written as shown in Eq. 6.11.

$$\boxed{A_{Cr} L_{tot} \frac{d\rho_m}{d\tau} + \dot{m}_{rint} = \dot{m}_{ri}} \quad (6.11)$$

To determine the state variables at each time-step, equations 6.6-6.9, 6.11 can be combined with equations 2.93-2.98, 2.100, 2.101 if the condenser is working in the V-TP-L formulation, or with equations 2.101, 2.120-2.125 if the condenser is working in TP-L formulation.

6.2.2 Two-phase conditions at the condenser outlet

If the refrigerant leaves the condenser as a two-phase mixture, only a fraction of the intermediate mass flow rate \dot{m}_{rint} contributes to the mass balance of the liquid phase, which can be written as shown in Eq. 6.12, where x_o is the refrigerant quality at the condenser outlet.

$$\boxed{V_{sc} \frac{d\rho_{sc}}{d\tau} + \rho_{sc} \frac{dV_{sc}}{d\tau} - (1 - x_o) \dot{m}_{rint} = -\dot{m}_{ro}} \quad (6.12)$$

As for the energy balance of the liquid phase, reported in Eq. 6.13, it has been considered that the refrigerant, entering the receiver in two-phase conditions, is separated in its liquid and vapour phases, and only the enthalpy of the former, h_l , contributes to the internal energy variation of the liquid contained therein.

$$\boxed{-\left(\frac{\partial \rho_{sc}}{\partial P} \Big|_{h_{sc}} + \frac{1}{\rho_{sc}} \frac{\partial \rho_{sc}}{\partial h_{sc}} \Big|_P \right) \frac{dP}{d\tau} + \frac{d\rho_{sc}}{d\tau} - \frac{\partial \rho_{sc}}{\partial h_{sc}} \Big|_P \frac{(h_l - h_{sc})}{\rho_{sc} V_{sc}} (1 - x_o) \dot{m}_{rint} = 0} \quad (6.13)$$

In this case, the mass balance of the vapour phase can be written as shown in Eq. 6.14, where $x_o \dot{m}_{rint}$ is the vapour mass flow rate coming from the condenser.

$$\boxed{V_v \frac{\partial \rho_v}{\partial P} \frac{dP}{d\tau} + \rho_v \frac{dV_v}{d\tau} - x_o \dot{m}_{rint} = 0} \quad (6.14)$$

Also in this case, Eqs. 6.9 and 6.11 are solved to ensure the total volume conservation and the mass conservation in the combined model.

To determine the state variables at each time-step, Eqs. 6.9, 6.11-6.14 are combined with Eqs. 2.100, 2.111-2.116 if the condenser is working in the V-TP formulation or with Eqs. 2.131-2.136 if the condenser is working in the TP formulation.

6.3 Results

The model of the water-to-water refrigerating machine with suction accumulator and liquid receiver was used to simulate the dynamic behaviour of the machine located in the laboratories of the Polytechnic of Milan under the experimental test conditions (Test 1 and Test 2) discussed in Chapter 5. Similarly to what was presented there, the combined model of the brazed-plate evaporator and the suction accumulator was tested with an open-loop model first, connecting it to the EEV and the compressor models, in order to find suitable values of the correction factors for the heat transfer coefficients in the evaporator (C_{TP}, C_V, C_f) and for the global heat transfer coefficient α_{ac} in the accumulator. The same values $C_{TP} = 1$, $C_V = 2$ and $C_f = 1$ used for the evaporator model without accumulator were adopted and α_{ac} was set to $12 \text{ W} \cdot \text{m}^{-2} \cdot \text{K}^{-1}$. As for the combined model of the brazed-plate condenser and the liquid receiver, the tuning procedure resulted in the following values of the correction factors: $C_{TP} = 1$, $C_L = 0.7$, $C_V = 0.7$ and $C_f = 0.7$. Moreover, the value of the liquid volume in the receiver, V_{sc} , was initialized to the 67% of the total volume V_{rec} , in order to capture the total refrigerant charge in the machine (about 2.7 kg).

In the following the results obtained with the tuned model of the whole machine will be compared to the experimental data and to the results obtained with the tuned model without accumulators.

6.3.1 Test 1

This section presents the results obtained under Test 1 conditions. Figure 6.3 shows the results for the pressure at the condenser ((a) and (b)) and at the evaporator ((c) and (d)). The introduction of the liquid receiver and of the suction accumulator allows to better reproduce the pressure dynamics at the two heat exchangers; at the condenser the maximum percentage deviation drops from 3.6% to 2.3%, whilst at the evaporator, excluding the spikes in correspondence of the sudden steps in the EEV opening, it always lies below 3% instead of 4%.

The refrigerant temperature and degree of subcooling at the outlets of the condenser and the receiver are reported in Fig. 6.4 (a) and (b) respectively. It can be noticed how the temperature at the outlet of the receiver (purple curve) is superimposed to that related to the outlet of the condenser (green curve), because of the condition of adiabaticity imposed to the receiver. When introducing the receiver and the accumulator, no significant improvements are highlighted for the refrigerant outlet temperature at the condenser. However, since the condensation pressure P_c is captured with higher reliability, the prediction of the refrigerant subcooling ΔT_{sc} is significantly improved, both qualitatively and quantitatively (the maximum absolute deviation with respect to experimental data drops from 2 K to 1 K).

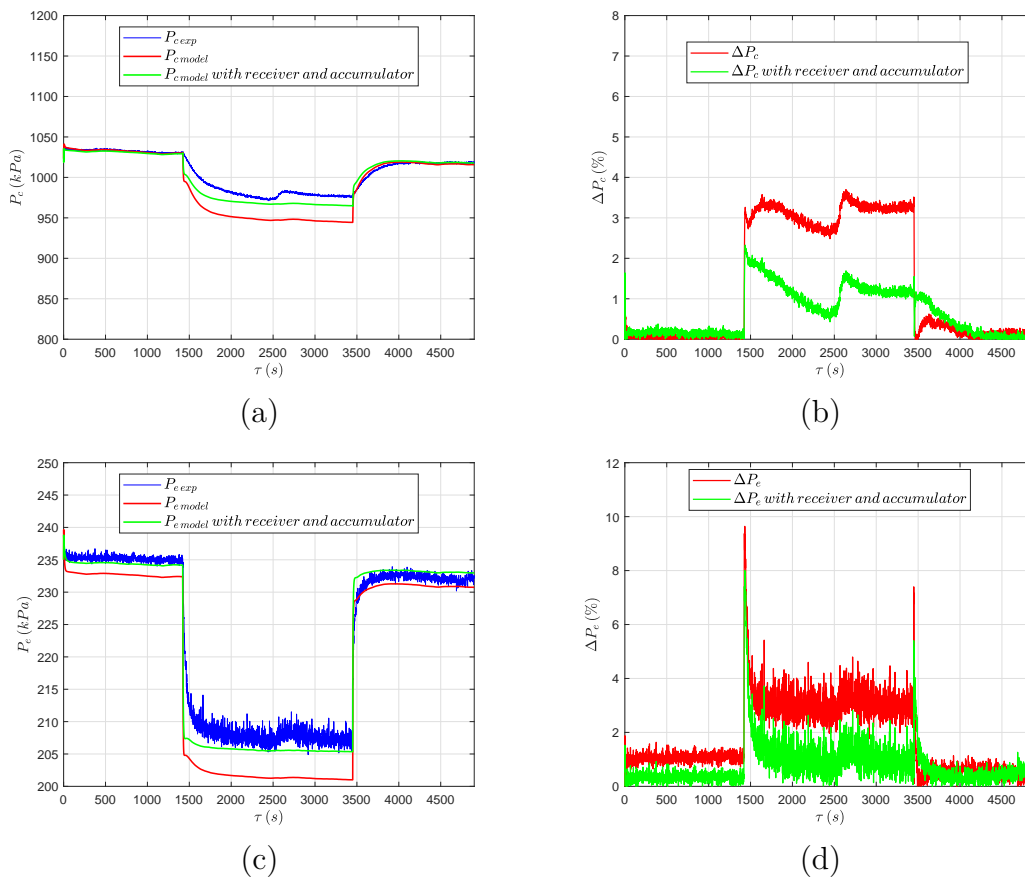


Figure 6.3: Validation of the complete model. Pressure at the condenser ((a) and (b)) and at the evaporator ((c) and (d)) under Test 1 conditions.

Figure 6.5 (a) shows how the pressure drop in the high pressure side of the circuit makes degree of filling for the receiver decrease. Indeed, as can be seen from Fig. 6.5 (b), the refrigerant mass in the condenser m_c slightly increases, consistently with the slight increment in the refrigerant subcooling at the condenser outlet, whilst the refrigerant mass in the receiver m_{rec} decreases. The

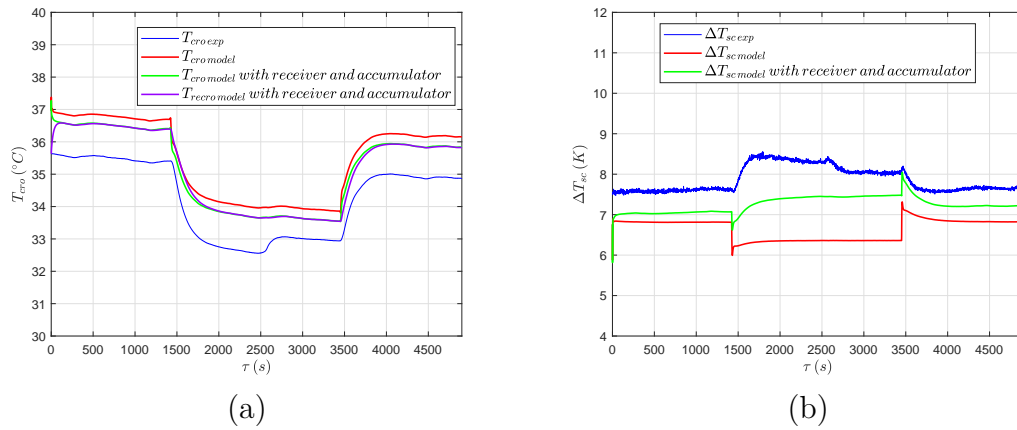


Figure 6.4: Validation of the complete model. Refrigerant outlet temperature (a) and subcooling (b) at the condenser outlet under Test 1 conditions.

results also prove how the combined model of the brazed-plate condenser and the receiver allows the coexistence of a non-zero degree of subcooling and a partial filling condition of the receiver.

Figure 6.6 reports the results obtained for the refrigerant temperature (a)

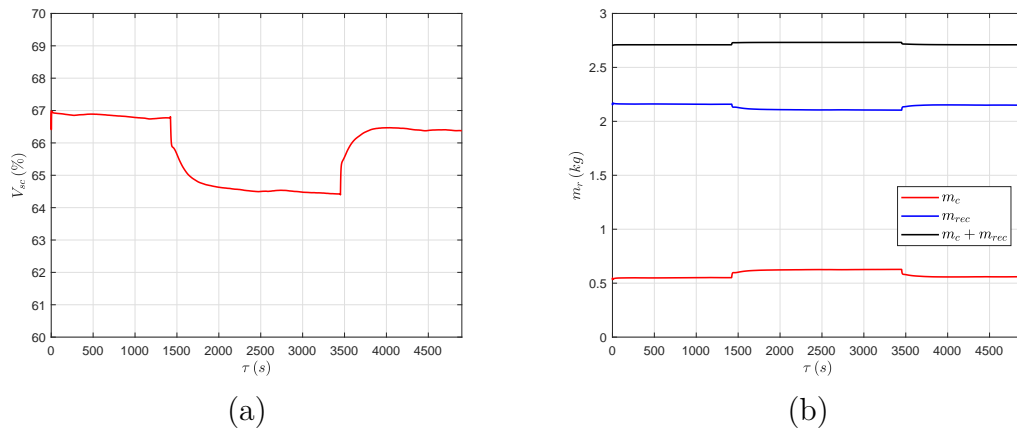


Figure 6.5: Receiver degree of filling (a) and refrigerant mass in the high pressure side of the circuit (b) under Test 1 conditions.

and superheating (b) at the evaporator outlet. The introduction of the suction accumulator does not influence significantly the prediction of T_{ero} and ΔT_{sh} , since the green and red curves overlap (absolute deviations around 1 K). Figure 6.6 (a) also shows the refrigerant temperature at the outlet of the suction accumulator, and thus at the compressor inlet, highlighting a good match between numerical predictions and experimental data. It can also be noticed how the refrigerant gains between 1 K and 2 K when flowing from the evaporator to the compressor. The presence of the accumulator thus allows to better capture the fluid conditions at the compressor inlet.

As shown in Fig. 6.7, the accumulator always works with a unitary void fraction $\bar{\gamma}_{ac}$, which means that it is completely filled with superheated vapour,

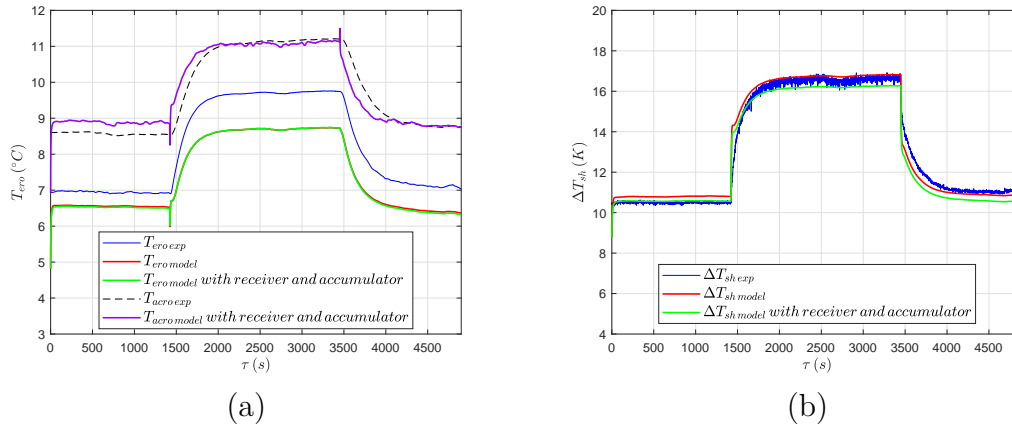


Figure 6.6: Validation of the complete model. Refrigerant outlet temperature (a) and superheating (b) at the evaporator outlet under Test 1 conditions.

consistent with the conditions at the evaporator outlet.

The outlet temperatures of the secondary fluids are reported in Fig. 6.8,

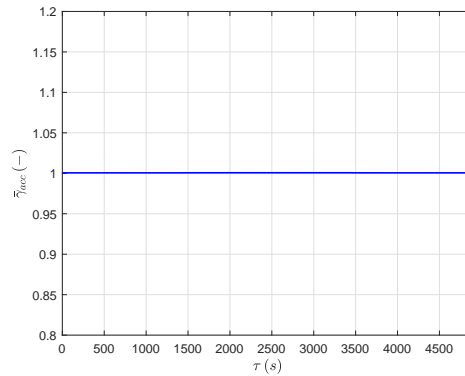


Figure 6.7: Void fraction in the accumulator under Test 1 conditions.

confirming the good predictive capability already shown by the model without accumulators.

Prediction of the electric power absorbed by the compressor, Fig. 6.9, slightly improves introducing the suction accumulator and the liquid receiver. This is mainly due to the more accurate estimate of the evaporation and condensation pressure. In particular, neglecting the spikes, the maximum percentage deviation with respect to experimental data drops from 4% to 3% confirming the usefulness of the model in the energy analysis in transient regime.

The results in terms of COP are reported in Fig. 6.10. The predictive capability of the model with accumulators is as good as that shown by the model with the main components only.

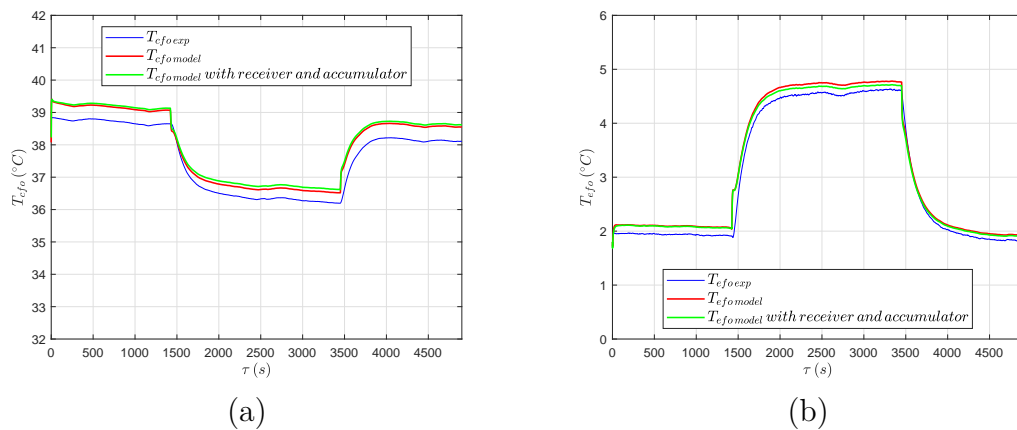


Figure 6.8: Validation of the complete model. Outlet temperature of the secondary fluid at the condenser (a) and at the evaporator (b) under Test 1 conditions.

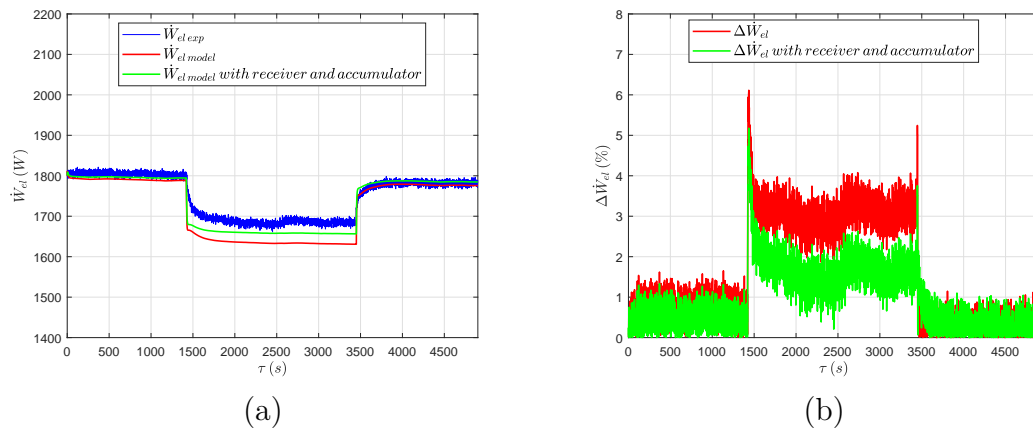


Figure 6.9: Validation of the complete model. Electric power absorption (a) and its percentage deviation (b) under Test 1 conditions.

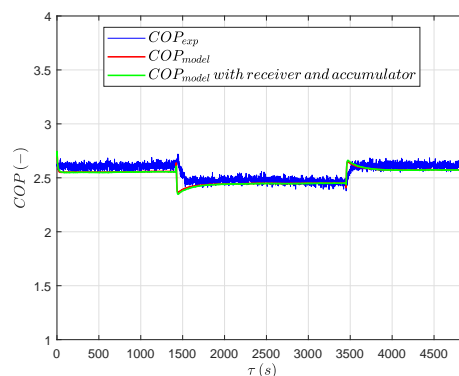


Figure 6.10: Validation of the complete model. COP under Test 1 conditions.

6.3.2 Test 2

The plots in this section illustrate the results obtained under Test 2 conditions. Figure 6.11 shows the results for condensation pressure ((a) and (b))

and evaporation pressure ((c) and (d)). As already seen for Test 1 conditions, condensation pressure is captured more precisely thanks to the introduction of the liquid receiver. In fact, the percentage deviation with respect to experimental data drops sharply, especially at high rotational frequency (from 2% to 1%). No particular variations in the prediction of the evaporation pressure are noted.

The results obtained for T_{cro} and ΔT_{sc} are shown in Fig. 6.12 (a) and (b) re-

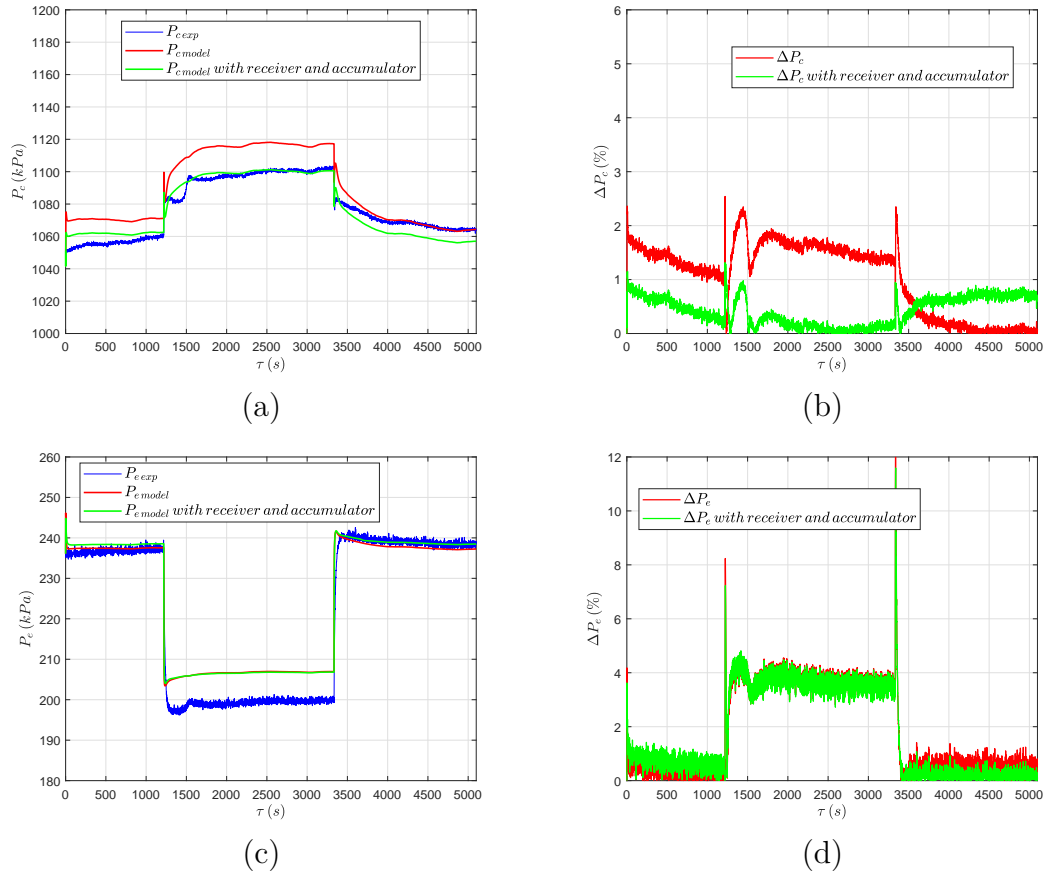


Figure 6.11: Validation of the complete model. Pressure at the condenser ((a) and (b)) and at the evaporator ((c) and (d)) under Test 2 conditions.

spectively. Like for Test 1, the refrigerant temperature at the condenser outlet is not significantly affected by the presence of the receiver. The trend of T_{recro} and of T_{cro} overlap here too, because of adiabaticity. In this case, prediction of the subcooling is slightly worse, as can be noticed in Fig. 6.12 (b). In particular, the model with the receiver predicts a subcooling about 0.5 K lower than the value predicted by the model without receiver, when the frequency is at 65 Hz.

Under Test 2 conditions, the increase in compressor speed causes a transfer of refrigerant from the low to the high pressure side of the circuit, increasing the amount of liquid in the receiver (which is consistent with the increase in condensation pressure), as shown in Fig. 6.13 (a). Part (b) of the same figure

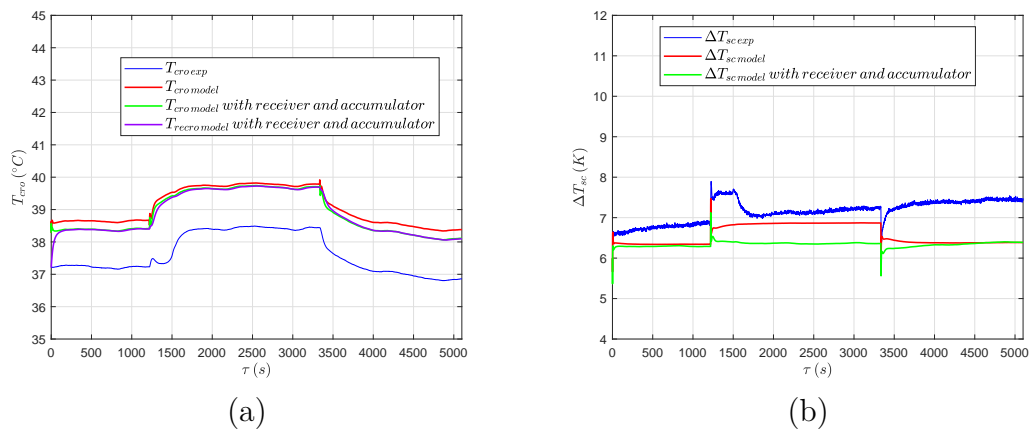


Figure 6.12: Validation of the complete model. Refrigerant outlet temperature (a) and subcooling (b) at the condenser outlet under Test 2 conditions.

reports the time evolution of the refrigerant mass in the high pressure side of the circuit, confirming the slight increase of mass in the receiver when the frequency steps from 50 Hz to 65 Hz.

Also in this case, the effects of the suction accumulator on the refrigerant

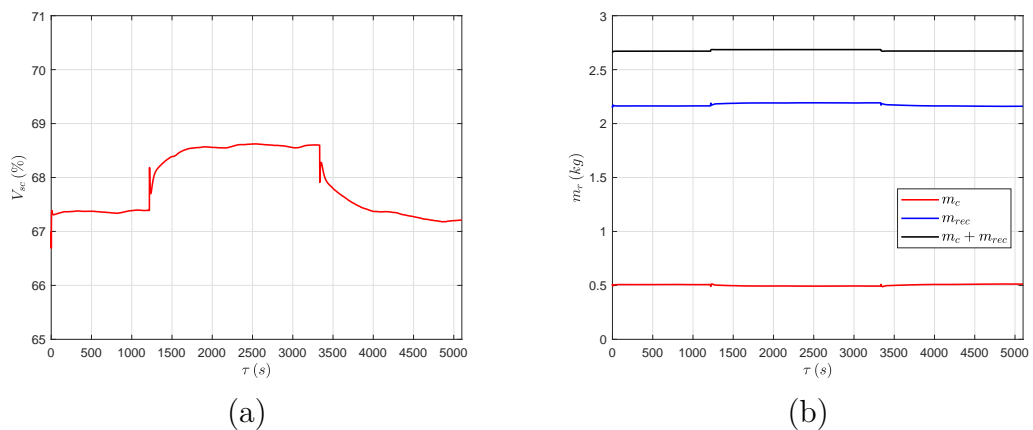


Figure 6.13: Receiver degree of filling (a) and refrigerant mass in the high pressure side of the circuit (b) under Test 2 conditions.

temperature and superheating at the evaporator outlet are negligible, as can be seen from Fig. 6.14 (a) and (b) respectively. Tuning of the heat transfer coefficient α_{ac} in the accumulator, which is completely filled with superheated vapour, allows to better match the refrigerant temperature at the compressor inlet.

As shown in Fig. 6.15, the models with and without accumulators offer the same prediction capability for the temperature of the secondary fluids at the outlet of the heat exchangers. Figure 6.16 reports the time trend of the electric power absorbed by the compressor in Test 2 (a) and the percentage deviation with respect to experimental data (b). The predictive capability of the two

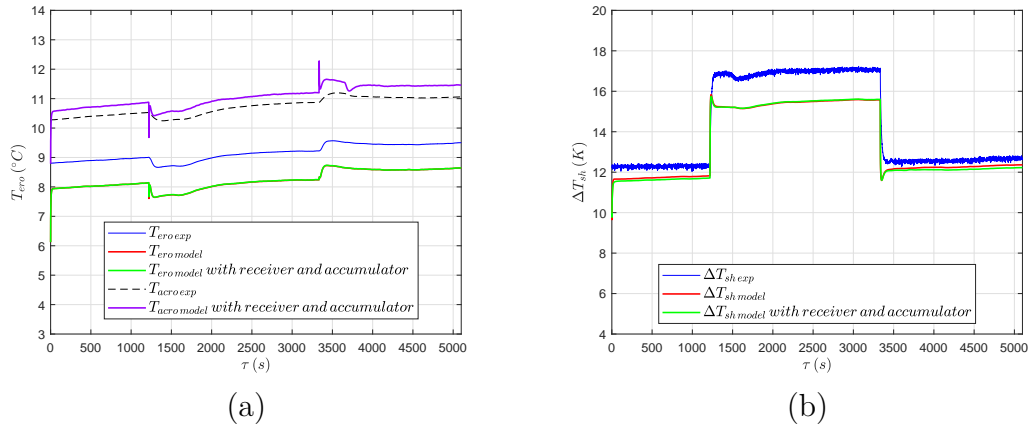


Figure 6.14: Validation of the complete model. Refrigerant outlet temperature (a) and superheating (b) at the evaporator outlet under Test 2 conditions.

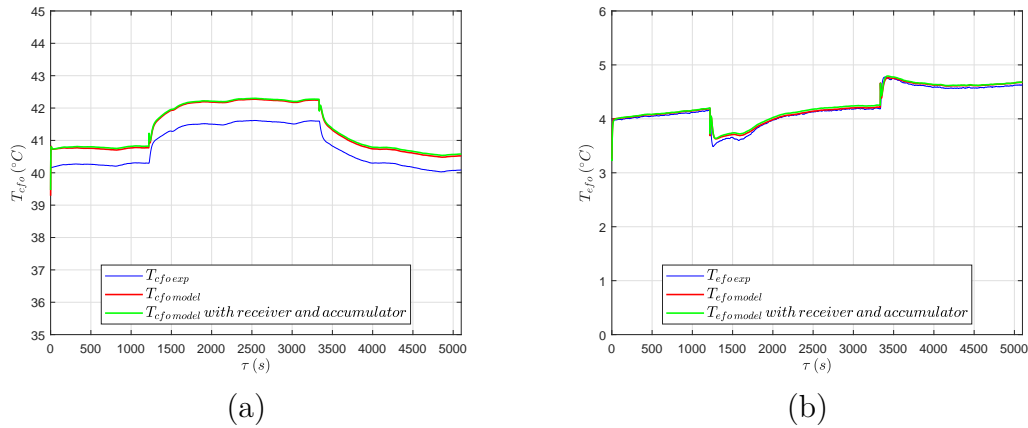


Figure 6.15: Validation of the complete model. Outlet temperature of the secondary fluid at the condenser (a) and at the evaporator (b) under Test 2 conditions.

models is identical. In fact, the main cause of the larger discrepancy at high rotational speeds can be associated to uncertainties in the polynomials used and to simplifying assumptions in modelling the compressor. The same considerations can be made for the COP, which is plotted in Fig. 6.17.

6.4 Conclusions

In this chapter, the combined dynamic models of the brazed-plate evaporator together with the suction accumulator and of the brazed-plate condenser with the liquid receiver were presented in order to investigate the effects of the accumulators in transients generated by control actions (e.g. those imposed in Test 1 and Test 2). Whilst the suction accumulator was treated as a single lumped parameter characterized by the refrigerant mean density and pressure

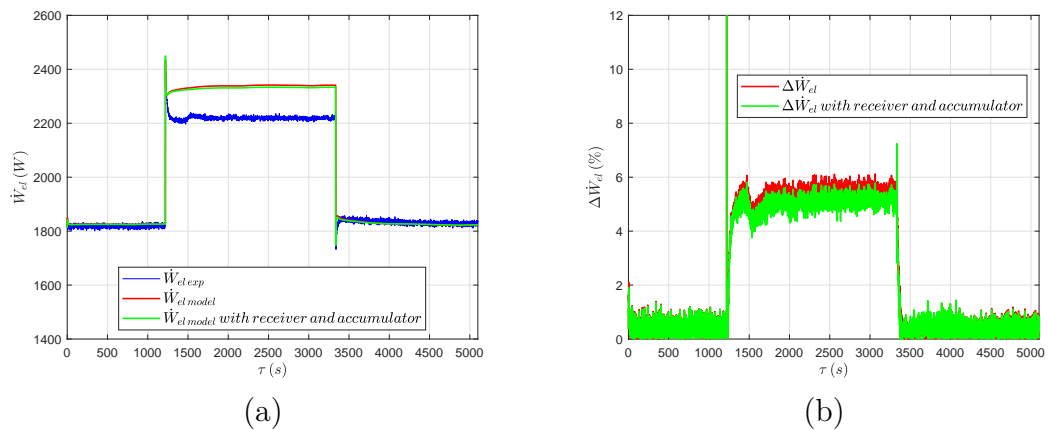


Figure 6.16: Validation of the complete model. Electric power absorption (a) and its percentage deviation (b) under Test 2 conditions.

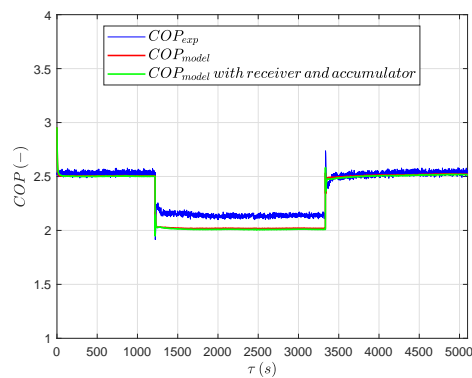


Figure 6.17: Validation of the complete model. COP under Test 2 conditions.

(the same as the evaporator), the receiver was modelled with two nodes, associated with the liquid and vapour phase respectively. To allow the coexistence of a non-zero degree of subcooling at the condenser outlet and partial filling condition of the receiver when the machine reaches steady-state conditions, which is a quite common situation in practice, the vapour phase was considered as incondensable and the heat and mass transfer between the liquid and vapour phases were neglected. The pressure within the receiver was assumed to be the same as that at the condenser.

A dynamic model of the whole water-to-water refrigerating machine was then implemented and used to simulate the transients which characterized the experimental tests presented in Chapter 5. Results were compared to experimental data and to the numerical predictions obtained by means of the model without accumulators. Under both Test 1 and Test 2 conditions, the presence of the liquid receiver allowed to better capture the pressure, whilst the suction accumulator ensured a better agreement between the predicted and experimental temperatures of the refrigerant at the compressor inlet. The better prediction of the refrigerant pressures also allowed to better estimate the electric power consumption of the compressor. Under Test 1 conditions, the

combined model of the condenser with the liquid receiver also offered a better estimation of the degree of subcooling, whilst under Test 2 conditions an under-estimation of about 0.5 K with respect to the simpler model was highlighted. In both tests, the combined model of the condenser with the receiver proved its capability to work with a non-zero degree of subcooling and a partial filling condition. To the author's best knowledge, this is the first model realized with a lumped-parameter approach able to simulate such a behaviour. No particular differences were highlighted between the two models as for the prediction of the refrigerant outlet temperatures and superheating, secondary fluid outlet temperatures and COP. Further investigations, including experimental validation, will focus on the simulation of the off-duty conditions, considering the dynamics of the liquid receiver and of the suction accumulator too.

Conclusions and outlook

Advanced control strategies represent a central field of investigation for the refrigeration sector and dynamic models represent a useful analysis tool and a potential source of economic savings. The aim of this work was to obtain a library of models able to simulate the transient behaviour of each component of a vapour compression refrigerating machine (evaporator, condenser, EEV and compressor) in order to investigate the influence of regulation systems on energy consumption, efficiency and control quality of this kind of systems.

When dealing with transient energy analysis of vapour-compression refrigerating machines, the fundamental time-scale to be investigated is mainly influenced by the thermal dynamics of the components, and in particular by that of the heat exchangers. In order to obtain a good trade-off between model reliability and low computational cost, thus making the model useful for control design, the SMB approach was preferred to the FCV technique in the modelling of the evaporator and the condenser. Besides finned-tube heat exchangers, the moving boundary approach was also extended to the brazed-plate heat exchangers, of high interest in the applications with secondary fluids different from air, because of their low volume which requires a smaller refrigerant charge and subsequently reduces the environmental impact. Moreover, an off-duty formulation of the heat exchangers model to simulate the machine off periods was realized, in order to ensure better numerical stability and mass conservation.

A dynamic model of a reciprocating compressor was realized on the basis of polynomials given by manufacturers. Whilst the refrigerant mass flow rate and the electric power absorption were algebraically computed through the polynomials, the refrigerant outlet enthalpy was evaluated through a first-order ODE, in order to consider the thermal dynamics of the machine too.

The electronic expansion valve was described by algebraic equations in the calculation of both the refrigerant mass flow rate and of outlet enthalpy, since the time-scales of the transformations occurring inside the component are orders of magnitude lower than those related to the thermal dynamics of the heat exchangers and compressor.

A first proof of the in-house code reliability for the prediction of the main physical variables of a vapour-compression cycle and of its behaviour in transient conditions was given by the numerical verification of the finned-tube heat exchangers and the EEV carried out using the Thermosys[®] toolbox as a benchmark, since it also uses the SMB approach in the modelling of the heat exchangers and it has been devised for control design purposes. A comparison

between the numerical predictions of the Unibo and Thermosys[®] models was carried out imposing sudden steps in the EEV aperture and in the compressor rotation frequency, which give rise to transients typical of control actions. Very similar responses were highlighted in terms of refrigerant mass flow rate through the EEV, refrigerant pressure and air outlet temperature. The main discrepancies were highlighted for the refrigerant superheating and subcooling at the outlet of the heat exchangers, mainly because of possible differences in the heat transfer correlations used; in addition, the Unibo model showed a better repeatability in the prediction of these two quantities and of the refrigerant charge, which is a variable of high interest, as it directly affects the environmental impact of such systems. Also, some drawbacks like the absence of the electric power consumption among the compressor outlets and numerically forced behaviour of the heat exchangers under certain conditions limit the use of Thermosys in transient energy analysis, thus justifying the development of another code more suited to the task.

The experimental validation carried out through comparisons between the numerical predictions and the experimental data measured on a water-to-water machine during transients imposed by typical control actions gave a strong proof of the model predictive capabilities in terms of refrigerant and secondary fluid conditions at the heat exchangers (thus justifying the use of the SMB approach in the modelling of the brazed-plates heat exchangers), electric power absorption and COP, making the model suitable to analyse the effects of control logics on the energy efficiency of VCSs. After tuning of the EEV fully-open discharge coefficient C_{D0} , of the time-constant τ_k and the tuning coefficients $C_{\dot{m}_r}$, $C_{\dot{W}_{el}}$ and C_T in the compressor model, leaving the correction factors related to the heat transfer coefficients in the heat exchangers untouched, the agreement between numerical and experimental data was already good. This aspect proves that reliability of the whole system strongly depends on the accuracy of the models of the components that ensure proper mass flow rate throughout the loop and especially on the compressor model. The main cause of the discrepancies highlighted for the compressor is thought to lie in possible inaccuracies of the polynomials at frequencies different from the nominal value and in the oversimplified nature of the model. Increasing the complexity and thus the order of the compressor model can lead to more precise results. Tuning the correction factors for the heat transfer coefficients in the model of the heat exchangers allowed to better capture the refrigerant pressure and, in particular, the refrigerant outlet temperature; a subsequent improvement in the prediction of the electric power absorption and of the COP was also highlighted.

In the last part of the work, the effects of the suction accumulator and of the liquid receiver on the dynamics of the vapour-compression refrigerating machine during transients caused by typical control actions were investigated. Particular attention was paid in the development of a model which combined the dynamics of the condenser and the receiver, allowing the coexistence of a non-zero degree of subcooling at the condenser outlet and partial filling condition of the receiver when the machine reaches steady-state conditions.

Simulations were carried out considering the model of the whole machine including the accumulators and imposing the same control actions used in the experimental campaign. The results were compared to experimental data and to the numerical predictions of the model without accumulators, showing an improvement in the estimation of the pressure and of the refrigerant conditions at the compressor inlet. The combined model of the condenser with receiver proved its capability to work with a non-zero degree of subcooling and a partial filling condition, and represents, to the author's best knowledge, the first lumped-parameter model able to simulate such a behaviour. In the near future, the combined models of the evaporator and the suction accumulator, and of the condenser and the receiver will be integrated with an off-duty formulation in order to allow transient energy analysis involving on-off control strategies for the compressor.

Further investigations, including experimental validation, will focus on the simulation of the off-duty conditions, considering the dynamics of the liquid receiver and of the suction accumulator too.

Bibliography

- [1] A. Mota-Babiloni, J. Navarro-Esbri, A. Barragan-Cervera, F. Molés, B. Peris, and G. Verdu. Commercial refrigeration - an overview of current status. *International Journal of Refrigeration*, 57:186–196, 2015.
- [2] I. P. Koronaki, D. Cowan, G. Maidment, K. Beerman, M. Schreurs, K. Kaar, I. Chaer, G. Gontarz, R. I. Christodoulaki, and X. Cazauran. Refrigerant emissions and leakage prevention across europe - results from the realskillseurope project. *Energy*, 45(1):71–80, 2012.
- [3] C.Park, H.Lee, Y.Hwang, and R.Radermacher. Recent advances in vapor compression cycle technologies. *International Journal of Refrigeration*, 60:118–134, 2015.
- [4] C. Arpagaus, F. Bless, J. Schiffmann, and S. S. Bertsch. Multi-temperature heat pumps: A literature review. *International Journal of Refrigeration*, 69:437–465, 2016.
- [5] J. Lundén, V. Vanhanen, T. Myllymaki, E. Laamanen, K. Kotilainen, and K. Hemminki. Temperature control efficacy of retail refrigeration equipment. *Food Control*, 45:109–114, 2014.
- [6] P. Li, H. Qiao, Y. Li, J. E. Seem, J. Winkler, and X. Li. Recent advances in dynamic modeling of hvac equipment. part i: Equipment modeling. *HVAC&R Research*, 20:136–149, 2014.
- [7] *Refrigeration and air conditioning*. Butterworth-Heinemann, 2008.
- [8] B. Palm. Hydrocarbons as refrigerants in small heat pump and refrigeration systems - a review. *International Journal of Refrigeration*, 31(4):552–563, 2008.
- [9] *Refrigeration systems and applications*. Wiley, 2010.
- [10] P. A. Domanski, D. A. Didion, and J. P. Doyle. Evaluation of suction-line/liquid-line heat exchange in the refrigeration cycle. *International Journal of Refrigeration*, 17(7):487–493, 1994.
- [11] A. Rozhentsev and C. Wang. Some design features of a CO_2 air conditioner. *Applied Thermal Engineering*, 21(8):871–880, 2001.

- [12] H. Cho, C. Ryu, and Y. Kim. Cooling performance of a variable speed CO_2 cycle with an electronic expansion valve and internal heat exchanger. *International Journal of Refrigeration*, 30(4):664–671, 2007.
- [13] M. Preissner, B. Cutler, R. Radermacher, and C. A. Zhang. Suction line heat exchanger for R134a automotive air-conditioning system. *Proceedings of the International Refrigeration Conference*, pages 289–294, 2000.
- [14] J. Navarro-Esbrí, F. Molés, and Á. Barragán-Cervera. Experimental analysis of the internal heat exchanger influence on a vapour compression system performance working with R1234yf as a drop-in replacement for R134a. *Applied Thermal Engineering*, 59(1-2):153–161, 2013.
- [15] H. Cho, H. Lee, and C. Park. Performance characteristics of an automobile air conditioning system with internal heat exchanger using refrigerant R1234yf. *Applied Thermal Engineering*, 61(2):563–569, 2013.
- [16] G. Pottker and P. Hrnjak. Experimental investigation of the effect of condenser subcooling in R134a and R1234yf air-conditioning systems with and without internal heat exchanger. *International Journal of Refrigeration*, 50:104–113, 2015.
- [17] J. W. Thornton, S. A. Klein, and J. W. Mitchell. Dedicated mechanical subcooling design strategies for supermarket applications. *International Journal of Refrigeration*, 17(8):508–515, 1994.
- [18] J-U-R Khan and S. M. Zubair. Design and rating of an integrated mechanical-subcooling vapor-compression refrigeration system. *Energy Conversion and Management*, 41(11):1201–1222, 2000.
- [19] B. A. Qureshi and S. M. Zubair. The effect of refrigerant combinations on performance of a vapor compression refrigeration system with dedicated mechanical sub-cooling. *International Journal of Refrigeration*, 35(1):47–57, 2012.
- [20] X. She, Y. Yin, and X. Zhang. A proposed subcooling method for vapor compression refrigeration cycle based on expansion power recovery. *International Journal of Refrigeration*, 43:50–61, 2014.
- [21] J. Bush, M. Beshr, V. Aute, and R. Radermacher. Experimental evaluation of transcritical CO_2 refrigeration with mechanical subcooling. *Science and Technology for the Built Environment*, 23(6):1013–1025, 2017.
- [22] J. Bush, V. Aute, and R. Radermacher. Transient simulation of carbon dioxide booster refrigeration system with mechanical subcooler in demand response operation. *Science and Technology for the Built Environment*, 24(7):687–699, 2018.

- [23] J. Schoenfeld, Y. Hwang, and R. Radermacher. CO_2 transcritical vapor compression cycle with thermoelectric subcooler. *HVAC and R Research*, 18(3):297–311, 2012.
- [24] J. Sarkar. Performance optimization of transcritical CO_2 refrigeration cycle with thermoelectric subcooler. *International Journal of Energy Research*, 37(2):121–128, 2013.
- [25] B. Dai, S. Liu, K. Zhu, Z. Sun, and Y. Ma. Thermodynamic performance evaluation of transcritical carbon dioxide refrigeration cycle integrated with thermoelectric subcooler and expander. *Energy*, 122:787–800, 2017.
- [26] L. Cecchinato, M. Corradi, and S. Minetto. Energy performance of supermarket refrigeration and air conditioning integrated systems. *Applied Thermal Engineering*, 30:1946–1958, 2010.
- [27] K. Wang, M. Eisele, Y. Hwang, and R. Radermacher. Review of secondary loop refrigeration systems. *International Journal of Refrigeration*, 33(2):212–234, 2010.
- [28] S. A. Tassou, Y. Ge, A. Hadawey, and D. Marriott. Energy consumption and conservation in food retailing. *Applied Thermal Engineering*, 31(2-3):147–156, 2011.
- [29] V. Minea. Supermarket refrigeration system with completely secondary loops. *ASHRAE Journal*, 49(9):40, 2007.
- [30] V. Minea. Low charge and low emission supermarket refrigeration systems. In *Proceedings of the Eighth IIR Gustav Lorentzen Conference on Natural Working Fluids*.
- [31] G. Bagarella. *Regolazione ottima dei circuiti frigoriferi con particolare attenzione all'efficienza energetica*. PhD thesis, Universita' di Padova, 2015.
- [32] G. Bagarella, R. Lazzarin, and M. Noro. Annual energy analysis of a water-loop self-contained refrigeration plant and comparison with multiplex systems in supermarkets. *International Journal of Refrigeration*, 45:55–63, 2014.
- [33] L. Vaitkus and V. Dagilis. Refrigerant charge reduction in low-temperature transport refrigerator with the eutectic plate evaporator. *International Journal of Refrigeration*, 47:46–57, 2014.
- [34] *Le centrali frigorifere*. Editoriale Delfino, 2006.
- [35] *Controlli automatici*. Zanichelli, 2008.
- [36] M. J. P. Janssen, J. A. de Wit, and L. J. M. Kuijpers. Cycling losses in domestic appliances: an experimental and theoretical analysis. *International Journal of Refrigeration*, 15(3):152–158, 1992.

- [37] P. J. Rubas and C. W. Bullard. Factors contributing to refrigerator cycling losses. *International Journal of Refrigeration*, 18(3):168–176, 1995.
- [38] E. Björk and B. Palm. Refrigerant mass charge distribution in a domestic refrigerator, part i: Transient conditions. *Applied Thermal Engineering*, 26(8-9):829–837, 2006.
- [39] G. Bagarella, R. M. Lazzarin, and B. Lamanna. Cycling losses in refrigeration equipment: An experimental evaluation. *International Journal of Refrigeration*, 36(8):2111–2118, 2013.
- [40] Y.T. Ge and S. Tassou. Mathematical modelling of supermarket refrigeration systems for design, energy prediction and control. In *Proceedings of the Institution of Mechanical Engineers*.
- [41] C. Cuevas and J. Lebrun. Testing and modelling of a variable speed scroll compressor. *Applied Thermal Engineering*, 29(2-3):469–478, 2009.
- [42] H. Madani, N. Ahmadi, J. Claesson, and P. Lundqvist. Experimental analysis of a variable capacity heat pump system focusing on the compressor and inverter loss behavior. In *Proceedings of the International Refrigeration and Air Conditioning Conference*.
- [43] S. A. Tassou and T. Q. Qureshi. Comparative performance evaluation of positive displacement compressors in variable-speed refrigeration applications. *International Journal of Refrigeration*, 21(1):29–41, 1998.
- [44] H. Madani, J. Claesson, and P. Lundqvist. Capacity control in ground source heat pump systems part ii: Comparative analysis between on/off controlled and variable capacity systems. *International Journal of Refrigeration*, 34(8):1934–1942, 2011.
- [45] W. Gruhle and R. Isermann. Modeling and control of a refrigerant evaporator. *Journal of Dynamic Systems, Measurement and Control, Transactions of the ASME*, 107(4):235–240, 1985.
- [46] Z.R. Huelle. Heat load influence upon evaporator parameters. In *Proceedings of the XIIth International Refrigeration Congress*.
- [47] Z.R. Huelle. Thermal balance of evaporators fed through thermostatic expansion valve. In *Proceedings of the XIIth International Refrigeration Congress*.
- [48] Z.R. Huelle. New points of view on evaporator liquid supply control by thermostatic expansion valves. part 1. *Danfoss Journal*, (1), 1968.
- [49] Z.R. Huelle. New points of view on evaporator liquid supply control by thermostatic expansion valves. part 2. *Danfoss Journal*, (3), 1969.

- [50] M. Dhar and W. Soedel. Transient analysis of a vapor compression refrigeration system. part 1 - the mathematical model. volume 2, pages 1035–1048, 1980.
- [51] M. Dhar and W. Soedel. Transient analysis of a vapor compression refrigeration system. part 2- computer simulation and results. volume 2, pages 1049–1067, 1980.
- [52] K. Higuchi and M. Hayano. Dynamic characteristics of thermostatic expansion valves. *International Journal of Refrigeration*, 5(4):216–220, 1982.
- [53] P. Mithraratne, N. E. Wijesundera, and T. Y. Bong. Dynamic simulation of a thermostatically controlled counter-flow evaporator. *International Journal of Refrigeration*, 23(3):174–189, 2000.
- [54] H. Yasuda, S. Nakayama, Y. Hibino, and K. Tanaka. Modelling of refrigeration cycle dynamics for air conditioner. *Transactions of the Japan Society of Mechanical Engineers Series C*, 60(573):1589–1596, 1994.
- [55] W. Chen, C. Zhijiu, Z. Ruiqi, and W. Yezheng. Experimental investigation of a minimum stable superheat control system of an evaporator. *International Journal of Refrigeration*, 25:1137–1142, 2002.
- [56] S. Tassou and H.O. Al-Nizari. Effect of refrigerant flow control on the thermodynamic performances of reciprocating chillers. *Applied Energy*, 45:101–116, 1993.
- [57] F. W. Yu, K. T. Chan, and H. Y. Chu. Constraints of using thermostatic expansion valves to operate air-cooled chillers at lower condensing temperatures. *Applied Thermal Engineering*, 26(17-18):2470–2478, 2006.
- [58] Donal P. Finn and Cormac J. Doyle. Control and optimization issues associated with algorithm-controlled refrigerant throttling devices. In *ASHRAE Transactions*, volume 106, 2000.
- [59] P. G. Jolly, C. P. Tso, P. K. Chia, and Y. W. Wong. Intelligent control to reduce superheat hunting and optimize evaporator performance in container refrigeration. *HVAC&R Research*, 6(3):243–255, 2000.
- [60] Q. Qi, S. Deng, X. Xu, and M. Y. Chan. Improving degree of superheat control in a direct expansion (dx) air conditioning (a/c) system. *International Journal of Refrigeration*, 33(1):125–134, 2010.
- [61] Q. Qi and S. Deng. Multivariable control-oriented modeling of a direct expansion (dx) air conditioning (a/c) system. *International Journal of Refrigeration*, 31(5):841–849, 2008.
- [62] Q. Qi and S. Deng. Multivariable control of indoor air temperature and humidity in a direct expansion (dx) air conditioning (a/c) system. *Building and Environment*, 44(8):1659–1667, 2009.

- [63] T. S. S. Siqueira Dantas, I. C. Franco, A. M. F. Fileti, and F. V. Silva. Dynamic linear modeling of a refrigeration process with electronic expansion valve actuator. *International Journal of Refrigeration*, 75:311–321, 2017.
- [64] K. A. Manske, D. T. Reindl, and S. A. Klein. Evaporative condenser control in industrial refrigeration systems. *International Journal of Refrigeration*, 24(7):676–691, 2001.
- [65] F. W. Yu and K. T. Chan. Advanced control of heat rejection airflow for improving the coefficient of performance of air-cooled chillers. *Applied Thermal Engineering*, 26(1):97–110, 2006.
- [66] F. W. Yu and K. T. Chan. Improved energy performance of air cooled centrifugal chillers with variable chilled water flow. *Energy Conversion and Management*, 49(6):1595–1611, 2008.
- [67] J. Arias and P. Lundqvist. Heat recovery and floating condensing in supermarkets. *Energy and Buildings*, 38(2):73–81, 2006.
- [68] Y. T. Ge and S. A. Tassou. Control optimizations for heat recovery from co2 refrigeration systems in supermarket. *Energy Conversion and Management*, 78:245–252, 2014.
- [69] A. Polzot, P. D’Agaro, and G. Cortella. Energy analysis of a transcritical co2 supermarket refrigeration system with heat recovery. In *Energy Procedia*, volume 111, pages 648–657, 2017.
- [70] B. P. Rasmussen. Dynamic modeling for vapor compression systems-Part I: Literature review. *HVAC&R Research*, 18(5):934–955, 2012.
- [71] S. Bendapudi and J.E. Braun. A review of literature on dynamic models of vapor compression equipment. Technical report, ASHRAE, 2002.
- [72] J. M. Fasl. Modeling and control of hybrid vapor compression cycles. Master’s thesis, University of Illinois - Urbana-Champaign, 2013.
- [73] B. P. Rasmussen and B. Shenoy. Dynamic modeling for vapor compression systems-Part II: Simulation tutorial. *HVAC&R Research*, 18(5):956–973, 2012.
- [74] S. Bendapudi, J. E. Braun, and E. A. Groll. A comparison of moving-boundary and finite-volume formulations for transients in centrifugal chillers. *International Journal of Refrigeration*, 31(8):1437–1452, 2008.
- [75] G.L. Wedekind, B.L. Bhatt, and B.T. Beck. A system mean void fraction model for predicting various transient phenomena associated with two-phase evaporating and condensing flows. *International Journal of Multiphase Flow*, 4(1):97–114, 1978.

- [76] E. W. Grald and J. W. MacArthur. A moving-boundary formulation for modeling time-dependent two-phase flows. *International Journal of Heat and Fluid Flow*, 13(3):266–272, 1992.
- [77] X. . He, S. Liu, H. H. Asada, and H. Itoh. Multivariable control of vapor compression systems. *HVAC&R Research*, 4(3):205–230, 1998.
- [78] D. Leducq, J. Guilpart, and G. Trystram. Low order dynamic model of a vapor compression cycle for process control design. *Journal of Food Process Engineering*, 26(1):67–91, 2003.
- [79] M. Kumar, I. N. Kar, and A. Ray. State space based modeling and performance evaluation of an air-conditioning system. *HVAC&R Research*, 14(5):797–816, 2008.
- [80] B. P. Rasmussen and A. G. Alleyne. Control-oriented modeling of transcritical vapor compression systems. *Journal of Dynamic Systems, Measurement and Control, Transactions of the ASME*, 126(1):54–64, 2004.
- [81] Z. Lei and M. Zaheeruddin. Dynamic simulation and analysis of a water chiller refrigeration system. *Applied Thermal Engineering*, 25(14-15):2258–2271, 2005. Cited By :37.
- [82] M. Willatzen, N. B. O. L. Pettit, and L. Ploug-Sørensen. A general dynamic simulation model for evaporators and condensers in refrigeration. Part I: Moving-boundary formulation of two-phase flows with heat exchange. *International Journal of Refrigeration*, 21(5):398–403, 1998.
- [83] N. B. O. L. Pettit, M. Willatzen, and L. Ploug-Sørensen. A general dynamic simulation model for evaporators and condensers in refrigeration. Part II: Simulation and control of an evaporator. *International Journal of Refrigeration*, 21(5):404–414, 1998. Cited By :58.
- [84] B. Li and A.G. Alleyne. A dynamic model of a vapor compression cycle with shut-down and start-up operations. *International Journal of Refrigeration*, 33 (3):538–552, 2010.
- [85] T.L. McKinley and A.G. Alleyne. An advanced nonlinear switched heat exchanger model for vapor compression cycles using the moving-boundary method. *International Journal of Refrigeration*, 31:1253–1264, 2008.
- [86] B. D. Eldredge, B. P. Rasmussen, and A. G. Alleyne. Moving-boundary heat exchanger models with variable outlet phase. *Journal of Dynamic Systems, Measurement and Control, Transactions of the ASME*, 130(6):0610031–06100312, 2008.
- [87] L. Cecchinato and F. Mancini. An intrinsically mass conservative switched evaporator model adopting the moving-boundary method. *International Journal of Refrigeration*, 35:349–364, 2012.

- [88] H. Qiao, C. R. Laughman, V. Aute, and R. Radermacher. An advanced switching moving boundary heat exchanger model with pressure drop. *International Journal of Refrigeration*, 65:154–171, 2016.
- [89] E. Rodriguez and B. Rasmussen. A comparison of modeling paradigms for dynamic evaporator simulations with variable fluid phases. *Applied Thermal Engineering*, 112:1326–1342, 2017.
- [90] B.P. Rasmussen, R. Shah, A.B. Musser, A.G. Alleyne, C.W. Bullard, P.S. Hrnjak, and N.R. Miller. Control-oriented modeling of transcritical vapor compression systems. Technical report, Air Conditioning and Refrigeration Center - University of Illinois at Urbana-Champaign, 2002.
- [91] B.P. Rasmussen and A.G. Alleyne. Dynamic modeling and advance control of air conditioning and refrigeration systems. Technical report, Air Conditioning and Refrigeration Center - University of Illinois at Urbana-Champaign, 2006.
- [92] F. Poggi, H. Macchi-Tejeda, D. Leducq, and A. Bontemps. Refrigerant charge in refrigerating systems and strategies of charge reduction. *International Journal of Refrigeration*, 31(3):353–370, 2008.
- [93] S. M. Zivi. Estimation of steady-state steam void-fraction by means of the principle of minimum entropy production. *Journal of Heat Transfer*, 86(2):247–251, 1964.
- [94] G.A. Longo, S. Mancin, G. Righetti, and C. Zilio. A new model for refrigerant boiling inside brazed plate heat exchangers (bphes). *International Journal of Heat and Mass Transfer*, 91:144–149, 2015.
- [95] J. P. Wattlelet, J. C. Chato, B. R. Christoffersen, M. Ponchner J. A. Gaibel, P. J. Kenney, R. L. Shimon, T. C. Villaneuva, N. L. Rhines, K. A. Sweeney, D. G. Allen, , and T. T. Hershberger. Heat transfer flow regimes of refrigerants in a horizontal-tube evaporator. Technical report, ACRC, 1994.
- [96] *Fundamentals of heat and mass transfer*. JOHN WILEY & SONS, 2011.
- [97] *Compact heat exchangers*. Krieger Publishing, 1998.
- [98] B. Palm and J. Claesson. Plate heat exchangers: Calculation methods for single- and two-phase flow. *Heat Transfer Engineering*, 27(4):88–98, 2006.
- [99] G.A. Longo, G. Righetti, and C. Zilio. A new computational procedure for refrigerant condensation inside herringbone-type brazed plate heat exchangers. *International Journal of Heat and Mass Transfer*, 82:530–536, 2015.

- [100] M. Lucchi, M. Lorenzini, and P. Valdiserri. Energy performance of a ventilation system for a block of apartments with a ground source heat pump as generation system. In *Journal of Physics: Conference Series*, volume 796, 2017.
- [101] MathWorks. Simulink[®]developing s-functions. 2018.
- [102] I. H. Bell, J. Wronski, S. Quoilin, and V. Lemort. Pure and pseudo-pure fluid thermophysical property evaluation and the open-source thermophysical property library coolprop. *Industrial and Engineering Chemistry Research*, 53(6):2498–2508, 2014.
- [103] E. W. Lemmon, , Ian H. Bell, M. L. Huber, and M. O. McLinden. NIST Standard Reference Database 23: Reference Fluid Thermodynamic and Transport properties-REFPROP, Version 10.0, National Institute of Standards and Technology, 2018.
- [104] CU Aerospace. Thermosys version 4. 2013, [<http://thermosys.us>].
- [105] A. Alleyne et al. Thermosys 4 toolbox. University of Illinois at Urbana-Champaign, 2012, [<http://arg.mechse.illinois.edu/index.php?id=1161%7CTHERMOSYS>].
- [106] F. Bocchinfuso. Experimental investigation of r1234ze(e) and r1234yf as r134a drop-in alternatives in a vapour compression system. Master’s thesis, Politecnico di Milano, 2019.
- [107] L. Molinaroli, A. Lucchini, and L. Pietro Maria Colombo. Design and commissioning of an experimental facility for performance evaluation of pure and mixed refrigerants. In *Journal of Physics: Conference Series*, volume 1224, 2019.
- [108] J. R. García-Cascales, F. Vera-García, J. M. Corberán-Salvador, and J. González-Maciá. Assessment of boiling and condensation heat transfer correlations in the modelling of plate heat exchangers. *International Journal of Refrigeration*, 30(6):1029–1041, 2007.
- [109] Giulio Busato. *Analisi teorica e sperimentale sulle pompe di calore*. PhD thesis, Università di Padova - Scuola di Dottorato di Ricerca in Ingegneria Industriale (Fisica Tecnica), 2013.